Hydrogen injection in an air-filled two-vented cavity: numerical simulations, experimental comparisons and 1D modelling

Yanshu Wang

▶ **To cite this version:**

Yanshu Wang. Hydrogen injection in an air-filled two-vented cavity: numerical simulations, experimental comparisons and 1D modelling. Fluids mechanics [physics.class-ph]. Sorbonne Université, 2021. English. NNT : . tel-03850705v1

HAL Id: tel-03850705

https://theses.hal.science/tel-03850705v1

Submitted on 15 Jul 2021 (v1), last revised 14 Nov 2022 (v2)

HAL is a multi-disciplinary open access archive for the deposit and dissemination of scientific research documents, whether they are published or not. The documents may come from teaching and research institutions in France or abroad, or from public or private research centers.

L'archive ouverte pluridisciplinaire **HAL**, est destinée au dépôt et à la diffusion de documents scientifiques de niveau recherche, publiés ou non, émanant des établissements d'enseignement et de recherche français ou étrangers, des laboratoires publics ou privés.

SORBONNE UNIVERSITÉ

École doctorale 391 - Sciences Mécaniques, Acoustique, Électronique et Robotique de Paris (SMAER)

Laboratoire d'Instrumentation et Expérimentation en mécanique des Fluides et Thermohydraulique (LIEFT), CEA Saclay

Laboratoire Interdisciplinaire des Sciences du Numérique (LISN) - UMR9015 CNRS

Injection d'hydrogène dans une cavité à deux évents : simulations numériques, comparaisons expérimentales et modélisation 1D

Hydrogen injection in an air-filled two-vented cavity: numerical simulations, experimental comparisons and 1D modelling

Par **WANG YANSHU**

Thèse de doctorat de **MÉCANIQUE DES FLUIDES**

Dirigée par **ANNE SERGENT**
Co-encadrée par **GILLES BERNARD-MICHEL** et **PATRICK LE QUÉRÉ**

Présentée et soutenue publiquement le 28 juin 2021

Devant un jury composé de :

LAGRÉE PIERRE-YVES	Directeur de l'Institut Jean le Rond ∂'Alembert Sorbonne Université, Directeur de recherche CNRS	Président Examinateur
SALIZZONI PIETRO	Professeur à l'École Centrale de Lyon	Rapporteur
VAUQUELIN OLIVIER	Professeur à l'université d'Aix-Marseille	Rapporteur
VYAZMINA ELENA	Ingénieure docteure R&D Spécialiste internationale chez Air Liquide	Examinatrice
SERGENT ANNE	Maître de conférences HDR à Sorbonne Université	Directrice de thèse
BERNARD-MICHEL GILLES	Ingénieur docteur de recherche Chef de Laboratoire LIEFT, CEA Saclay	Co-encadrant de thèse
LE QUÉRÉ PATRICK	Directeur de recherche CNRS	Co-encadrant de thèse

Résumé

L'hydrogène est considéré comme une source d'énergie verte et alternative pour sa faible émission de CO_2. En raison du risque élevé de déflagration et détonation du mélange air-hydrogène, des mesures de sécurité spécifiques sont nécessaires pour son utilisation pratique. Nous nous intéressons à une configuration modélisant la distribution d'hydrogène (ou d'hélium) en situation accidentelle pour des environnements confinés. Des simulations numériques directes (DNS) d'un jet turbulent d'hydrogène dans une cavité à deux évents sont réalisées, obtenant une distribution en bicouche de l'hydrogène avec un mélange homogène en moyenne en partie haute. Les DNS sont d'abord comparées à des mesures par vélocimétrie par images de particules (PIV) pour validation, puis l'écoulement est analysé. Afin d'estimer la pertinence des modèles prédictifs de ventilation proposés dans la littérature pour évaluer la sûreté des installations, les champs DNS sont intégrés pour calculer les grandeurs caractéristiques du jet et celles de la distribution d'hydrogène. Ces résultats sont comparés à des modèles simplifiés de ventilation naturelle basés sur différents modèles de jets turbulents. Ces modèles reposent sur une série d'hypothèses dont la validité est examinée. L'influence du coefficient d'entraînement du jet et des méthodes de son estimation sont discutées, (i) dans le cadre des modèles de jet à coefficient constant ou variable, (ii) sous l'approximation de Boussinesq ou en tenant compte des variations de masse volumique du mélange. Enfin, des formulations modifiées des modèles de ventilation sont proposées pour les adapter au cas d'une injection d'hydrogène dans une cavité à deux évents. gène dans une cavité à deux évents.

Mots clés : Sécurité et sûreté d'hydrogène ; Dispersion des gaz ; Simulation numérique directe (CFD-DNS) ; Modèles de jet turbulent ; Modèles de ventilation naturelle ; Coefficient d'entraînement

Abstract

Hydrogen is considered as one of the green and alternative energy sources because of its low CO_2 emission. Due to the high risk of deflagration and detonation of air-hydrogen mixture, appropriate safety measures are required for its practical use. We are interested in a configuration modelling the distribution of hydrogen (or helium) in accidental release situation for confined environments. Direct numerical simulations (DNS) of a turbulent hydrogen jet in a two-vented cavity are performed, leading to the establishment of a bilayer hydrogen distribution with a homogeneous top layer on average. Numerical results are compared with Particle Image Velocimetry (PIV) measurements for validation. The flow is then analysed. In order to assess the relevance of the predictive ventilation models proposed in the literature to evaluate the installation safety, the DNS fields are integrated to calculate the characteristic quantities of the jet and of the hydrogen distribution. These results are compared to simplified natural ventilation models based on different turbulent jet models. These models are developed on the basis of a series of assumptions the validity of which is examined. The influence of the jet entrainment coefficient and its estimation methods are discussed, (i) in the context of turbulent jet models with constant or variable coefficient, (ii) under Boussinesq approximation or with consideration of the mixture density variation. Finally, modified formulations of the ventilation models are proposed to adapt them to the case of hydrogen injection in a two-vent cavity.

Keywords: Hydrogen safety; Gas dispersion; Direct Numerical Simulation (CFD-DNS); Turbulent jet model; Natural ventilation model; Entrainment coefficient

Acknowledgements

This thesis is prepared in *Laboratoire d'Instrumentation et Expérimentation en mécanique des Fluides et Thermohydraulique* (LIEFT) - CEA Saclay DES/ISAS/DM2S/STMF, in collaboration with *Laboratoire Interdisciplinaire des Sciences du Numérique* (LISN) - UMR9015 CNRS from the middle of October 2017, under the direction of Ms Anne SERGENT, Associate Professor at Sorbonne University, Mr Gilles BERNARD-MICHEL, Laboratory Manager LIEFT and Mr Patrick LE QUÉRÉ, CNRS Exceptional-Grade Senior Research Director. The author would like to firstly express his sincere gratitude to his thesis advisor and supervisors for their immense knowledge, plentiful experience, enthusiasm, patience, and their invaluable supervision and continuous guidance all along the project.

The author would like to acknowledge his thesis reviewers: Mr Pietro SALIZZONI and Mr Olivier VAUQUELIN and other members of defence committee: Mr Pierre-Yves LAGRÉE and Ms Elena VYAZMINA for their valuable advice.

The author would like to acknowledge the thesis funder: *Service de Thermohydraulique et de Mécanique des Fluides* (STMF), CEA Saclay and its (current and former) direction members: Mr Pierre GAVOILLE, Ms Danielle GALLO-LEPAGE, Mr Jacques SEGRE, Mr Philippe FILLION, Mr Jean-Paul GARANDET, Mr Xavier TIRATAY, Mr Gilles BERNARD-MICHEL, Mr Eric PROUST and Mr Bertrand MERCIER. The author would also like to acknowledge Paris-Saclay University for its financial support during the final stage of this project. The author would also like to thank direction members of laboratory LISN and LIMSI (the old name of LISN before 2021): Ms Sophie ROSSET, Mr François YVON and Mr Christian TENAUD.

The numerical part of this work is granted access to the HPC resources of three French national computing centres CINES, IDRIS, and TGCC-CEA under allocation made by GENCI *(Grand Equipement National de Calcul Intensif)*. This work has benefited from the financial support of the LabeX LaSIPS (ANR-10-LABX-0032-LaSIPS) managed by the French National Research Agency under the *"Investissements d'avenir"* programme.

The author would like to thank all his colleagues and lab-mates in CEA and LISN for their support and encouragements. Special thanks to Dr Elie SAIKALI to his continuous help all along this work. Special thanks to Alexandre SCHORTGEN and Clément MELIN for their support of pre-processing work of experimental measurements. Special thanks to TrioCFD/TRUST support team especially to Nabil DJATI and Marthe ROUX for their assistance of the use of TrioCFD software.

The author would like to thank other people providing assistance at some stage of this work, including but not limited to: Ulrich BIEDER, Christophe BOURCIER, Benjamin CARITEAU, GAI Guodong, Nabil GHODBANE, Nikos LETERRIER, Étienne STUDER and Stéphane VINCENT. Special thanks to members of secretariat at CEA, LISN and Sorbonne University for their assistance in administrative procedures: Véronique LECHOPIED, Sophie PAGEAU-MAU -RICE and Charlotte VALLIN.

Finally, the author would like to appreciate personally all material and spiritual help, support and encouragements from his friends and family members during these years of study.

Contents

Nomenclature

Geometrical parameters

Symbol	Unit	Description
O		Global origin (injection centre) or local origin (jet centre)
(x, y, z) or (x_1, x_2, x_3)	m	Global Cartesian coordinates
(r, z)	m	Local polar coordinates (in 1D analysis)
H	m	Height of the cavity (in z direction)
W	m	Width of the cavity (in y direction)
L	m	Length of the cavity (in x direction)
H_v	m	Height of the openings (in z direction)
d	m	Injection tube diameter
h	m	Injection tube length (in z direction)
V_{cavity}	m^3	Volume of the main cavity ($H \times L \times W$)
S_{cavity}	m^2	Cross-section area of the main cavity ($L \times W$)

State quantities

Symbol	Unit	Description
P	Pa	Pressure
subscript P_{th}		Thermodynamic pressure
subscript P_H		Hydrodynamic pressure
T	$K(°C)$	Temperature

Mixture physical properties

Symbol	Unit	Description
M	kg/mol	Molar mass
ρ	kg/m^3	Density
μ	$kg/(m.s)$	Dynamic viscosity
ν	m^2/s	Kinematic viscosity ($= \mu/\rho$)
$D_{1,2}$	m^2/s	Diffusion coefficient
Y_1, Y_2		Mixture mass fraction (1 for injected gas He or H_2, 2 for pure air)
X_1, X_2		Mixture volume/molar fraction (1 for injected gas He or H_2, 2 for pure air)
subscript $_{inj}$		Injected pure gas related
subscript $_a$ or $_{air}$		Fresh air related
subscript $_{mix}$		Mixture related

Universal constant

Symbol	Unit	Description
R	$J/mol.K$	Ideal gas constant (=8.314 J/mol.K)

Vectors and tensors

Symbol	Unit	Description
$\overrightarrow{u}$ or (u,v,w) or (u_1,u_2,u_3)	m/s	Velocity vector
$\overrightarrow{g}=(0,0,-g)$	m/s^2	Gravitational vector ($g = 9.81 m/s^2$ gravitational acceleration)
$\overline{\overline{\tau}}=[\tau_{ij}]$ or τ_{ij}	$kg/(m.s^2)$	Viscosity stress tensor
S_{ij}	s^{-1}	Symmetrical part of strain rate tensor

Operators

Symbol	Unit	Description
div		Divergence
$\overrightarrow{\textbf{grad}}$		Gradient

Dimensionless number

Symbol	Unit	Description
Gr		Grashof number
Ra		Rayleigh number
Re		Reynolds number
Ri		Richardson number
Sc		Schmidt number

Local jet physical quantities

Symbol	Unit	Description
w or $w(r,z)$	m/s	Local vertical velocity
ρ or $\rho(r,z)$	kg/m^3	Local mixture density
X_1or $X_1(r,z)$		Local injected pure gas (He or H_2) volume/molar fraction
G' or $G'(r,z)$	m/s^2	Local buoyancy force acceleration
subscript $_T$		Top-hat characteristic quantities
subscript $_G$		Gaussian characteristic quantities
subscript $_e$		Environmental quantities (in the far field of the jet)
subscript $_0$		Reference quantities

Local jet shape parameters

Symbol	Unit	Description
b	m	Local characteristic jet radius
subscript b_T		Top-hat characteristic radius
subscript b_G		Gaussian characteristic radius
λ		Diffusion-convection ratio

Entrainment modelling

Symbol	Unit	Description
u_e	m/s	Entrainment velocity
α		Entrainment coefficient
subscript α_T		Entrainment coefficient under Top-hat assumption
subscript α_G		Entrainment coefficient under Gaussian assumption

Characteristic jet quantities

Symbol	Unit	Description
$\mathcal{Q}$	m^3/s	Volume flux
$\mathcal{Q}_m$	kg/s	Mass flux
$\mathcal{M}$	m^4/s^2	Momentum flux
$\mathcal{M}_m$	$kg.m/s^2$	Mass momentum flux
$\mathcal{B}$	m^4/s^3	Buoyancy flux
$\mathcal{B}^*$	m^4/s^3	Specific buoyancy flux as if the jet were immersed in an unstratified environment
subscript $_0$		Quantities at injection point or at position where z=0

Virtual origin related

Symbol	Unit	Description
z_t	m	Total virtual origin displacement ($z_t = z_0 + z_v + z_{avs}$)
z_0	m	Injection geometrical correction displacement
z_v	m	Source correction displacement
z_{avs}	m	Jet-length based correction displacement
z_B	m	Characteristic length of non-Boussinesq effect
Γ_0		Source parameter

Bi-layer parameters and related

Symbol	Unit	Description
z_i	m	Bi-layer interface height
z_n	m	Neutral plane height
ρ_i	kg/m^3	Mixture density in the top homogeneous layer
ρ_a	kg/m^3	Density of the pure air (fresh air)
ρ_0	kg/m^3	Reference density (= ρ_a in this problem)
ρ_e	kg/m^3	Mixture density in the far field of the jet
$X_{1,i}$		Corresponding mixture volume fraction in the top homogeneous layer
$X_{1,e}$		Corresponding mixture volume fraction in the far field of the jet
g'	m/s^2	Environmental reduced gravity in the homogeneous layer

Global balance related

Symbol	Unit	Description
u_b or u_{in}	m/s	Mean inlet velocity through the bottom opening
u_t or u_{out}	m/s	Mean outlet velocity through the top opening
S_b	m^2	Surface of bottom opening
S_t	m^2	Surface of top opening
c_b		Pressure-loss coefficient related to bottom opening
c_t		Pressure-loss coefficient related to top opening
Q_b or Q_{in}	m^3/s	Inlet volume flux through the bottom opening
Q_t or Q_{out}	m^3/s	Outlet volume flux through the top opening
$Q_{m,b}$ or $Q_{m,in}$	kg/s	Inlet mass flux through the bottom opening
$Q_{m,t}$ or $Q_{m,out}$	kg/s	Outlet mass flux through the top opening
Q_{inj}	m^3/s	Injection volume flux

Abbreviations

ACF	Autocorrelation function, see eq. (4.26)
CFD	Computational Fluid Dynamics
DNS	Direct Numerical Simulation
EDM	Equi-distant Mesh, see appendix D
GCI	Grid Convergence Index, see eq. (4.23)
LES	Large Eddy Simulation
LGRM	Local-Grid Refinement Mesh, see appendix D
LMN	Low Mach Number, see section 1.4
ODE	Ordinary Differential Equation
PDF	Probability Density Function
PIV	Particle Image Velocimetry
PSD	Power Spectral Density
RANS	Reynolds-averaged Navier–Stokes
RMS	Root-Mean-Square, see eq. (4.31)

Introduction

Hydrogen is considered as one of the green energies in the future due to its carbon-free nature. For over 40 years, industry has used hydrogen in vast quantities as an industrial chemical and fuel. In 2019, about 70 million tonnes of dedicated production per year all over the world, larger than the primary energy supply of Germany (IEA (2019)). In the recent years, hydrogen-based systems are well developed and marketed. In autumn 2020, French government has provided an ambitious Covid-19 Recovery Plan with 7 billion euros of public support for hydrogen industry, see report of Ministere de l'Economie et des Finances (2020).

Use of hydrogen requires special safety and security measures due to its high flammability and high risk of detonation. Hydrogen possesses a very large interval of flammability limits: 4%-75% in ambient condition (Edwards et al. (2008)). As its density is 14 times lighter than air, the hydrogen risk is mostly presented in indoor circumstance, as hydrogen-based systems are stocked or operated in a confined environment. Accidental scenarios usually begin with hydrogen release. Hydrogen escapes and rises in form of a plume-jet flow that entrains ambient air. The dispersion of released gas in confined environment will result in the accumulation of hydrogen, generating a dangerous flammable air-hydrogen mixture which is physically the origin of the risk.

In order to prevent the accumulation, ventilation system are usually required in the confined environment where placed hydrogen-based system. These systems are commonly designed to prevent concentration exceeding lower flammability limit for realistic expected hydrogen release rates. In most of the cases, two passive vents located at different heights are preferable, as this configuration is more effective than a single one only located at the top of the enclosure (L'Hostis et al. (2012)). We focus on this configuration in this study and idealise this kind of two-vented passive ventilation system by a simplified geometrical configuration of a cavity with two openings in different levels.

From a physical point of view, this hydrogen release problem is an intrusion of a light fluid into a heavier fluid filling initially in the confined environment. The release of hydrogen will generate a momentum and buoyant source, and form a buoyant jet or plume in the cavity. Meanwhile, the combination of the jet and the two-vented configuration generate an aspiration flow by entrainment in the medium. Different injection conditions and geometrical configurations will form variable stratification regime of hydrogen mixture in the medium due to continuous intrusion. Either a homogeneous mixed layers or a density stratification can build-up inside the cavity (Baines and Turner (1969)). It is important to quantify the distribution of hydrogen concentration in the medium according to the stratification regime and its sensibility to both the release conditions and the ventilation design for related safety analysis.

Predictive models have therefore to be developed to assess the potential indoor use of hydrogen in this specific two-vented configuration. Macroscopic model such that proposed by Linden (1999), and reviewed by Kaye (2008) and Hunt and Van den Bremer (2011) has been used to predict hydrogen concentrations and the volume of inflammable region in two-vented

cavities. In this model, it is assumed that the hydrogen release results in a bi-layer stratification in the cavity with a concentration of the light gas accumulating in the top part of the cavity depending on various geometrical and dynamic parameters. The model provided an analytical approach to estimate the height of the interface and the mixture density, so that the hydrogen concentration. This theoretical approach is the fastest and the easiest way to employ in safety pre-calculations. Nonetheless, its practical use possesses some limits. The model is based on an entrainment assumption where a parameter referred as "entrainment coefficient" shall be provided beforehand. This entrainment coefficient plays an important role in the estimation of hydrogen concentration and flammable volume due to its high sensitivity to turbulent jet modelling results. This issue makes the practical use of this model challenging as its value is not easy to be correctly estimated. Consequently, a highly conservative safety strategy is usually needed. The conservative safety strategy, also called conservatism, means "being on the safe side". It is an approach where the use of models, data and assumptions would be expected to lead to a result that bounds the best-estimate on the safe side. For example estimating a potential hydrogen concentration in an accident scenario to be higher than the best estimate of the concentration. Under conservative safety strategy, the entrainment coefficient is not provided from its physical value, but from a highly conservative value which guarantees a safety margin in hydrogen concentration estimation (overestimation). Besides, the inflammable volume is usually not corrected estimated. All of these will result in a huge additional cost which may be prejudicial.

In these circumstances, experimental approach is often needed to provide accurate information about the flow pattern and concentration in order to improve the theoretical model. In the early work, Baines and Turner (1969) and Linden et al. (1990) used a concentrated salt solution injected into fresh water to investigate the global flow and validate their simplified modelling. Then other methods are developed to obtain a precise velocity field, for example, Elicer-Cortés et al. (2000) used ultrasound scattering to study the development of a buoyancy plume in an enclosure. In recent years, Particle Image Velocimetry (PIV) is a common-used optical method of flow visualisation. Veser et al. (2011) observed the structure of a turbulent hydrogen jet by PIV measurement. Ngondiep et al. (2012) presented a PIV measurement of a forced jet in a ventilated enclosure. Specific concentration measurements are realised by gas sensor in particular positions. For example, Merilo et al. (2011) measured the hydrogen concentration in an accidental scenario, by using a series of gas sensors, in a vehicle garage. In addition, experimental approach is also used to validate theoretical and numerical results.

Numerical approach is another way to treat the problem. In this approach, the complete 3D dimensional flow equations are solved numerically based on time and space discretisation. It breaks the limitations of the theoretical models and experimental approaches and provides complete and simultaneous 3D velocity and concentration fields. For example, Papanikolaou and Venetsanos (2005) realised a large scale simulation for the light gas (helium) release from a car in a two-vented garage by a standard $k - \varepsilon$ model. In this study, the distribution of release gas concentration in the garage is directly obtained. However, challenges and difficulties mainly linked to specifying a turbulence model to handle classical closure problem of turbulence. It is reported that statistical CFD turbulence models, like Reynolds-averaged Navier-Stokes (RANS) usually cannot correctly simulate the flow of a turbulent jet and the convection mixing (Bernard-Michel et al. (2012), Bernard-Michel et al. (2013), Giannissi et al. (2015)). Thus, these methods are not recommended in security studies. Spatial filtered large eddy simulations (LES) are also proposed to be used to simulate the light gas release in an enclosure (Abdalla et al. (2009), Molkov and Shentsov (2014), Prasad et al. (2011), Bauwens and Dorofeev (2014)). Some other numerical methods solving unsteady flows are also used. Carasik et al. (2015) use Unsteady Reynolds Averaged (URANS) method to simulate accidental scenario. However, most of these works lacks experimental comparisons thus cannot

be strictly considered valid. Finally, Direct Numerical Simulation (DNS) is the most recommended way as no additional turbulent models are applied. But DNS simulation requires large computational resources. It is nearly impossible to obtain a fine resolution in large configurations (in order of 1m). Therefore, in literature, DNS simulations are mainly based on small-scale configurations. Other DNS simulations are mainly focused on the study of a jet in a free space, like Craske and van Reeuwijk (2015a), Van Reeuwijk et al. (2016), Pham et al. (2007) and Plourde et al. (2008).

Context of the work

Several international and European projects were carried out to investigate the indoor hydrogen release problematic. HyIndoor for example, is a European research project led by Air Liquide S.A. started from January 2012, dedicated to developing safety design guidelines and engineering tools for indoor hydrogen use. In this project, a series of benchmarks are provided based on predictive analytical models in literature and CFD simulations for dispersion of hydrogen, in a general confined environment with one vent or two vents. It is found that the numerical result provided by RANS method is largely different from the related experimental results, see L'Hostis et al. (2012), Jallais (2010). The RANS method seems not appropriate to simulate the turbulent jet generated by hydrogen release. Simulation results from Large-Eddy-Simulation (LES) presented a slightly better agreements with experimental results but not precise enough.

The French Alternative Energies and Atomic Energy Commission (CEA) conducts fundamental and applied research in nuclear safety and operating safety of the nuclear power plant, also contributed to the project HyIndoor. The hydrogen risk is also an important subject in nuclear safety analysis. An example is the severe accident of Fukushima Daiichi in 2011 which was caused by hydrogen accumulation and explosion inside the reactor pressure vessel (a confined environment). A series of research project on the theme of hydrogen release, most of which are experimental studies, have been carried out in CEA since 2000s, for double interest of a general hydrogen indoor use and its applications in nuclear safety. Some experimental facilities are fabricated dedicated to simulating hydrogen release and accumulation in a confined environment with different geometrical configurations, without vent, with one vent and two vents. Particle Image Velocimetry (PIV) is used to measure the velocity field and flow patten, see Cariteau (2010a,b); Cariteau et al. (2011); Cariteau and Tkatschenko (2012); Cariteau (2012); Cariteau and Tkatschenko (2013), and Bernard-Michel et al. (2012, 2013); Bernard-Michel (2014); Bernard-Michel and Houssin-Agbomson (2017).

Interdisciplinary Laboratory of Digital and Numerical Sciences (LISN), also recognised as Computer Science Laboratory for Mechanics and Engineering Sciences (LIMSI), is a French CNRS plural-disciplinary science laboratory with an expertise in the development of advanced numerical methodologies associated to academic and industrial configurations. LISN is also interested in the research of turbulent convection flow. In their recent work, high-performance large-scale simulation are realised and potentially validated with experimental results, in order to improve the relevant physical models. LISN collaborates with CEA, working in the theme of hydrogen release simulation and related physical analysis for more than 10 years.

Under the collaboration framework of CEA and its academic partner LISN, two PhD projects have been carried out Tran (2013), Saikali (2018) to analyse the flow structure presented in the natural ventilation problem and to improve the simplified theoretical models. A reference geometrical configuration has been selected. It is a parallelepiped cavity with two vents at different altitudes on the same lateral side. The dimension of the cavity is $5 \times 4.9 \times 14.9 cm^3$

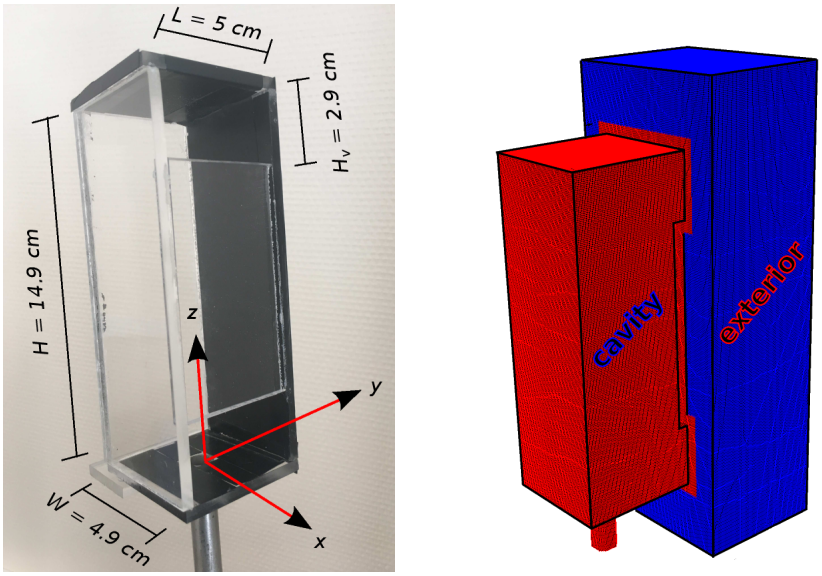

Figure 0.1: Experimental facility (left) and corresponding CFD computational domain (right), with an additional volume (in blue) in the exterior of the cavity (in red) to model the flow of surrounding fluids. Figures extracted from Saikali (2018)

with height of each vent equal to $2.9cm$, see figure 0.1. The injection gas is selected as helium instead of hydrogen for safety reasons. Helium is injected into the cavity, initially at rest and filling with fresh air, from a tube situated at the centre floor of the cavity, with a flux $9.096 \times 10^{-5} m^3/s$. Based on this configuration, PIV measurements as well as LES and DNS simulation are performed. It is found that an additional exterior domain shall be taken into account into simulation to ensure an accurate inlet/outlet boundary conditions through the two openings (Saikali et al. (2017)). The dimension of exterior domain has been previously evaluated to optimise the computation cost.

The numerical calculation was based on the CFD code TrioCFD/TRUST developed by CEA. The computation was done in parallel with MPI, on high-performance computer platform of GENCI. The flow structure obtained from PIV, LES and DNS have been compared and analysed, validating the numerical models, see figure 0.2. The global LES-DNS-PIV flow pattern is almost similar. The difference between LES and DNS is not remarkable in the lower part of the cavity, where a good agreement with PIV results is observed. However, in the upper part of the cavity where the flow is highly turbulent, both LES and DNS overestimate the velocity compared with PIV results. Monitoring point variations show that LES underestimate 70% velocity fluctuations in the laminar-turbulent transition area, principally related to its sub-grid model for multi-species flow. DNS results is thus considered reference. The detailed analysis are presented in Bernard-Michel et al. (2017); Saikali et al. (2017).

However, the configuration chosen in this project (Saikali (2018)) does not present a bi-layer distribution of helium concentration, which is the key assumption of simplified model of Linden et al. (1990), while it is commonly observed in industrial context. In the figure 0.3, the distribution of the time-averaged volume fraction of the helium in the main cavity is presented. Due to important ventilation and confinement effects, the jet direction is inclined towards the x-negative direction so that the helium volume fraction attains a local maximum in the corner formed between the jet and the backward wall. The distribution of the helium volume fraction in the upper part of the cavity is not homogeneous.

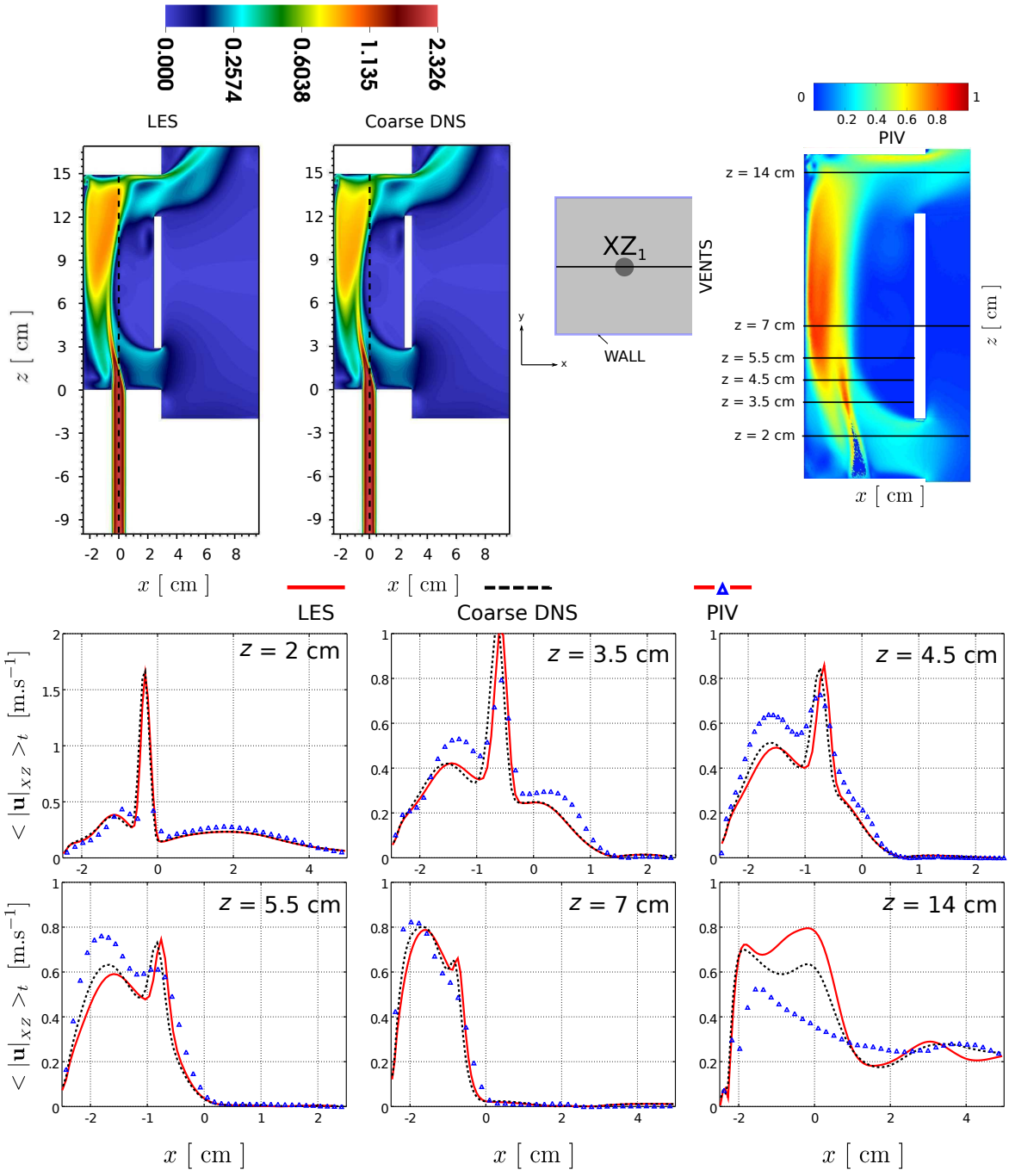

Figure 0.2: CFD-PIV comparison for the time-averaged flow pattern illustrated by 2D velocity magnitude in y direction $u_{\bar{XZ}}(m/s)$, in the vertical plane $y = 0$ (noted XZ_1 in sketch). Top: contour plot; Bottom: horizontal profiles respectively at z =2, 3.5, 4.5, 5.5, 7 and 14 cm. Thick dashed black lines denotes the vertical axis passing through the injection origin. Figure extracted from Saikali (2018)

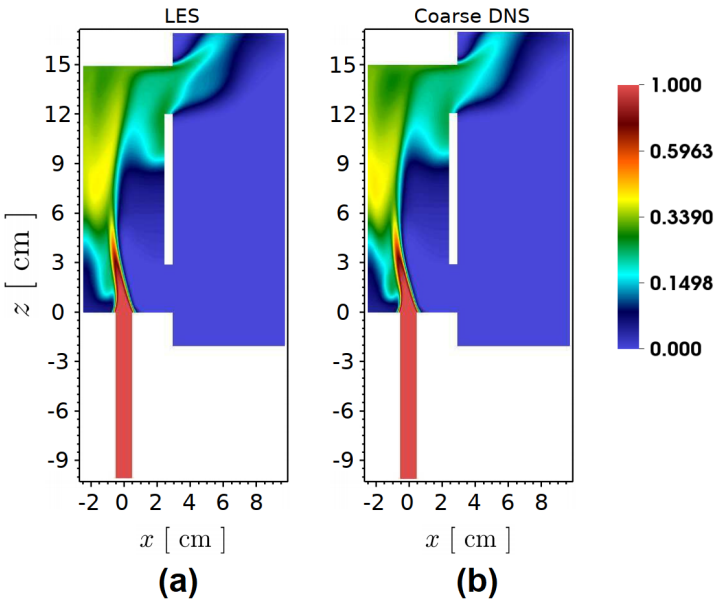

Figure 0.3: CFD comparison of the time-averaged flow pattern illustrated by the helium volume fraction X_1 contour plot in vertical plane $y = 0$. (a) LES results, (b) Coarse DNS results. Figures extracted from Saikali (2018)

Motivation and objective of this work

Motivation

Hydrogen indoor risk is physically related to air-hydrogen mixture and generally linked to hydrogen volume fraction (concentration) in the mixture. Hydrogen possesses a very large inflammability limits in air 4%-75%. In ambient condition, hydrogen-air mixture possesses large deflagration (when hydrogen concentration exceeds 4%) and detonation (when hydrogen concentration exceeds 8%) risks as its minimal inflammation energy is twice smaller than other combustible gas (e.g. methane, propane and essence). In figure 0.4, we present the evolution of hydrogen combustion conditions varied with its concentration in air-hydrogen mixture. The combustion temperature and pressure reach their maximums for concentration around 30% while the flame velocity achieves its maximal value for concentration around 40%. Effectively, 30%-40% is the interval where hydrogen-air mixture may generate the most serious consequence.

Physically, formation of air-hydrogen mixture is related to global convection flow presented in the cavity. In the case of accidental release, the development of the jet facilitates air-hydrogen mixing in the jet region. Besides, global flow at far field of the jet, generated by ventilation system will also contribute to global air-hydrogen mixing. Depending on hydrogen release flow rate (injection flux), the flammable region where hydrogen risk is present can be classified into two cases, as shown in figure 0.5:

- **Low injection flux case:** Hydrogen mixes quickly with ambient air. The air-hydrogen mixture at far field of the jet is below hydrogen lower flammability limit (4%). Therefore, the flammable region of hydrogen risk is mainly presented in the jet region (Jallais et al. (2018)).
- **High injection flux case:** Hydrogen accumulates in the cavity mixing with ambient air and inlet fresh air. It generates a flammable mixture in the whole top part of the cavity

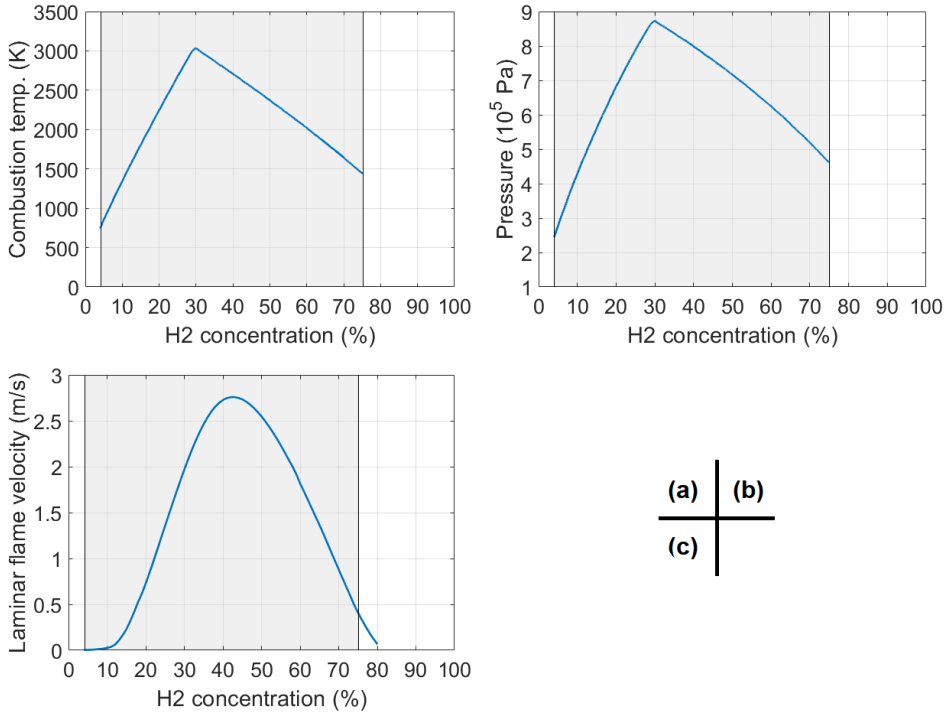

Figure 0.4: Evolution of hydrogen combustion characteristics with its concentration with air. (a): equilibrium combustion temperature (K), (b): equilibrium combustion pressure (10^5Pa), (c): laminar frame velocity (m/s), results came from reference Gai (2020). Hydrogen inflammability limits 4%-75%, coloured in grey.

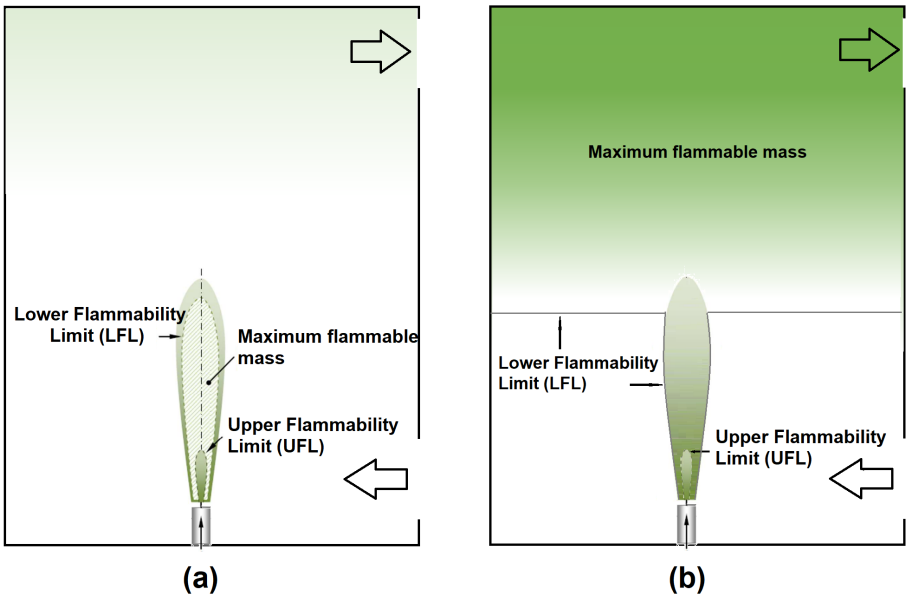

Figure 0.5: Sketches of hydrogen inflammable region with different release flux. (a) Small injection flux case, hydrogen inflammable region is located only in the jet region; (b) Large injection flux case, hydrogen flammable region includes the corresponding jet region but also the whole top part of the cavity.

where hydrogen concentration exceeds hydrogen lower flammability limit (4%). In this case, the flammable region is not only located in the jet region, but also in the whole upper part of the cavity.

Consequently, assessment of the hydrogen flammable region and potential accidental consequences requires a good estimate of concentration both along the jet and at top homogeneous layer.

The classic ventilation model of Linden et al. (1990) which is commonly used in industrial context, is initially proposed to solve thermal air-conditioning problem where the air is heated by a thermal source. The model is proposed to treat air-hydrogen mixing problem because the basic equations of heat transfer and mass diffusion are similar. However, some additional assumptions are also admitted in this model. But they are not necessarily valid in air-hydrogen mixing. This ventilation model is based on the conservation principles of the global flow rate in the cavity combined with different turbulent jet models. The jet modellings can be classified by two main assumptions applied in the demonstration: the Boussinesq approximation and entrainment modelling. Analytical jet solutions of classic Boussinesq model (Morton et al. (1956)) is applied in the original model of Linden et al. (1990). However, the Boussinesq approximation assumption may not be valid for air-hydrogen problem due to large density difference between the two gases.

The objective of this study is to clarify the validity of these assumptions. For this propose, we shall "measure" the real jet evolution developed in confined environment, i.e. the complete information of velocity and concentration fields in the whole cavity. This is clearly not feasible by experimental approach. Therefore, we consider applying numerical simulation. The idea is to firstly establish a well-converged and well-validated simulation against experiments, providing reference evolution of the jet flow and the global density distribution, treated as the "ground truth". Then the validity of these various assumptions in theoretical models will be easily investigated by comparing the evolution of characteristic quantities along the jet with that provided by turbulent jet models.

Objective and methodology

One of the main assumptions of the classic ventilation model of Linden et al. (1990) is the bi-layer distribution of the concentration of the injected light gas. All demonstration in the model is based on this hypothesis. It is reported that hydrogen indoor release generates this bi-layer distribution assumption in most cases, see Bernard-Michel et al. (2012). However, there is no explicit criteria on appearance of this bi-layer distribution in the literature.

As a continuation of the PhD work of Saikali (2018), we need to determine firstly a new reference configuration where in the steady state, hydrogen mixture presents a bi-layer distribution in the cavity. Consequently, the main objective of this study is:

- **To study the light gas injection problem in a two-vented cavity, with presence of bi-layer distribution, and to improve the performance and the applicability of simplified 1D models used in industry context.**

We aim to perform well-converged DNS simulation based on the reference configuration. In order to well simulate the fine structure of turbulent flow, the mesh should be enough fine with its cell size chosen in order of magnitude of Kolmogorov length scale. Due to limited computation resources, we cannot provide a DNS simulation in the scale of a room. We consider reducing the simulation domain to a small cavity in size order 10^{-1}m. As proposed in

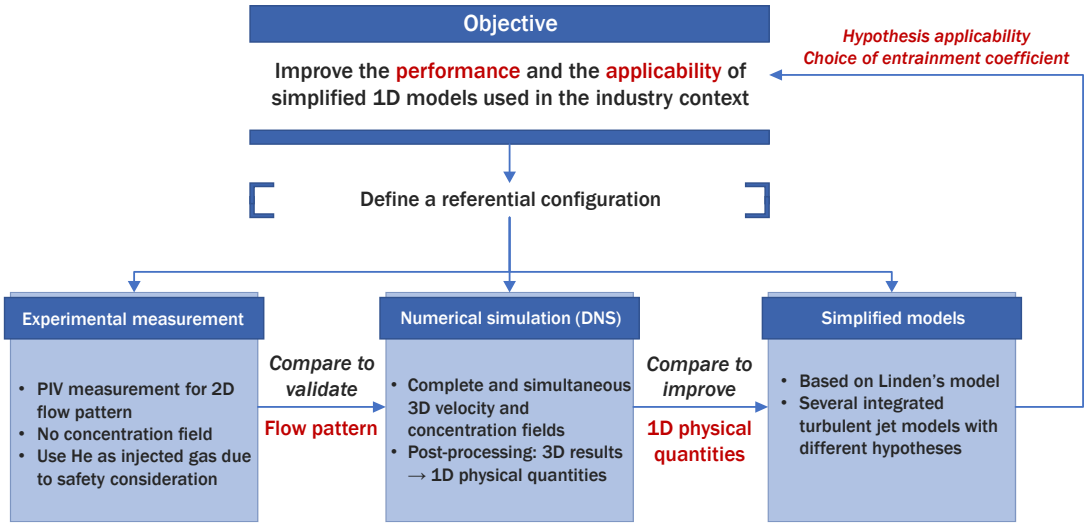

Figure 0.6: Principal methodology of this work

the previous work Saikali (2018), an additional computation domain is added on the outside of the cavity.

The DNS simulation will be validated against PIV measurements. The validated DNS results is then used to compare with different simplified models, in order to study the applicability of each hypothesis and the choice of certain key parameters. The outline of the methodology is illustrated in figure 0.6.

This thesis is divided into 4 parts. The first part (chapters 1-3) is a presentation of physical models of air-hydrogen (helium) mixture, turbulent jet models and natural ventilation model. The second part (chapter 4) is dedicated to introduce the numerical and experimental setup, convergence validation, error estimation and post-processing methodologies. The third part (chapter 5) is the results analysis of DNS 3D flow pattern and its experimental comparison. The last part is about 1D modelling (chapters 6 and 7). In chapter 6, different turbulent jet models are evaluated. We discuss particularly the influence of the jet entrainment coefficient, on one hand, in the context of turbulent jet models with constant or variable coefficient, on the other hand, under Boussinesq approximation or with consideration of the mixture density variation. In the last chapter (chapter 7), we will study the applicability of several assumptions applied in natural ventilation model.

Part I

State of the art

Chapter 1

Physical analysis for air-hydrogen or air-helium mixture

1.1 Physical problem

We study a parallelepiped cavity with two vents inside situated at different altitudes on the same solid wall boundary (see figure 1.1). The two vents are identical, located respectively at the extreme top and bottom of the cavity. The cavity is immersed in an external environment of fresh air, initially at rest. From initial state, helium or hydrogen gas is continuously injected into the cavity with a constant flow rate through a cylindrical pipe, situated in the centre of the floor of the cavity. The pipe is considered sufficiently long enough to ensure a fully developed velocity. We suppose that after some time, the flow in the cavity attains a steady state.

A 3D Cartesian coordinates system is introduced in this problem with an origin on the floor of the cavity and situated at the top centre of the injection pipe. Direction x is normal to the vent plane and direction z is aligned with the axis of the cylindrical tube. The height of the cavity (H) is large enough to ensure a global turbulent flow regime inside the cavity. The horizontal width (W) and length (L) of the cavity are chosen to be equal. The two vents are considered to be of the same height (H_v) and located over the entire width of a same vertical wall. The injection pipe is of diameter d and long enough (h) to ensure a well-developed Poiseuille flow. The temperature of the system is assumed to be constant ($T = 25°C$) with a constant thermodynamic pressure P_{th}=$10^5 Pa$.

After the initial time, the light gas is continuously injected into the cavity. The flow pattern of the injected gas in the cavity can be classified, as presented in Lee and Chu (2003), depending on, on the one hand, whether the fluid is intruded with buoyant and/or momentum (inertia) flux, and on the other hand, whether the flow is laminar or turbulent. The term "jet" is usually employed for a flow regime with inertial flux dominance and the term "plume" is used when buoyancy flux is dominant. We call a "buoyant jet" the flow regime when both terms, momentum and buoyancy, are presented.

When a light buoyant jet enters a calm medium, high shearing occurs leading to the formation of eddies. These eddies capture the ambient fluid from the surrounding into the rotational flow, then mix with the interior fluid, forming a shearing mixing layer all along the edge of the jet. This phenomenon is called entrainment. Due to the entrainment effect, the fresh air is entering into the cavity through the bottom opening, mixing with the injected light gas, and flowing out through the top opening. This is called aspiration effect. Both the entrainment effect and the ventilation effect give rise to global recirculation in the cavity, which produces a turbulent flow in the cavity. Generally, the entrainment effect, the aspiration effect, as well

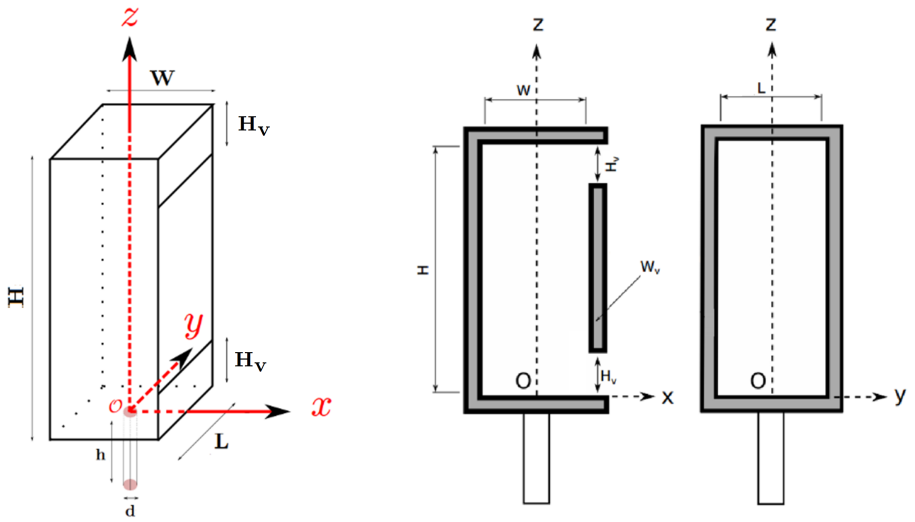

Figure 1.1: Sketch of the open cavity

as the turbulent flow, are the origin of mixing. We will start from a simple mixing problem to establish the governing equations of the problem.

1.2 Mixture state equation

In order to define physical parameters in the mixture, we start from a very simple situation. Before mixture (noted state A), we have pure gas number 1 with mass m_{A1} and density ρ_{A1} occupies a volume V_{A1}, and pure gas number 2 with mass m_{A2} and density ρ_{A2} in a volume V_{A2}, as presented in the figure 1.2.

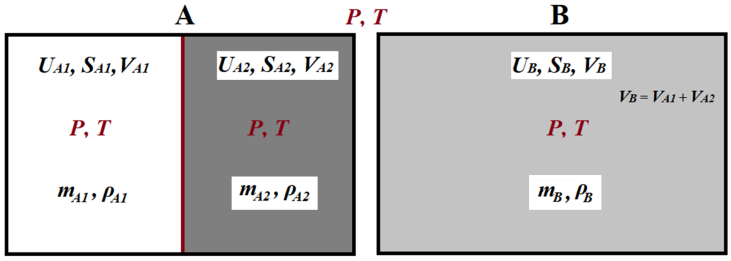

Figure 1.2: Sketch of binary gas mixture

From the first and the second principle of thermodynamics, two extensive state functions, the internal energy U and the entropy S can be defined for the system. Then the thermodynamic pressure and temperature are defined by

$$\frac{1}{T_{th}} = \left(\frac{\partial S}{\partial U}\right)_V \qquad P_{th} = T_{th}\left(\frac{\partial S}{\partial V}\right)_U \tag{1.1}$$

We suppose that two pure gases mix in an isothermal and isobar condition (p, T constant). After a complete mixing, we obtain a gas mixture with mass m_B and density ρ_B, occupies a volume V_B, the subscript $_B$ indicates the steady state after mixing. We suppose that there is no chemical reaction which will create additional enthalpy.

We have clearly the conservation of mass

$$m_B = m_{A1} + m_{A2} \tag{1.2}$$

We suppose all these two gases are ideal gas, so we have the conservation of volume

$$V_B = V_{A1} + V_{A2} \tag{1.3}$$

For the mixture (state B), we define mass fraction of each component

$$Y_1 = \frac{m_{A1}}{m_{A1} + m_{A2}}, \quad Y_2 = \frac{m_{A2}}{m_{A1} + m_{A2}} \tag{1.4}$$

and volume (molar) fraction of each component

$$X_1 = \frac{V_{A1}}{V_{A1} + V_{A2}}, \quad X_2 = \frac{V_{A2}}{V_{A1} + V_{A2}} \tag{1.5}$$

We have of course: $Y_1 + Y_2 = X_1 + X_2 = 1$.

For mixture density, we have

$$\rho_B = \frac{m_B}{V_B} = \frac{m_{A1} + m_{A2}}{V_{A1} + V_{A2}} = X_1 \frac{m_{A1}}{V_{A1}} + X_2 \frac{m_{A2}}{V_{A2}} = X_1 \rho_{A1} + X_2 \rho_{A2} \tag{1.6}$$

So that

$$X_1 = \frac{\rho_B - \rho_{A2}}{\rho_{A1} - \rho_{A2}}, \quad X_2 = \frac{\rho_B - \rho_{A1}}{\rho_{A2} - \rho_{A1}} \tag{1.7}$$

For mass fraction, we have

$$Y_1 = X_1 \frac{\rho_{A1}}{\rho_B} = \frac{\rho_B - \rho_{A2}}{\rho_{A1} - \rho_{A2}} \cdot \frac{\rho_{A1}}{\rho_B}, \quad Y_2 = X_2 \frac{\rho_{A2}}{\rho_B} = \frac{\rho_B - \rho_{A1}}{\rho_{A2} - \rho_{A1}} \cdot \frac{\rho_{A2}}{\rho_B} \tag{1.8}$$

We have also following relations between mass fraction (Y_1, Y_2) and volume (molar) fraction (X_1, X_2)

$$Y_1 = \frac{1}{1 + \frac{1-X_1}{X_1} \frac{\rho_{A2}}{\rho_{A1}}}, \quad Y_2 = \frac{1}{1 + \frac{1-X_2}{X_2} \frac{\rho_{A1}}{\rho_{A2}}} \tag{1.9}$$

$$X_1 = \frac{1}{1 + \frac{1-Y_1}{Y_1} \frac{\rho_{A1}}{\rho_{A2}}}, \quad X_2 = \frac{1}{1 + \frac{1-Y_2}{Y_2} \frac{\rho_{A2}}{\rho_{A1}}} \tag{1.10}$$

By using the state equation of ideal gas at constant p, T, we have

$$\frac{\rho_{A1}}{\rho_{A2}} = \frac{M_{A1}}{M_{A2}} \tag{1.11}$$

with M_{A1}, M_{A2} the molar mass of pure gas 1 and 2 before mixing. Hence,

$$\frac{Y_1}{Y_2} = \frac{X_1}{X_2} \frac{\rho_{A1}}{\rho_{A2}} = \frac{X_1}{X_2} \frac{M_{A1}}{M_{A2}} \tag{1.12}$$

Let us decide the gas number 1 is the injected light gas (pure helium or pure hydrogen) and gas number 2 is the fresh air. The mixture state (state B) is noted with subscript $_{mix}$. The figure 1.3 illustrates the relation between X_1 and Y_1 for air-hydrogen and air-helium mixture. Typically, if $X_1 = 0.4$, we have $Y_1 = 0.084$ for air-helium mixture and $Y_1 = 0.044$ for air-hydrogen mixture. Usually, the volume fraction X_1 is used in the industrial context for safety analysis. X_1 is also called "concentration" in this study.

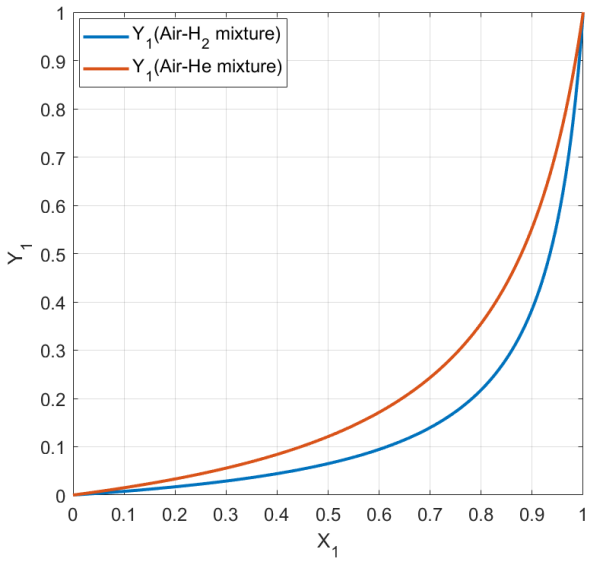

Figure 1.3: Variation of $Y_1(X_1)$ for air-hydrogen/air-helium mixture

The injected gas and ambient air are considered as ideal gases, by using its state equation (Williams (1965)), the mixed gas can also be proved as ideal gas, with

$$M_{mix} = \frac{1}{\frac{Y_1}{M_1} + \frac{1-Y_1}{M_2}} \tag{1.13}$$

The equation of state for gas mixture could be written as

$$\rho_{mix} = \frac{pM_{mix}}{RT} \tag{1.14}$$

with ρ_{mix} the density of the gas mixture and R the specific gas constant equal to 8.314 J.mol^{-1}.K^{-1}.

1.3 Conservation equations

The conservation equations consist of species equation, mass equation and momentum equation. As the problem is placed within a justified isothermal assumption, it is not necessary to solve for an additional energy conservation equation.

1.3.1 Species equation

We choose in the flow domain a fluid parcel in the diffusion length scale. As there is no chemical reaction as source term, the general transport equation of injected gas could be written as (Bird et al. (2007))

$$\frac{\partial \rho_{R1}}{\partial t} + \mathbf{div}\left(\rho_{R1}\,\overrightarrow{u_1}\right) = 0 \tag{1.15}$$

with ρ_{R1} the relative density of injected gas presented in the local fluid parcel defined as the quotient of the total mass of injected pure gas presented in the fluid parcel (m_1) and the volume of the fluid parcel $\rho_{R1} = m_1/V_{mix}$, which is also equal to $Y_1\rho_{mix}$. Vector $\overrightarrow{u_1}$ is the velocity vector of injected gas in the fluid parcel. We define same variables ρ_{R2} and $\overrightarrow{u_2}$ for ambient gas in the same fluid parcel.

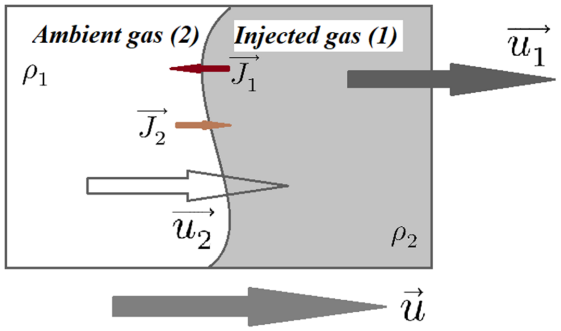

Figure 1.4: Sketch of local convection-diffusion study

Based on the conservation of the total mass flux ($m_{mix}\overrightarrow{u} = m_1\overrightarrow{u_1} + m_2\overrightarrow{u_2}$), we have the mass-averaged velocity in the fluid parcel

$$\overrightarrow{u} = Y_1\overrightarrow{u_1} + Y_2\overrightarrow{u_2} \tag{1.16}$$

Considering now the difference between the mixture's mass-averaged velocity and the absolute velocity of each component, the mass diffusion flux of injected and ambient gas (noted $\overrightarrow{J_1}$ and $\overrightarrow{J_2}$) can be defined as follows. The definition of these parameters in the local fluid parcel are presented in figure 1.4.

$$\overrightarrow{J_1} = \rho_{mix}Y_1\left(\overrightarrow{u_1} - \overrightarrow{u}\right) = \rho_{R1}\left(\overrightarrow{u_1} - \overrightarrow{u}\right) \tag{1.17}$$

$$\overrightarrow{J_2} = \rho_{mix}Y_2\left(\overrightarrow{u_2} - \overrightarrow{u}\right) = \rho_{R2}\left(\overrightarrow{u_2} - \overrightarrow{u}\right) \tag{1.18}$$

Note that we have $\overrightarrow{J_1} + \overrightarrow{J_2} = 0$, the general transport equation of injected gas could be rewritten as

$$\frac{\partial\rho_{R1}}{\partial t} + \mathbf{div}\left(\rho_{R1}\overrightarrow{u}\right) = -\mathbf{div}\ \overrightarrow{J_1} \tag{1.19}$$

The mass diffusion flux can be modelled by Fick's first law (Brébec et al. (2004)), thus

$$\overrightarrow{J_1} = -D_{1,2}\rho_{mix}\overrightarrow{\mathbf{grad}}\ Y_1 \tag{1.20}$$

$$\overrightarrow{J_2} = -D_{1,2}\rho_{mix}\overrightarrow{\mathbf{grad}}\ Y_2 \tag{1.21}$$

with $D_{1,2}$ the Fick's diffusion coefficient of injected and ambient gas. We may remark that, when we choose the mass fraction Y_1 as the main parameter for solving the problem, the effective diffusion coefficient is $\rho_{mix}D_{1,2}$, instead of $D_{1,2}$.

Thus, noting simply ρ the local mixture density instead of ρ_{mix}, we have for injected gas

$$\frac{\partial\rho Y_1}{\partial t} + \mathbf{div}\left(\rho Y_1\cdot\overrightarrow{u}\right) = \mathbf{div}\left(\rho D_{1,2}\cdot\overrightarrow{\mathbf{grad}}\ Y_1\right) \tag{1.22}$$

And similarly for ambient gas

$$\frac{\partial\rho Y_2}{\partial t} + \mathbf{div}\left(\rho Y_2\cdot\overrightarrow{u}\right) = \mathbf{div}\left(\rho D_{1,2}\cdot\overrightarrow{\mathbf{grad}}\ Y_2\right) \tag{1.23}$$

These are the conservation equations of species.

These equations may also be written in Einstein notation if we study in Cartesian coordinate system $(x_1, x_2, x_3) = (x, y, z)$ with a summation over the index i

$$\frac{\partial\rho Y_1}{\partial t} + \frac{\partial\rho Y_1 u_i}{\partial x_i} = \frac{\partial}{\partial x_i}\left(\rho D_{1,2}\frac{\partial Y_1}{\partial x_i}\right) \tag{1.24}$$

and similar for another one.

1.3.2 Mass equation

If we add together two conservation equations of species (1.22 and 1.23) respectively for injected gas and for ambient gas, we have the conservation equation for the total mass of the mixture

$$\frac{\partial \rho}{\partial t} + \mathbf{div}\left(\rho \overrightarrow{u}\right) = 0 \tag{1.25}$$

And in Einstein notation with a summation over the index i

$$\frac{\partial \rho}{\partial t} + \frac{\partial \rho u_i}{\partial x_i} = 0 \tag{1.26}$$

1.3.3 Momentum equation

Considering the mass average velocity vector $\overrightarrow{u}$ of the gas mixture, by application of the fundamental principle of dynamics, we can write the momentum conservation equation of mixture as follows.

$$\frac{\partial \rho \overrightarrow{u}}{\partial t} + \left(\rho \overrightarrow{u} \cdot \overrightarrow{\mathbf{grad}}\right)\overrightarrow{u} = -\overrightarrow{\mathbf{grad}}\ p + \mathbf{div}\ \overline{\overline{\tau}} + \rho \overrightarrow{g} \tag{1.27}$$

This equation could also be written in Einstein notation with a summation over the index i

$$\frac{\partial \rho u_j}{\partial t} + \frac{\partial}{\partial x_i}\left(\rho u_j u_i\right) = -\frac{\partial p}{\partial x_j} + \frac{\partial \tau_{ij}}{\partial x_i} + \rho g_j \tag{1.28}$$

where $\overline{\overline{\tau}} = \left[\tau_{ij}\right]$ is the viscous stress tensor and $\overrightarrow{g} = (0,\ 0,\ -g)$ the gravitational vector in Cartesian or cylinder system with $g = 9.81 m/s^2$ and p the local pressure.

We suppose that the air-light gas mixture is a Newtonian fluid. The viscous stress depends linearly on the velocity gradients. It can be written as follows, with μ dynamic viscosity of the mixture, using Stoke's hypothesis (coefficient of bulk viscosity $\lambda = -2/3 \cdot \mu$).

$$\tau_{ij} = 2\mu e_{ij} = 2\mu\left(\frac{1}{2}\left(\frac{\partial u_j}{\partial x_i} + \frac{\partial u_i}{\partial x_j}\right) - \frac{1}{3}\delta_{ij}\frac{\partial u_k}{\partial x_k}\right) \tag{1.29}$$

The term δ_{ij} is equal to 1 when $i = j$ and 0 if not (Kronecker-Delta symbol). The tensor e_{ij} denotes the strain rate tensor and its symmetrical part S_{ij} is defined as

$$S_{ij} = \frac{1}{2}\left(\frac{\partial u_j}{\partial x_i} + \frac{\partial u_i}{\partial x_j}\right) \tag{1.30}$$

So that the momentum equation could be rewritten as

$$\frac{\partial \rho u_j}{\partial t} + \frac{\partial}{\partial x_i}\left(\rho u_j u_i\right) = -\frac{\partial p}{\partial x_j} + 2\frac{\partial \mu S_{ij}}{\partial x_i} - \frac{2}{3}\frac{\partial}{\partial x_j}\left(\mu \frac{\partial u_k}{\partial x_k}\right) + \rho g_j \tag{1.31}$$

1.4 Low Mach Number approximation and governing equations

Low Mach Number approximation

The Mach number is defined as the ratio of velocity of the fluid u and the local sound speed. For ideal gas, this number is written as

$$Ma = \frac{u}{\sqrt{\gamma R T_0}} \tag{1.32}$$

with R ideal gas constant and T_0 reference temperature and $\gamma = 1.4$ for gas with diatomic molecule. The sound speed in the air is around 340 m/s. Considering a flow velocity in order of magnitude $10 m/s$, a typical value for gas leak rate through small orifices, the corresponding Mach number is $Ma \approx 0.01 << 1$. Generally for $Ma < 0.1$, the compressibility effects can be neglected. This is the main hypothesis of Low Mach Number (LMN) approximation. (Müller (1998))

In mixing problem with large density variation, the incompressible momentum equations are not applicable. However, as the compressible momentum equations consist of the acoustic wave term, its resolution may be very difficult. The idea is to separate the pressure term in equation (1.31), into a thermodynamic term $P_{th}(t)$ and a hydrodynamic term $P_H(\overrightarrow{x}, t)$

$$p(\overrightarrow{x}, t) = P_{th}(t) + P_H(\overrightarrow{x}, t) \tag{1.33}$$

This hydrodynamic pressure fluctuates in an order of Ma^2 in first order development.

$$P_H(\overrightarrow{x}, t) \sim Ma^2 p\left(\overrightarrow{x}, t\right) \tag{1.34}$$

Replacing the decomposition of total pressure p in momentum equation (1.31) in first order, this equation will be transformed into the same form with the term p replaced by the hydrodynamic pressure P_H.

And in the state equation (1.14), the pressure term p will be replaced by the thermodynamic pressure P_{th}.

Governing equations

The governing equations are based on conservation equations and state equation. The governing equations under LMN approximation are given as follows.

$$\begin{cases} \dfrac{\partial \rho}{\partial t} + \mathbf{div}\left(\rho \overrightarrow{u}\right) = 0 \\ \dfrac{\partial \rho Y_1}{\partial t} + \mathbf{div}\left(\rho Y_1 \cdot \overrightarrow{u}\right) = \mathbf{div}\left(\rho D_{1,2} \cdot \overrightarrow{\mathbf{grad}}\ Y_1\right) \\ \dfrac{\partial \rho \overrightarrow{u}}{\partial t} + \left(\rho \overrightarrow{u} \cdot \overrightarrow{\mathbf{grad}}\right)\overrightarrow{u} = -\overrightarrow{\mathbf{grad}}\ P_H + \mathbf{div}\ \overline{\overline{\tau}} + \rho \overrightarrow{g} \\ \rho = \dfrac{P_{th}}{RT} \dfrac{1}{\dfrac{Y_1}{M_{inj}} + \dfrac{1 - Y_1}{M_{air}}} \end{cases} \tag{1.35}$$

We have one vectorial equation and three scalar equations, and ρ, Y_1, P three unknown scalar fields and one unknown vectorial field $\overrightarrow{u}$.

1.5 Estimation of physical properties of mixture

Some characteristic parameters related to the physical properties of mixture, like the mixture density ρ, the mixture molar mass M, the dynamic viscosity μ and the diffusion coefficient $D_{1,2}$, have been presented in the above governing equations. In this section, we present the physical models to link these parameters of mixture to the unknown quantities P, ρ, Y_1 of the mixture presented in the governing equations.

1.5.1 Mixture molar mass

The molar mass of atoms of an element is given by the Standard atomic weight of the element multiplied by the molar mass constant. The molar mass of a molecule or mixture is calculated by combination of the molar mass of its composition elements. We use the results presented in Arcipreti (2006) and Turrin (2008):

$$M(Air) = 28.97 \text{ g/mol} \tag{1.36}$$

$$M(H_2) = 2.016 \text{ g/mol} \tag{1.37}$$

$$M(He) = 4.003 \text{g/mol} \tag{1.38}$$

For the mixture of ideal gas, its molar mass could be calculated by (1.13).

1.5.2 Mixture density

The ideal gas density is depended on its pressure and temperature:

$$\rho = \frac{PM}{RT} \tag{1.39}$$

with $R = 8.314$ J/mol·K ideal gas constant.

Under isobar and isothermal conditions $P = 10^5$Pa, $T = 25℃ = 298.15$K, we have

$$\rho(Air) = 1.168 \text{kg/m}^3 \tag{1.40}$$

$$\rho(H_2) = 0.0813 \text{kg/m}^3 \tag{1.41}$$

$$\rho(He) = 0.161 \text{kg/m}^3 \tag{1.42}$$

We have typically $\rho(Air)/\rho(H_2) = 14.4$ and $\rho(Air)/\rho(He) = 7.3$, that corresponds to a large difference of density between air and injected light gas. The calculation of the mixture density is similar, by applying (1.14).

We present in the figure 1.5 the variation of mixture density ρ as function of mass fraction Y_1 and of volume (molar) fraction X_1 of injected gas, respectively for hydrogen-air and helium-air mixture. Note that a linear relation between ρ_{mix} and X_1 is observed. For example, for the case where volume fraction of injected gas $X_1 = 0.4$, we have $\rho_{mix} = 0.73 kg/m^3$ for air-hydrogen mixture and $\rho_{mix} = 0.76 kg/m^3$ for air-helium mixture, corresponding to $\rho_{air}/\rho_{mix} \approx 1.6$ for air-hydrogen mixture and 1.5 for air-helium mixture.

1.5.3 Mixture dynamic viscosity

According to references (Lemmon and Jacobsen (1999), Reid et al. (1987), Turrin (2008)), in the 0.1MPa condition, we have the dynamic viscosity of pure gas that varied as polynomial functions of absolute temperature (see table 1.1).

Gas	$\mu\ (Pa \cdot s)$	Relative error (%)
Air	$2.02910 \cdot 10^{-6} + 6.21004 \cdot 10^{-8} T - 2.40179 \cdot 10^{-11} T^2$	-0.22
H_2	$2.15245 \cdot 10^{-6} + 2.50715 \cdot 10^{-8} T - 8.05458 \cdot 10^{-12} T^2$	0.18
He	$5.03696 \cdot 10^{-6} + 5.40569 \cdot 10^{-8} T - 1.47908 \cdot 10^{-11} T^2$	0.14

Table 1.1: Variation of μ with temperature (around 300K) for different gases

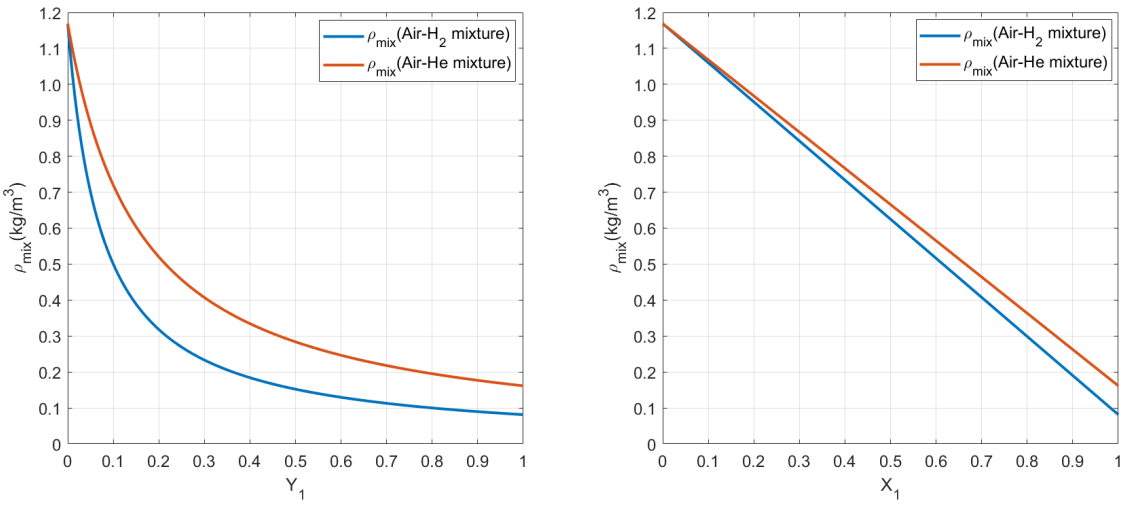

Figure 1.5: Variation of ρ_{mix} as function of mass fraction Y_1 and of volume (molar) fraction $X_1$for air-hydrogen/air-helium mixture

Consequently, the dynamic viscosity of pure gas at 298.15K can be calculated by using the above formulas. The value for pure air and pure helium are in the same order of magnitude (relative difference 8%). However, a large difference between pure air and hydrogen (related difference 50%) is observed, hydrogen is less viscous.

$$\mu(Air) = 1.84093 \times 10^{-5} kg/(m \cdot s) \tag{1.43}$$

$$\mu(H_2) = 0.89115 \times 10^{-5} kg/(m \cdot s) \tag{1.44}$$

$$\mu(He) = 1.98392 \times 10^{-5} kg/(m \cdot s) \tag{1.45}$$

The value of dynamic viscosity of the mixture μ_{mix} depends on the properties of two injected pure gases and their concentrations in the mixture. It is evaluated by using the semi-empirical formula of Wilke (Wilke (1950)). Attention the formula presented in the article of Wilke is in molar fractions not in mass fractions.

$$\mu_{mix} = \frac{\mu_{inj}}{1 + \dfrac{\dfrac{1-Y_1}{Y_1}\dfrac{M_{inj}}{M_{air}}\left(1 + \sqrt{\dfrac{\mu_{inj}}{\mu_{air}}}\left(\dfrac{M_{air}}{M_{inj}}\right)^{1/4}\right)^2}{2\sqrt{2}\sqrt{1 + \dfrac{M_{inj}}{M_{air}}}}} + \frac{\mu_{air}}{1 + \dfrac{\dfrac{Y_1}{1-Y_1}\dfrac{M_{air}}{M_{inj}}\left(1 + \sqrt{\dfrac{\mu_{air}}{\mu_{inj}}}\left(\dfrac{M_{inj}}{M_{air}}\right)^{1/4}\right)^2}{2\sqrt{2}\sqrt{1 + \dfrac{M_{air}}{M_{inj}}}}} \tag{1.46}$$

The variation of μ_{mix} for air-hydrogen and air-helium mixture is presented in figure 1.6. We can remark that the variation of μ_{mix} is monotone for air-hydrogen mixture but not for air-helium mixture. The air-helium mixture presents a larger dynamic viscosity than that of the fresh air, but contrary results for air-hydrogen mixture. If we take a typical point for example $X_1 = 0.4$, for air-hydrogen mixture, the related change of μ_{mix} compared to that of fresh air μ_{air} is 0.08%, for air-helium mixture, the related change is 0.55%. The change of dynamic viscosity may be neglected except in the injection area where the percentage of light gas is high.

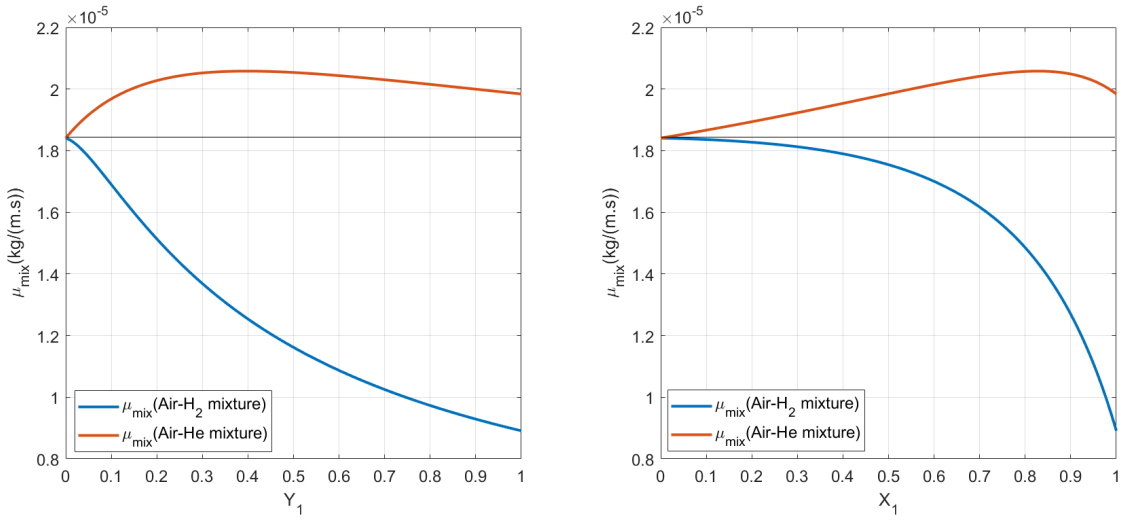

Figure 1.6: Variation of μ_{mix} with mass fraction Y_1 and volume (molar) fraction X_1 for air-hydrogen/air-helium mixture

1.5.4 Diffusion coefficient

For non-polar molecules, Lennard-Jones potentials provide a basis of computing diffusion coefficients of binary gas mixtures. The binary diffusion coefficient $D_{1,2}$ in m^2/s is given by the Chapman-Enskog's formula (Bird et al. (2007)) as follows.

$$D_{1,2} = 0.018583 \cdot T^{3/2} \cdot \frac{\sqrt{\frac{1}{M_1} + \frac{1}{M_2}}}{P \cdot \sigma_{12}^2 \cdot \Omega_{D12}} \tag{1.47}$$

in which P pressure in Pa, T temperature in K and M_i molar mass in g/mol. The coefficient σ_{12} is the Lennard-Jones force constant (in $10^{-10}m$) for the mixture which is the average of its value for two pure gases.

$$\sigma_{12} = \frac{\sigma_1 + \sigma_2}{2} \tag{1.48}$$

And the coefficient Ω_{D12} is the collision integral. Neufeld et al. (1972) proposes a formula of 8 parameters to calculate Ω_{D12} as a function of T^*.

$$\Omega_{D12} = \frac{1.06036}{(T^*)^{0.15610}} + \frac{0.19300}{\exp(0.47635T^*)} + \frac{1.03587}{\exp(1.52996T^*)} + \frac{1.76474}{\exp(3.89411T^*)} \tag{1.49}$$

where $T^* = kT/\epsilon_{12}$ with T in K and $k = 1.38065 \times 10^{-23}$ kg·m^{2}s^{-2}K^{-1} the Boltzmann constant. The coefficient ϵ_{12} is the characteristic energy appearing in the Lennard-Jones potential for the binary mixture pair, which is calculated by

$$\epsilon_{12} = \sqrt{\epsilon_1 \epsilon_2} \tag{1.50}$$

We have numerical values of σ and ϵ/k for air, hydrogen and helium (Bird et al. (2007)).

Gas	Air	Hydrogen	Helium
σ $(10^{-10}m)$	3.617	2.915	2.576
ϵ/k (K)	97.0	38.0	10.2

Table 1.2: Numerical values of σ and ϵ/k for air, hydrogen and helium

We then calculate the diffusion coefficient of air-hydrogen, air-helium and air-air mixture, by applying above formulas. Results are presented in the following table. We may remark that the self-diffusion coefficient for air is largely smaller than that of air-helium(hydrogen) diffusion.

Mixture	**Air-H_2** (25°C)	**Air-He** (25°C)	**Air-H_2** (20°C)	**Air-He** (20°C)	**Air-Air** (25°C)
$\epsilon_{12}/k\ (K)$	60.7	31.5	60.7	31.5	97.0
$\sigma_{12}\ (10^{-10}m)$	3.27	3.10	3.27	3.10	3.62
T^*	4.91	9.48	4.83	9.32	3.07
Ω_{D12}	0.85	0.75	0.85	0.75	0.94
$\boldsymbol{D_{1,2}\ (m^2/s)}$	$\mathbf{7.72\times10^{-5}}$	$\mathbf{7.11\times10^{-5}}$	$\mathbf{7.50\times10^{-5}}$	$\mathbf{6.91\times10^{-5}}$	$\mathbf{2.04\times10^{-5}}$

Table 1.3: Diffusion coefficient of air-hydrogen/air-helium mixture and air-air mixture

We may also compare the above results with that presented in Marrero-Mason (Marrero and Mason (1973), Marrero and Mason (1972), Reid et al. (1987), Turrin (2008)). The variation of diffusion coefficient $D_{1,2}$ is proportional to T^s, with T temperature in K, s coefficient determined by experiments. For air-hydrogen mixture, $s = 1.750$, and for air-helium mixture, $s = 1.729$. After calculation, the relative error based on results in the above is less than 0.1%. We may consider the above calculation is accurate.

1.6 Characteristic dimensionless numbers and fluid motion

Some dimensionless numbers may be used to predict the flow pattern. In this section, we present definitions of a series of important dimensionless numbers to characterise the fluid motion, typically the diffusion-convection phenomenon and the stratified flow regime.

1.6.1 Convection-diffusion phenomenon

The Reynolds number is usually considered as indicative to laminar-turbulent transition in the flow regime. The Schmidt number is used to characterise the fluid propriety concerning momentum transfer and mass transfer, depending on the fluid nature. Rayleigh number is used to indicate if convection or diffusion is dominant on flow regime in convection-diffusion phenomenon. Besides, as we study in the situations involving buoyancy effect, Grashof number could also be used.

Reynolds number (Re)

The Reynolds number is the ratio of inertial forces to viscous forces. The Reynolds number for a general flow is defined as

$$\mathrm{Re} = \frac{\rho u L}{\mu} = \frac{u L}{\nu} \tag{1.51}$$

with ρ fluid density, u velocity, μ dynamic viscosity, $\nu = \mu/\rho$ kinematic viscosity and L characteristic dimension.

The characteristic length L will be defined differently in different situations. Particularly, in order to characterise the laminar or turbulent regime for the injection source of a jet into the

cavity, we define the injection Reynolds number (Re_{inj}) as follows (Lee and Chu (2003)).

$$\mathrm{Re}_{\mathrm{inj}} = \frac{\rho_{inj} u_{inj} d}{\mu_{inj}} \tag{1.52}$$

u_{inj} is the average injection velocity calculated as $u_{inj} = Q_{inj}/S_{inj}$ and d the diameter of injection tube.

Grashof number (Gr)

Grashof number is generally defined as the ratio of buoyancy to viscous forces. For jet flow, the local Grashof number is defined as a function of the vertical position as follows.

$$\mathrm{Gr}\,(z) = g\frac{\rho_{air}(\rho_{air} - \rho(z))}{\mu_{air}^2} z^3 \tag{1.53}$$

with $\rho(z)$ the local density of mixed gas and z the altitude compared to the injection plane.

Schmidt number (Sc)

The Schmidt number is defined as the ratio of momentum diffusivity (kinematic viscosity) and mass diffusivity.

$$\mathrm{Sc} = \frac{\nu}{D} = \frac{\mu}{\rho D} \tag{1.54}$$

For characterising a gas mixture of a jet, the Schmidt number can be calculated separately for the injection fluid and the ambient fluid. Note that the diffusivity coefficient is given in pair species for a multi-species system. We have for air-hydrogen mixture, $\mathrm{Sc}_{H_2} = 1.42$ and $\mathrm{Sc}_{air} = 0.204$. For air-helium mixture, $\mathrm{Sc}_{He} = 1.73$ and $\mathrm{Sc}_{air} = 0.222$. The Schmidt number of hydrogen and helium is in the same order of magnitude.

Rayleigh number (Ra)

Rayleigh number is defined as product of Grashof number and Schmidt number:

$$\mathrm{Ra} = \mathrm{Gr}{\cdot}\mathrm{Sc} \tag{1.55}$$

The Rayleigh number describes the behaviour of fluids when the mass density of the fluid is non-uniform (due to mass transfer or temperature differences) in an acceleration field. When the Rayleigh number is below a critical value for a fluid, mass transfer is primarily in the form of diffusion; when it is superior to the critical value, mass transfer is primarily in the form of convection. In the case of buoyant jet in an enclosure, a global Rayleigh number is defined as follows

$$\mathrm{Ra}_{\mathrm{global}} = \mathrm{Gr}_{\mathrm{global}}{\cdot}\mathrm{Sc}_{\mathrm{a}} = \frac{g\left(\rho_a - \rho_{inj}\right)H^3}{\mu_a D} \tag{1.56}$$

For a cavity height $H = 20cm$, we have $\mathrm{Ra}_{\mathrm{global}} = 6.0 \times 10^7$, almost the same value for air-hydrogen and air-helium mixture.

1.6.2 Mixed convection

In this problem of injection of light gas in an air-filled cavity, the prediction of mixture density distribution in steady state is important to validate the validity of relative models. For this purpose, the Richardson number is used in the literature.

Richardson number (Ri)

The Richardson number is defined as the ratio of the buoyancy term and the flow shear term.

$$\mathrm{Ri} = \frac{g}{\rho} \frac{\left\| \overrightarrow{\mathbf{grad}}\ \rho \right\|}{\left\| \overrightarrow{\mathbf{grad}}\ u \right\|^2} \tag{1.57}$$

The Richardson number can also be expressed by using a combination of Gr and Re

$$\mathrm{Ri} = \frac{\mathrm{Gr}}{\mathrm{Re}^2} \tag{1.58}$$

Typically, the natural convection is negligible when Ri < 0.1, forced convection is negligible when Ri > 10.

We use Richardson number at injection region (Ri_{inj}) for prediction of the flow regime rising in the medium, which is defined as follows. (Chen and Rodi (1980a,b))

$$\mathrm{Ri}_{\mathrm{inj}} = g \frac{\left(\rho_a - \rho_{inj}\right) d}{\rho_{inj} u_{inj}^2} \tag{1.59}$$

with d the diameter of injection tube. When $\mathrm{Ri}_{\mathrm{inj}} \gg 1$, the buoyancy force is dominant at the source, the flow regime is pure plume. If we have $\mathrm{Ri}_{\mathrm{inj}} \ll 1$, the momentum flux is dominant at the source, a pure jet is predicted to rise.

Besides, the Richardson number can also be used for characterising different regimes of concentration distribution of injected light gas in the cavity by introducing the **Volume Richardson number ($\mathbf{Ri}_v$)** (Cleaver et al. (1994))

$$\mathrm{Ri}_{\mathrm{v}} = g \frac{\rho_a - \rho_{inj}}{\rho_{inj}} \frac{\sqrt[3]{V_{cavity}}}{u_{inj}^2} \tag{1.60}$$

with V_{cavity} volume of the enclosure.

For a cavity with one opening, Cleaver et al. (1994) summarise three concentration regimes associated with Ri_v. In situations where $\mathrm{Ri}_{\mathrm{v}} \ll 1$, overturning occurs and the inertia of the jet is sufficient to mix the entire enclosure so that we have a homogeneous mixture. When $\mathrm{Ri}_{\mathrm{v}} \gg 1$, a complicated vertical stratified regime is obtained. In case where $\mathrm{Ri}_{\mathrm{v}} \approx 1$, a homogeneous layer will be formed at the top part of the enclosure and stratification layers formed below, as illustrated in the following figure. In order to obtain a bi-layer distribution of mixture gas concentration, we shall let the volume Richardson number around 1. Note that this result is based on a flow study in a one-vented cavity. So it may be not directly applicable in present problem.

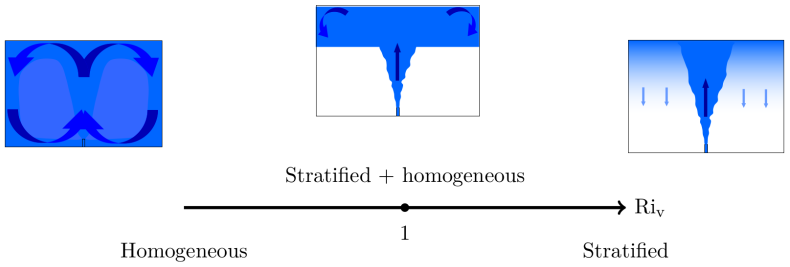

Figure 1.7: Illustration of predicted flow regime by Ri_v, sketch extracted from Saikali (2018)

1.7 Summary

In this chapter, we have presented

- Physical configuration studied in this work
- Physical modelling of the air-hydrogen mixing problem and conservation equations
- Principal dimensionless numbers characterising the flow regime

These constitute the general modelling of the problem. Besides, theoretical approaches are also developed to provide simplified modelling. One important phenomenon is the jet flow after injection. We will present the modelling of jet in the next chapter.

Chapter 2

Theoretical models of turbulent buoyant jet

In this chapter, we present a series of 1D simplified models from literature for turbulent buoyant jets in a free place. Firstly, we present general assumptions in these models. Based on different treatments of these assumptions, 3 analytical approaches are summarised. Model of Morton et al. (1956) is the classic free jet model under Boussinesq approximation with a constant entrainment coefficient. Model of Kaminski et al. (2005) presents a Boussinesq approach with a variable entrainment coefficient. Model of Rooney and Linden (1996) provides a non-Boussinesq approach with a constant entrainment coefficient.

2.1 General assumptions

The development of turbulent jet models is usually based on simplified assumptions. In this section, we summarise general assumptions in three aspects: Boussinesq approximation, auto-similarity assumption and entrainment modelling. Note that the third one, entrainment modelling will depend on first two assumptions: the formulation will be different for Boussinesq or non Boussinesq case, under Top-hat or Gaussian profile assumption. The entrainment modelling is based on the conservation equations of turbulent jet models that will be presented in the following sections.

2.1.1 Boussinesq approximation

In fluid dynamics, the Boussinesq approximation (Boussinesq (1897)) is used in the field of natural convection flow. It ignores density differences of mixed fluids except where they appear in terms of buoyancy force. This kind of flows is commonly observed in nature (such as oceanic circulation), in industry (dense gas dispersion, fume cupboard ventilation), and the built environment (natural ventilation, central heating) (Kleinstreuer (1997), Tritton (2012)).

Boussinesq approximation is based on a reference physical state, characterised by state temperature. In a general case, based on a reference temperature T_0 (with subscript $_0$ indicating the reference). We have the following first order development (linearisation) of local density:

$$\rho = \rho_0 \left(1 + \left.\frac{\partial \rho}{\partial T}\right|_{T_0} (T - T_0) + \left.\frac{\partial \rho}{\partial P_H}\right|_{P_{H_0}} (P_H - P_{H_0}) \right) \tag{2.1}$$

with pressure variation term is that from hydrodynamic pressure P_H. This linearisation with then integrated in flow momentum equations (1.28). The hypothesis is valid generally in

condition of small temperature variation in the flow as well as a small vertical scale so that density variations due to temperature and hydrostatic pressure variations are negligible.

However, in this problem, as we study in an isothermal condition, the linearisation near (ρ_0, T_0) is not necessary. We apply $\rho \approx \rho_0$ in momentum equation (1.28) everywhere except for the buoyancy force term.

$$\frac{\partial u_j}{\partial t} + \frac{\partial}{\partial x_i}\left(u_j u_i\right) = -\frac{1}{\rho_0}\frac{\partial P_H}{\partial z} + \frac{1}{\rho_0}\frac{\partial \tau_{ij}}{\partial x_i} - g_j\frac{\rho}{\rho_0} \tag{2.2}$$

If we consider separating the hydrostatic variation from hydrodynamic pressure variation, we can define the pressure related to fluid motion $P_M = P_H - P_h$, as the difference between P_H and hydrostatic pressure $P_h = P_{H_0} - \rho_0 g z$. Thus the above equation can be transformed into:

$$\frac{\partial u_j}{\partial t} + \frac{\partial}{\partial x_i}\left(u_j u_i\right) = -\frac{1}{\rho_0}\frac{\partial P_M}{\partial z} + \frac{1}{\rho_0}\frac{\partial \tau_{ij}}{\partial x_i} + g_j\frac{\rho_0 - \rho}{\rho_0} \tag{2.3}$$

The Boussinesq approximation is valid if

$$\frac{\rho_0 - \rho}{\rho_0} \ll 1 \tag{2.4}$$

In this problem, the density reference is selected as the density of fresh air $\rho_0 = \rho_a = 1.168 kg/m^3$. Boussinesq approximation can be considered perfectly valid if

$$\frac{\rho_a - \rho_{inj}}{\rho_a} \ll 1 \tag{2.5}$$

If not, the condition 2.4 can be rewritten as

$$X_1 \ll \frac{\rho_a}{\rho_a - \rho_{inj}} \tag{2.6}$$

As we have $\rho_a/\rho(H_2) = 14.4$ and $\rho_a/\rho(He) = 7.3$ a large difference of density between air and injected light gas, Boussinesq approximation is clearly not valid for the whole cavity, especially for the injection area. The term $\rho_a/(\rho_a - \rho_{inj})$ equals to 1.16 for helium and 1.07 for hydrogen. Therefore, Boussinesq approximation may be considered valid only for the region where local concentration is less than 10%.

2.1.2 Auto-similarity and profile assumptions

The auto-similarity assumption is initially proposed in classic turbulent jet model Morton et al. (1956). Auto-similarity means that the profiles of steady-state vertical velocity and buoyancy force in horizontal sections are of similar form at all heights of the jet. The word "similar form" could be explained as the same type of form with different characteristic parameters. As the buoyancy force is linearly related to mixture density and volume fraction, this condition is equivalent to the similar form of the latter two fields. In original model of Morton et al. (1956), two characteristic profiles are selected: the steady-state vertical velocity w and mixture density ρ, assumed both in Top-hat profile with same characteristic radius. In other models, like Kaminski et al. (2005), the profiles of w and ρ are not precisely assumed, but in later development, Carazzo et al. (2006) gave the explicit analytical solutions under Gaussian profiles. Based on PIV measurement, Cariteau (2012) also showed that w and ρ could be better assumed in Gaussian profiles. Thus, Gaussian assumptions of vertical velocity w and mixture density ρ are recommended to be applied in post-processing method.

Here we summarise two approaches, Top-hat profiles and Gaussian profiles.

Top-hat profiles

Top-hat assumption is the simplest way of jet modelling. Under Top-hat assumption, the profile of vertical velocity varies as a function of altitude z over the injection point.

$$w(r,z) = \begin{cases} w_T(z), & \text{for } r \leq b_T(z) \\ 0, & \text{for } r > b_T(z) \end{cases} \tag{2.7}$$

with b_T characteristic radius of the jet defined as the border of the jet area.

The density profile in the jet is in the same Top-hat form with same characteristic radius b_T and a uniform mixture density ρ_T if we assumed self-similar solutions.

$$\rho(r,z) = \begin{cases} \rho_T(z), & \text{for } r \leq b_T(z) \\ \rho_e(z), & \text{for } r > b_T(z) \end{cases} \tag{2.8}$$

with ρ_e the mixture density in the far field of the jet, called hereinafter environmental density.

Gaussian profiles

Under Gaussian assumption, the profile of vertical velocity is under a 2D Gaussian distribution

$$w(r,z) = w_G(z)\exp\left(-\frac{r^2}{b_G^2(z)}\right) \tag{2.9}$$

with w_G the maximum vertical velocity in the jet centre, also called Gaussian characteristic vertical velocity and b_G the characteristic radius of the jet defined by

$$w(r = b_G, z) = \frac{w_G(z)}{e} \tag{2.10}$$

with e the Euler's number ($e = 2.718...$). Note that in Gaussian profile, the notion of "jet edge radius" does not exist. The area based on $b_G(z)$ is defined as the standard deviation (σ) of this 2D Gaussian distribution.

The mixture density profile in the jet is in the similar 2D Gaussian form, but with different characteristic radius λb_G.

$$\rho(r,z) = \rho_e(z) - (\rho_e(z) - \rho_G(z))\exp\left(-\frac{r^2}{(\lambda b_G)^2}\right) \tag{2.11}$$

with λ called diffusion ratio. It represents the ratio of radial convection-diffusion of mass and momentum. ρ_G is the characteristic density in the jet centre, representing the minimum value of the mixture density, ρ_e is the environment density at far-field of the jet with

$$\lim_{r\to\infty} \rho = \rho_e \tag{2.12}$$

For simple reason, some literature use $\lambda = 1$. In this case, the mixture density profile is considered exactly in the same 2D Gaussian form as vertical velocity profile.

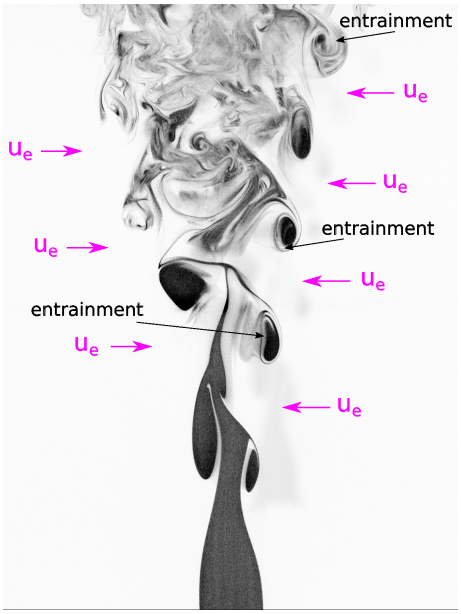

Figure 2.1: Illustration of the entrainment process at the edges of the buoyant jet (internal communication CEA)

2.1.3 Entrainment modelling

As illustrated in figure 2.1, for a buoyant jet, entrainment effect is formed by a series of eddies capturing the ambient fluid from the surrounding into the rotational flow, then mixing with the fluid in the jet. Physically, the phenomenon is characterised by a horizontal velocity called entrainment velocity u_e, which represent the centripetal velocity contribution of the exterior to the jet, pushing the environmental ambient gas into the jet. This entrainment velocity depends generally on radial and vertical positions. However, in 1D modelling, as the steady flow is axisymmetric, the entrainment velocity can be considered as a function of vertical position z only. The modelling of entrainment velocity depends on retained hypothesis.

Boussinesq case

In literature, two different types of assumptions are presented. One is typically in Morton et al. (1956) and Morton (1967) models under the Boussinesq assumption: the entrainment velocity u_e at the edge of the jet is proportional to a entrainment characteristic vertical velocity w_c at this height, with the proportionality noted α called entrainment coefficient.

$$u_e = \alpha w_c \tag{2.13}$$

Generally, the value of α depends on profile assumption applied for vertical velocity. Following the Top-hat or Gaussian profiles are considered, we have the following relation:

$$\alpha_T = \sqrt{2}\alpha_G \tag{2.14}$$

with α_T the value of entrainment coefficient under Top-hat profile assumption of vertical velocity and α_G that under Gaussian profile assumption. The classic turbulent jet model takes this entrainment coefficient as a constant along the jet, as in Morton et al. (1956). It is reported in literature, under a Top-hat profile assumption, that $\alpha_T \approx 0.05$ for a turbulent jet and $\alpha_T \approx 0.155$ for a pure turbulent plume, as summarised in table 2.1. Note that the characteristic velocity in the jet w_c depends on velocity profile assumption (Top-hat or Gaussian).

Experimental measurements	Type	α_T	α_G
Rouse et al. (1952)	Jet	-	0.041
Kotsovinos (1975)	Jet	0.04-0.06	-
Kotsovinos (1976)	Jet	0.06	-
Chen and Rodi (1980a)	Jet	0.05-0.06	-
Antonia et al. (1983)	Jet	0.05	-
Linden (2000)	Jet	0.05	-
Lee and Emmons (1961)	Plume	-	0.16
Kotsovinos (1975)	Plume	-	0.10
Ramaprian and Chandrasekhara (1989)	Plume	0.16	0.11
Yuana and Cox (1996)	Plume	-	0.13
Paillat and Kaminski (2014)	plume	-	0.12
Parker et al. (2020)	Plume	0.14	0.10

Table 2.1: Values of entrainment coefficient for gas-gas mixture, as reported in literature

For a general turbulent buoyant jet, experiments suggest that α varies with development of the jet to a plume and takes the asymptotic values α_j in momentum-driven (jet-like) and α_p in buoyancy driven (plume like) flows. $\alpha(z)$ values in between at transition from jets to plumes, as a function of altitude z. Priestley and Ball (1955) propose an expression for a general case based on the conservation of energy

$$\alpha(z) = \alpha_j - (\alpha_j - \alpha_p)\frac{\mathrm{Ri}(z)}{\mathrm{Ri}_p} \tag{2.15}$$

with Ri the local jet Richardson number and Ri_p the typical Richardson number for a pure plume. Note that for a general case. This number may change along the jet thus the coefficient α is in fact a function of vertical position z.

Based on this model, Fischer et al. (1979), List (1982) estimated these parameters $\alpha_j = 0.0535$, $\alpha_p = 0.0833$, $\mathrm{Ri}_p = 0.557$. These results have been re-evaluated experimentally by Papanicolaou and List (1988) which reported $\alpha_j = 0.0545, \alpha_p = 0.0875, \mathrm{Ri}_p = 0.63$ for a liquid-liquid mixture. More recently, Jirka (2004) has employed an expression similar to that proposed by Priestley and Ball (1955) and found $\alpha_j = 0.055, \alpha_p = 0.083, \mathrm{Ri}_p = 0.522$ for a liquid-liquid mixture. These results are summarised in Papanicolaou et al. (2008).

Moreover, another theoretical approach Craske and van Reeuwijk (2015a,b) based on energy analysis proves that the entrainment coefficient α can be decomposed into three terms

$$\alpha = \alpha_{\mathrm{conv}} + \alpha_{\mathrm{diff}} + \alpha_{\mathrm{turb}} \tag{2.16}$$

with α_{conv} the entrainment effect related to the convection and the redistribution of kinetic energy, α_{diff} that related to the mass diffusion and α_{turb} that related to the local turbulence flow. This term is zero if flow is laminar. It is found that for a turbulent jet, the first term α_{conv} is the leading-order term for entrainment both in the steady state and unsteady state and the other two terms related to the diffusion and local turbulence flow can be correctly ignored in steady state.

Non-Boussinesq case

Apart from above various approaches under Boussinesq approximation, there is another type of entrainment assumption presented in Crapper and Baines (1977), Rooney and Linden

(1996), Carlotti and Hunt (2005), Xiao et al. (2009), El-Amin et al. (2010), under non-Boussinesq condition: the entrainment velocity u_e at the edge of the jet is not only proportional to a characteristic vertical velocity w_c at this altitude, but also related to a characteristic mixture density ρ_c.

$$u_e = \alpha \sqrt{\frac{\rho_c}{\rho_0}} w_c \tag{2.17}$$

with ρ_0 a density reference.

The evaluation of w_c and ρ_c will depend on applied profile assumptions. Under Top-hat assumption, we have simply $w_c = w_T$ and $\rho_c = \rho_T$. No clear relation for Gaussian profiles is found in the literature. However, in both cases, the relation (2.14) is still valid.

2.2 Characteristic jet quantities

In 1D models, the development of the jet is characterised by a series of 1D physical quantities. These quantities, called **characteristic jet quantities**, are defined as integration on horizontal plane. Here are presented its original definitions:

Volume flux

$$\mathcal{Q}(z) = \int_{S(z)} w \, dS(z) \tag{2.18}$$

where the integral surface $S(z)$ indicates the jet area on the cross-section at altitude z and $w(r,z)$ is the vertical velocity in steady state.

Mass flux

$$\mathcal{Q}_m(z) = \int_{S(z)} \rho w \, dS(z) \tag{2.19}$$

with $\rho(r,z)$ the local mixture density in steady state.

Momentum flux

$$\mathcal{M}(z) = \int_{S(z)} w^2 \, dS(z) \tag{2.20}$$

Mass momentum flux

$$\mathcal{M}_m(z) = \int_{S(z)} \rho w^2 \, dS(z) \tag{2.21}$$

Buoyancy flux

$$\mathcal{B}(z) = \int_{S(z)} G' w \, dS(z) \tag{2.22}$$

with $G'(r,z)$ the reduced gravity defined as

$$G'(r,z) = \frac{\rho_e(z) - \rho(r,z)}{\rho_0} g \tag{2.23}$$

$\rho_e(z)$ is the environmental density in the far field outside the jet and ρ_0 is a reference density used as reference state in the Boussinesq approximation, here chosen equal to density of air $\rho_0 = \rho_{air}$.

Expressions under Top-hat assumption

Based on the Top-hat assumption, these characteristic jet quantities can be simply rewritten as

$$\mathcal{Q} = \int_0^\infty w\ 2\pi r dr = \int_0^{b_T} w_T\ 2\pi r dr = \pi w_T b_T^2 \tag{2.24}$$

$$\mathcal{Q}_m = \int_0^\infty \rho w\ 2\pi r dr = \int_0^{b_T} \rho_T w_T\ 2\pi r dr = \pi \rho_T w_T b_T^2 \tag{2.25}$$

$$\mathcal{M} = \int_0^\infty w^2\ 2\pi r dr = \int_0^{b_T} w_T^2\ 2\pi r dr = \pi w_T^2 b_T^2 \tag{2.26}$$

$$\mathcal{M}_m = \int_0^\infty \rho w^2\ 2\pi r dr = \int_0^{b_T} \rho_T w_T^2\ 2\pi r dr = \pi \rho_T w_T^2 b_T^2 \tag{2.27}$$

$$\mathcal{B} = \int_0^\infty G' w\ 2\pi r dr = \int_0^{b_T} G'_T w_T\ 2\pi r dr = \pi G'_T w_T b_T^2 \tag{2.28}$$

with G'_T the reduced gravity in horizontal sections defined by

$$G'_T(z) = \frac{\rho_e(z) - \rho_T(z)}{\rho_0} g \tag{2.29}$$

2.3 Boussinesq approach Morton et al. (1956)

We present in this section the classic turbulent jet model based on Morton et al. (1956), a Boussinesq approach with a constant entrainment coefficient α.

2.3.1 Basic assumptions

The model is based on the following assumptions.

Assumption 1: The flow is incompressible, so that we have a conservation of volume flux.

Assumption 2: The steady state is achieved. The flow pattern is assumed axisymmetric on jet axis. Thus, the vertical velocity w and the density of local mixture ρ of jet at steady state are theoretically independent of θ. Therefore, we can define a series of 1D physical quantities in the jet area which are functions of altitude z only (1D modelling).

Assumption 3: The profiles of the vertical velocity and the mixture density in the jet are modelled by a Top-hat approximation.

Assumption 4: The Boussinesq approximation is considered valid.

Assumption 5: The velocity of entrainment (u_e) is proportional to Top-hat characteristic velocity at that height (w_T), with an entrainment coefficient α_T, assumed as a constant along the jet.

$$u_e(z) = \alpha_T w_T(z) \tag{2.30}$$

2.3.2 Conservation equations

Three characteristic quantities are used in this model: the volume flux $\mathcal{Q}$, the momentum flux $\mathcal{M}$ and the buoyancy flux $\mathcal{B}$. The demonstration of conservation equations are based on differential governing equations, that consist of conservation of volume flux, mass flux and momentum. The detailed demonstration is presented in appendix A.1. Here we just present the final relations.

$$\frac{d\mathcal{Q}}{dz} = 2\alpha_T \sqrt{\pi \mathcal{M}} \tag{2.31}$$

$$\frac{d\mathcal{M}}{dz} = \frac{\mathcal{B}\mathcal{Q}}{\mathcal{M}} \tag{2.32}$$

$$\frac{d\mathcal{B}}{dz} = -N^2\mathcal{Q} \tag{2.33}$$

with $N^2 = -\frac{g}{\rho_0}\frac{d\rho_e}{dz}$ the square of the Brunt-Vaisala buoyancy frequency.

This system of equations is non-linear. Thus generally it does not possess explicit analytical solutions. However, some analytical solutions may be existed under specific conditions. If we study in homogeneous environment, that is to say, the far field environmental density ρ_e does not change with altitude z, the conservation equations possess explicit analytical solutions.

2.3.3 Virtual origin and analytical solutions in homogeneous environment

In this section, we focus on analytical solutions of Morton's equations in a homogeneous environment. The environmental density ρ_e is thus a constant along the jet and independent on altitude z. Thus, we have directly

$$\frac{d\mathcal{B}}{dz} = 0 \tag{2.34}$$

As a consequence, we have for any altitude z, $\mathcal{B}(z) = \mathcal{B}_0$ the conservation of buoyancy flux at injection point $z = 0$. We note also $\mathcal{Q}_0 = \mathcal{Q}(0)$, $\mathcal{M}_0 = \mathcal{M}(0)$ the initial conditions at injection level $z = 0$.

Morton's system possess an ordinary polynomial solution for a pure plume which possesses zero initial conditions $(\mathcal{Q}_0, \mathcal{M}_0, \mathcal{B}_0)$=(0,0,$\mathcal{B}_0$), presented in the original article of Morton et al. (1956). In the latter study, Morton (1959) shows that it is always possible to relate the flow above a general point source to an equivalent a source of pure plume no matter in a homogeneous environment or a stratified environment. This conversion is more complicated for a stratified environment than a homogeneous environment, which for the former one needs more information about environment variation along the jet. Here, in homogeneous environment, this change of initial conditions $(\mathcal{Q}_0, \mathcal{M}_0, \mathcal{B}_0)$ to (0,0,$\mathcal{B}_0$) is done by introducing an virtual origin displacement. Following the steps of Morton (1959), Hunt and Kaye (2001) summarised a three-step conversion method.

Step 1: Injection geometrical correction

In this first step, we transfer an ordinary jet injection to a point source. A general buoyant jet often possess a geometrical opening, eventually circular with diameter d. Chen and Rodi (1980b) say that this kind of buoyant jet with a circular injection source could be considered as a point jet, with the asymptotic virtual origin located below the injection source plan, with a displacement $z_0 < 0$, as illustrated in figure 2.2.

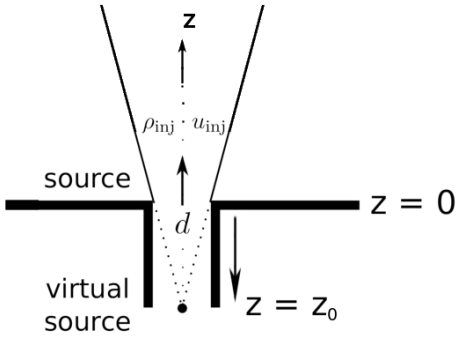

Figure 2.2: Schematic representation of a real source and its associated virtual source

Generally, the displacement z_0 is depended on the actual source diameter d and some characteristic quantities of the injection source, such as its vertical velocity profile. If d is smaller enough, comparing with vertical extension of the jet, the correction of z_0 could be neglected.

Step 2: Source correction

In the second step, we transfer the obtained point source $(\mathcal{Q}_0, \mathcal{M}_0, \mathcal{B}_0)$ to a forced plume. From the demonstration of Morton (1959), a general point source with initial conditions $(\mathcal{Q}_0, \mathcal{M}_0, \mathcal{B}_0)$ at injection level $z = 0$ is exactly equivalent to a source forced plume with initial conditions $(0, \zeta\mathcal{M}_0, \mathcal{B}_0)$, of buoyancy and momentum only, with modified strength $\zeta\mathcal{M}_0$ and modified position $z = z_v$. The parameter ζ is called the modification factor and could be calculated by

$$\zeta^5 = 1 - \Gamma_0 \tag{2.35}$$

where Γ_0 is the source parameter, indicating the nature of source. $\Gamma_0 < 1$ corresponds the case "forced plume", while $\Gamma_0 > 1$ corresponds to a "lazy plume".

$$\Gamma_0 = \frac{5}{8\sqrt{\pi}\alpha_T}\frac{\mathcal{B}_0\mathcal{Q}_0^2}{\mathcal{M}_0^{5/2}} \tag{2.36}$$

The modified position z_v is related to the momentum jet length L_M

$$\frac{z_v}{L_M} = \begin{cases} -\sqrt{10}\,|\zeta|^{3/2}\int_{\mathrm{sgn}\zeta}^{1/|\zeta|}|T^5 - \mathrm{sgn}\zeta|^{-1/2}T^3 dT & \text{if } \Gamma_0 \neq 1 \\ -2.108 & \text{if } \Gamma_0 = 1 \end{cases} \tag{2.37}$$

with sgnζ the sign of ζ (+1 or -1). Hunt and Kaye (2001) propose a definition of L_M related to $\mathcal{M}_0$ and $\mathcal{B}_0$

$$L_M = \frac{1}{2\sqrt{\alpha_T}\pi^{1/4}}\frac{\mathcal{M}_0^{3/4}}{\mathcal{B}_0^{1/2}} \tag{2.38}$$

Step 3: Jet-length-based correction

The third step is to transfer initial conditions $(0, \zeta\mathcal{M}_0, \mathcal{B}_0)$ to a pure plume $(0, 0, \mathcal{B}_0)$. Theoretical demonstration of Morton (1959) proved that the flow from the source $(0, \zeta\mathcal{M}_0, \mathcal{B}_0)$ exhibits the behaviour of the flow above the point source pure plume $(0,0,\mathcal{B}_0)$ positioned at $z = z_{avs}$ calculated as follows, with accurate range of height deduced later by Baines and Turner (1969).

$$\frac{z_{avs}}{L_M} = \begin{cases} -1.057\zeta^{3/2} & \text{if } 0 < \Gamma_0 < 1 \quad \text{accurate to within 1\% for } z/L_M > 6\zeta^{3/2} \\ 0 & \text{if } \Gamma_0 = 1 \\ -3.253|\zeta|^{3/2} & \text{if } \Gamma_0 > 1 \quad \text{accurate to within 1\% for } z/L_M > 4|\zeta|^{3/2} \end{cases} \tag{2.39}$$

Total virtual origin displacement

Once we have corrected the injection geometry and twice the injection conditions $(\mathcal{Q}_0, \mathcal{M}_0, \mathcal{B}_0)$ to $(0,0,\mathcal{B}_0)$, we have introduced three displacement pf the source z_0, z_v and z_{avs}. Consequently, an ordinary turbulent jet can be considered physically as a pure plume, with its origin situated at $z = z_t$, with

$$z_t = z_v + z_{avs} + z_0 \tag{2.40}$$

The origin of this equivalent pure plume is called virtual origin of the jet and z_t is called total virtual origin displacement.

General analytical solutions for homogeneous environment

As presented in the original model of Morton et al. (1956), conservation equations possess analytical solutions for a pure plume with initial conditions $(0,0,\mathcal{B}_0)$, taking into account the total virtual origin displacement z_t. We have the general solution for conservation equations in homogeneous environment.

$$\mathcal{Q}(z) = \frac{6}{5}\left(\frac{9}{10}\right)^{1/3} \pi^{2/3} {\alpha_T}^{4/3} \mathcal{B}_0^{1/3} (z - z_t)^{5/3} \tag{2.41}$$

$$\mathcal{M}(z) = \frac{1}{\zeta}\left(\frac{9}{10}\right)^{2/3} \pi^{1/3} {\alpha_T}^{2/3} \mathcal{B}_0^{2/3} (z - z_t)^{4/3} \tag{2.42}$$

$$G_T'(z) = \frac{5}{6}\left(\frac{9}{10}\right)^{-1/3} \pi^{-2/3} {\alpha_T}^{-4/3} \mathcal{B}_0^{2/3} (z - z_t)^{-5/3} \tag{2.43}$$

$$b_T(z) = \frac{6}{5}\alpha_T (z - z_t) \tag{2.44}$$

$$w_T(z) = \frac{5}{6}\left(\frac{9}{10\pi}\right)^{1/3} {\alpha_T}^{-2/3} \mathcal{B}_0^{1/3} (z - z_t)^{-1/3} \tag{2.45}$$

with $\zeta = (1 - \Gamma_0)^{1/5}$. Note that these solutions are valid only for sufficiently large distances above the original source. The equation (2.42) is not valid for case $\Gamma_0 = 1$.

2.3.4 Further development

The model of Morton et al. (1956) is a classic turbulent jet model under Boussinesq approximation. It has been validated by a series of experimental studies like Shabbir and George (1994) and Papanicolaou and List (1988). Recently, developments based on this model are various. For example, Caulfield (1991) determines the source conditions where a jet or plume initially contracts, or called "neck", after rising above its source. The contraction occurs directly above the source if the local change rate of jet radius b_T with height satisfies $\left.\frac{db_T}{dz}\right|_{z=0} = (2 - 0.8\Gamma_0)\alpha_T < 0$, providing Γ_0 the source parameter ($\Gamma_0 > 2.5$). By analysis of the jet undergoing contraction, Caulfield (1991); Caulfield and Woods (1995) deduce later that the jet can accelerate above the source without contracting if $\Gamma_0 > 1.25$. Moreover, Scase and Hewitt (2012), Woodhouse et al. (2016) and Craske and van Reeuwijk (2016) present an unsteady approach with volume, momentum and buoyancy fluxes varying in time. Papanicolaou et al. (2008), Carazzo et al. (2010), Mehaddi et al. (2012) focus on a particular case called fountain when the environmental density is lighter than that of the injection fluid. Wang and Law (2002) propose a second-order general model for turbulent jet under a constant entrainment coefficient. Van Reeuwijk and Craske (2015) and Van Reeuwijk et al. (2016) propose a decomposition method of entrainment coefficient based on a DNS simulation.

2.4 Boussinesq approach Kaminski et al. (2005)

In this section, we present a turbulent jet model proposed by Kaminski et al. (2005) and Carazzo et al. (2006), under Boussinesq approximation with a variable entrainment coefficient $\alpha(z)$. Note that this model is valid only for homogeneous environment where the environmental density ρ_e in the far-field of the jet is constant along the jet.

2.4.1 Basic assumptions and characteristic jet quantities

We study in the cylinder-polar coordinates system (r, θ, z). The origin is placed at injection point. Recall that in this coordinates system the velocity vector can be written as $\overrightarrow{u} = u\overrightarrow{e_r} + v_\theta \overrightarrow{e_\theta} + w\overrightarrow{e_z}$. The basic assumption of this model is presented as follows.

Assumption 1: The flow is incompressible, so that we have a conservation of volume flux.

Assumption 2: The steady state is achieved.

Assumption 3: The flow pattern is assumed axisymmetric on jet axis. The jet behaviour is characterised by 1D physical quantities as functions of altitude z only (1D modelling).

Assumption 4: The jet develops in a uniform environment, so that the environment density ρ_e is a constant along the jet.

Assumption 5: The largest local variations of density in the field of motion are small in comparison with chosen reference density $\rho'/\rho_0 \ll 1$, Boussinesq approximation is considered valid.

Three characteristic quantities are defined in this model, similarly to the model of Morton et al. (1956): the volume flux $\mathcal{Q}$, defined in equation (2.18), the momentum flux $\mathcal{M}$, defined in equation (2.20) and the buoyancy flux $\mathcal{B}$, defined in equation (2.22).

2.4.2 Conservation equations and entrainment parameters

The conservation equation of Kaminski et al. (2005) is like that of classic Boussinesq model of Morton et al. (1956), we have three conservation equations:

$$\frac{d\mathcal{Q}}{dz} = 2\alpha(z)\sqrt{\pi\mathcal{M}} \tag{2.46}$$

$$\frac{d\mathcal{M}}{dz} = \frac{\mathcal{B}\mathcal{Q}}{\mathcal{M}} \tag{2.47}$$

$$\frac{d\mathcal{B}}{dz} = 0 \tag{2.48}$$

In this model the entrainment coefficient is no longer considered as a constant, but variable along the jet $\alpha(z)$. The variation of $\alpha(z)$ depends on two entrainment parameters $A(z)$, $C(z)$ as well as on the equivalent Top-hat radius variation $b_T(z)$ and the local Richardson number $\mathrm{Ri}(z)$.

$$\alpha(z) = \frac{C(z)}{2} + \left(1 - \frac{1}{A(z)}\right)\mathrm{Ri}(z) + \frac{b_T(z)}{2}\frac{d\ln A(z)}{dz} \tag{2.49}$$

The local Richardson number Ri(z) is originally defined for Top-hat profiles parameters. By identification of $\mathcal{Q}$ (2.24), $\mathcal{M}$ (2.26) and $\mathcal{B}$ (2.28), the local Richardson number (2.50) can be rewritten as function of characteristic jet quantities.

$$\mathrm{Ri}(z) = \frac{b_T G_T'}{w_T^2} = \frac{1}{\sqrt{\pi}}\frac{\mathcal{B}_0\mathcal{Q}^2(z)}{\mathcal{M}^{5/2}(z)} \tag{2.50}$$

with $\mathcal{B}_0$ the buoyancy flux at source, considered constant along the jet.

The variation of entrainment coefficient $\alpha(z)$ is defined by equation (2.49) with parameters $A(z)$, $C(z)$ called entrainment parameters. Based on 16 independent experimental measurements (for gas and liquid, jet and plume), Carazzo et al. (2006, 2008) summarised these experimental results and found that the parameter $C(z)$ in (2.49) could be considered as a constant, universal for jet and plume:

$$C = 0.135 \pm 0.005 \tag{2.51}$$

However, another parameter $A(z)$ depends on the shapes of velocity and buoyancy profiles. No accurate analytical formulas are found in the literature. Based on experimental studies of Papanicolaou and List (1988) and Wang and Law (2002), Carazzo et al. (2008) proposed a formula for $A(z)$ valid at large distances from the source, typically for $z/d > 10$ with d the injection diameter.

$$A(z) = \begin{cases} A_j(z) & z \leq L_{mix} \\ A_j(z) + \frac{1}{4}\left(A_p(z) - A_j(z)\right)\left(\frac{z}{L_{mix}} - 1\right) & L_{mix} < z < 5L_{mix} \\ A_p(z) & z \geq 5L_{mix} \end{cases} \tag{2.52}$$

with $A_j(z)$ and $A_p(z)$ are two typical parameters related to pure jet and pure plume respectively

$$A_j(z) = 2.45 - 1.05 \exp(-0.00465\ z/d) \tag{2.53}$$

$$A_p(z) = 1.42 - 4.42 \exp(-0.2188\ z/d) \tag{2.54}$$

And d is the injection diameter and L_{mix} is the Fischer's characteristic mixing length, related to the injection condition (Fischer et al. (1979)).

$$L_{mix} = \pi^{1/4} \mathrm{Ri}_{\mathrm{inj}}^{-1/2} \frac{d}{2} \tag{2.55}$$

with $\mathrm{Ri}_{\mathrm{inj}}$ injection Richardson number defined in (1.59).

In 2010s, CEA seeks to test the reliability of these empirical formulas in application of hydrogen release problem. An experimental project has been carried out with PIV measurement on a facility in which light gas (helium) was released in a two-metre-high cavity. This work provides experimental validation for equations (2.51), (2.52) and (2.53), but not for (2.54). Based on experimental measurements, Bernard-Michel (2014) proposes another correction formula for parameter $A_p(z)$

$$A_p(z) = 1.28\ \frac{1 + \tanh(-0.1\,(z/d - 9))}{2} + 1.65\ \frac{1 + \tanh(0.1\,(z/d - 7))}{2} \tag{2.56}$$

which matches better than that proposed initially by Carazzo et al. (2006) equation (2.54). Nonetheless, these formulas related to parameter $A(z)$ are all empirical without precise validity study. Consequently, these formulas cannot be considered as universal and thus may not be valid and be directly used in our problem.

2.4.3 Further development

The Boussinesq approach of Kaminski et al. (2005) and Carazzo et al. (2006) is a typical α-variable model which provides an explicit formula for variation of entrainment coefficient along the jet. Some recent work are based on this model. Papanicolaou et al. (2008) proposed an experience-valid theoretical analysis of decomposition of entrainment coefficient for negatively buoyant jets (where the jet buoyancy flux is negative). Bloomfield and Kerr (2000)

developed an analytical model for the turbulent fountain, where the injection is occurred in a lighter environment. The model is validated by the LES simulation of Devenish et al. (2010). Paillat and Kaminski (2014) proposed an analytical approach for plane turbulent plume with variable entrainment coefficient. Experimental study of Ezzamel et al. (2015) related model of Kaminski et al. (2005) under Gaussian assumption and the jet source parameter (defined in equation (2.36)).

2.5 Non-Boussinesq approach Rooney and Linden (1996)

In this section, we present a different turbulent jet model proposed by Rooney and Linden (1996), based on a non-Boussinesq approach with constant entrainment coefficient α.

2.5.1 Basic assumptions and characteristic jet quantities

We study in the cylinder-polar coordinates system (r, θ, z). The origin is placed at injection point with z axis of the jet. Basic assumptions of this model are presented as follows.

Assumption 1: The density of the mixture is a volume-weighted average of the densities of the components (linear mixing assumption).

Assumption 2: The steady state is achieved. The flow pattern is assumed axisymmetric by the vertical line through the jet point. We define a series of 1D physical quantities in the jet area which are functions of altitude z only (1D modelling).

Assumption 3: The profiles of vertical velocity $w(r,z)$ and density $\rho(r,z)$ in steady state are assumed in Top-hat form at all heights, with characteristic vertical velocity w_T, characteristic mixture density ρ_T and characteristic jet radius b_T defined the same in (2.7) and (2.8).

Assumption 4: The entrainment velocity at the edge of the jet, noted $u_e(z)$, on the one hand, is proportional to characteristic velocity at that height $w_c(z)$, with an entrainment coefficient α, assumed as constant along the jet, and on the other hand, is related to the entrainment characteristic density of mixture ρ_c in the jet at altitude z, presented in (2.17) with ρ_0 is a density reference. Under Top-hat assumption, we have $w_c(z) = w_T(z), \rho_c(z) = \rho_T(z)$ and in this case we note the entrainment coefficient α_T under Top-hat assumption. The entrainment velocity is written as

$$u_e(z) = \alpha_T \sqrt{\frac{\rho_T(z)}{\rho_0}} w_T(z) \tag{2.57}$$

In non-Boussinesq model, the conservation of volume flux is no longer assumed. The flow is no longer considered incompressible. Three characteristic jet quantities are analysed: the volume flux $\mathcal{Q}$, the mass flux $\mathcal{Q}_m$ and the momentum mass flux $\mathcal{M}_m$.

2.5.2 Conservation equations

The conservation equations consist of conservation of mass flux, momentum flux and a third equation related to the fluid state and enthalpy to enclose the system. The detailed demonstration are presented in appendix A.3. The conservation equations are written as:

$$\frac{d\mathcal{Q}_m}{dz} = 2\pi b_T u_e \rho_e \tag{2.58}$$

$$\frac{d\mathcal{M}_m}{dz} = 2\pi g \int_0^{b_T} (\rho_e - \rho) r dr = \pi g (\rho_e - \rho_T) b_T^2 \tag{2.59}$$

$$\frac{d\mathcal{Q}}{dz} = 2\pi b_T u_e \tag{2.60}$$

Under Top-hat assumption, by using relations (2.24), (2.25) and (2.27), we have profile parameters expressed using the following characteristic jet quantities

$$w_T = \frac{\mathcal{M}_m}{\mathcal{Q}_m}, \quad b_T = \sqrt{\frac{\mathcal{Q}\,\mathcal{Q}_m}{\pi \mathcal{M}_m}}, \quad \rho_T = \frac{\mathcal{Q}_m}{\mathcal{Q}} \tag{2.61}$$

The conservation equations can be rewritten as follows.

$$\frac{d\mathcal{Q}_m}{dz} = 2\alpha_T \rho_e \sqrt{\frac{\pi \mathcal{M}_m}{\rho_0}} \tag{2.62}$$

$$\frac{d\mathcal{M}_m}{dz} = g\left(\rho_e - \frac{\mathcal{Q}_m}{\mathcal{Q}}\right)\frac{\mathcal{Q}\mathcal{Q}_m}{\mathcal{M}_m} \tag{2.63}$$

$$\frac{d\mathcal{Q}}{dz} = 2\alpha_T \sqrt{\frac{\pi \mathcal{M}_m}{\rho_0}} \tag{2.64}$$

Equations (2.62)-(2.64) constitute a non-linear ODE system where only the characteristic jet quantities $\mathcal{Q}, \mathcal{Q}_m, \mathcal{M}_m$ appear.

2.5.3 Virtual origin and analytical solutions in homogeneous environment

In this section, we aim at solving the conservation equations (2.58), (2.59) and (2.60) in an homogeneous environment, which means ρ_e is constant along the jet. We choose the environmental density as the density reference presented in (2.57), that is to say $\rho_0 = \rho_e$. The analytical solutions are based on the discussion in Rooney and Linden (1996), Woods (1997) and developed in Carlotti and Hunt (2005) and Salizzoni et al. (2017).

By comparing equations (2.58) and (2.60), we have firstly the conservation of buoyancy flux under homogeneous environment assumption.

$$\mathcal{B}(z) = \int \frac{\rho_e - \rho}{\rho_0} g w \cdot 2\pi r dr = \mathcal{B}_0 \tag{2.65}$$

where $\mathcal{B}_0$ is the buoyancy flux at the injection point. At the injection point, the density is uniformly distributed in the jet (ρ_{inj}), so we have simply

$$\mathcal{B}_0 = \mathcal{Q}(0)\frac{\rho_e - \rho_{inj}}{\rho_0} g \tag{2.66}$$

Thus the initial condition for volume flux $\mathcal{Q}(0)$ is directly equivalent to the initial condition for injection buoyant flux $\mathcal{B}_0$. For a general jet, the initial condition at injection ($z = 0$) could be reconsidered as ($\mathcal{Q}_m(0)$, $\mathcal{M}_m(0)$, $\mathcal{B}_0$).

The analytical solution for a pure plume with initial conditions ($\mathcal{Q}_m(0) \neq 0$, $\mathcal{M}_m(0) \neq 0$, $\mathcal{B}_0$) is deduced by Rooney and Linden (1997) after a dimensional analysis introduced in Rooney and Linden (1996). Then the idea is the same as presented in Hunt and Kaye (2001) for Boussinesq case, try to link a general source ($\mathcal{Q}_m(0) = 0$, $\mathcal{M}_m(0) = 0$, $\mathcal{B}_0$) with a pure plume (0, 0, $\mathcal{B}_0$). For this purpose, we introduce the notion of virtual origin. Carlotti and Hunt (2005)

present a three-step correction method for non-Boussinesq jet to determine this virtual source displacement. The approach is very similar as in Boussinesq case in which correction parameters depends on the value of source parameter Γ_0, differently defined in non Boussinesq case, and presented as follows. Detailed formula are presented in appendix B.

$$\Gamma_0 = \frac{5\sqrt{\rho_e}}{8\sqrt{\pi}\alpha_T}\frac{\mathcal{B}_0\mathcal{Q}_{m,0}^2}{\mathcal{M}_{m,0}^{5/2}} \tag{2.67}$$

General analytical solutions for homogeneous environment

By applying the solutions of conservation equations applied for a pure plume, we have following general solutions, considering the total virtual origin displacement z_t.

$$\mathcal{Q}_m(z) = \frac{36}{25}\left(\frac{25}{48}\right)^{1/3}\pi^{2/3}\rho_e{\alpha_T}^{4/3}\mathcal{B}_0^{1/3}(z-z_t)^{5/3} \tag{2.68}$$

$$\mathcal{Q}(z) = \frac{36}{25}\left(\frac{25}{48}\right)^{1/3}\pi^{2/3}\frac{\rho_e}{\rho_T(z)}{\alpha_T}^{4/3}\mathcal{B}_0^{1/3}(z-z_t)^{5/3} \tag{2.69}$$

$$\mathcal{M}_m(z) = \frac{36}{25}\left(\frac{25}{48}\right)^{2/3}\pi^{1/3}\rho_e{\alpha_T}^{2/3}\mathcal{B}_0^{2/3}(z-z_t)^{4/3} \tag{2.70}$$

$$\frac{\rho_e-\rho_T(z)}{\rho_T(z)}g = \frac{25}{36}\left(\frac{25}{48}\right)^{-1/3}\pi^{-2/3}{\alpha_T}^{-4/3}\mathcal{B}_0^{2/3}(z-z_t)^{-5/3} \tag{2.71}$$

Thus

$$\rho_T(z) = \frac{\rho_e}{1+\left(\frac{z_B}{z-z_t}\right)^{5/3}} \tag{2.72}$$

and

$$w_T = \left(\frac{25}{48}\right)^{1/3}\pi^{-1/3}{\alpha_T}^{-2/3}\mathcal{B}_0^{1/3}(z-z_t)^{-1/3} \tag{2.73}$$

with z_B the characteristic length of non-Boussinesq effect defined as follows. Below this altitude, the non-Boussinesq effects are dominant.

$$z_B = \left(\frac{25}{36}\right)^{3/5}\left(\frac{25}{48}\right)^{-1/5}\pi^{-2/5}{\alpha_T}^{-4/5}\frac{{\mathcal{B}_0}^{2/5}}{g^{3/5}} \tag{2.74}$$

Consequently, under Top-hat assumption, the profile of jet radius reads as

$$b_T = \frac{6\alpha_T}{5}(z-z_t)\sqrt{1+\left(\frac{z_B}{(z-z_t)}\right)^{5/3}} \tag{2.75}$$

Asymptotic behaviour and physical interpretation of z_B

Woods (1997) compared the above solutions with that of Morton et al. (1956), typically for the profile of the characteristic radius of the jet or plume $b_T(z)$, presented in figure 2.3. Neglecting the total virtual origin displacement z_t, for a pure plume, the structure in the area far higher of the origin, non-Boussinesq (solid line) converges to the Boussinesq pure plume solution. The limit $z_B = 0$ corresponds to the classical solution of Morton et al. (1956) (see equations (2.41-2.45)). The adjustment of the radius b_T to within about 10% of a Boussinesq plume occurs over the distance around $z - z_t = 4z_B$ above the virtual point source. Thus, the Boussinesq characteristic length z_B is an indicator for the region where non-Boussinesq effects dominant. Generally, for area $z - z_t > 4z_B$, the non-Boussinesq may be neglected.

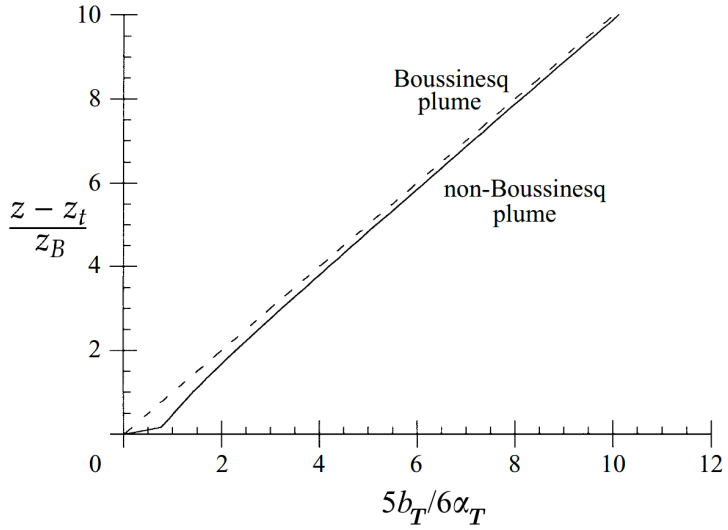

Figure 2.3: Variation of the characteristic radius of the pure plume (plotted as a function of $5b_T/6\alpha_T$) under Boussinesq approximation (dashed line) or in non-Boussinesq case (solid line). The behaviour of the non-Boussinesq plume (solid line) converges to the Boussinesq plume solution for $z - z_t > 4z_B$. Figure from Rooney and Linden (1996).

2.5.4 Further development

The model of Rooney and Linden (1996) is a non-Boussinesq modelling of the turbulent jet. In recent research, Van Den Bremer and Hunt (2014) extended this theory on planar sources. Hunt and Kaye (2005) presented a similar analytical approach for lazy plume where the source parameter $\Gamma_0 > 1$. Vaux et al. (2019) concentrated on a particular case for turbulent fountains where the environmental density is lighter than that of injected fluid.

El-Amin (2009) and El-Amin et al. (2010) discussed the non-Boussinesq effect for hydrogen jet in the ambient air. The analysis is similar to that of Rooney and Linden (1996) and Carlotti and Hunt (2005), but with hydrogen volume fraction X_1 used in the demonstration instead of the mixture density. The numerical simulation results with different injection Froude number are also presented to validate their analytical approach.

Another approach is based the virtual origin correction proposed by Carlotti and Hunt (2005), to identify the similitude of Boussinesq model of Morton et al. (1956) and non-Boussinesq approach of Rooney and Linden (1996). Van Den Bremer and Hunt (2010) proposed universal solutions for Boussinesq and non-Boussinesq plumes, in which a flux balanced parameter is defined not only at source position, but also along the entire jet, called the plume parameter (or jet parameter) defined by

$$\Gamma(z) = \frac{5\mathcal{B}(z)\mathcal{Q}_s^2(z)}{8\alpha\sqrt{\pi}\mathcal{M}_s^{5/2}(z)} \tag{2.76}$$

where $\mathcal{B}(z)$ is the buoyancy flux defined the same as in equation (2.22). $\mathcal{Q}_s$ and $\mathcal{M}_s$ are respectively specific volume flux and momentum flux in the jet, defined as

$$\mathcal{Q}_s(z) = \int_{S(z)} \eta w dS(z), \qquad \mathcal{M}_s(z) = \int_{S(z)} \eta w^2 dS(z) \tag{2.77}$$

with coefficient η equal to 1 in Boussinesq case and $\eta = \rho/\rho_0$ in non-Boussinesq case. The entrainment assumption is changed to $u_e = \alpha w_c \sqrt{\eta}$. The definition is very similar to that of Rooney and Linden (1996). The conservation equations are established on the plume parameter Γ, the characteristic radius of the plume or jet b and the characteristic vertical velocity w_c.

The analysis is based on Top-hat assumption. Based on this approach, Michaux and Vauquelin (2010) and Candelier and Vauquelin (2012) studied the asymptotic solutions for this universal model in homogeneous layer. However, the application of this approach in the present study presents additional difficulties as the Top-hat parameters like jet radius, vertical velocity cannot be directly measured from numerical results. In order to determine its values, we shall reconsider the identification of certain integrated characteristic quantities defined in section 2.2. Note that the relations between Top-hat quantities and Gaussian quantities will not be the same in the Boussinesq model and in the non Boussinesq case (see section 4.5.3). Consequently, we choose to study the variation of integrated quantities ($\mathcal{Q}, \mathcal{B}, ...$) rather than the profile parameters ($w_T, \rho_T, b_T, ...$).

2.6 Summary and discussion

In this chapter we have presented three theoretical approaches for turbulent jet modelling.

- Model of Morton et al. (1956), based on the Boussinesq approximation and an α-constant entrainment modelling
- Model of Kaminski et al. (2005), based on the Boussinesq approximation and an α-variable entrainment modelling
- Model of Rooney and Linden (1996), a non-Boussinesq approach with α-constant entrainment modelling

The model Morton et al. (1956) is the classic model for turbulent jet, which is commonly used in the relevant industrial context. It contains three enclosed conservation equations contains one non-linear equation, which usually, does not possess general analytical solutions. However, by introducing virtual origin displacement, a jet flow can be transformed to a pure plume and the latter one possesses explicit analytical solutions in unstratified environment. Two important hypotheses are assumed in this model, Boussinesq approximation and constant containment coefficient. Different experimental studies give us the value of constant entrainment coefficient depended on the flow pattern. For a pure jet, this parameter is around 0.05 and for a pure plume around 0.155. For practical use in the problem of hydrogen release, on the one hand, the determination of this entrainment coefficient is required before application of analytical results. On the other hand, by considering the density difference, Boussinesq approximation may be not valid for air-hydrogen mixture, but no more reliability study is found in the literature concerning its use in hydrogen release context.

In the previous experimental study Cariteau (2012), due to the ratio of buoyancy and momentum effect, the flow pattern (laminar/turbulent, jet/plume) is found changing along the jet, which means the entrainment coefficient is not a constant. The analytical approach of Kaminski et al. (2005) gives us an explicit formula of the variation of the entrainment coefficient along the jet but only for homogeneous environment. The conservation equations are the same as the classic model of Morton et al. (1956) but with variable entrainment coefficient. Later experimental studies Carazzo et al. (2006, 2008) provided us empirical formulas to determine certain parameters defined in the model.

Rooney and Linden (1996) proposed another analytical approach without Boussinesq approximation. The conservation equations are non-linear thus the model does not possess general analytical solutions. Particularly, for a turbulent jet situated in homogeneous environment, analytical solutions can be established thanks to a two-step correction proposed by Carlotti and Hunt (2005), transferring a general jet flow to a pure plume. The entrainment coefficient

is assumed constant in this model, while non Boussinesq entrainment coefficient depends also on the mixture density in the jet. This approach is proposed to be used in hydrogen release problem in El-Amin (2009); El-Amin et al. (2010).

We compare the assumptions and the differences between these 3 models in the table 2.2.

In summary, none of these models is perfect and prepared to be used. Analytical solutions from Morton et al. (1956) and Rooney and Linden (1996) are valid for homogeneous environment only. The applicability of these analytical solutions needs to be validated for stratified environment of air-hydrogen mixture. Besides, the profiles of entrainment coefficient provided by Kaminski et al. (2005) and Carazzo et al. (2006), as well as its validation domain need to be re-evaluated in this study as their formulas are based on specific configurations.

Moreover, turbulent jet models as well as its analytical solutions are used in ventilation model to solve hydrogen concentration distribution in the cavity. We will present this approach in the next chapter.

Approach	Morton et al. (1956)	Kaminski et al. (2005)	Rooney and Linden (1996)
General validity	Turbulent jet or plume	Turbulent jet or plume in homogeneous environment	Turbulent jet or plume
Boussinesq approximation	Yes	Yes	No
Entrainment coefficient	Constant	Variable	Constant
Entrainment assumption	$u_e(z) = \alpha w_c(z)$	$u_e(z) = \alpha(z) w_c(z)$	$u_e(z) = \alpha w_c(z) \sqrt{\rho(z)/\rho_0}$
Method to determine α	No explicit method	Explicit formula + empirical parameters	No explicit method
Main characteristic jet quantities	$\mathcal{Q}, \mathcal{M}, \mathcal{B}$	$\mathcal{Q}, \mathcal{M}, \mathcal{B}$	$\mathcal{Q}_m, \mathcal{M}_m, \mathcal{Q}$
Profiles assumptions	Top-hat (may be extended to Gaussian under additional assumptions)	Any profiles	Top-hat (may be extended to Gaussian under additional assumptions)
Analytical solution for homogeneous environment	Yes, with virtual source correction	No explicit analytical solutions	Yes, with virtual source correction

Table 2.2: Comparison of basic assumptions and validity of different approaches for turbulent jet modelling

Chapter 3

Natural ventilation model for two-vented cavity

In this chapter, we present analytical models for solving natural ventilation problem. The model is originally presented in Linden et al. (1990), and then developed in Linden (1999), is dedicated to the air-conditioning context: a thermal source is placed in a two-vented cavity, generating a thermal plume inside. Temperature gradient leads to the mixing of warm air heated by the thermal source and the ambient cool air initially presented in the cavity. The model is used to solve the temperature distribution in the steady state where a bi-layer distribution is assumed. It provides explicit analytical solutions, using geometrical parameters and injection conditions only. The model is based on Boussinesq jet model Morton et al. (1956). Afterwards, Rooney and Linden (1997) discussed density effect when applying this model for a light gas injection, and proposed related non-Boussinesq analytical solutions. Vauquelin et al. (2017b) evaluate this non-Boussinesq effect in 2D flow by experiments.

3.1 Model of Linden et al. (1990)

In this section, we present the original natural ventilation model proposed by Linden et al. (1990), its flow pattern analysis, basic assumptions and related global conservation equations.

3.1.1 Steady state flow pattern

We consider the injection of a light gas in a two-vented cavity, immersed in an external environment of fresh air, and two openings located at the top and bottom of the cavity (see figure 1.1). The height of the cavity is noted as H. The injection takes place at the centre of the cavity floor at the altitude $z = 0$. The temperature of the system is assumed to be constant with a constant thermodynamic pressure. We recall here the analysis of steady flow pattern in the cavity presented in Linden et al. (1990).

The injection of light gas (with density ρ_{inj}) generates a buoyancy-momentum source, entraining a turbulent buoyant jet above the injection point in the cavity. Within the jet, the flow is rising. Outside the jet, the horizontal entrainment component of velocity will be towards to the jet centre, making the air in the far field of the jet entering into the jet and mixing with the light gas in the jet flow. Due to the effect of the injected momentum and positive buoyancy, the light gas in the jet will quickly reach the ceiling of the cavity, then spread to the side-walls and descend in the space between the side-walls and the jet, generating a mixture of injected light gas and fresh air in the upper part of the cavity. Due to the mixing, the density of the

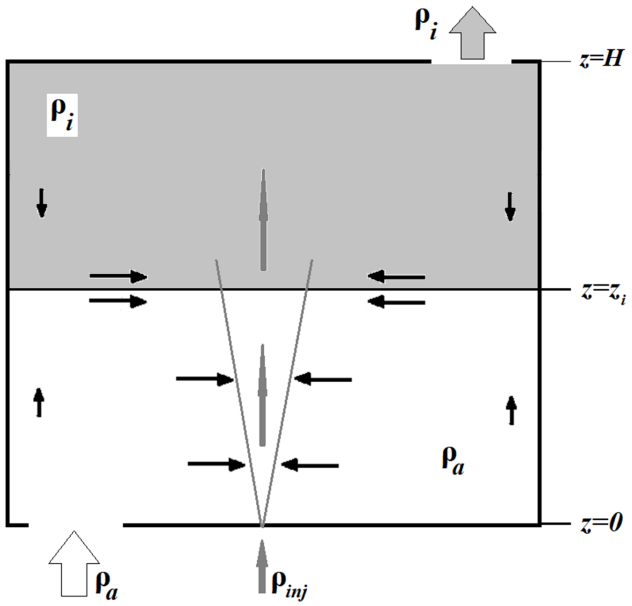

Figure 3.1: Steady flow pattern in two-vented cavity with injection of light gas as a source of buoyancy with a bi-layer distribution of the mixture density. Fresh air enters through the bottom opening, density ρ_a; density in the homogeneous layer ρ_i, interface plane at $z = z_i$.

mixture gas surrounding the jet in the upper part of the cavity will be lighter. Finally, a stable stratification develops in the cavity.

The density stratification in the cavity generates a hydrostatic pressure gradient in vertical direction. The pressure difference between the top and bottom of the cavity will be smaller than that between the same altitudes outside the cavity in fresh air (which is denser). As the result of pressure difference, gas flow through the two openings will be observed. This will generate a global vertical upward flow from the bottom opening to the top opening through the whole cavity.

In steady state, a constant level, with altitude z_i, will appear, below which ($z < z_i$) the vertical component of velocity will be upward, so that all the fluid outside the jet will be ambient fresh air (with density ρ_a); and above which ($z > z_i$) the vertical component of velocity will be downward outside the jet, so that the far-field field will be lighter than the ambient air (with density noted ρ_i). The vertical velocity outside the jet will decrease to zero when approaching the interface ($z = z_i$). We consider the interface is steady, and the flow is upward only in the jet cross-section area, connecting the two parts in the cavity.

The steady flow pattern is presented in figure 3.1. We call this two-layer stratification distribution of mixture density a bi-layer distribution.

3.1.2 General assumptions

We resume the basic assumptions of ventilation model proposed by Linden et al. (1990).

Assumption 1 (Steady state): The steady flow state is achieved.

Assumption 2 (Incompressibility): The flow is incompressible, so that we have a global conservation of volume flux in the cavity.

Assumption 3 (1D modelling): In the cavity, the distribution of mixture density as well as the injected gas concentration can be modelled as a function depended on the altitude z only, except for the jet area where the concentration is considered as a 3D distribution.

Assumption 4 (Bi-layer distribution): A constant level is formed in steady state with a bi-layer distribution of mixture density. Below this level, the far-field region is filled with ambient air with density ρ_a, while a homogeneous layer is considered above this level where the mixture density is noted ρ_i. We call this level the bi-layer interface altitude, noted $z = z_i$. In summary, the distribution of mixture density at far-field of the jet is

$$\rho_e(z) = \begin{cases} \rho_a, & 0 \leq z < z_i \\ \rho_i, & z_i \leq z \leq H \end{cases} \tag{3.1}$$

Assumption 5 (Small openings): The opening area of two openings are largely smaller than the cross-section area of the main cavity S_{cavity}.

Assumption 6 (Horizontal openings): Two horizontal vents are situated on the ceiling and the floor of the main cavity, so that the exterior hydrostatic pressure P_e is constant in the area of vents.

3.1.3 Hydrostatic pressure and neutral level

Based on the flow pattern analysis, an inlet flow of fresh air is presented through the bottom opening. The hydrostatic pressure outside cavity at this level $P_e(0)$ is larger that the pressure inside the cavity $P_i(0)$. Similarly, we have the relation between the inside and outside pressure through the top opening (altitude H): $P_i(H) > P_e(H)$. Based on the bi-layer distribution and 1D modelling assumptions, there must exist an altitude, where the inside hydrostatic pressure is equal to that outside of the cavity. We call this level the neutral level with its altitude noted z_n, see figure 3.2. We have by definition

$$P_i(z_n) = P_e(z_n) \tag{3.2}$$

Based on the 1D hydrostatic model, the profile of exterior pressure $P_e(z)$ as well as the interior pressure $P_i(z)$, can be written as

$$P_e(z) = P_e(z_n) - \rho_a g(z - z_n), \text{ for } 0 \leq z \leq H \tag{3.3}$$

and

$$P_i(z) = P_i(z_i) - \rho_i g(z - z_i), \text{ for } z \geq z_i \tag{3.4}$$

$$P_i(z) = P_i(z_i) - \rho_a g(z - z_i), \text{ for } z \leq z_i \tag{3.5}$$

The profile of $P_e(z)$ and $P_i(z)$ are presented in the figure 3.2.

Note that for horizontal openings, we have $z_n > z_i$ always valid. In the later correction of Bernard-Michel (2014), where the height of two openings are considered, the neutral level ($z = z_n$) and/or the interface level ($z = z_i$) may be located through the height of the top opening (see appendix C). However, the relation (3.3-3.5) will not change.

3.1.4 Environmental reduced gravity

Based on 1D assumption, we define the environmental reduced gravity as a function of altitude z for any point outside of jet area

$$g'(z) = \frac{\rho_a - \rho_e(z)}{\rho_a} g \tag{3.6}$$

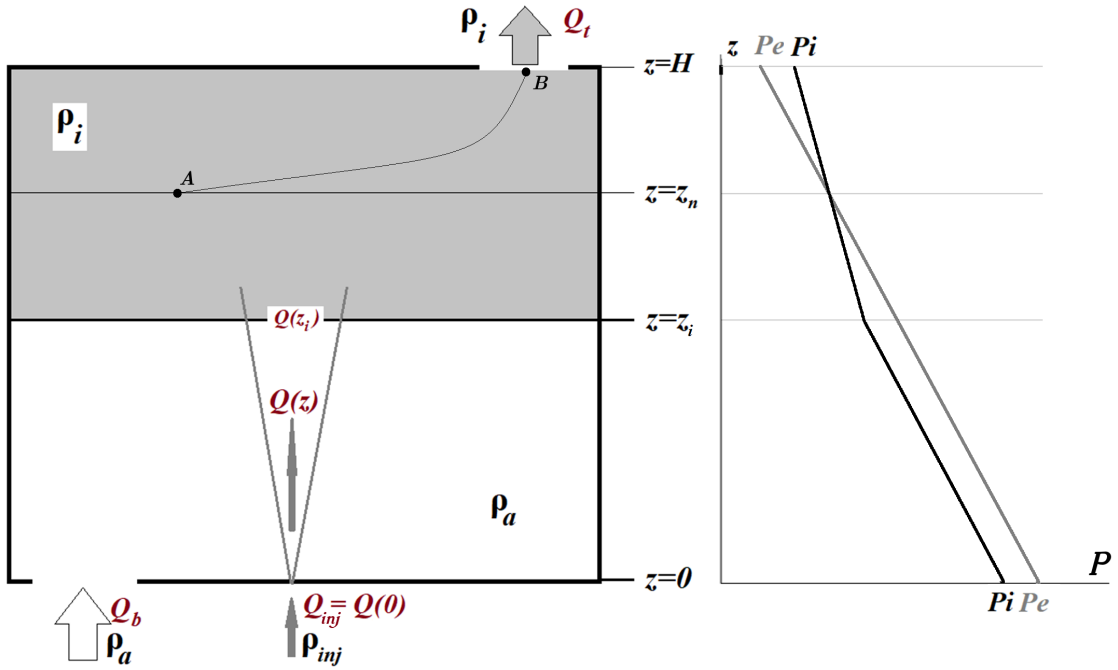

Figure 3.2: Notations of physical quantities in Linden's ventilation model and variation of interior pressure P_i and exterior pressure P_e with altitude z

where $\rho_e(z)$ is the mixture density at far field of the jet area, at altitude z and ρ_a the density of the fresh air. By applying the bi-layer distribution assumption, we have

$$g'(z) = \begin{cases} 0, & 0 \le z < z_i \\ \frac{\rho_a - \rho_i}{\rho_a} g, & z_i \le z \le H \end{cases} \tag{3.7}$$

We note in the following paragraph the environmental reduced gravity in the homogeneous layer simply

$$g' = \frac{\rho_a - \rho_i}{\rho_a} g \tag{3.8}$$

Note that this definition is different from the reduced gravity defined in the jet (see equation (2.23)) and no longer treated as a function of vertical position.

3.1.5 Calculation of inlet/outlet velocity and flux

In this section, we calculate the inlet/outlet velocity through the bottom/top opening, as well as its related inlet/outlet volume flux. We apply the Bernoulli theorem for incompressible and steady flow.

Outlet velocity through the top opening

We apply Bernoulli's equation between a point A, situated on the neutral plan $z_A = z_n$, and a point B, situated on the exterior border of top vent with altitude $z_B = H$, as presented in figure 3.2. We have

$$P_A + \rho_A g z_A + \frac{\rho_A u_A^2}{2} = P_B + \rho_B g z_B + \frac{\rho_B u_B^2}{2} \tag{3.9}$$

where $\rho_A = \rho_B = \rho_i$, $P_A = P_i(z_n) = P_e(z_n)$, $P_B = P_e(H)$ and u_A, u_B the velocities at A and B respectively.

As the cross-section of the main cavity is much larger than that of the top opening, by using the incompressible flow assumption, we have the fluid velocity $u_A \ll u_B$, so that we can suppose $u_A \approx 0$ and let $u_B = u_t$ the mean outlet velocity. Thus, we rewrite the Bernoulli's equation using hydrostatic distribution of $P_e(z)$ equation (3.3):

$$P_e(z_n) + \rho_i g z_n = P_e(H) + \rho_i g H + \frac{1}{2}\rho_i u_t^2 \tag{3.10}$$

Therefore,

$$\rho_i \frac{u_t^2}{2} = P_e(z_n) - P_e(H) - \rho_i g(H - z_n) = (\rho_a - \rho_i) g(H - z_n) \tag{3.11}$$

and thus

$$\frac{u_t^2}{2} = \frac{\rho_a - \rho_i}{\rho_i} g(H - z_n) = \frac{\rho_a}{\rho_i} g'(H - z_n) \tag{3.12}$$

We shall take into account the pressure loss from openings. For this purpose, we introduce a coefficient c_t, called discharge coefficient or pressure loss coefficient depending generally on geometry form of the top vent. This coefficient is lying between 0.5, for a sharp expansion, and 1, for a perfectly smooth expansion (Linden (1999)). In engineering applications, this discharge coefficient is taken approximately equal to 0.6. We thus modify the above equation as

$$u_t^2 = 2c_t \frac{\rho_a}{\rho_i} g'(H - z_n) \tag{3.13}$$

Inlet velocity through the bottom opening

For bottom opening, the analysis is simpler. We shall firstly note that the difference between the interior pressure and the exterior pressure at level $z = 0$ is equal to that at interface level z_i, as shown in figure 3.2.

$$P_i(0) - P_e(0) = P_i(z_i) - P_e(z_i) \tag{3.14}$$

This difference can be calculated by

$$P_i(z_i) - P_e(z_i) = (P_i(z_i) - P_i(z_n)) + (P_e(z_n) - P_e(z_i)) = g(\rho_a - \rho_i)(z_i - z_n) \tag{3.15}$$

Consequently, the mean inlet velocity u_b is deduced by inlet press loss $P_i(0) - P_e(0)$:

$$u_b^2 = 2c_b g'(z_n - z_i) \tag{3.16}$$

with c_b geometrical pressure loss coefficient.

Inlet/outlet flux

We note Q_b the inlet volume flux through the bottom opening and Q_t the outlet volume flux through the top opening. As two openings are assumed horizontal, the inlet/outlet fluxes can be calculated simply from u_b and u_t with S_b and S_t the surface of bottom/top openings:

$$Q_b = u_b S_b, \quad Q_t = u_t S_t \tag{3.17}$$

By applying equations (3.13) and (3.16), we have

$$Q_t = S_t \sqrt{2c_t g' \frac{\rho_a}{\rho_i}(H - z_n)} \tag{3.18}$$

$$Q_b = S_b \sqrt{2c_b g'(z_n - z_i)} \tag{3.19}$$

3.1.6 Global conservation equations

We have three bilayer parameters (z_i, z_n, ρ_i) as well as two flux quantities (Q_t, Q_b) in this problem. We have already established two equations for Q_t and Q_b (3.18-3.19). Thus, another three independent conservation equations are needed to close the system.

Global conservation of volume flux in the cavity

As the flow is assumed incompressible, we have firstly the global conservation of volume flux in the cavity.

$$Q_b + Q_{inj} = Q_t \tag{3.20}$$

Conservation of volume flux within the homogeneous layer

In steady state, at interface level $z = z_i$, the jet region is assumed the only area where the vertical velocity is non-zero. As defined in equation (2.18), we note $\mathcal{Q}(z_i)$ the variation of volume flux within the jet through the interface plane, representing the entering flux into homogeneous layer ($z > z_i$). This quantity shall be equal to the top outlet flux Q_t as the conservation of volume flux applies also within the top homogeneous layer. This provides us the second conservation equation.

$$Q_t = \mathcal{Q}(z_i) \tag{3.21}$$

The jet volume flux variation $\mathcal{Q}(z)$ will be provided by jet models, as presented in the chapter 2. Depended on selected jet model, $\mathcal{Q}(z)$ may possess or not explicit analytical solutions.

Conservation of jet buoyancy flux below the interface coupled with global conservation of mass flux

Below the interface $z < z_i$, the environmental density in the far field of the jet can be considered as a constant $\rho_e = \rho_a$ so that a conservation of the buoyancy flux will be established in the jet. We note the jet buoyancy flux at injection

$$\mathcal{B}_0 = G'_T(0)\mathcal{Q}(0) = G'_T(0)Q_{inj} \tag{3.22}$$

with $G'_T(0) = \frac{\rho_a - \rho_{inj}}{\rho_a} g$ the reduced density at injection. The conservation of jet buoyancy flux between $z = 0$ and $z = z_i$ can be written as

$$G'_T(0)Q_{inj} = G'_T(z_i)\mathcal{Q}(z_i) \tag{3.23}$$

Besides, we consider also the global conservation of mass flux:

$$\rho_{inj}Q_{inj} + \rho_a Q_b = \rho_i Q_t \tag{3.24}$$

Regrouping this equation with global conservation of volume flux (3.20), we obtain

$$(\rho_a - \rho_{inj})Q_{inj} = (\rho_a - \rho_i)Q_t \tag{3.25}$$

By applying relation (3.21), this is equivalent to

$$G'_T(0)Q_{inj} = g'\mathcal{Q}(z_i) \tag{3.26}$$

with g' defined in equation (3.8). Comparing it with equation (3.23), we have finally

$$g' = G'_T(z_i) \tag{3.27}$$

which provides us the last equation.

Linden's model - Summary

5 unknown variables ($Q_b, Q_t, \rho_i, z_i, z_n$), 5 equations

- $Q_t = S_t \sqrt{2c_t g' \frac{\rho_a}{\rho_i}(H - z_n)}$
- $Q_b = S_b \sqrt{2c_b g'(z_n - z_i)}$
- $Q_b + Q_{inj} = Q_t$
- $Q_t = \mathcal{Q}(z_i)$ with $\mathcal{Q}(z)$ provided by jet modelling
- $g' = \frac{\rho_a - \rho_i}{\rho_a} g = G'_T(z_i)$ with $G'_T(z_i)$ provided by jet modelling

3.2 Solutions of the model

Depending on the turbulent jet model used in the model of Linden et al. (1990), the variation of volume flux in the jet $\mathcal{Q}(z)$ may possess or not analytical solutions. In this section, we present two analytical approaches, specifically under particular additional assumptions: (i) a Boussinesq approach proposed by Linden et al. (1990), and (ii) a non-Boussinesq approach by Rooney and Linden (1997).

3.2.1 Analytical approach under Boussinesq approximation

Linden et al. (1990) proposed an explicit analytical approach in which the classic model of Morton et al. (1956), with a constant entrainment coefficient is used.

3.2.1.1 Additional assumptions

We have the following two additional assumptions to hypotheses mentioned in section 3.1.2.

Assumption 7 (Small injection): The volume flux of the injection Q_{inj} is largely smaller than that of the inlet flow through the bottom opening Q_b. Consequently, we neglect Q_{inj} in equation (3.20). The conservation equation of volume flux can be rewritten as

$$Q_b = Q_t \tag{3.28}$$

Assumption 8 (Point source): The injection radius is relatively small and its flux is negligible. The injection is considered as a point source of the jet. The virtual origin displacement is not considered in the jet resolution.

Assumption 9 (Small density range assumption): The ratio $\rho_a/\rho_i \approx 1$, this ratio is neglected in equation (3.18) thus this equation is rewritten as

$$Q_t = S_t \sqrt{2c_t g'(H - z_n)} \tag{3.29}$$

Assumption 10 (Boussinesq approximation): The ratio $(\rho_a - \rho_i)/\rho_a$ is much smaller than 1, so that the variation of ρ in the jet can be neglected in jet equations except in the buoyancy force term. Boussinesq jet model is thus applied in the resolution.

3.2.1.2 Jet evolution by Morton's analytical equations

The equations for a buoyant jet in a large steady, unstratified ambient fluid are given in Morton et al. (1956), see section 2.3.2. Recall that this model is based on Boussinesq approximation and Top-hat profile assumption. A constant entrainment coefficient α_T is used in entrainment modelling.

In homogeneous environment, the conservation of jet buoyancy flux is valid: $\mathcal{B}(z) = \mathcal{B}_0 = G'_T(0)\mathcal{Q}(0)$ for $0 \leq z \leq z_i$. By using equation (2.41) with $z_t = 0$ by applying point source assumption,

$$\mathcal{Q}(z) = C(\mathcal{B}_0 z^5)^{1/3} \tag{3.30}$$

$$G'_T(z) = \frac{1}{C}\left({\mathcal{B}_0}^2 z^{-5}\right)^{1/3} \tag{3.31}$$

with C a universal constant depending on the entrainment constant α_T.

$$C = \frac{6}{5}\left(\frac{9}{10}\right)^{1/3}\pi^{2/3}{\alpha_T}^{4/3} \approx 2.4852{\alpha_T}^{4/3} \tag{3.32}$$

3.2.1.3 Solutions of ventilation model

Regrouping equations (3.29) (3.28) and (3.19), we have

$$\frac{z_n - z_i}{H - z_n} = \frac{c_t S_t^2}{c_b S_b^2} \tag{3.33}$$

thus

$$z_n = \frac{c_b S_b^2 H + c_t S_t^2 z_i}{c_b S_b^2 + c_t S_t^2} \tag{3.34}$$

Therefore, equation (3.29) could be rewritten as

$$Q_t = A\sqrt{g'(H - z_i)} \tag{3.35}$$

where A is called effective surface of the two openings, defined as

$$A = \frac{\sqrt{c_t}\ S_b S_t}{\sqrt{\frac{1}{2}\left(\frac{c_t}{c_b}S_t^2 + S_b^2\right)}} \tag{3.36}$$

A is largely dependent upon the smaller one between S_t and S_b.

Regrouping equations (3.21), (3.30) and (3.35), we obtain

$$A\sqrt{g'(H - z_i)} = C(\mathcal{B}_0 z_i^5)^{1/3} \tag{3.37}$$

We define ξ the ratio of interface height and height of the main cavity

$$\xi = \frac{z_i}{H} \tag{3.38}$$

Regrouping (3.37) with (3.27) and (3.31), eliminating g', we obtain finally

$$\frac{\xi^5}{1 - \xi} = \frac{A^2}{C^3 H^4} \tag{3.39}$$

This is a relation between two geometric quantities: the height of the interface z_i as a fraction of the ceiling height H and the effective area of the openings A. The z_i will be obtained from equation (3.39).

Then, by applying the conservation of buoyancy (3.27) and equation (3.20), we obtain finally

$$g' = \frac{1}{C}{\mathcal{B}_0}^{2/3} z_i^{-5/3} \tag{3.40}$$

The mixture density in the homogeneous layer ρ_i can be determined by this equation and the previously obtained z_i.

From the result, we find that there is no dependence of the interface height z_i on the strength of the source $\mathcal{B}_0$, nor on the cross-section surface area of the cavity. Only the geometrical conditions and the entrainment coefficient α_T are presented in the final equation (3.39), with the latter one considered as a constant.

In addition, the location of the lower opening will not change the position of the interface, in condition that it is situated below the interface, as mentioned in Linden (1999). This position is not considered affecting the global flow in the jet, even though it may affect the vertical velocity in the region outside the jet below the interface.

Linden-Morton solutions

- $\dfrac{\xi^5}{1-\xi} = \dfrac{A^2}{C^3 H^4}$

  with $\xi = \dfrac{z_i}{H}$, $C = 2.4852{\alpha_T}^{4/3}$ and $A = \dfrac{\sqrt{c_t}\, S_b S_t}{\sqrt{\dfrac{1}{2}\left(\dfrac{c_t}{c_b} S_t^2 + S_b^2\right)}}$

- $g' = \dfrac{1}{C}{\mathcal{B}_0}^{2/3} z_i^{-5/3}$

  with $g' = \dfrac{\rho_a - \rho_i}{\rho_a} g$ and $\mathcal{B}_0 = \dfrac{\rho_a - \rho_{inj}}{\rho_a} g Q_{inj}$

- $Q_t = A\sqrt{g'(H - z_i)}$

3.2.2 Analytical non-Boussinesq approach

Boussinesq approximation is not strictly valid for an air-hydrogen or air-helium mixture due to their large density difference. Rooney and Linden (1997) proposed a non-Boussinesq approach using the turbulent jet model of Rooney and Linden (1996). A constant coefficient α_T is used to model entrainment effect. In this approach, resolutions of interface height z_i and mixture density ρ_i are no longer separated, but regrouped in an equation system.

3.2.2.1 Additional assumption

We have the following additional assumptions applied in this section.

Assumption 7 (Small injection): The volume flux of the injection Q_{inj} is largely smaller than that of the inlet flow through the bottom opening Q_b. Consequently, we neglect Q_{inj} in

equation (3.20). The conservation equation of volume flux can be rewritten as

$$Q_b = Q_t \tag{3.41}$$

Assumption 8 (Point source): The injection radius is relatively small and its flux is negligible. The injection is considered as a point source of the jet. The virtual origin displacement is not considered in the jet resolution.

3.2.2.2 Jet evolution by Rooney's analytical solutions

By assuming the jet is placed in a homogeneous environment below the interface, we apply the analytical solutions (equations (2.69), (2.71) and (2.72)) of turbulent jet model Rooney and Linden (1996) with $z_t = 0$ according to point source assumption. We have following solutions for jet volume flux and reduced gravity

$$\mathcal{Q}(z) = C^*(z)(\mathcal{B}_0 z^5)^{1/3} \tag{3.42}$$

$$G'_T(z) = \frac{1}{C^*(z)}\left(\mathcal{B}_0{}^2 z^{-5}\right)^{1/3} \tag{3.43}$$

with parameter $C^*(z)$ a function of altitude z defined as

$$C^*(z) = \frac{36}{25}\left(\frac{25}{48}\right)^{1/3}\pi^{2/3}\alpha_T{}^{4/3}\left(1+\left(\frac{z_B}{z}\right)^{5/3}\right) \approx 2.4852\alpha_T{}^{4/3}\left(1+\left(\frac{z_B}{z}\right)^{5/3}\right) \tag{3.44}$$

with z_B the characteristic length of Boussinesq effect defined in equation (2.74). Note that z_B depends on the value of α_T.

3.2.2.3 Solutions of ventilation model

Regrouping equation (3.18), (3.19) and (3.41), we have

$$\frac{z_n - z_i}{H - z_n} = \frac{c_t^* S_t^2}{c_b S_b^2} \tag{3.45}$$

with

$$c_t^* = c_t \frac{\rho_a}{\rho_i} \tag{3.46}$$

We are thus back to Linden-Morton resolution. All equations are in the same form with replacement c_t to c_t^* and C to C^*. Consequently, we have

$$\frac{\xi^5}{1-\xi} = \frac{A^{*2}}{C^*(z_i)^3 H^4} \tag{3.47}$$

with effective opening area

$$A^* = \frac{\sqrt{c_t^*}\, S_b S_t}{\sqrt{\frac{1}{2}\left(\frac{c_t^*}{c_b}S_t^2 + S_b^2\right)}} \tag{3.48}$$

and for conservation of buoyancy (3.27), we have

$$g' = \frac{1}{C^*(z_i)H^{5/3}}\mathcal{B}_0{}^{2/3}\xi^{-5/3} \tag{3.49}$$

Equations (3.47) and (3.49) provide a system for two unknown variables (ξ, ρ_i) and may be solved numerically by Newton's method.

The results shows that both the interface height and the mixture density will depend on the geometrical conditions (S_b, S_t, c_b, c_t, H), injection condition $\mathcal{B}_0$ and jet entrainment coefficient α_T. Same as before, Rooney and Linden (1997) proves that the position of lower opening will not change the position of interface, in condition that the previous one is situated below the interface.

Linden-Rooney solutions

- $\dfrac{\xi^5}{1-\xi} = \dfrac{A^{*2}}{C^{*3}H^4}$
- $g' = \dfrac{1}{C^*(z_i)H^{5/3}}{\mathcal{B}_0}^{2/3}\xi^{-5/3}$
- $Q_t = A^*\sqrt{g'(H-z_i)}$

  with $\xi = \dfrac{z_i}{H}$, $C^*(z) = 2.4852{\alpha_T}^{4/3}\left(1+\left(\dfrac{z_B}{z}\right)^{5/3}\right)$ and $A^* = \dfrac{\sqrt{c_t^*}\,S_bS_t}{\sqrt{\dfrac{1}{2}\left(\dfrac{c_t^*}{c_b}S_t^2+S_b^2\right)}}$ with $c_t^* = c_t\dfrac{\rho_a}{\rho_i}$

  as well as $g' = \dfrac{\rho_a-\rho_i}{\rho_a}g$ and $\mathcal{B}_0 = \dfrac{\rho_a-\rho_{inj}}{\rho_a}gQ_{inj}$

3.3 Summary and discussion

In this chapter, we have presented

- Natural ventilation model of Linden et al. (1990)
- Two analytical approaches for its solutions (Linden-Morton and Linden-Rooney)

In the model of Linden et al. (1990), injected gas distribution is assumed in bi-layer form with a homogeneous layer at top part of the cavity. The model is dedicated to solving bi-layer parameters (the interface height and the homogeneous density) by using geometrical conditions and injection conditions. Analytical solutions of turbulent jet model (Morton or Rooney) are used in the ventilation model to provide connection between the jet flow and the global conservation equations. A series of assumptions are applied in the demonstration.

In 2000s, Linden's model is proposed to be applied in industrial context to evaluate the hydrogen release risk for its storage in semi-confined environment, see Fuster et al. (2015, 2017). A series of experimental measures were carried out in CEA to build the benchmark. A theoretical correction of geometrical conditions is introduced in CEA internal report (see appendix C). (Bernard-Michel (2012); Cariteau (2012); Houssin (2012); Bernard-Michel (2014)).

The reliability of the ventilation model depends on the choice of certain key parameters. Choice of entrainment coefficient for example, is relatively difficult without knowing the jet flow pattern in the cavity whereas this parameter plays an important role in the jet modelling.

Apart from the entrainment coefficient α_T, discharge parameter c_t is also discussed in the literature. In the final result of original model of Linden et al. (1990), equation (3.39), the

bi-layer interface height is a function of a geometrical parameter only (noted effective opening area A), which is defined from openings areas, the height of the cavity and the discharge coefficient (or called pressure-loss coefficient). Holford and Hunt (2001) and Hunt and Holford (2000) quantified experimentally the dependence of this discharge coefficient on inside-outside density difference, typically presented on the upper opening. The discharge coefficient corresponding to the top opening c_t can rapidly decrease with increasing density contrast between homogeneous mixture density ρ_i and that of ambient air ρ_a.

Vauquelin et al. (2017a) applied the non-Boussinesq turbulent jet model of Rooney and Linden (1996) in natural ventilation model to study the influence of inside-outside density difference on the top opening's discharge coefficient c_t. In this work, analytical solutions of Candelier and Vauquelin (2012) are used. An indicative parameter Γ_d is defined to characterise the outlet flow through the top opening.

$$\Gamma_d = \frac{5g}{8\sqrt{\pi}\alpha_T}\frac{S_t^{5/2}}{Q_t^2}\frac{\rho_a - \rho_i}{\sqrt{\rho_a \rho_i}} \tag{3.50}$$

Vauquelin et al. (2017a) summarised the experimental results of Hunt and Holford (2000) and Holford and Hunt (2001), and proposed a simple model for correction of c_t, as a function of parameter Γ_d. Note that these corrections are only on top vent discharge coefficient c_t and based on the horizontal openings assumption. For the bottom vent, no further correction is needed as there is no inside-outside density difference.

Correction proposed by Vauquelin et al. (2017a)

$$c_t = \begin{cases} 0.6, & \text{if } 0 < \Gamma_d < 4.9 \\ 1.3\ \frac{(\Gamma_d - 1)^{3/5}}{\Gamma_d}, & \text{if } \Gamma_d > 4.9 \end{cases} \tag{3.51}$$

Furthermore, an important point is that the model of Linden et al. (1990) is based on its flow pattern analysis, specifically the bi-layer distribution of the mixture density in the cavity. This is the essential assumption of the whole theory. However, experimental studies show that this assumption is not always valid. For example, CEA researchers have measured the concentration distribution in a cavity with a height $H = 207cm$ for air-helium mixture (Bernard-Michel (2014)). It is found that the bi-layer distribution is not always observed (see figure 3.3) by changing the injection point position from $z = 27cm$ to $z = 197cm$ and an injection volume flux up to $210L/min$. The bi-layer distribution of helium concentration is presented for the majority cases. For the other cases, either a full stratification or a homogeneous distribution is observed.

From the flow pattern analysis of Linden et al. (1990), the formation of the bi-layer structure is due to the concurrence of reverse flow of the jet arriving at the ceiling of the cavity and the global vertical flow generating by pressure difference between two openings. The injection of light gas generates a momentum (inertia) and positive buoyancy source of the jet. Physically, the formation of bi-layer distribution is related to three aspects, the source momentum, the source buoyancy and the pressure difference outside the cavity. As seen in equation (1.60), Cleaver et al. (1994) proposed a criterion about the volumetric Richardson number for estimation of stratification in a one-vented cavity. No more information found in literature about its reliability in a two-vented cavity.

No clear criteria is found in literature indicating the formation of bi-layer distribution for a general case. As this assumption is essential in ventilation model, we have to make sure the bi-layer distribution appears in the reference case chosen in this study.

Direct use of natural ventilation model often provides wrong estimation of hydrogen concentration and flammable region, see report Kotchourko et al. (2014), especially for large release

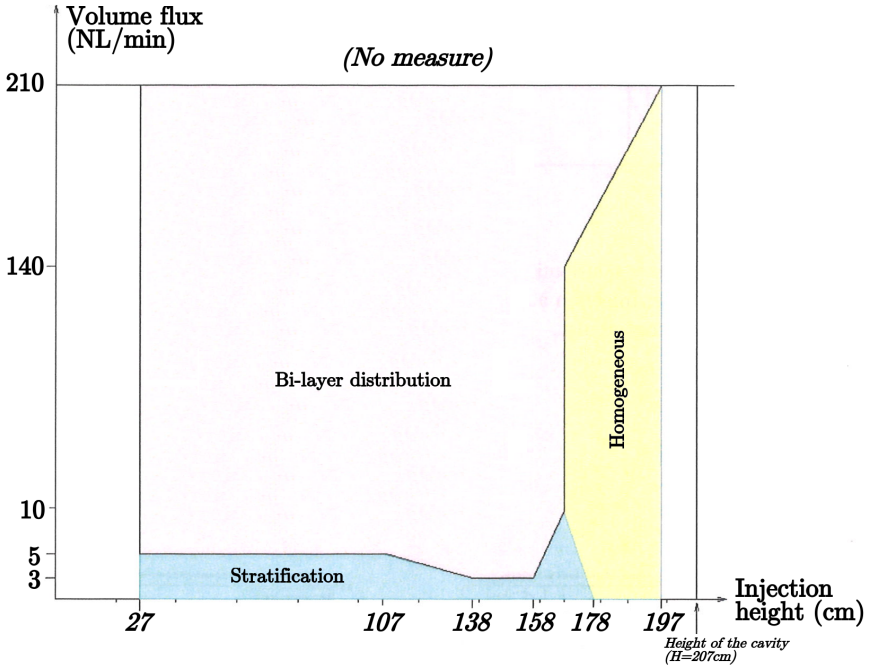

Figure 3.3: Experimental result of Bernard-Michel (2014) with air-helium mixture, with height of cavity $H = 207cm$, the injection point varies from $z = 27cm$ to $z = 197cm$ and a change of injection volume flux up to $210NL/min$. The bi-layer distribution is presented for majority cases

flow rate. Physically, this is related to non validity of certain hypotheses assumed in the model. On the one hand, due to large density difference, Boussinesq approximation is not systematically valid for air-hydrogen mixing problem. On the other hand, for large injection condition, the point source assumption may be not valid as well. We have seen in chapter 2 that in turbulent jet modelling, it is proposed to use the notion of virtual origin displacement to correct the injection condition.

In conclusion, the natural ventilation model need to be improved with some possible approaches to be validated, especially for its practical use in air-hydrogen mixing problem. As presented in thesis introduction, experimental studies possess a series of restrictions so that we pass to a well-converged DNS calculation to study in detail the validity of these assumptions in different analytical approaches. We suppose beforehand the existence of a bi-layer distribution and try to establish a well-selected reference DNS case. Then we associated the obtained well-converged DNS 3D results to characteristic quantities defined in the model in order to compare its variations with that reported by theoretical models. Besides, a Particle Image Velocimetry (PIV) measurement is carried out under the same geometrical and physical conditions. The comparison PIV-DNS will validate the numerical results.

Part II

Methodology

Chapter 4

Numerical and experimental setup and post-processing methodology

We present in this chapter the principal methodology used in this study, the numerical simulation as well as the experimental measurement. The numerical simulation is in type of DNS (Direct Numerical Simulation). The geometrical configuration is chosen to ensure a bi-layer distribution of concentration at steady state in order to match the basic assumption of the ventilation model. An exterior domain of the cavity is added into simulation geometry to ensure good boundary conditions through the two openings. A convergence check both in space and in time is achieved to make sure the mesh is fine enough, the steady state is well achieved and the averaging duration is long enough to cover all potential low-frequency oscillations. We present also the integral method to transfer 3D results to 1D characteristic quantities defined in the theories. In the last part, we present briefly the experimental setup and its post-processing method under the same geometrical configuration defined in numerical simulation.

4.1 Study case

The basic idea of this study is to simulate the flow and mixing phenomena of injected light gas and ambient air in the two-vented cavity. Previous works have shown that it is important to consider an additional computation domain in exterior of the cavity to simulate correctly the flow through two vents, see Saikali et al. (2019). The complete computational domain is shown in figure 4.1, with the main cavity on the left and additional exterior domain in the middle. We consider 4 parts in the geometrical configuration.

- **Main cavity**, is the main area where we simulate the gas flow, with geometry $L \times W \times H$ corresponding to the physical problem. The cavity is semi-enclosed with three openings. One circle opening on the floor centre, connected with injection tube. The other two are respectively two vents, both with height H_v, located over the entire width on the same vertical wall. Two vents are similar and located at the top and bottom extremities ($z = 0$ to H_v and $z = H - H_v$ to H) on the x-positive extremity wall ($x = L/2$).
- **Injection pipe**, or called pre-injection area, is a cylinder tube placed straight below the main cavity, connecting the centre of the floor ($z = 0$). It possesses a diameter d and a length h considered long enough to ensure a smooth and stable injection.
- **Exterior domain**, is also a cuboid domain representing the area outside the main cavity. Compared with the side of two vents, it possesses an additional extension L_y in y

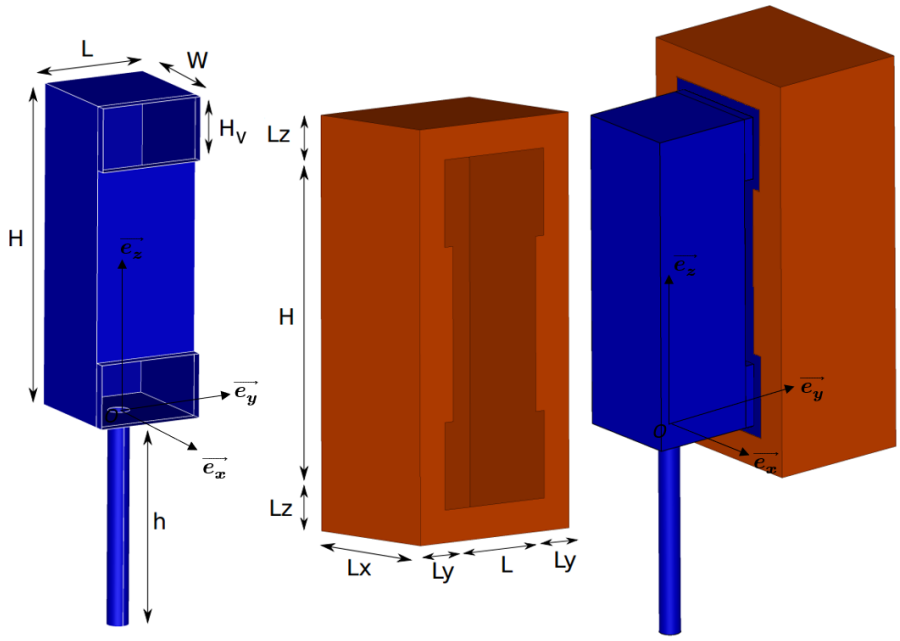

Figure 4.1: Sketch of the computational domain exhibiting boundary groups. Blue surfaces depict wall group while orange for free surface boundaries. Left: the main cavity, middle: the exterior region, right: the complete computational domain. Figure extracted from Saikali et al. (2020).

direction and L_z in z direction. Its horizontal extension is L_x. The exterior domain has a volume $L_x \times (W + 2 \times L_y) \times (H + 2 \times L_z)$.

- **Two identical connection areas**, connecting the main cavity and the exterior domain via the two vents. Its x-direction extension W_v represents the thickness of cavity lateral wall.

The outer surface of this geometry is divided into three face groups, corresponding to three types of boundary conditions, shown in different colours in figure 4.1. The detailed description of these groups is presented in appendix D.

4.2 Numerical method

We use the code TrioCFD in the platform TRUST to provide numerical solutions of the time-dependent system of governing equations. This code TRUST-TrioCFD is developed in the Division of Energies (DES) of the French Atomic Energy Commission (CEA) (http://www-trio-u.cea.fr), in order to study and solve a wide range of industrial problems, such as turbulent flows, fluid/solid coupling, mono or multi-phase flows (Angeli et al. (2015)). The code is capable to treat complex and coupled geometries. TRUST-TrioCFD is an open-source code, can be downloaded from its website. The code is written in C++ language.

As the local density varies in the cavity, gas flow cannot be considered completely incompressible in this problem. Here we apply the **quasi-incompressible module** of the code. The governing equations (already presented in section 1.4) that will be solved numerically read:

$$\frac{\partial \rho}{\partial t} + \mathbf{div}\left(\rho \vec{u}\right) = 0 \tag{4.1}$$

$$\frac{\partial \rho Y_1}{\partial t} + \mathbf{div}\left(\rho Y_1 \cdot \overrightarrow{u}\right) = \mathbf{div}\left(\rho D_{1,2} \cdot \overrightarrow{\mathbf{grad}}\ Y_1\right) \tag{4.2}$$

$$\frac{\partial \rho \overrightarrow{u}}{\partial t} = -\left(\rho \overrightarrow{u} \cdot \overrightarrow{\mathbf{grad}}\right)\overrightarrow{u} - \overrightarrow{\mathbf{grad}}\ P_H + \mathbf{div}\ \overline{\overline{\tau}} + \rho \overrightarrow{g} \tag{4.3}$$

$$\rho = \frac{P_{th}}{RT}\left(\frac{Y_1}{M_{inj}} + \frac{1 - Y_1}{M_{air}}\right)^{-1} \tag{4.4}$$

The numerical algorithm implemented in this quasi-incompressible module is based on discretisation of two main equations: the species conservation equation, or generally called convection-diffusion equation (4.2) and the momentum conservation equation (Navier-Stokes equation) (4.3).

4.2.1 Spatial and time discretisation

In the code, the above flow equations are discretised by a **finite difference volume (VDF)** method. The discretisation of each term is performed by integrating over a control volume where the diffusion gradient terms are approximated by a linear difference equation.

Spatial discretisation is performed on a staggered (parallelepiped) grid. On such grid, the scalars (pressure, density and mass fraction,...) are stored at the centre of the control volumes, whereas the velocity components are defined on the faces of the control volumes (Harlow et al. (1965), Versteeg and Malalasekera (2007)).

In accordance with the staggered grid, all the terms of convection-diffusion equation are always stored at the centre of the control volumes while those of Navier-Stokes equation (4.3) are at the faces. For all the spatial derivatives defined in equations, a **second order central scheme** is employed. This scheme will be stable only if Pe < 2 for convection-diffusion scheme, which is not systematically valid in the transition regime, especially just after injection. In this case, Quadratic Upstream Interpolation for Convective Kinematics (QUICK) is applied for convection term only in the convection-diffusion equation.

The time advancement of these equations is treated by a two-stage **second order Rational Runge-Kutta discretisation scheme** (RRK2) in order to approximate the time derivative term. A **semi-implicit scheme** is chosen (implicit for diffusive and viscous terms and explicit for convective term). The choice of time step δt is thus up to the convective criterion only, that is to say

$$\delta t = \delta t_{conv} = \min\left(\frac{V_{cell}}{\zeta_{cell}}\right) \tag{4.5}$$

where ζ_{cell} in m^3/s corresponds to the volume flux entering at each arbitrary control volume (cell) of volume V_{cell}. This is basically equivalent to a **CFL = 1**, which means that a fluid particle does not cross more than one mesh cell per time step.

4.2.2 Resolution algorithm

The numerical resolution is carried out sequentially. Three variables (5 scalars) are considered main unknowns in this algorithm: the mass fraction (Y_1), the hydrodynamic pressure (P_H) and the velocity (u, v, w). The objective of each time step is to solve these fields for t^{n+1} by using its values at t^n.

The resolution begins with the convection-diffusion equation which can be simply rewritten as follows by regrouping equation (4.2) with mass equation (4.1).

$$\rho \frac{\partial Y_1}{\partial t} + C_{Y_1} = D_{Y_1} \tag{4.6}$$

with $C_{Y_1} = \rho u_i \cdot \frac{\partial Y_1}{\partial x_i}$ the species convective term and $D_{Y_1} = \frac{\partial}{\partial x_i}\left(D_{1,2}\rho\frac{\partial Y_1}{\partial x_i}\right)$ the diffusion term. This equation will be discretised in semi-implicit scheme.

$$\frac{\partial Y_1^{n+1}}{\partial t} = \frac{1}{\rho^n}\left(-C_{Y_1}^n + D_{Y_1}^{n+1}\right) \tag{4.7}$$

Using the fields ρ^n, $\overrightarrow{u}^n$, the field Y_1^{n+1} is evaluated. Then, using the gas mixture viscosity equation (1.46), the mixture dynamic viscosity μ^{n+1} is updated. Next, we apply the equation of the state (4.4) to solve for the mixture density field ρ^{n+1}.

Then the Navier-Stokes equation will be treated. This equation can be written as (see detailed demonstration in section 1.3.3).

$$\frac{\partial \rho u_j}{\partial t} + \frac{\partial}{\partial x_i}\left(\rho u_j u_i\right) = -\frac{\partial P_H}{\partial x_j} + 2\frac{\partial \mu S_{ij}}{\partial x_i} - \frac{2}{3}\frac{\partial}{\partial x_j}\left(\mu\frac{\partial u_k}{\partial x_k}\right) + \rho g\overrightarrow{e_z} \tag{4.8}$$

Regroup the first and the third term of right side of the above equation, we can simplify it as

$$\frac{\partial \rho u_j}{\partial t} + C_{u_j} = D_{u_j} + S_{u_j} \tag{4.9}$$

with $C_{u_j} = \frac{\partial}{\partial x_i}\left(\rho u_j u_i\right)$ the convective term, $D_{u_j} = \frac{\partial 2\mu S_{ij}}{\partial x_i}$ the viscous term and $S_{u_j} = -\frac{\partial P^*}{\partial x_j} + \rho g\overrightarrow{e_z}$ with here $P^* = P_H + \frac{2}{3}\mu\mathbf{div}(\overrightarrow{u})$ as the source term containing both the buoyant and the pressure gradient terms. (Bieder (2007); Vandroux and Barthel (2013); Roux (2017b,a))

The numerical resolution for Navier-Stokes equation is carried out by a prediction-projection method to treat velocity-pressure coupling (Guermond et al. (2006)). This method consists of three steps: velocity prediction, resolution of Poisson equation, velocity correction to satisfy the conservation of mass (equation 4.1).

In the first step (prediction), the pressure gradient term is treated explicitly to obtain a provisional field of $\left(\rho u_j\right)^{prov}$:

$$\frac{\partial\left(\rho u_j\right)^{prov}}{\partial t} = -C_{u_j}^n + D_{u_j}^{n+1} + S_{u_j}^n \tag{4.10}$$

The integration of this equation is performed from t^n to a provisional time t^{prov}. Note that the obtained $\left(\rho u_j\right)^{prov}$ does not satisfy the conservation of mass (equation 4.1) at this step.

The second step is to solve the Poisson equation. We apply here the discretisation on the whole time increment between t^n and t^{n+1} with implicit pressure term (but explicit for gradient term), thus Navier-Stokes equation can be discretised as follows

$$\frac{\partial\left(\rho u_j\right)^{n+1}}{\partial t} = -C_{u_j}^n + D_{u_j}^{n+1} - \frac{\partial P^{*n+1}}{\partial x_j} + \rho^n g\overrightarrow{e_z} \tag{4.11}$$

Subtracting equation (4.11) from equation (4.10) and applying divergence to both sides, we have

$$\frac{\partial}{\partial x_j}\left(\frac{\partial}{\partial x_j}\left(P^{*n+1} - P^{*n}\right)\right) = \frac{1}{t^{n+1}-t^n}\left(\frac{\partial}{\partial x_j}\left(\rho u_j\right)^{prov} - \frac{\partial}{\partial x_j}\left(\rho u_j\right)^{n+1}\right) \tag{4.12}$$

The term $\frac{\partial}{\partial x_j}\left(\rho u_j\right)^{n+1}$ shall satisfy the conservation of mass (equation 4.1), thus

$$\frac{\partial}{\partial x_j}\left(\rho u_j\right)^{n+1} = -\frac{\rho^{n+1}-\rho^n}{t^{n+1}-t^n} \tag{4.13}$$

with ρ^{n+1} obtained from the above convection-diffusion resolution.

The above equation (4.12) is thus an elliptic Poisson equation, which is solved by an iterative Symmetric Successive Over Relaxation (SSOR) procedure (Wesseling (1995), Saad (2003)). This step takes 3/4 of the computational time. The term P^{*n+1} then will be deduced.

The last step is to correct the velocity term by a projection method. The term $\left(\rho u_j\right)^{n+1}$ will be firstly corrected by the projection formula.

$$\left(\rho u_j\right)^{n+1} = \rho^{n+1} u_j^{n+1} = \left(\rho u_j\right)^n - \left(t^{n+1} - t^n\right) \frac{\partial}{\partial x_j} \left(P^{*n+1} - P^{*n}\right) \tag{4.14}$$

The correct velocity field u_j is finally deduced. Here, all fields are up to date for t^{n+1}, a new time iteration is then lanced to perform again this resolution.

An important remark of this algorithm is as we solve in fact the pressure term P^* instead of P, in which the velocity divergence is calculated via resolution of Poisson equation. However, the final corrected velocity field at end of each time step may not satisfy explicitly this velocity divergence constraint.

4.2.3 Initial and boundary conditions

At the initial state, the whole cavity is filled with pure air ($Y_1 = 0$) at rest ($\overrightarrow{u} = 0$). Light gas then will be continuously injected into the cavity via the injection pipe with a constant volume flux Q_{inj}.

Different boundary conditions are applied on the different boundary face groups, defined in the geometry configuration.

Wall group

The wall group includes the enclosed wall of the cavity, the lateral surface of the injection tube and lateral surface of an extension of the two openings connected to the exterior domain. No-slip boundary conditions are imposed on the wall area, with a homogeneous Neumann condition for all scalars ρ, Y_1 and P.

$$\overrightarrow{u} = 0 \text{ and } \frac{\partial \phi}{\partial \overrightarrow{n}} = 0, \phi \in \{P_H,\ \rho,\ Y_1\} \tag{4.15}$$

with $\overrightarrow{n}$ the outward unit normal at considered boundary surface.

Free surface group

The free surface group is defined as the frontier surface of the exterior domain, where a free inlet-outlet condition will be set. A linear distribution of the hydrodynamic pressure with the vertical coordinate z is applied, modelling a fluid at hydrostatic equilibrium. This pressure is fixed (per outlet cell) during the whole simulation (Dirichlet condition).

$$P_H = -\rho_{air} g z \tag{4.16}$$

For the other variables ($\overrightarrow{u}$, ρ and Y_1), homogeneous Neumann conditions are imposed on the boundaries of the external domain when the fluid is going outward.

$$\frac{\partial \phi}{\partial \overrightarrow{n}} = 0, \phi \in \left\{\overrightarrow{u},\ \rho,\ Y_1\right\} \text{ if } \overrightarrow{u} \cdot \overrightarrow{n} \geq 0 \tag{4.17}$$

with $\overrightarrow{n}$ the unit vector outward normal to the wall.

Otherwise, if the fluid enters into the calculation domain, a pure air is assumed at the surface (Dirichlet conditions).

$$Y_1 = 0, \quad \rho = \rho_{air} \quad \text{if } \overrightarrow{u} \cdot \overrightarrow{n} < 0 \tag{4.18}$$

Injection group

The injection group is the bottom boundary of the injection pipe, where we prescribe a constant mass flux $\rho_{inj} Q_{inj}$ as far as the diffusive contribution is set to zero. The velocity vector is oriented along the z-direction with a parabolic vertical velocity profile. The vertical velocity value in the centre of the surface is calculated to ensure a well-posed injection flux (Q_{inj}).

$$w(x,y) = \epsilon_Q \times \left(\frac{d^2}{4} - x^2 - y^2 \right), \text{ with } \epsilon_Q = \frac{Q_{inj}}{\sum_{P \in \Omega_{inj}} \left(\frac{d^2}{4} - x^2(P) - y^2(P)^2 \right) dS(P)} \tag{4.19}$$

where d is the diameter of the injection tube and $x(P), y(P)$ indicates the X-Y coordinates of the centre position of each mesh cell on this pre-injection plane and $dS(P)$ the corresponding cell surface area. The pipe is designed long enough to ensure stable injection condition in the underside of the main cavity.

Uniform profiles are applied for the mixture's density and light gas mass fraction with

$$\rho = \rho_{inj}, \quad Y_1 = 1 \tag{4.20}$$

For the hydrodynamic pressure P_H, a homogeneous Neumann condition is applied ($\frac{\partial P_H}{\partial z} = 0$).

4.3 Physical configuration and simulation process

In the previous study Saikali (2018), light gas concentration did not present a clear bi-layer distribution. Thus, this simulation cannot directly be used to analyse ventilation model. Therefore, our first step is to change the geometrical configuration to ensure the appearance of bi-layer distribution. We shall note that the Linden's model is based on two horizontal openings but in our case the vents are vertical (representing specific structures in the industrial context like windows). Consequently, the height of openings shall be not chosen too large. As presented in appendix C, the vertical opening theoretically does influence the vertical profile of outlet velocity. For small vertical extension, this effect could be considered negligible and the outlet flow could be considered uniformly distributed.

Finding new geometrical configuration to obtain a bi-layer distribution

In the first step, the objective is to fix a new geometrical configuration that appears the bi-layer distribution. For this purpose, three pre-calculations are performed based on three equidistant meshes, named A, B and C with $\delta x = 0.7$mm. The height of the cavity is chosen as $H = 20cm$, taken constant for each configuration in order to keep the same turbulence level. Only the horizontal size of the cavity is modified to test confinement effect. The width of the cavity changes from $L = W = 5cm$ for case A, almost the same as in Saikali (2018), $L = W = 7cm$ for case B to $L = W = 10cm$ for case C. The exterior domain is chosen a little smaller for case C compared to cases A and B for computation resource consideration. The geometrical dimensions of the main cavity and the exterior domain, compared with its values in Saikali (2018), are summarised in the table 4.1. The length h and the diameter d of the injection pipe, as well as the cavity additional thickness W_v are set as in Saikali (2018): $h = 10cm, d = 1cm, W_v = 0.5cm$. The injection volume flux is chosen as $Q_{inj} = 15L/min$, 3 times larger than that in Saikali (2018) where $Q_{inj} = 5L/min$.

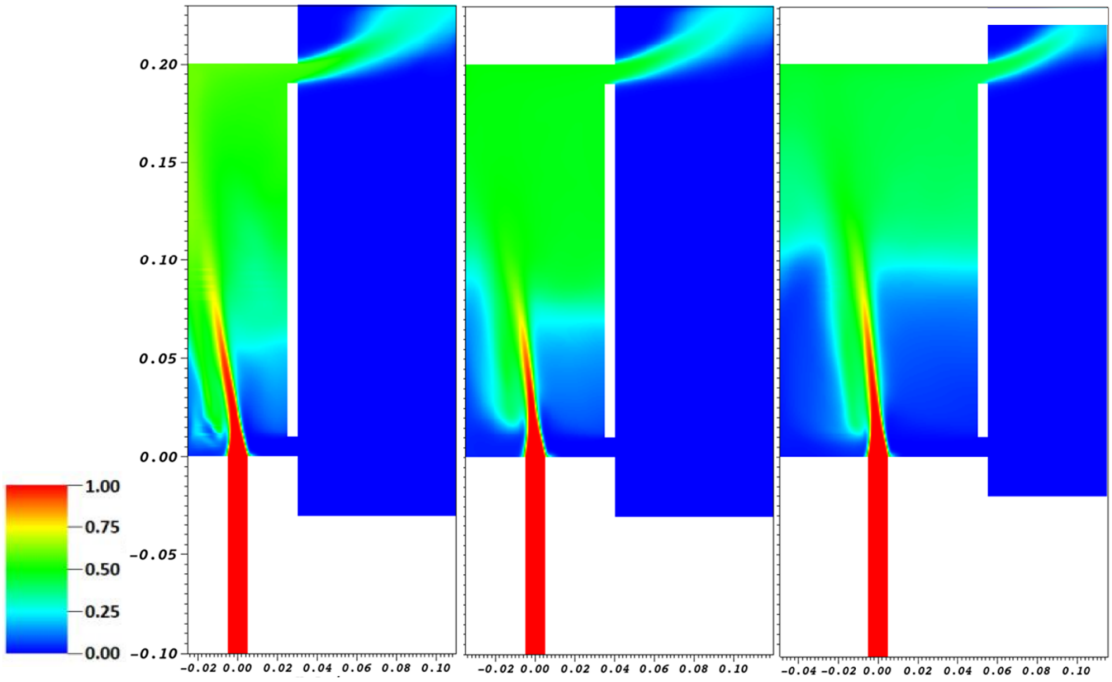

Figure 4.2: Time-averaged helium volume fraction field (X_1) on the vertical mid-plane (y=0) for three test geometrical configurations, from left to right A, B and C

Configuration	**Main cavity dimension** $L \times W \times H$ **(cm^3)**	**Dimension of exterior domain (cm^3)**	**Height of vents** H_v **(cm)**	**Volume Richardson number**
Saikali (2018)	$4.9 \times 5 \times 14.9$	$6.75 \times 9 \times 18.9$	2.9	3.37
A	$5 \times 5 \times 20$	$8 \times 11 \times 26$	1	0.41
B	$7 \times 7 \times 20$	$8 \times 13 \times 26$	1	0.52
C	$10 \times 10 \times 20$	$6 \times 14 \times 24$	1	0.65

Table 4.1: Description of three test configurations: geometry of main cavity and exterior domain, compared with Saikali (2018)

Geometrical parameter	**Value**
Main cavity dimension $L \times W \times H$	$10\ cm \times 10\ cm \times 20\ cm$
Main cavity volume V_{cavity}	2 L
Exterior extension in x-direction L_x	$8\ cm$
Exterior extension in y and z directions L_y and L_z	$3\ cm$ for each direction
Exterior domain dimension $L_x \times (W + 2L_y) \times (H + 2L_z)$	$8\ cm \times 16\ cm \times 26\ cm$
Height of vents H_v	$1\ cm$ each
Injection pipe diameter d	$1\ cm$
Injection pipe length h	$10\ cm$
Separating wall thickness W_v	$0.5\ cm$

Table 4.2: Geometrical parameters applied in this study

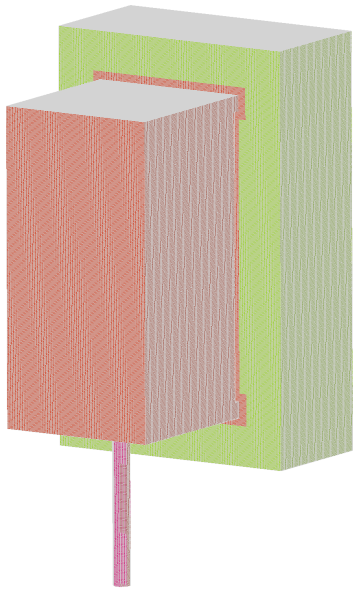

Figure 4.3: Global view of geometrical configuration and mesh applied in this study with three surface groups where applied different boundary conditions, wall group in red, free inlet/outlet group in green, injection group not presented (underside of injection pipe)

In Figure 4.2, we present time-averaged field of helium volume fraction X_1 at the mid vertical plane y=0, for three test cases. From configuration A to C, the cavity is less and less confined and the homogeneous layer is more and more clear. The bi-layer distribution is obvious in configuration C.

Thus, we may take configuration C as the reference geometrical configuration. However, pre-calculation results show that the exterior domain seems not large enough to cover the entire outflux zone. Saikali et al. (2019) shows the horizontal extension of exterior domain should around the length of the main cavity. Taking into account the outflux zone and computation resource, we fix following geometrical configuration in this study, presented in table 4.2. For illustration, a global view of this configuration is presented in figure 4.3.

4.3.1 Physical configuration

The whole system is placed in an isothermal environment ($25°C$, 298.15K) with a constant thermodynamic pressure (10^5 Pa). Pure helium or pure hydrogen will be continuously injected into the cavity, the choice of injection volume flux is initially proposed to respect the volume Richardson number Ri_v (see equation (1.60)) around 1.

The injection volume flux is fixed as 12NL/min in this study. Here the unity "NL/min", usually used in experimental studies, means 1 litre of gas per minute in normal condition, or standard state, corresponding to 273.15K ($0°C$) and 10^5 Pa. Ideal gas state equation is used to change from NL/min to L/min according to operation condition, thus:

$$Q_{inj} = 12NL/min = 12L/min \times \frac{298.15K}{273.15K} = 13.1L/min = 2.183 \times 10^{-4} m^3/s \tag{4.21}$$

The local maximum injection velocity is around 5.5m/s at the jet centre and 2.8 m/s in average. In this case, the temperature correction presents a difference around 9.2% of volume flux. Several characteristic dimensionless numbers of these two cases are summarised in table 4.3. From injection Re and Ri, the injection flow is deduced as a laminar jet.

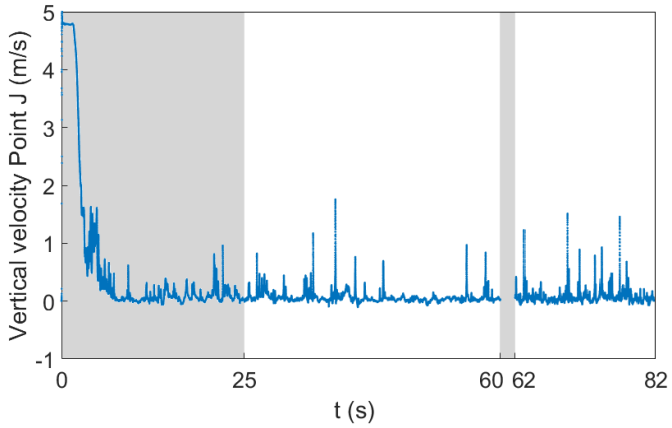

Figure 4.4: Illustration of two-steps simulation process: vertical velocity variation at a monitoring point (0,0,6cm), first step simulation (EDM) from t=0 to 60s, second step simulation (LGRM) from t=60s to 82s, transition periods , first 25s in first-step as well as first 2s in second-step are coloured in grey

Dimensionless number	**Hydrogen case**	**Helium case**
Re_{inj}	255	228
Ri_{inj}	0.167	0.078
Ri_{v}	2.13	1.00
Sc	1.42	1.73
Γ_0^B	0.021	0.026
Γ_0^{NB}	0.046	0.049

Table 4.3: Dimensionless numbers of two reference cases, Γ_0^B defined in Boussinesq jet model, see eq. (2.36), Γ_0^{NB} defined in non Boussinesq jet model, see eq. (2.67).

Simulation step	**First step**	**Second step**
Mesh	EDM	LGRM
Min. cell size	0.7mm	0.2mm
Nb. of cells	15.44M	80.2M
MPI procs	560	2016
Cells / proc	27.5k	39.8k
Time-step ≈	1.3×10^{-4}s	3.6×10^{-5}s
Phys. time in transition period	25s	2s
Phys. time for statistical operation	35s	20s
Sampling frequency	1kHz	5kHz
Nb. of statistical samples	35k	100k

Table 4.4: Computation parameters for two simulation steps

4.3.2 Simulation process

For the need of mesh convergence test, based on this geometrical configuration, we construct firstly an **Equi-distant Mesh (EDM)** with the cell size $\delta x = 0.7$mm. We construct a second mesh, where the jet region is well refined with the smallest cell size $\delta x = 0.2$mm, corresponding to the local Kolmogorov length scale, called **Local Grid Refinement Mesh (LGRM)**. These 2 meshes are presented in appendix D. Results comparison will be presented in the next section to evaluate the necessity of mesh refinement.

The whole simulation could be divided into 2 parts. The first-step simulation is based on equi-distant mesh (EDM), from initial state $t = 0$ where the whole cavity and the injection pipe are fulfilled with fresh air. The jet flow will arrive at the ceiling of the cavity in 0.1s. The global flow then goes into the transition period for almost 10s before quasi-steady state is established. The statistical operation begins at $t = 25s$ to ensure the quasi-steady flow regime in the whole cavity. The simulation continues for at least 35s during which statistical quantities (time-averaged quantities and root-mean-square quantities) are calculated.

The second-step simulation is based on local grid refinement mesh (LGRM). We retake the last-time instantaneous velocity and density field at the end of first-step simulation, as the initial condition for the second-step. A projection procedure is needed. We wait 2 seconds physical time to re-establish a new quasi-steady state before the statistical operation. Then simulation continues for around 20s during which statistical quantities are calculated. The whole simulation process is illustrated by velocity variation at a monitoring point situated at (0,0,6cm), see figure 4.4.

The equidistant mesh possesses 15.44 millions of cells and is divided into 560 MPI processors, so that 27.5k cells per processor. This number is in the reported optimal interval 25-40k by Bieder (2007) and Vandroux and Barthel (2013) of the code. The monitoring points output period as well as statistical sample period is around 1ms, corresponding to around 8 time-steps. The statistical time lag (35s) corresponds to 270k time-steps and 35k samples.

The local grid refinement mesh possesses 80.2M cells and divided into 2016 MPI procs. The monitoring points output period as well as statistical sample period is around 0.2ms, corresponding to 5 or 6 time-steps. The statistical time lag (20s) corresponds to 556k time-steps and 100k samples.

The parallel implementation is based on the domain decomposition method using the MPI library. The computation is run on French national supercomputers CEA-CCRT, Jean-Zay of IDRIS and OCCIGEN of CINES, all of them are under the framework of GENCI (www.genci.fr). The detailed computation parameters of these two steps are summarised in table 4.4.

4.4 Numerical convergence validation

In the simulation, statistical quantities are calculated from a series of samples output in the quasi-steady state. The accuracy of these statistical quantities are directly linked to the convergence of numerical simulation. In this section, we focus on the convergence in space and in time. On the one hand, we will evaluate the mesh convergence by comparing statistical results from two meshes (EDM and LGRM) with different cell sizes. A check of Kolmogorov length scale is also presented. On the other hand, statistical accuracy is directly linked to the number of independent samples, deduced by local autocorrelation function.

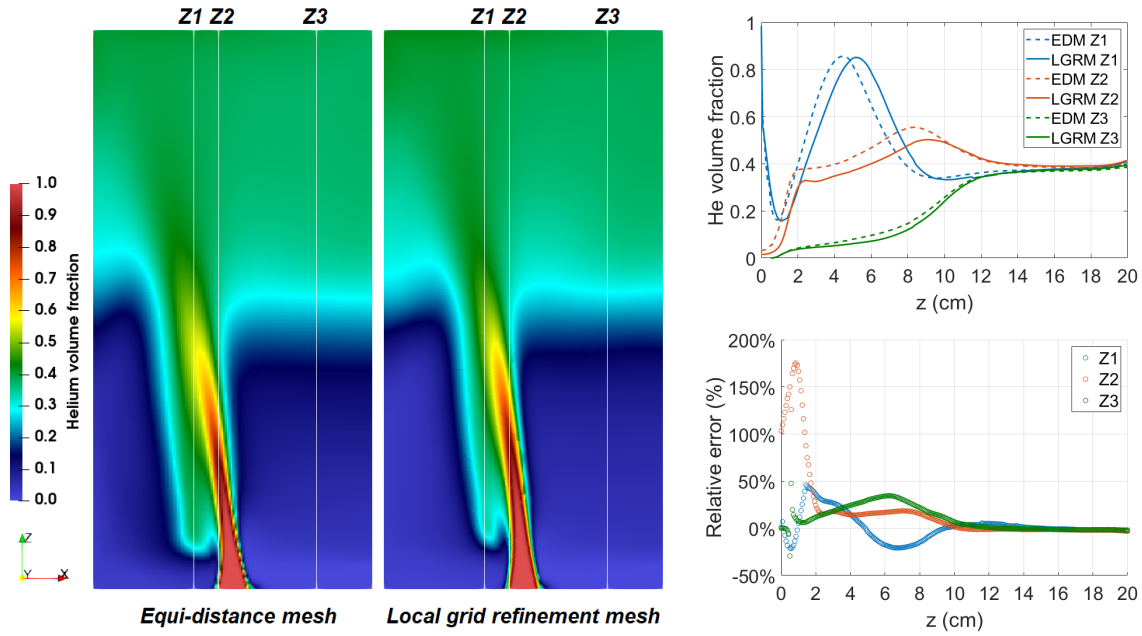

Figure 4.5: Result comparison equi-distant mesh (EDM) and local grid refinement mesh (LGRM) for helium case: time-averaged volume fraction distribution (left) on plane y=0, variation of Y_1 along three monitoring lines Z1: x=-1.4cm, Z2: x=-0.5cm, Z3: x=3cm (upper-right) and associated relative error (lower-right)

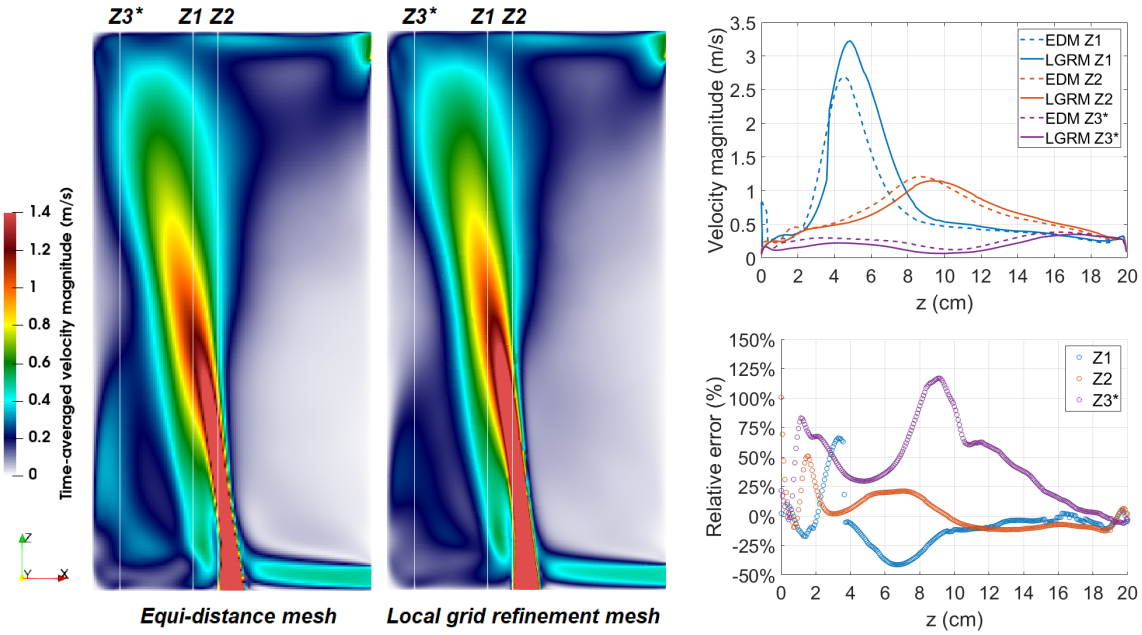

Figure 4.6: Result comparison equi-distant mesh (EDM) and local grid refinement mesh (LGRM) for helium case: time-averaged velocity magnitude (left) on plane y=0, its variation along three monitoring lines Z1: x=-1.4cm, Z2: x=-0.5cm, Z3*: x=-4cm (upper-right) and associated relative error (lower-right)

4.4.1 Mesh convergence and numerical accuracy

We will check if the mesh is fine enough to simulate the structure of turbulent flow. Firstly we evaluate the necessity of mesh refinement and try to identify the numerical error related to the cell size, by comparing the results obtained from two meshes. Then we verify if the refinement mesh is in the Kolmogorov length scale to provide a proper DNS simulation.

Results comparison between two meshes (EDM and LGRM)

In figure 4.5 and 4.6, we present respectively the time-averaged volume fraction and velocity magnitude distributions on plane $y = 0$ for helium case. Both velocity and concentration distributions are in the similar structure. However, some important differences could be also identified. The jet is little less inclined with LGRM where the grid in the jet area is 3.5 times finer. Velocity in the area ($x < -4$cm, $z < 8$cm) is less obvious in LGRM.

We set three vertical monitoring lines to illustrate these differences. The concentration distribution is almost the same in the top homogeneous layer, but local relative difference may up to 150% at jet border ($x = -1.4$cm for Z1). For velocity magnitude, in the jet region (Z1 and Z2, $z < 10cm$), the relative difference can up to $\pm 50-75\%$, especially for jet region $z = 2-4$cm. This is mainly due to the different inclination of jet centre. The jet is less inclined in LGRM case. Besides, near the backward wall line Z3*, the velocity magnitude is quite different in the recirculation region $z = 2-4$cm. Local velocity for LGRM is nearly a half of that in EDM, representing a relative error around 50% to 75%.

Global estimation of numerical error

From above results, we conclude that the equidistant mesh could not be considered fine enough to guarantee simulation quality especially in the jet area. We define the global relative difference between these two results: for a statistical-based scalar field ϕ, the global difference is defined as

$$\mathrm{Diff}(\phi) = \sqrt{\frac{\sum_{P\in\Omega}\left(\phi(P,EDM)-\phi(P,LGRM)\right)^2}{\sum_{P\in\Omega}\left(\phi(P,LGRM)\right)^2}} \tag{4.22}$$

where P monitoring points selected in the main cavity region Ω, corresponding to **every** cell centre position of the EDM ($140\times140\times280 = 5.488$M probes). The results are presented in the table 4.5.

The convergence of these statistical-based scalar fields will be detailed studied in the following section.

From the guideline Mahaffy et al. (2015) concerning CFD numerical error related to mesh size, at least 3 meshes with different refinements are generally needed to estimate numerical accuracy. Due to computation resource consideration, we only have two meshes to compare. Consequently, the Grid Convergence Index (GCI) is used to estimate the global numerical accuracy which is defined as follows (Richardson (1911))

$$\mathrm{GCI}(\phi) = F_s\frac{1}{r^p-1}\mathrm{Diff}(\phi) \tag{4.23}$$

where coefficient F_s is chosen as 3.0 in a conservative way as recommendation in Roache (1998) as only two meshes are used in comparison (otherwise $F_s = 1.25$). r is the grid refinement ratio (here equals to 3.5). $p = 2$ is the truncation error order of the discretisation scheme.

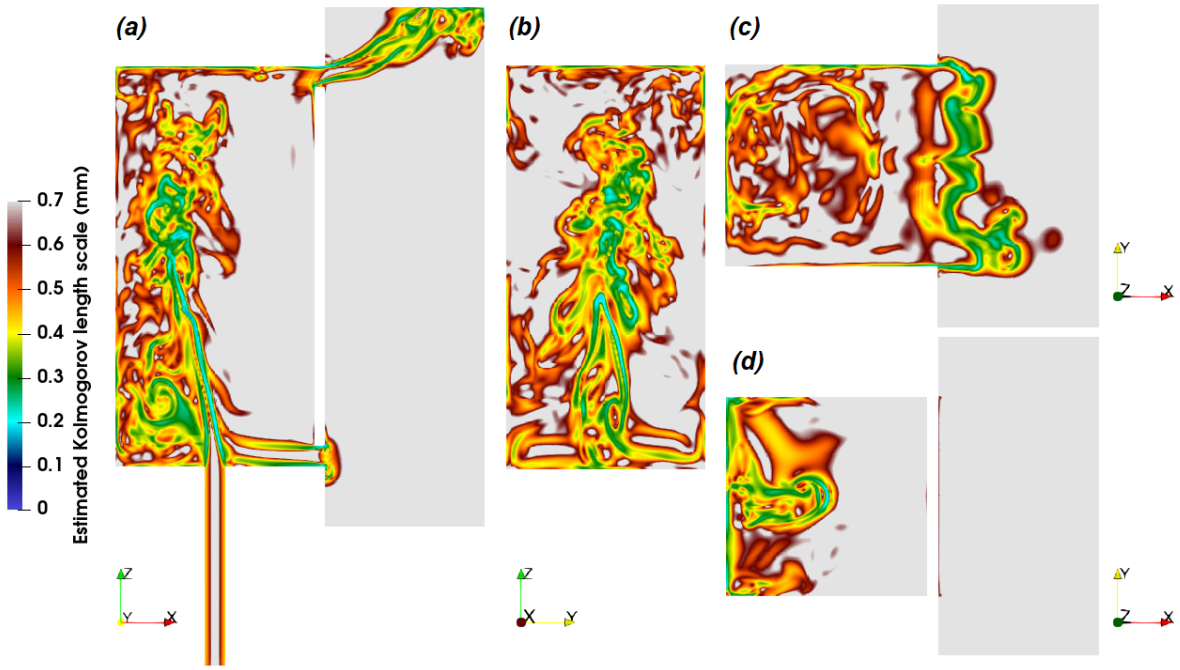

Figure 4.7: Estimation of Kolmogorov length scale η^{DNS} based on instantaneous result on helium case (LGRM), using local grid refinement mesh. (a) plane y=0 (b) plan x=-1.5cm (c) z=19.5cm (d) z=2cm. Areas with estimated Kolmogorov length larger than 0.7mm are coloured in light grey.

Statistical quantity ϕ	**Global relative difference** Diff(ϕ)	**Estimated Grid Convergence Index (GCI)**
Time-averaged mixture density	2.31%	0.617%
Time-averaged x-direction velocity	29.3%	7.82%
Time-averaged y-direction velocity	48.1%	12.8%
Time-averaged z-direction velocity	26.0%	6.94%
Time-averaged velocity magnitude	23.7%	6.32%
RMS mixture density	20.3%	5.43%
RMS x-direction velocity	98.6%	26.3%
RMS y-direction velocity	92.1%	24.6%
RMS z-direction velocity	60.8%	16.2%
RMS velocity magnitude	58.1%	15.5%

Table 4.5: Global relative difference of statistical quantities between two meshes as well as estimated Grid Convergence Index (GCI)

Results of GCI are also presented in table 4.5. In the first-order approximation, the GCI index could be considered (in a conservative way) as the numerical error of LGRM related to mesh convergence.

Globally, we have a very good numerical convergence for density field and for x and z components of velocity field. The GCI of RMS in x-y directions (horizontal plan) is around 25% which proves the necessity of mesh refinement. The perturbation of jet and effect of entrainment is well simulated in the refinement mesh.

4.4.2 Kolmogorov length scale

For a proper DNS simulation, the cell length should be inferior to the Kolmogorov length scale η. The notion of Kolmogorov length is based on the energy cascade theory of turbulent flow. It was introduced by Richardson (1922) to describe how the energy is transferred between rotational flow structures (eddies). The Kolmogorov length scale η is defined as the smallest length scale of eddies. At the scale of η, the viscous effects become dominant and the transported energy is completely dissipated.

The local Kolmogorov length scale η^{DNS} can be estimated as follows

$$\eta^{DNS} = \left(\frac{\nu^3}{\epsilon^{DNS}} \right)^{1/4} \tag{4.24}$$

with $\nu = \mu/\rho$ kinetic viscosity ϵ^{DNS} the local dissipation rate can be evaluated as

$$\epsilon^{DNS} = 2\mu(S_{ij}S_{ji}) \tag{4.25}$$

with μ local dynamic viscosity and S_{ij} symmetrical part of strain rate tensor defined in equation (1.30).

As presented in figure 4.7, an instantaneous field of η^{DNS} for helium case in quasi-steady regime, using local LGRM. The Kolmogorov length is larger than 0.7mm for the majority area in the main cavity. It can reach up to 0.2-0.3mm in the jet region. Apparently, the EDM with cell size 0.7mm is not precise enough to realise a proper DNS simulation in strict sense. The LGRM, where the cell size is equal to 0.2mm in the jet region and in maximum 0.45mm in the main cavity, seems suitable with the estimated Kolmogorov length scale.

Consequently, we confirm the necessity of mesh refinement. All validated statistical analysis will be based on refinement mesh LGRM only (second-step in computation process).

4.4.3 Statistical convergence and sampling correlation

In this study, statistical quantities are used to characterise the flow and concentration distribution in quasi-steady state. Recall that in the second-step simulation process, statistical operation continues for a physical time around 20s. Statistical quantities are calculated based on a sampling frequency 5kHz thus possess around 100k samples in total at each cell. As illustration, we will present the variation at two representative monitoring points for helium case in this section.

- **Point J**: (0,0,6cm) within the jet to evaluate the jet flow
- **Point S**: (5cm,0,19.5cm) in the centre of the top opening to evaluate the outlet flow

The principal results of this section are presented in figure 4.8. In the first column, we present the temporal variations of velocity and density at these 2 monitoring points during last 20s of the second-step simulation. The initial time $t = 0$ in the figure corresponds to the physical time 62s. The flow is very turbulent at these points. Both velocity and density varies intensely with time.

In order to evaluate sample dependency (correlation), we use the (unbiased) autocorrelation function (ACF). ACF for a scalar field $\varphi(x,y,z,t)$, at observation point (x,y,z) is defined as a function of examined time-lag:

$$ACF_{\varphi(x,y,z)}(t) = \frac{\sum_{\tau=t_{start}}^{t_{end}-t} (\varphi(x,y,z,\tau) - \overline{\varphi}(x,y,z)) \cdot (\varphi(x,y,z,\tau+t) - \overline{\varphi}(x,y,z))}{\sum_{\tau=t_{start}}^{t_{end}-t} (\varphi(x,y,z,\tau) - \overline{\varphi}(x,y,z))^2} \tag{4.26}$$

with $\overline{\varphi}(x,y,z)$ the time-averaged field of φ at this point. The ACFs of these signals are presented in the second column of figure 4.8. These ACFs equal to 1 at $t = 0$ and drop rapidly to zero, then oscillate around the axis $ACF = 0$. This means that there exists correlated samples in these signals. By applying second-order Taylor development of these ACFs near their origins, we define related Taylor correlated time lag as follows (Spicker and Feitzinger (1988))

$$\lambda_{Taylor} = \frac{1}{\sqrt{-\frac{d^2 ACF(t)}{dt^2}\Big|_{t=0}}} \tag{4.27}$$

which can be interpreted as a parabolic fit to the ACF function near its origin and could be transferred to a linear regression (Batchelor (1953)).

$$\sqrt{1 - ACF(t)} = \frac{1}{\sqrt{2}\lambda_{Taylor}} t \tag{4.28}$$

In the third column of figure 4.8, we present the variation of $\sqrt{1 - ACF(t)}$ in solid lines as well as their linear regression near the origin (with time lag less than 3ms) in dashed lines. The Taylor correlated time lag is estimated from the slope of regression lines. All consecutive samples within duration λ_{Taylor} are considered as correlated. For velocities, correlated time lag equals 5.34ms at point J and 3.36ms at point S. Considering a sampling frequency 5000Hz, this means every around 20-30 consecutive samples are correlated. For mixture density variation, the correlated time lag is longer, 8.9ms at point J and 7.19ms at point S, corresponding to 45 and 36 consecutive sampling points.

Consequently, we consider the statistical samples are set enough dense to cover every characteristic oscillation period (typically λ_{Taylor}). In this case, the statistical accuracy can be considered only related to the number of uncorrelated samples during the whole observation.

Uncorrelated samples

We note $\mathcal{N}$ the number of uncorrelated samples during an observation from t_{start} to t_{end} (here indicating the start and the end of the second-step simulation with LGRM). From the above analysis, we have

$$\mathcal{N} = \left\lfloor \frac{(t_{end} - \lambda_{Taylor}) - t_{start}}{\lambda_{Taylor}} \right\rfloor \tag{4.29}$$

where $\lfloor x \rfloor$ indicates the greatest integer less than or equal to x (floor function).

Generally, the number of uncorrelated samples depends on observed position and observed physical quantity. Due to computation resource consideration, it is impossible to output all

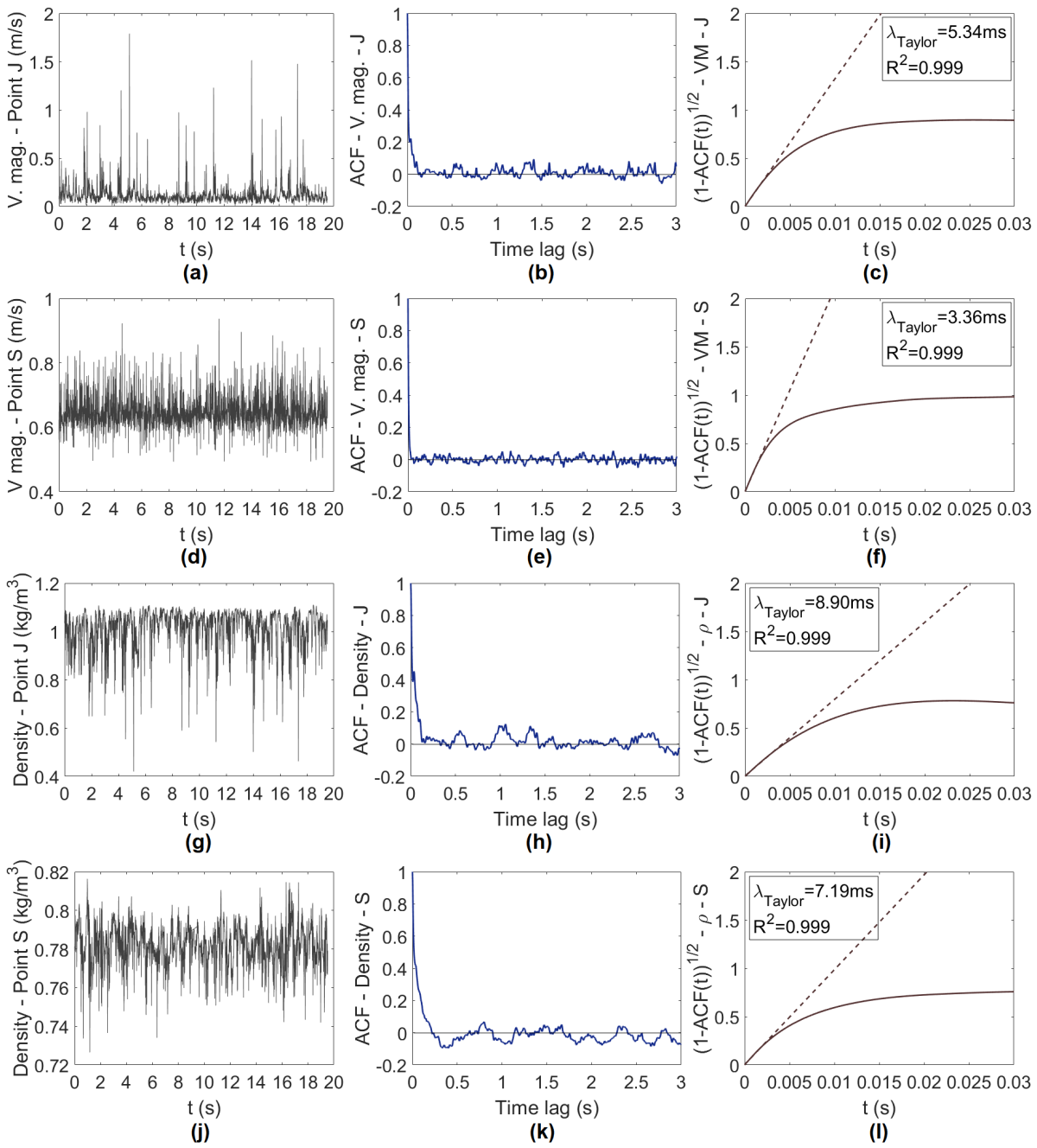

Figure 4.8: Study of statistical convergence at monitoring points, (a)-(c) quantities related to velocity magnitude at point J, (d)-(f) results related to velocity magnitude at point S, (g)-(i) results related to local mixture density at point J and (j)-(l) results related to local mixture density at point S. 1^{st} column: temporal variation with started time $t = 0$ corresponds here to the beginning of statistical operation. 2^{nd} column: auto-correlation function (ACF) of temporal variation. 3^{rd} column: linear regression (dashed lines) of variation $\sqrt{1 - ACF(t)}$ (solid lines) near origin, estimation of Taylor correlated time lag.

temporal variations at all cell points. To facilitate the calculation of statistical accuracy, we admit that results obtained from some characteristic monitoring points could be correctly applied in the whole cavity. During the whole observation, we have around 100k samples at each mesh cell with 20s physical observation duration. By applying a conservative strategy, for velocity field, the global correlated time is considered less than 10ms (frequency 100Hz) at everywhere in the cavity. This corresponds to 2000 uncorrelated samples. As density seems variable with low frequency at far field of the jet, we consider its global correlated time is less than 40ms (25Hz), correspond to 500 uncorrelated samples. Therefore, during the second-step simulation:

- **At least** $\mathcal{N} = 2000$ uncorrelated velocity samples obtained at each cell point
- **At least** $\mathcal{N} = 500$ uncorrelated density samples obtained at each cell point

4.4.4 Statistical quantities and its accuracies

Two kinds of statistic quantities are calculated in the simulation, the time-averaged quantity (mean value) as well as its root-mean-square (RMS), which can be considered as the first-order estimation of the standard deviation.

For a scalar field $\varphi(x,y,z,t)$, its time-averaged field $\overline{\varphi}(x,y,z)$ is calculated as

$$\overline{\varphi}(x,y,z) = \frac{1}{t_{end}-t_{start}}\left(\sum_{\tau=t_{start}}^{t_{end}} \varphi(x,y,z,\tau)\cdot\delta t\right) \tag{4.30}$$

And its root-mean-square (RMS) field is defined as

$$\mathrm{RMS}(\varphi)(x,y,z) = \sqrt{\frac{1}{t_{end}-t_{start}}\left(\sum_{\tau=t_{start}}^{t_{end}} \left(\varphi(x,y,z,\tau)-\overline{\varphi}(x,y,z)\right)\right)^2\cdot\delta t} \tag{4.31}$$

The general error of statistical quantities consists of two parts: numerical error and statistical error. For the first one, if we admit that the LGRM refinement mesh is in asymptotic regime and considered fine enough (thus strictly under Kolmogorov length scale), we may take the index GCI as an estimation of its numerical error in first order approximation. Note that the numerical error is a notion of global error related to the simulation quality. For the second one, statistical error depends on uncorrelated samples $\mathcal{N}$. We apply 95% (1.96-σ) as confidence interval. Consequently, the total error of statistical quantities is calculated as follows

For time-averaged field $\overline{\varphi}$:

- Upper 95% limit $= \overline{\varphi}\times(1+\mathrm{GCI}(\overline{\varphi})) + 1.96\frac{\mathrm{RMS}(\varphi)}{\sqrt{\mathcal{N}}}$
- Lower 95% limit $= \overline{\varphi}\times(1-\mathrm{GCI}(\overline{\varphi})) - 1.96\frac{\mathrm{RMS}(\varphi)}{\sqrt{\mathcal{N}}}$

For RMS field $\mathrm{RMS}(\varphi)$:

- Upper 95% limit $= \mathrm{RMS}(\varphi)\times\left(\mathrm{GCI}(\mathrm{RMS}(\varphi)) + \sqrt{\frac{\mathcal{N}}{\mathrm{CHIINV}(0.975,\mathcal{N})}}\right)$
- Lower 95% limit $= \mathrm{RMS}(\varphi)\times\left(-\mathrm{GCI}(\mathrm{RMS}(\varphi)) + \sqrt{\frac{\mathcal{N}}{\mathrm{CHIINV}(0.025,\mathcal{N})}}\right)$

where the function CHIINV(p, n) returns the inverse of the right-tailed probability of the chi-squared distribution with probability p and number of degrees of freedom n.

We define the relative accuracy (in %) for statistical quantity ϕ of a time-averaged or an RMS field as follows

$$\mathrm{Err}(\phi) = \frac{\text{Upper 95\% limit} - \text{Lower 95\% limit}}{2\phi} \tag{4.32}$$

For example, we present in table 4.6 the estimation of relative error of statistical quantities on the velocity magnitude and mixture density at monitoring points J and S. We compare the contribution of numerical error (related to GCI) and statistical error (relative to uncorrelated samples) in the total relative accuracy. For time-averaged fields, numerical error is generally larger than statistical error, sometimes dominant. The GCI is 6.32% for time-averaged velocity magnitude field (see table 4.5), compared with statistical error from 0.2% to 3% depended on monitoring position. The GCI is 0.62% for time-averaged density field, compared with statistical error from 0.1% to 0.6%. For RMS field, numerical error is dominant to statistical error for velocity fields. The velocity magnitude RMS GCI is 15.5%, compared with a statistical error around 3%. Statistical error presents only around 1/5 in the total error.

We shall note that all above estimation is in a conservative way. On one hand, numerical error GCI is estimated based on only two meshes. On the other hand, the uncorrelated samples, directly related to statistical error, is treated globally thus underestimated. Generally, the total relative accuracy is considered less than 8% for time-averaged velocity field and 1% for time-averaged density field and less than 18% for velocity RMS and 12% for density RMS. Statistical fields for density are more precise than that for velocity.

In conclusion, we consider the second-step simulation using LGRM is long enough to provide necessary uncorrelated samples. The statistical error is generally smaller (sometimes negligible) than that of numerical error.

4.5 Numerical 1D post-processing methodology

DNS simulation provides us complete 3D fields of flow variables, which could be treated as reference to compare and improve analytical models. In this section, we present the post-processing methods to calculate the characteristic 1D physical quantities, defined in the 1D turbulent jet models.

The post-processing method is based on Gaussian profiles assumption. Characteristic jet quantities are calculated from DNS time-averaged fields and corrected by a series of integral calculations on well-selected zones. Some parameters will then need to be converted into Top-hat to compare with theoretical results. In addition, variations of entrainment coefficient are estimated both for Boussinesq and non Boussinesq models.

4.5.1 Vertical velocity and mixture density profiles under Gaussian assumption

In turbulent jet models, two characteristic profiles are selected to describe the jet: the vertical velocity w and the mixture density ρ. Recall that under Gaussian profile assumption, we have for vertical velocity:

$$w(r,z) = w_G(z)\exp\left(-\frac{r^2}{b_G^2(z)}\right) \tag{4.33}$$

with w_G the Gaussian characteristic vertical velocity and b_G the characteristic radius of the jet (of the vertical velocity). The mixture density profile in the jet is in the similar 2D Gaussian

	Velocity Point J	**Velocity** Point S	**Density** Point J	**Density** Point S
Time-averaged	0.1044m/s	0.6395m/s	1.015kg/m^3	0.7842kg/m^3
RMS	0.0672m/s	0.0270m/s	0.0770kg/m^3	0.0111kg/m^3
Conservative uncorrelated samples	2000	2000	500	500
Numerical accuracy (GCI) - time-averaged	6.32%	6.32%	0.62%	0.62%
Statistical accuracy - time-averaged	2.82%	0.19%	0.66%	0.12%
Total relative accuracy - time-averaged	**9.14%**	**6.51%**	**1.28%**	**0.74%**
Numerical accuracy (GCI) - RMS	15.5%	15.5%	5.43%	5.43%
Statistical accuracy - RMS	3.1%	3.1%	6.17%	6.17%
Total relative accuracy - RMS	**18.6%**	**18.6%**	**11.6%**	**11.6%**

Table 4.6: Estimation of relative accuracy of statistical quantities of velocity magnitude and local mixture density at two monitoring points J and S

form, but with different characteristic radius.

$$\rho(r,z) = \rho_e(z) - (\rho_e(z) - \rho_G(z))\exp\left(-\frac{r^2}{(\lambda b)_G^2}\right) \tag{4.34}$$

ρ_G is the characteristic density at jet centre and ρ_e is the environment density at far-field of the jet. The term λb_G is the characteristic radius of the density with λ called convection-diffusion ratio.

These profile parameters can be divided into two categories, where $w_G, b_G, \rho_G, \lambda$ are related to the jet and ρ_e is related to the far-field of the jet. Therefore, each horizontal cross-section of the main cavity at altitude z, noted $S(z)$, can be divided into two parts: the jet region, noted $\Omega(z)$, and its complementary $\mathcal{C}(\Omega)(z)$, called the far-field or environmental region.

$$S(z) = \Omega(z) \cup \mathcal{C}(\Omega)(z) \tag{4.35}$$

The vertical velocity should be positive in $\Omega(z)$ and the mixture density should be quasi-homogeneous in $\mathcal{C}(\Omega)(z)$. As the jet axis is not straight, a dedicated methodology has to be applied to restrict the jet region on the horizontal jet cross-sections.

Jet centre, jet region and environmental density

DNS results show that the jet is slightly inclined towards the x-negative backward wall due to ventilation effect but the lateral width of the cavity is large enough to provide a gap for the environmental downward flow. Therefore, we observe on any cavity cross-sections, that the position where the maximum of the time-averaged vertical velocity located, defined here as the jet centre, is coincided with the point where light gas concentration attains its maximum at

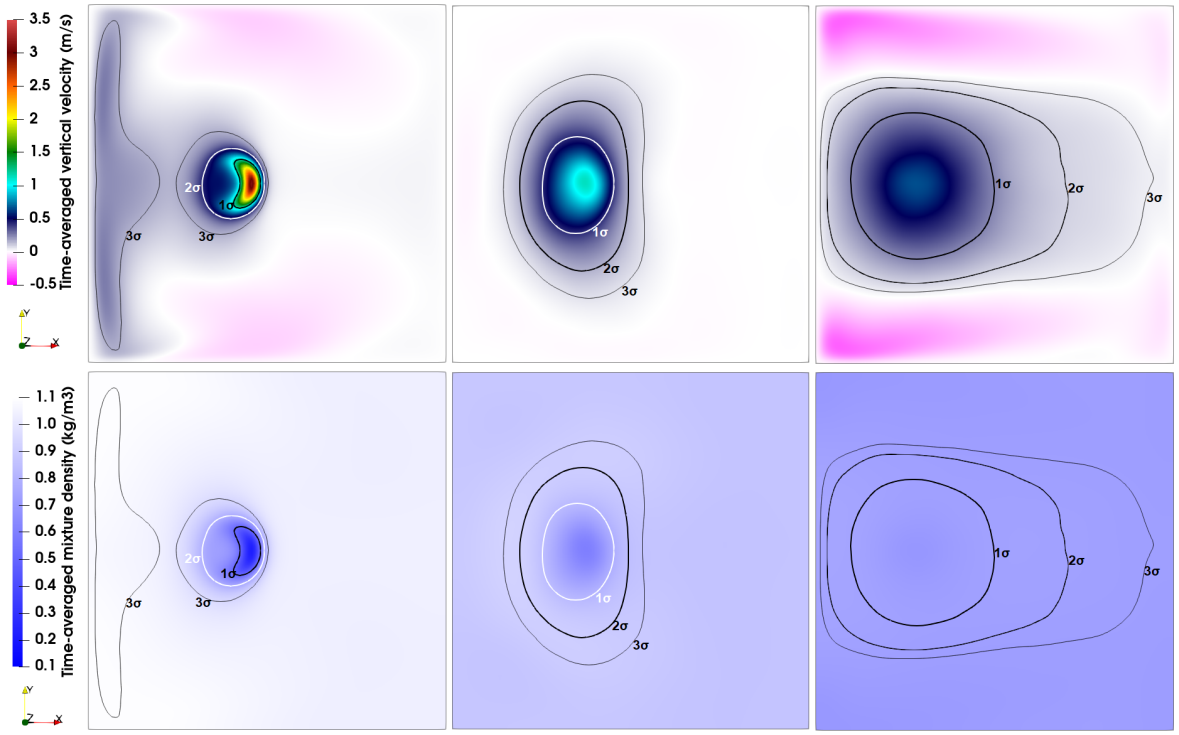

Figure 4.9: Edge of $\Omega^{DNS}(z)$, noted $1, 2, 3\sigma$, corresponding to the choice of ε_w as $1/e, 1/e^2, 1/e^3$, and the distribution of time-averaged vertical velocity field $\overline{w}$ (on the left side) and mixture density field $\overline{\rho}$ (on the right side) on horizontal planes $z = 5cm$ (left), $z = 10cm$ (middle) and $z = 15cm$ (right) for helium case

this level. The characteristic vertical velocity $w_G^{DNS}(z)$ and the characteristic density $\rho_G^{DNS}(z)$ are defined as:

$$w_G^{DNS}(z) = \max_{(x,y,z)\in S(z)} \overline{w(x,y,z)} \tag{4.36}$$

$$\rho_G^{DNS}(z) = \min_{(x,y,z)\in S(z)} \overline{\rho(x,y,z)} \tag{4.37}$$

The determination of the jet region $\Omega(z)$ is based on the time-averaged fields of vertical velocity and mixture density. The choice of $\Omega(z)$ should take into account the majority vertical velocity contribution and remove as much as possible the influence of environmental flow.

The vertical velocity is the most representative flow variable of the jet. We define the jet region $\Omega(z)$ by introducing a threshold value $\varepsilon_w \in [0,\ 1]$ of the time-averaged vertical velocity $\overline{w}$.

$$\Omega(z) = \left\{(x,y,z) | \overline{w(x,y,z)} \geq \varepsilon_w \cdot w_G^{DNS}(z)\right\} \tag{4.38}$$

The DNS-based environmental density ρ_e^{DNS} then can be calculated by the mean value of the time-averaged density on the far field region $\mathcal{C}(\Omega)(z)$.

$$\rho_e^{DNS}(z) = \frac{\sum_{(x,y,z)\in\mathcal{C}(\Omega)(z)} \overline{\rho(x,y,z)} dS(x,y,z)}{\sum_{(x,y,z)\in\mathcal{C}(\Omega)(z)} dS(x,y,z)} \tag{4.39}$$

with $dS(x,y,z)$ the horizontal surface of local cell at position (x,y,z).

Note that this threshold ε_w cannot be chosen too large in order to cover the majority of jet zone. It cannot be selected too small or even zero as well in order to ensure environmental flow, such as inlet/outlet flow is not significantly presented in the jet region. In addition,

the time-averaged mixture density should be homogeneous in the complementary of the jet region. Figure 4.9 illustrates for helium case, the influence of ε_w on the approximation of the jet region $\Omega^{DNS}(z)$ with three values, $1/e, 1/e^2, 1/e^3$ with e Euler's number, corresponding to once, twice and three times of standard deviation of 2D Gaussian distribution (noted 1σ, 2σ, 3σ respectively). Results comparisons are carried out on three horizontal planes with altitude z =5cm, 10cm and 15cm.

At the two lowest planes (z =5cm and 10cm), the choice of 1σ or 2σ appears providing a reasonable approximate of the jet region for $\overline{\rho}$. The jet region is less clear for the vertical velocity $\overline{w}$, where a part of the rising flow is not covered. Additionally, in the top part of the cavity (see for example altitude $z = 15cm$). It is more complicated to define a jet region by density variation. We finally decide to retain the jet region 3σ, which covers an area maybe just little larger than the jet region but provides a better estimate of environmental density.

Consequently, we take

$$\varepsilon_w = \frac{1}{e^3} \approx 0.05 \tag{4.40}$$

Characteristic jet radius and diffusion-convection ratio

We notice that the inlet flow through the bottom opening presents a large influence on the jet cross-section shape close to the injection, the distribution of $\overline{w}$ on the horizontal plane is not as regular as a round Gaussian profile. In this section, we aim to evaluating the characteristic jet radius b_G and diffusion-convection ratio λ.

Note that the notion of characteristic jet radius b_G does not correspond to the radius of jet border. Its definition is linked to the ratio w_G/e (see equation (2.10))

$$w(r = b_G, z) = \frac{w_G(z)}{e} \tag{4.41}$$

Consequently, we identify firstly the section area $S_b(z)$ at each altitude z, where the local vertical velocity $\overline{w}$ is superior to the ratio w_G^{DNS}/e:

$$S_b(z) = \sum_{(x,y,z)\in\Omega_b(z)} dS(x,y,z), \text{ with } \Omega_b(z) = \left\{ (x,y,z) | \overline{w(x,y,z)} \geq \frac{w_G^{DNS}(z)}{e} \right\} \tag{4.42}$$

with $dS(x,y,z)$ the horizontal surface of local mesh at position (x,y,z). Then, the characteristic radius of the jet under Gaussian assumption can be estimated by

$$b_G^{DNS}(z) = \sqrt{\frac{S_b(z)}{\pi}} \tag{4.43}$$

Similarly, the DNS-based diffusion-convection ratio λ^{DNS}, related to the distribution of time-averaged mixture density $\overline{\rho}$, can be determined by a specific surface $S_\rho(z)$ defined as

$$S_\rho(z) = \sum_{(x,y,z)\in\Omega_\rho(z)} dS(x,y,z), \text{ with } \Omega_\rho(z) = \left\{ (x,y,z) | \overline{\rho(x,y,z)} \leq \rho_e^{DNS}(z) + \frac{1}{e}\left(\rho_G^{DNS}(z) - \rho_e^{DNS}(z)\right) \right\} \tag{4.44}$$

And then the quantity diffusion-convection ratio λ^{DNS} can be calculated as follows.

$$\lambda^{DNS}(z) = \frac{1}{b_G^{DNS}(z)} \sqrt{\frac{S_\rho(z)}{\pi}} = \sqrt{\frac{S_\rho(z)}{S_b(z)}} \tag{4.45}$$

Remark

In the literature, other definitions for diffusion-convection ratio λ are presented. Apart from the mixture density ρ that used in this study, the mass fraction of injected gas Y_1, the volume fraction of injected gas X_1 as well as the reduced density G' are also introduced. Recall the relation between these parameters

$$X_1 = \frac{\rho_{air} - \rho}{\rho_{air} - \rho_{inj}}, \quad Y_1 = X_1 \frac{\rho_{inj}}{\rho} = \frac{\rho_{inj}\rho_{air}}{\rho_{air} - \rho_{inj}} \frac{1}{\rho} - \frac{\rho_{inj}}{\rho_{air} - \rho_{inj}}, \quad G' = \frac{\rho_e - \rho}{\rho_0} g \tag{4.46}$$

with $\rho_{inj}, \rho_{air}, \rho_0$ the density of injected light gas, fresh air and that of reference respectively. Owing to linear relationships between ρ, X_1 and G', similar Gaussian profiles with same deviation can be assumed for these 3 flow variables. Thus, the diffusion-convection ratio λ is the same based on any flow variable among ρ, X_1 or G'. This is not the case for Y_1. It is contradictory to assume Gaussian profile both for ρ and Y_1.

4.5.2 Characteristic jet quantities

In this section, we aim at calculating the characteristic jet quantities defined in turbulent jet models. We focus on five physical quantities, both as functions of altitude z only:

- **Volume flux** $\mathcal{Q}(z)$, defined in equation (2.18)
- **Momentum flux** $\mathcal{M}(z)$, defined in equation (2.20)
- **Mass flux** $\mathcal{Q}_m(z)$, defined in equation (2.19)
- **Mass momentum flux** $\mathcal{M}_m(z)$, defined in equation (2.21)
- **Buoyancy flux** $\mathcal{B}(z)$, defined in equation (2.22)

Except for the buoyancy flux $\mathcal{B}(z)$, the other four quantities can be approximated by integration of corresponding time-averaged fields on the jet region $\Omega(z)$ defined in (4.38) with index 3σ.

$$\mathcal{Q}^{num}(z) = \sum_{(x,y,z)\in\Omega(z)} \overline{w(x,y,z)}\, dS(x,y,z) \tag{4.47}$$

$$\mathcal{M}^{num}(z) = \sum_{(x,y,z)\in\Omega(z)} \overline{w^2(x,y,z)}\, dS(x,y,z) \tag{4.48}$$

$$\mathcal{Q}_m^{num}(z) = \sum_{(x,y,z)\in\Omega(z)} \overline{\rho w(x,y,z)}\, dS(x,y,z) \tag{4.49}$$

$$\mathcal{M}_m^{num}(z) = \sum_{(x,y,z)\in\Omega(z)} \overline{\rho w^2(x,y,z)}\, dS(x,y,z) \tag{4.50}$$

with $dS(x,y,z)$ the mesh vertical surface at point (x,y,z).

The obtained integration zone $\Omega(z)$ does not cover the entire jet area by construction based on Gaussian self-similarity assumption which does not rely on a well-defined description of jet edge. For this reason, the theoretical correction based on Gaussian profile assumption is applied on these flux estimates.

Theoretical correction for volume and momentum fluxes

Under Gaussian assumption, we have by definition eq. (2.18) and (2.20)

$$Q = \int_{r=0}^{\infty} w_G \exp\left(-\frac{r^2}{b_G^2}\right) \cdot 2\pi r dr = \pi w_G b_G^2 \tag{4.51}$$

$$M = \int_{r=0}^{\infty} w_G^2 \exp\left(-\frac{2r^2}{b_G^2}\right) \cdot 2\pi r dr = \frac{1}{2}\pi w_G^2 b_G^2 \tag{4.52}$$

We define jet border radius $b_\Omega(z)$ a specific radius related to the integration surface $\Omega(z)$ with index 3σ.

$$b_\Omega(z) = \sqrt{\frac{S_\Omega(z)}{\pi}}, \text{ with } S_\Omega(z) = \sum_{(x,y,z)\in\Omega^{DNS}(z)} dS(x,y,z) \tag{4.53}$$

Under the assumption of a Gaussian vertical velocity profile, we have the relation of $b_\Omega(z)$, $b_G(z)$ and ε_w.

$$w(r,z) = w_G(z)\exp\left(-r^2/b_G(z)^2\right), \quad w(r = b_\Omega(z), z) = \varepsilon_w \cdot w_G(z) \tag{4.54}$$

Thus,

$$\exp(-b_\Omega^2/b_G^2) = \varepsilon_w \tag{4.55}$$

The theoretical value of $\mathcal{Q}^{num}(z)$ corresponding to integral zone $\Omega(z)$ is

$$\mathcal{Q}^{num}(z) = \int_0^{b_\Omega} w_G \exp\left(-\frac{r^2}{b_G^2}\right) 2\pi r dr = \pi b_G^2 \cdot w_G \cdot \left(1 - \exp\left(-\frac{b_\Omega^2}{b_G^2}\right)\right) = \pi b_G^2 w_G (1 - \varepsilon_w) \tag{4.56}$$

Consequently, regrouping it with (4.51) we have following relation between $\mathcal{Q}^{num}(z)$ and its theoretical corrected value $\mathcal{Q}^{DNS}(z)$.

$$\mathcal{Q}^{DNS}(z) = \frac{1}{1-\varepsilon_w}\mathcal{Q}^{num}(z) \tag{4.57}$$

Similarly, for relation between $\mathcal{M}^{num}(z)$ and its theoretical corrected value $\mathcal{M}^{DNS}(z)$:

$$\mathcal{M}^{num}(z) = \int_0^{b_\Omega} \left(w_G \exp\left(-\frac{r^2}{b_G^2}\right)\right)^2 2\pi r dr = \frac{1}{2}\pi b_G^2 w_G^2 \left(1 - \exp\left(-2\frac{b_\Omega^2}{b_G^2}\right)\right) = \frac{1}{2}\pi b_G^2 w_G^2 \left(1 - \varepsilon_w^2\right) \tag{4.58}$$

Regrouping it with (4.52), we have

$$\mathcal{M}^{DNS}(z) = \frac{1}{1-\varepsilon_w^2}\mathcal{M}^{num}(z) \tag{4.59}$$

Taking $\varepsilon_w = 1/e^3$ yields

$$\mathcal{Q}^{DNS} = 1.052\,\mathcal{Q}^{num}, \quad \mathcal{M}^{DNS} = 1.002\,\mathcal{M}^{num} \tag{4.60}$$

The correction presents 5% variation for $\mathcal{Q}$ and only 0.2% for $\mathcal{M}$. Correction for momentum flux $\mathcal{M}$ is thus not absolutely necessary.

Theoretical correction for mass and mass momentum fluxes

We apply Gaussian profiles for w and ρ eq. (2.9) (2.11) in the definition of $\mathcal{Q}_m$ and $\mathcal{M}_m$ eq. (2.19) (2.21).

$$\mathcal{Q}_m = \int_{r=0}^{\infty} \rho_e \left(1 - \left(\frac{\rho_e - \rho_G}{\rho_e}\right) \exp\left(-\frac{r^2}{\lambda^2 b_G^2}\right)\right) \cdot w_G \exp\left(-\frac{r^2}{b_G^2}\right) 2\pi r dr = \pi w_G b_G^2 \cdot \frac{\rho_e + \lambda^2 \rho_G}{\lambda^2 + 1} \tag{4.61}$$

$$\mathcal{M}_m = \int_{r=0}^{\infty} \rho_e \left(1 - \left(\frac{\rho_e - \rho_G}{\rho_e}\right) \exp\left(-\frac{r^2}{\lambda^2 b_G^2}\right)\right) \cdot w_G^2 \exp\left(-\frac{2r^2}{b_G^2}\right) 2\pi r dr = \frac{1}{2}\pi w_G^2 b_G^2 \cdot \frac{\rho_e + 2\lambda^2 \rho_G}{2\lambda^2 + 1} \tag{4.62}$$

We apply the same method used as before, by assuming Gaussian profile, we have theoretically

$$\mathcal{Q}_m^{num}(z) = \int_{r=0}^{b_\Omega} \rho_e \left(1 - \left(\frac{\rho_e - \rho_G}{\rho_e}\right) \exp\left(-\frac{r^2}{\lambda^2 b_G^2}\right)\right) \cdot w_G \exp\left(-\frac{r^2}{b_G^2}\right) 2\pi r dr \tag{4.63}$$

$$\mathcal{M}_m^{num}(z) = \int_{r=0}^{b_\Omega} \rho_e \left(1 - \left(\frac{\rho_e - \rho_G}{\rho_e}\right) \exp\left(-\frac{r^2}{\lambda^2 b_G^2}\right)\right) \cdot w_G^2 \exp\left(-\frac{2r^2}{b_G^2}\right) 2\pi r dr \tag{4.64}$$

with the radius b_Ω defined in (4.53) related to integral area surface Ω. By comparing its results with equations (4.61) (4.62), we have finally the relation between $\mathcal{Q}_m^{num}$, $\mathcal{M}_m^{num}$ and its theoretical corrected values $\mathcal{Q}_m^{DNS}$, $\mathcal{M}_m^{DNS}$

$$\mathcal{Q}_m^{DNS}(z) = \mathcal{Q}_m^{num}(z) \cdot \frac{\rho_e + \lambda^2 \rho_G}{\left(1 - (\lambda^2+1)\,\varepsilon_w + \lambda^2 \varepsilon_w \varepsilon_w^{\frac{1}{\lambda^2}}\right)\rho_e + \left(1 - \varepsilon_w \varepsilon_w^{\frac{1}{\lambda^2}}\right)\lambda^2 \rho_G} \tag{4.65}$$

$$\mathcal{M}_m^{DNS}(z) = \mathcal{M}_m^{num}(z) \cdot \frac{\rho_e + 2\lambda^2 \rho_G}{\left(1 - (2\lambda^2+1)\,\varepsilon_w^2 + 2\lambda^2 \varepsilon_w^2 \varepsilon_w^{\frac{1}{\lambda^2}}\right)\rho_e + \left(1 - \varepsilon_w^2 \varepsilon_w^{\frac{1}{\lambda^2}}\right) \cdot 2\lambda^2 \rho_G} \tag{4.66}$$

We may use the DNS estimated quantities ρ_e^{DNS}, ρ_G^{DNS} and λ^{DNS} to replace ρ_e, ρ_G, λ in the above equations. Generally the correction is necessary only for mass flux $\mathcal{Q}_m$, especially under bi-layer interface where the term of ρ_e dominates in denominator, corresponding to an error may up to 10%.

Calculation of buoyancy flux

From its definition eq. (2.22), the buoyancy flux $\mathcal{B}(z)$ can be calculated as

$$\mathcal{B}(z) = \int \frac{\rho_e - \rho}{\rho_0} g w dS = \frac{g}{\rho_0}\left(\rho_e(z) \int w dS - \int \rho w dS\right) = \frac{g}{\rho_0}\left(\rho_e(z)\mathcal{Q}(z) - \mathcal{Q}_m(z)\right) \tag{4.67}$$

Thus we have the same relation for its DNS estimation.

$$\mathcal{B}^{DNS}(z) = \frac{g}{\rho_0}\left(\rho_e^{DNS}(z)\mathcal{Q}^{DNS}(z) - \mathcal{Q}_m^{DNS}(z)\right) \tag{4.68}$$

with ρ_0 the reference density, chosen equal to density of fresh air in this study.

4.5.3 Parameter identification for Top-hat and Gaussian profiles

Previous post-processing methods are all based on Gaussian profiles. In order to compare DNS estimated Gaussian characteristic parameters with that used in turbulent jet models, we shall transfer the obtained Gaussian parameters to that under Top-hat assumption, by identification of characteristic jet quantities used in the model.

We first summarise in table 4.7, expressions of characteristic jet quantities, defined in different models, both in Top-hat and Gaussian profiles.

Profile assumption	Top-hat	Gaussian
Volume flux $\mathcal{Q}(z)$	$\pi w_T b_T^2$	$\pi w_G b_G^2$
Momentum flux $\mathcal{M}(z)$	$\pi w_T^2 b_T^2$	$\frac{1}{2}\pi w_G^2 b_G^2$
Buoyancy flux $\mathcal{B}(z)$	$\pi w_T b_T^2 \frac{\rho_e-\rho_T}{\rho_0} g$	$\frac{\lambda^2}{\lambda^2+1}\pi w_G b_G^2 \frac{\rho_e-\rho_G}{\rho_0} g$
Mass flux $\mathcal{Q}_m(z)$	$\pi \rho_T w_T b_T^2$	$\pi w_G b_G^2 \frac{\rho_e+\lambda^2\rho_G}{1+\lambda^2}$
Mass momentum flux $\mathcal{M}_m(z)$	$\pi \rho_T w_T^2 b_T^2$	$\frac{1}{2}\pi w_G^2 b_G^2 \frac{\rho_e+2\lambda^2\rho_G}{1+2\lambda^2}$

Table 4.7: Expressions of characteristic jet quantities under Top-hat and Gaussian profiles assumptions

Boussinesq model of Morton et al. (1956)

In Boussinesq model of Morton et al. (1956) (α-constant), by identification of three characteristic quantities $\mathcal{Q}$, $\mathcal{M}$ and $\mathcal{B}$, we have

$$b_T = \sqrt{2} b_G, \quad w_T = \frac{1}{2} w_G, \quad \rho_T = \frac{\rho_e + \lambda^2 \rho_G}{1+\lambda^2} \tag{4.69}$$

This solution is also compatible with identification of mass flux $\mathcal{Q}_m$.

Non-Boussinesq model of Rooney and Linden (1996)

In non-Boussinesq model of Rooney and Linden (1996) (α-constant), by identification of three characteristic quantities $\mathcal{Q}$, $\mathcal{Q}_m$ and $\mathcal{M}_m$, we have

$$b_T = \sqrt{2} b_G \sqrt{\frac{(2\lambda^2+1)(\rho_e+\lambda^2\rho_G)}{(\lambda^2+1)(\rho_e+2\lambda^2\rho_G)}}, \quad w_T = \frac{1}{2} w_G \frac{(\lambda^2+1)(\rho_e+2\lambda^2\rho_G)}{(2\lambda^2+1)(\rho_e+\lambda^2\rho_G)}, \quad \rho_T = \frac{\rho_e+\lambda^2\rho_G}{1+\lambda^2} \tag{4.70}$$

This solution is also compatible with identification of buoyancy flux $\mathcal{B}$.

Based on these relations, DNS estimated Top-hat parameters can be estimated, noted b_T^{DNS}, w_T^{DNS}, ρ_T^{DNS} corresponding to jet radius, vertical velocity and mixture density. These Top-hat parameters are calculated from b_G^{DNS}, w_G^{DNS}, ρ_e^{DNS}, ρ_G^{DNS} and λ^{DNS} parameters directly obtained from DNS results. However,we note that the result is identical for ρ_T in both models.

Characteristic Top-hat volume fraction in the jet

Particularly, instead of mixture density, the volume fraction of injected light gas, helium or hydrogen, will be used in results analysis as this parameter is directly linked to the safety analysis. The 1D characteristic volume fraction profile $X_{1,T}^{DNS}(z)$ is directly deduced from Top-hat mixture density $\rho_T^{DNS}(z)$:

$$X_{1,T}^{DNS}(z) = \frac{\rho_T^{DNS}(z) - \rho_a}{\rho_{inj} - \rho_a} \tag{4.71}$$

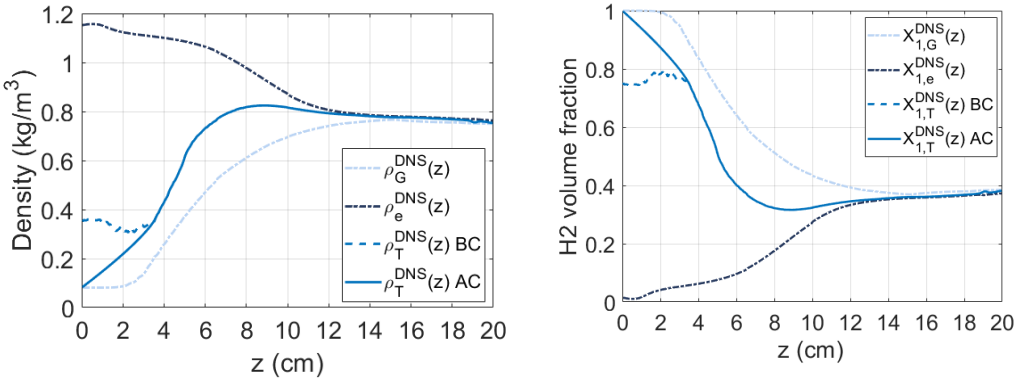

Figure 4.10: Environmental density $\rho_e^{DNS}(z)$, jet centre density ρ_G^{DNS} and Top-hat characteristic density $\rho_T^{DNS}(z)$ before (BC) and after (AC) correction, as well as corresponding volume fraction profiles, for hydrogen case

For example, in figure 4.10, we present the environmental density $\rho_e^{DNS}(z)$, jet centre density ρ_G^{DNS} and Top-hat characteristic density $\rho_T^{DNS}(z)$ (with indication BC), as well as corresponding volume fraction profiles, for hydrogen case. We could clearly identify that:

- Environmental fraction $X_{1,e}^{DNS}(z)$ can be used to investigate far-field variation along the jet
- Jet centre fraction $X_{1,G}^{DNS}(z)$ represents the maximum concentration at a given altitude, used to evaluate jet evolution
- Top-hat characteristic volume fraction $X_{1,T}^{DNS}(z)$ (with indication BC) is between environmental fraction and jet centre fraction, presenting the mean concentration in the jet region. Note that this profile is not representative near the injection area, typically for $z < 3$cm here for hydrogen case (for helium $z < 4$cm), where $X_{1,T} \approx 1$. We replace its value in this region by $\mathcal{Q}_m^{DNS}(z)/\mathcal{Q}^{DNS}(z)$. The corrected results are presented in figure 4.10 in solid lines with indication AC.

Besides, in the region where vertical position z larger than 14cm, all these 3 profiles superpose, which illustrate the existence of homogeneous layer in the top part of the cavity.

4.5.4 Entrainment velocity and entrainment coefficient

In this section, we aim at calculating the entrainment velocity and deducing the entrainment coefficient from DNS result. The entrainment assumption is defined differently in Boussinesq models and in non-Boussinesq models. The entrainment velocity, noted $u_e(z)$, is linked to the **specific entrainment characteristic vertical velocity** $w_c(z)$:

$$u_e(z) = \begin{cases} \alpha w_c(z), & \text{for Boussinesq case} \\ \alpha w_c(z)\sqrt{\frac{\rho_c(z)}{\rho_0}}, & \text{for non−Boussinesq case} \end{cases} \tag{4.72}$$

with $\rho_c(z)$ the **specific entrainment characteristic mixture density** of the jet. The choice of $w_c(z)$ and $\rho_c(z)$ are depended on the profiles of $w(r,z)$ and $\rho(r,z)$.

The value of α depends on the selected Top-hat or Gaussian profile assumption. We note α_T if this one is calculated under Top-hat assumption and α_G for Gaussian assumption.

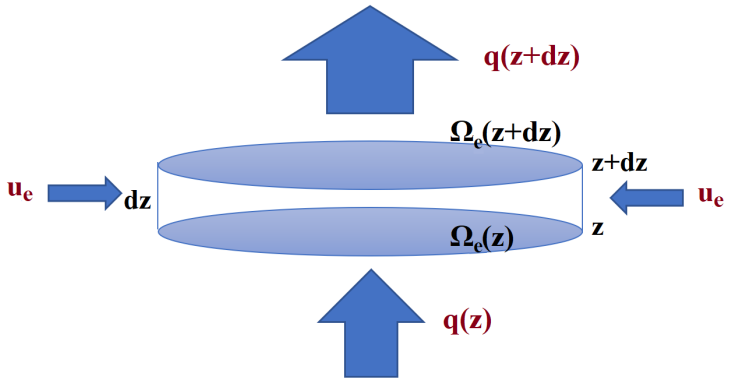

Figure 4.11: Conservation of volume flux of a control body with radius $\sqrt{2}b_G(z)$, definition of mean entrainment velocity

Entrainment coefficient profile under Gaussian assumption

Under Top-hat assumption, the entrainment velocity can be estimated from the boundary condition

$$-(ru)|_\infty = -(ru)|_{b_T} = b_T u_e \tag{4.73}$$

If profiles are assumed in Gaussian, by using relation (4.69), the above boundary condition can be rewritten as

$$-(ru)|_\infty = (\sqrt{2}b_G)u_e \tag{4.74}$$

Then we consider a thin layer of the jet cross-section as the control body with its radius $\sqrt{2}b_G$ and thickness dz, at altitude z, we apply the conservation of volume flux on this layer. The vertical volume flux through this specific control body is written as $q(z)$. Thus

$$q(z+dz) - q(z) = u_e(z)\, L_e(z)\, dz \tag{4.75}$$

with $L_e(z)$ the perimeter of the control body cross-section. This conservation of volume flux is illustrated in figure 4.11. Thus

$$\left.\frac{dq}{dz}\right|_z = u_e(z)\, L_e(z) \tag{4.76}$$

Consequently, for calculating entrainment velocity from DNS results, note that

$$w(r = \sqrt{2}b_G, z) = \frac{w_G}{e^2} \tag{4.77}$$

we firstly define a control area for cross-section plane at altitude z, corresponding to 2σ region

$$\Omega_e = \left\{(x,y)\,|\,\overline{w(x,y,z)} \geq \frac{1}{e^2} w_G^{DNS}(z)\right\} \tag{4.78}$$

Then we calculate the perimeter of this area $\Omega_e(z)$, noted $L_e^{DNS}(z)$. From figure 4.9, the $\Omega_e(z)$ is always a connected area so that its perimeter is well defined. Then the volume flux through $\Omega_e(z)$ is calculated as

$$q^{DNS}(z) = \sum_{(x,y,z)\in\Omega_e(z)} \overline{w(x,y,z)} dS(x,y,z) \tag{4.79}$$

The DNS estimated **mean entrainment velocity** is defined by applying the relation (4.76)

$$u_e^{DNS}(z) = \frac{1}{L_e^{DNS}(z)} \left.\frac{dq^{DNS}}{dz}\right|_z \tag{4.80}$$

The derivation operation requires smooth and derivable condition for $q^{DNS}(z)$. This quantity is calculated vertically cell by cell, with height discretisation chosen equal to vertical cell size. Its profile shall be smoothed in advance then derivation will be calculated in 4^{th} order. The smoothing process is based on the theory of least squares method presented in Savitzky and Golay (1964) and Press et al. (2007). Two parameters shall be provided in this algorithm, the window length N_W (must be an odd number) and degree (usually 2 or 3). A quick parameter test shows that $N_W = 15$ with degree 2 could provide the enough smooth results.

Once we have a smooth profile of $u_e^{DNS}(z)$ the entrainment coefficient can be determined from its definition.

Boussinesq case

Under Boussinesq approximation, the specific entrainment characteristic vertical velocity is chosen simply as

$$w_c = \begin{cases} w_T, & \text{for Top–hat profiles} \\ w_G, & \text{for Gaussian profiles} \end{cases} \tag{4.81}$$

Thus under Gaussian assumption, the entrainment coefficient estimated by DNS results will be

$$\alpha_G^{DNS-B}(z) = \frac{u_e^{DNS}(z)}{w_G^{DNS}(z)} \tag{4.82}$$

Note that in Boussinesq case, we have

$$b_T w_T = \frac{\sqrt{2}}{2} b_G w_G \tag{4.83}$$

Thus, by applying the identification of $\frac{dQ}{dz}$ in equation (A.15) in model demonstration, we have $\alpha_T = \sqrt{2}\alpha_G$.

Non-Boussinesq case

For non-Boussinesq cases, the specific entrainment characteristic density $\rho_c(z)$ has to be chosen correctly to ensure the relation $\alpha_T = \sqrt{2}\alpha_G$. Applying the identification of $\frac{dQ_m}{dz}$ in equation (2.58), we have

$$b_T w_T \sqrt{\rho_{c,T}} = \frac{\sqrt{2}}{2} b_G w_G \sqrt{\rho_{c,G}} \tag{4.84}$$

with $\rho_{c,T}, \rho_{c,G}$ the specific entrainment characteristic density under Top-hat and Gaussian assumptions. Thus, by using equitation (4.70), we apply

$$\rho_c = \begin{cases} \rho_T, & \text{for Top–hat profiles} \\ \frac{\rho_e + 2\lambda^2 \rho_G}{1+2\lambda^2}, & \text{for Gaussian profiles} \end{cases} \tag{4.85}$$

Consequently, the entrainment coefficient estimated by DNS results will be

$$\alpha_G^{DNS-NB}(z) = \frac{u_e^{DNS}(z)}{w_G^{DNS}(z)} \sqrt{\frac{\rho_a \left(1 + 2\lambda^{DNS^2}(z)\right)}{\rho_e^{DNS}(z) + 2\lambda^{DNS^2}(z)\rho_G^{DNS}(z)}} \tag{4.86}$$

with the reference density chosen as the density of fresh air $\rho_0 = \rho_a$.

Relation with Top-hat entrainment coefficient

Note that both $\alpha_G^{DNS-B}(z)$ and $\alpha_G^{DNS-NB}(z)$ are under Gaussian assumption. By using relation between α_T and α_G, the DNS estimated Top-hat entrainment coefficient is deduced

$$\alpha_T^{DNS}(z) = \sqrt{2}\alpha_G^{DNS}(z) \tag{4.87}$$

with $\alpha_G^{DNS}(z) = \alpha_G^{DNS-B}(z)$ for Boussinesq case or $\alpha_G^{DNS}(z) = \alpha_G^{DNS-NB}(z)$ for non-Boussinesq case.

4.6 Experimental setup and post-processing

In this section, we present briefly the experimental setup, facilities build-up and data treatment method. The principal idea is to measure a series of instantaneous velocity field by Particle Image Velocimetry (PIV) method. Statistical quantities as mean or RMS, are calculated from instantaneous measurements. Helium is used as the injected gas due to safety consideration. We shall particularly note that only on-plane velocity field are measured as we carried out a 2D2C (2 dimensions, 2 components) approach with only one camera operated. The velocity component perpendicular to the measured plane as well as the helium concentration are not able to be measured in this experiment.

4.6.1 Experimental facilities and process

Particle Image Velocimetry (PIV) is a measurement technique of velocity field. The flow is seeded with tracer particles, consistently moving with the flow velocity, which are illuminated by a high-frequency laser sheet. The position of the tracers, as well as the flow pattern, will be recorded by a CCD PIV camera through the light scattered by these particles. The camera records two consecutive snapshots for one measurement. The time lag between both shots and laser impulsions is small enough so that the displacement of each particle can be identified from the photo.

The experimental facilities used in this experiment consists of a cavity, a camera and a laser emitter. All of these are positioned in a T-form base, placed in a dark closed room.

The cavity used in this PIV measurement is in the same geometry as defined in numerical configuration. The cavity, presented in figure 4.12, is made by PMMA (methyl meth-acrylate resin), or called Plexiglas. This material is qualified by its good transparency and often used as a lightweight or shatter-resistant alternative to glass. A C-form shell frame consists of three non-transparent plates ($z = 0$ and $20cm, y = +5cm$), providing the stability of this structure. Another three side faces of the cavity are transparent, fixed by screws and adhesive on the frame. The two vents are created by a short plate, leaving an inter-space 1cm each in the top and bottom ends on the side $x = +5cm$. The thickness of Plexiglas plate is 0.5cm. The underside of the cavity is drilled in its centre with a well-polished round hole of 1cm diameter, connecting with a 20cm long vertical injection tube to ensure a well-established Poiseuille injection flow.

The laser used for this PIV experiment is a pulsed double cavity Yag laser (8ns - 200mJ). Optics are used to transform the laser beam into a laser plane, which allows a 2D measure inside the whole cavity. Laser optics are set to ensure that the laser sheet focuses inside the cavity in order to obtain a sheet thickness less than 1mm, reducing the detection of axial displacement of tracers and thus improves the quality of the 2D measures.

The camera used to record the pictures focused on the observation plane. Two pictures are taken within a very short time (0.1 or 0.5ms). By comparing positions of tracers on the 2 consecutive photos, the instantaneous velocity field on the plane will be deduced. The orthogonality between camera axis and laser direction is assured by the rail-base on which experimental facilities are fixed, see figure 4.12. The laser is free to move along the rail, so we can change the measurement plane coordinates and observe different planes inside the cavity.

The helium is stocked in room temperature. Its flux is controlled by a valve (pressure-regulator) connected to a computer where we indicate the requisite flux in normal conditions (12 NL/min), the flux will be automatically corrected by measurement of room temperature to ensure a correct injected mass flux.

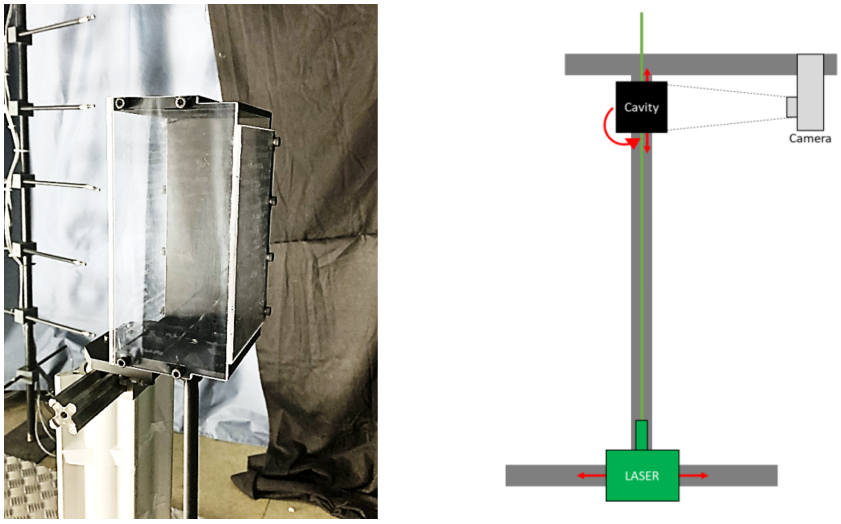

Figure 4.12: Experimental facility, left: the cavity, right: sketch of laser emitter, cavity and camera, on a T-form base

Two kinds of tracer are used in this measurement. In the injection flux, an oil-based tracer is added. The quantity of tracer is regulated to adjust the visibility of the photo. In addition, smoke is generated in the experimental room, in order to capture the flow of inlet ambient air.

The observation plane is fixed on the mid-plane $y = 0$. At initial time, pure helium is continuously injected into the cavity. Then we wait 10 minutes time to ensure a steady state flow is well established in the cavity before the measurement begins. At each time, the camera will take two consecutive photos within a fixed time lag, noted Δt, equals to 0.1ms and 0.5ms for two independent measurements. The observation interval between two measures are fixed as 1 second. For each Δt, we have taken 1000 measures (thus 2000 photos) for further treatment.

4.6.2 First-step post-processing

The first-step post-processing is done by using the software gpiv and DaVis. This step of work is realised in the context of an internship realised in spring 2020 in CEA. The objective is to transform the photos taken from experiments to instantaneous 2D velocity fields on the measure plane.

Before the post-processing, it is necessary to delete the environment noise and unnecessary area, see figure 4.13 for example, flow in the area outside the cavity is not kept in further treatment in this study.

Then the velocity calibration is realised by analysing the local tracer displacement in the corresponding interrogation window scale, chosen as non-overlapped squares 32x32 pixels in this study. The velocity is calibrated by the displacement of tracer point in each interrogation window during the fixed time lag Δt between two consecutive photos. The quality of this calibration depends on the time lag Δt applied in the measurement. See figure 4.14 for example, on the left-hand side, the case $\Delta t = 0.1ms$, local velocity can be calibrated almost everywhere in the cavity but in low precision. On the right-hand side, the case $\Delta t = 0.5ms$, the calibration quality is better for top area typically $z > 10cm$. However, velocity in region of jet centre (coloured in rose) is not correctly calibrated due to high local velocity. The displacement of local tracer in this region is not in the same interrogation window during Δt. Note that this rose region differs on each pair of photos. In the software, the deleting criteria is defined

Figure 4.13: Example of a photo taken in the PIV measurement, in inverted colour (black turns to white and vice versa), 1 pixel equals to 0.082mm. Black points indicate the positions of tracers, which are almost uniformly distributed in the whole cavity.

as local correlation index inferior to 0.7 or peak ratio less than 3. Besides, a median filter is also applied. We remove and replace the local velocity if this one is outside its 2-σ interval (95% confidence interval) which is defined by 2 times of standard deviation calculated from its neighbours.

An auto-correlation verification based on velocity temporal variations at a series of monitoring points is also carried out to ensure the non-dependency of each measurement (observation interval 1s).

4.6.3 Statistical quantities and its accuracies

Statistical quantities of time-averaged mean values and RMS are defined the same as presented in section 4.4.4 (equations (4.30) and (4.31)) with observation interval $\delta t = 1s$ and duration of observation $t_{end} - t_{start} = 1000s$. The accuracy of these statistical quantities consists of the system error related to the precision of camera and the statistical error.

For time-averaged field $\overline{\varphi}$ (a component of the plane velocity), the system error is far less than its statistical error as the camera could capture the displacement up to 0.1-0.2 pixel. Total error will be linked to its statistic accuracy only.

- Upper 95% limit = $\overline{\varphi} + 1.96\frac{\mathrm{RMS}(\varphi)}{\sqrt{\mathcal{N}}}$
- Lower 95% limit = $\overline{\varphi} - 1.96\frac{\mathrm{RMS}(\varphi)}{\sqrt{\mathcal{N}}}$

with number of independent samples $\mathcal{N} = 1000$.

For RMS field RMS(φ), its system error Δv is linked to camera precision which could be considered independent on local velocity. It corresponds to the minimum displacement (0.1-0.2 pixel) that camera is able to capture during the measure time lag Δt:

$$\Delta v = \frac{(0.1 \sim 0.2 \text{ pixel}) \times (0.082\ mm/\text{pixel})}{\Delta t} \tag{4.88}$$

It is around 2 cm/s for $\Delta t = 0.1ms$ and 10 cm/s for $\Delta t = 0.5ms$. Consequently,

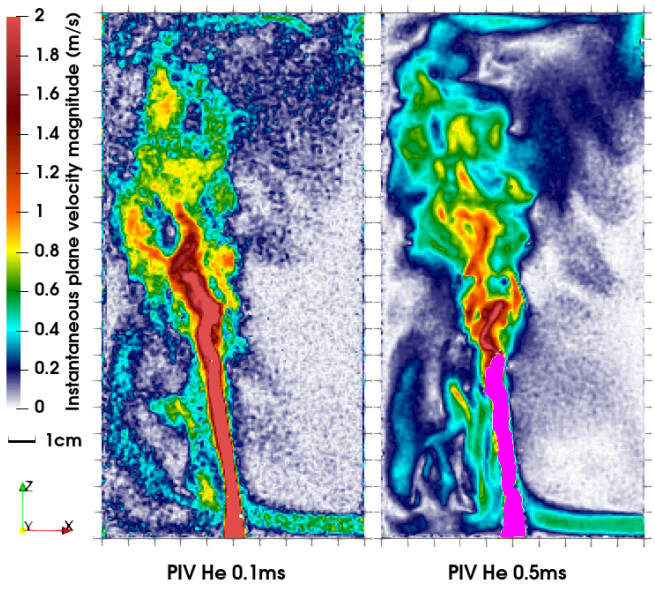

Figure 4.14: Instantaneous plane velocity magnitude calibrated by software, for $\Delta t = 0.1ms$ (left) and $\Delta t = 0.5ms$ (right), corresponding to different moments in the observation. Local velocity in the jet-centre region for $\Delta t = 0.5ms$ (in rose colour) is not able to be calibrated due to high local velocity. the calibration quality of $\Delta t = 0.5ms$ is better than $\Delta t = 0.1ms$.

- Upper 95% limit = $\mathrm{RMS}(\varphi) \times \sqrt{\frac{\mathcal{N}}{\mathrm{CHIINV}(0.975,\mathcal{N})}} + \Delta v$

- Lower 95% limit = $\mathrm{RMS}(\varphi) \times \sqrt{\frac{\mathcal{N}}{\mathrm{CHIINV}(0.025,\mathcal{N})}} - \Delta v$

where the function $\mathrm{CHIINV}(p, n)$ returns the inverse of the right-tailed probability of the chi-squared distribution with probability p and number of degrees of freedom n.

4.6.4 Integration of statistical results of two measurements

Two separate series of measurements with different time lag $\Delta t = 0.1$ or 0.5ms are realised in this experience. The case $\Delta t = 0.5$ms provides a more precise velocity field in the majority area, see figure 4.14. However, the jet centre region, where local velocity is typically superior to 1.5m/s could not be correctly captured. This region, which varies in time, will be removed in the statistical operation. Thus we need a smaller capture time lag $\Delta t = 0.1$ms to provide jet region velocity. In figure 4.15, we compare the statistical time-averaged plane velocity for 0.5ms case and 0.1ms. Both of them are in the same form, demonstrating the convergence of this measurement. The jet centre region is not correctly measured for 0.5ms case (but not equal to zero as the uncapturable region changes with time). Then we seek to integrate these two results into a precise and complete field.

The instantaneous uncapturable region of 0.5ms case is generally situated in the centre, below the altitude $z = 8$cm. Thus, we consider the 0.5ms result is valid for all area beyond this level. In the jet region, the validity region of 0.5ms result should benchmark by 0.1ms result. For a fixed horizontal level, from the jet centre to two ends, we take first interaction points between two profiles 0.1ms and 0.5ms as the intersection point of the validity domain of 0.5ms case. The 0.1ms result will be considered only within this interval. From figure 4.14 (d)-(g), we can easily identify the coincided region of two measurements in the far field of the jet. For example, for (f) where $z = 6$cm, the integrated profile takes 0.1ms result from

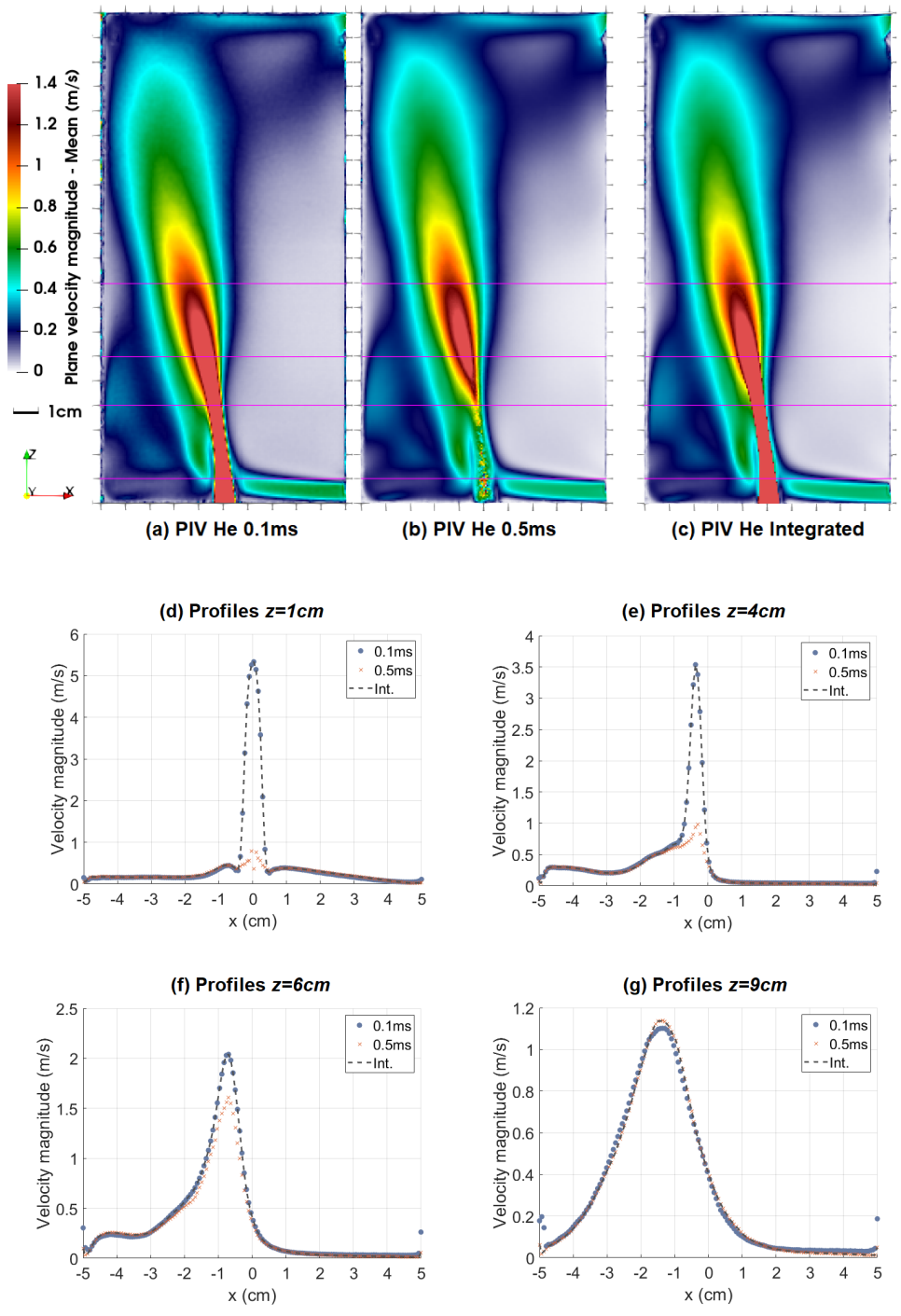

Figure 4.15: Results comparison of time-averaged plane velocity magnitude for PIV measurement time lag (a) Δt =0.1ms and (b) Δt =0.5ms as well as (c) the integrated results. Horizontal profiles for (d) z = 1cm, (e) z = 4cm, (f) z =6cm and (g) z = 9cm.

$x = -2.2$cm to $x = 0$ where two profiles across. In figure 4.14 (c), we present the integrated time-averaged plane velocity magnitude. Similar process will be done for other statistical quantities. Integrated statistical quantities will be compared with that calculated by DNS to validate the numerical approach.

4.7 Summary

In this chapter, we have presented the principal methodology applied in this study, mainly consisting of

- Geometrical, physical and numerical configurations
- Experimental setup and data treatment
- Method to determine the accuracies of statistical quantities from numerical simulation and experimental measurements
- Numerical 1D post-processing methodology to calculate 1D characteristic jet quantities from 3D DNS results

The accuracies of statistical quantities consist of that related to mesh convergence or camera precision as well as that related to uncorrelated samples. A conservative estimation is performed for DNS as GCI is directly used to characterise numerical error and numbers of uncorrelated samples are underestimated.

1D characteristic jet quantities are calculated by integration on DNS fields. A theoretical correction is conducted to associate Gaussian quantities with their corresponding Top-hat formulations.

We will present in the next chapter the DNS simulation results and their comparisons with experimental measurements.

Part III

Simulation results

Chapter 5

DNS results analysis and experimental comparisons

In this chapter, we present the DNS simulation results and their comparisons with PIV experimental measurements. The analysis is divided into three parts. Firstly, we focus on the flow structure. Specifically we compare the 3D time-averaged velocity field with that presented in the model of Linden et al. (1990) that illustrates the formation of bi-layer distribution. Secondly, we compare the DNS statistical velocity quantities, the time-averaged and the RMS, on the mid-plane $y = 0$ with that obtained by experimental measurements. We seek to validate the DNS jet flow in this step. Thirdly, we compare the two simulation cases (helium and hydrogen), to evaluate if helium could be treated as a substitutive gas in hydrogen safety analysis. We particularly focus on their concentration (volume fraction) distribution, as well as the inclination of the jet axis.

5.1 DNS flow analysis

5.1.1 Global turbulent flow

We first aim at analysing the global flow structure in the main cavity. Simulation results show that the flow in the cavity is highly turbulent almost everywhere, see figure 5.1 as an illustration for general flow pattern. On the left-hand side, an instantaneous flow field is displayed for the helium case where turbulent eddies are shown using Q-criterion. On the right-hand side, we present instantaneous 2D velocity magnitude on the mid-plane $y = 0$.

A light gas jet is injected from the cavity floor. Turbulent flow structures are developed around the jet in the lower part of the cavity then inside the jet in the upper part. In the lower cavity, jet entrainment generates the inlet flow of fresh air through the bottom opening. Inlet fresh air passes the injection flow and reaches to the back-end of the cavity, changing its direction to vertical and finally entering into the jet. This cross-flow contributes to the jet inclination towards x-negative direction. A recirculation zone is formed between the opposite wall to the openings and the jet. The rising jet passes through fluid layers with different densities while a quasi-homogeneous layer appears started from the middle height of the cavity. The helium jet reaches a higher altitude than hydrogen jet, showing the difference of injection momentum due to their density difference.

In figure 5.2, we present the distribution of turbulent kinetic energy as well as the term $\overline{\rho' w'}$ on the mid-plane $y = 0$ in the cavity. Local turbulent kinetic energy is maximal inside the buoyant jet. Large fluctuations are observed, (i) almost everywhere in the upper 1/3 height

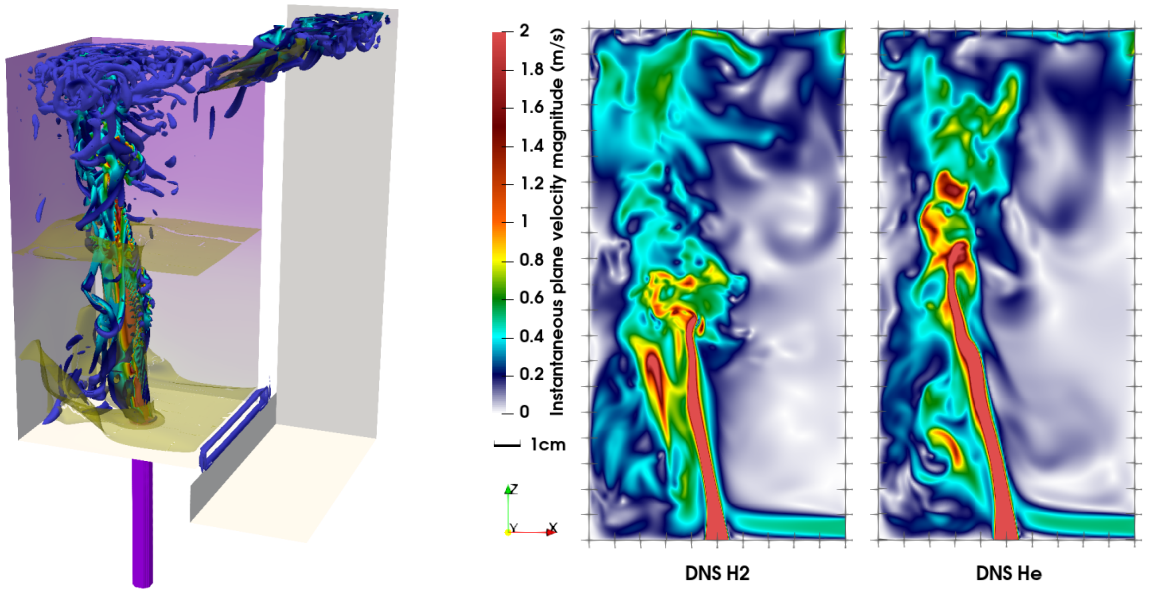

Figure 5.1: Instantaneous flow in the main cavity, Left: iso-contour of Q-criterion equal to 2000 (coloured with vertical velocity), with two iso-contours of volume fraction inlet fresh air ($X_1 = 0$) and bi-layer interface ($X_1 = 0.25$) in light yellow. Here the Q-criterion is defined as $Q = \frac{1}{2}\left(\|\Omega\|^2 - \|S\|^2\right)$ with Ω the local vorticity tensor and S the strain rate tensor and $\|\cdot\|$ is the norm defined by $\|T\| = T_{ij}T_{ji}$. Background colour indicates time-averaged volume fraction distribution close to walls. Helium case. Right: Instantaneous 2D velocity magnitude $\sqrt{u^2+w^2}$ on mid-plane $y = 0$, for hydrogen and helium cases

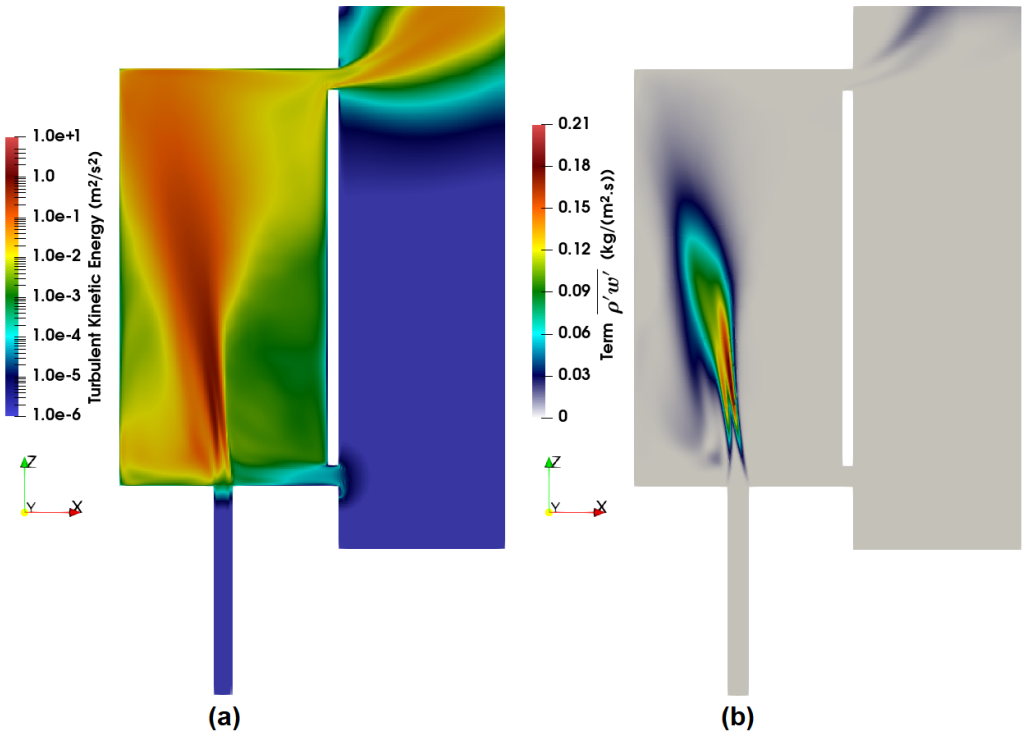

Figure 5.2: Distribution of (a) turbulent kinetic energy $E_{kt} = \frac{1}{2}\left(\overline{u'u'} + \overline{v'v'} + \overline{w'w'}\right)$, (b) the term $\overline{\rho' w'}$ on the mid-plane y =0. Helium case.

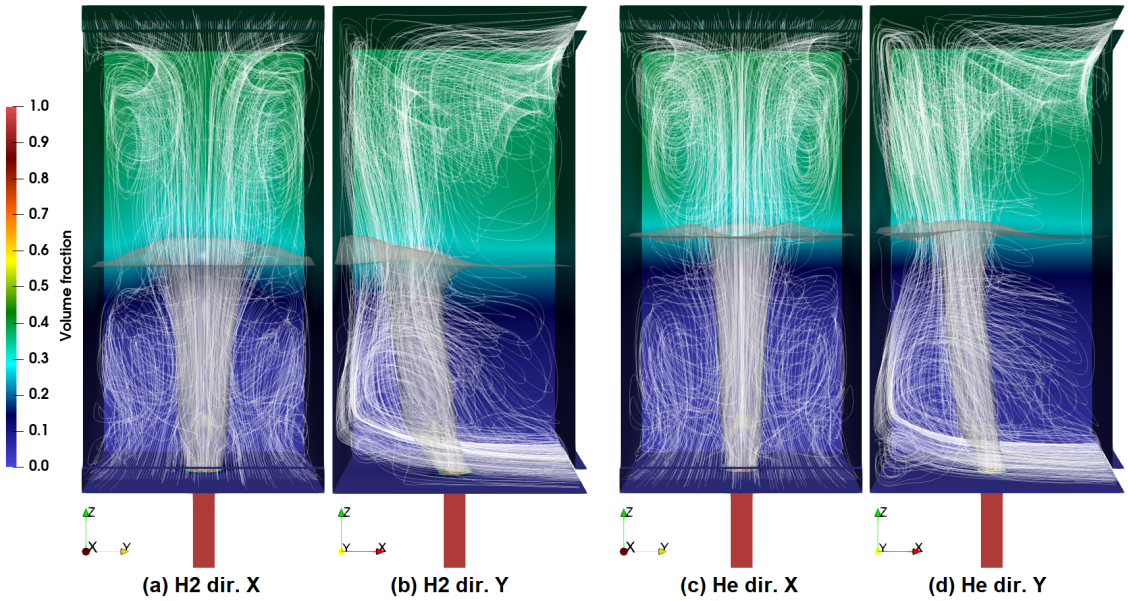

Figure 5.3: "Streamlines" of time-averaged flow in the main cavity for (a)-(b) hydrogen case and (c)-(d) helium case, background coloured by time-averaged volume fraction, iso-contour of volume fraction equal to 25%. Views from $x+$ to $x-$ direction for (a) and (c) on $x = 5$cm and from $y-$ to $y+$ direction for (b) and (d) on $y = -5$cm. The number of tracers released is proportional to volume flux through these faces.

of the cavity, and (ii) at lower height, in the recirculation zone in x-negative direction outside the jet. Fresh air enters into the cavity through the bottom opening by aspiration affect in a laminar regime. Besides, the term $\overline{\rho' w'}$, representing the mixing turbulent flow, is maximal at jet border in the lower middle part of the cavity.

In summary, the flow is mainly turbulent in the main cavity. Therefore, in order to compare with the flow structure assumed in model of Linden et al. (1990), we shall consider analysing the well-converged time-averaged fields.

5.1.2 Three-layer flow structure in quasi-steady state

In order to verify the existence of bi-layer flow structure assumed in the model of Linden et al. (1990), where an impenetrable interface is formed between two layers except for the jet region, we draw the "streamlines" on the time-averaged velocity field, as presented in figure 5.3. Technically, these lines cannot be called streamlines as the time-averaged velocity field is based on statistical operation and does not represent the flow structure at any time. Nevertheless, these "streamlines" describe, in statistical sense, the steady flow pattern and illustrate the formation of bi-layer distribution.

We can easily identify the aspiration of fresh air through the bottom opening, the recirculation zone in the volume opposite the inlet flow, and the entrainment effect pushing the fluid at exterior of the jet entering into the jet. The rising jet arrives at the ceiling of the cavity, generating toric flow in each side of the upper cavity. Below this toric flow, a small velocity zone is formed far away from the jet. This zone divides the cavity into two parts, and corresponds to a fluid layer in which mixture density varies with altitude. Below the interface, we have a mixture near fresh air. Above the interface, the mixture density is uniformly distributed.

The flow pattern outside the jet therefore corresponds to a bi-layer configuration. We note L_A the lower layer and L_H the upper homogeneous layer. We introduce a third layer, which could

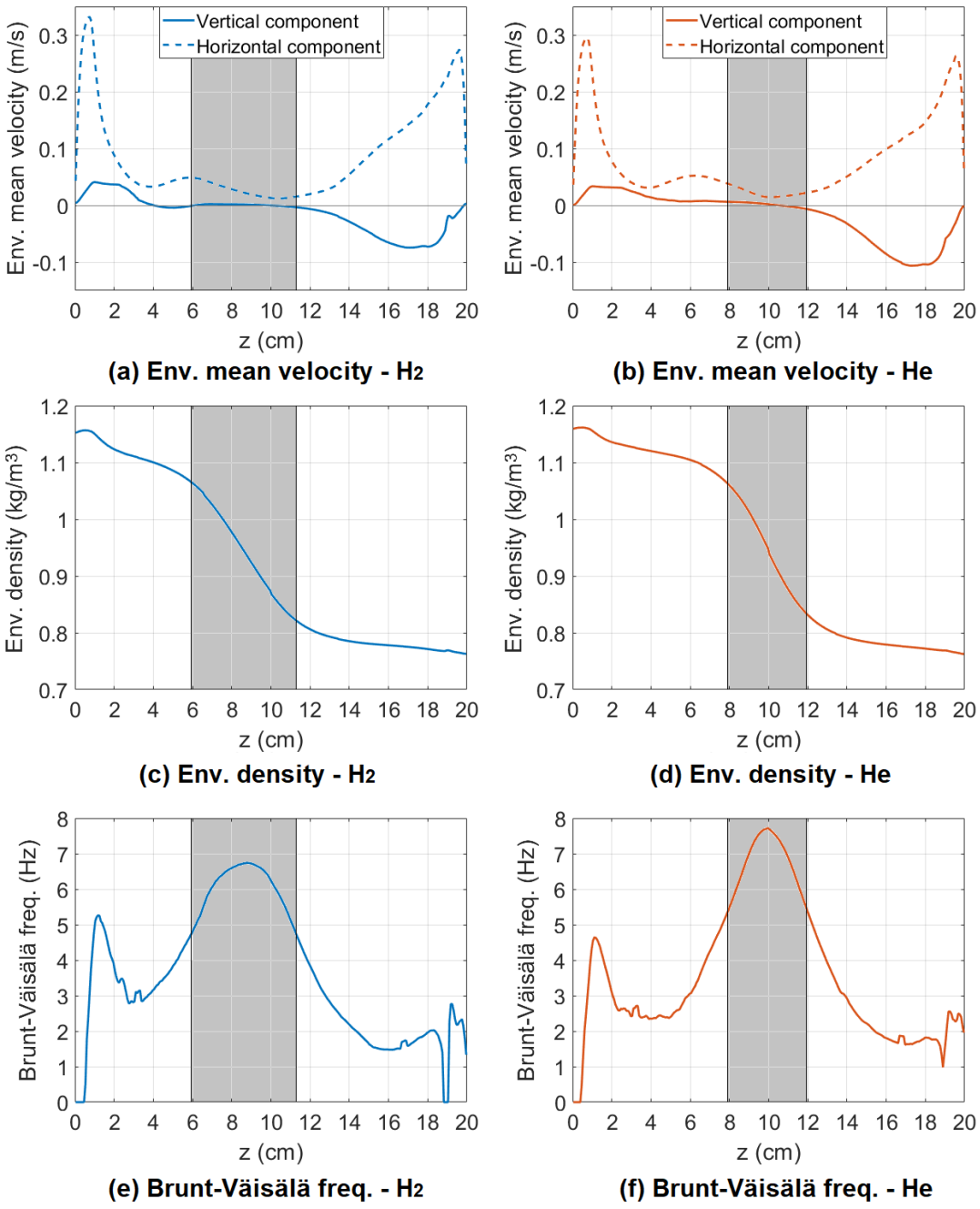

Figure 5.4: Velocity and density vertical distribution of the environment flow outside the jet. (a)(b) evaluation of vertical and horizontal components of environment mean velocity outside of jet region, (c)(d) variation of environmental density, (e)(f) deduced Brunt-Vaisala buoyancy frequency variation in the cavity. Hydrogen case (a)(c)(e), helium case (b)(d)(f). Stratified layers L_S are coloured in grey. Environmental mean velocity and density are calculated from far-field region, cf. eq. (4.38) and (4.39).

be considered as the "interface" in which the fluid is stratified. This layer is called stratified layer and noted L_S.

In order to evaluate the flow at exterior of the jet, called also the jet "environment", we consider applying the methodology presented in section 4.5 about definition of jet region as in equation (4.38). In figure 5.4-(a)(b), we present the variation of horizontal and vertical components of environmental mean velocity, defined as their mean values on the complementary of the jet region. We note that L_S is well impenetrable as the environmental mean vertical velocity is nearly zero.

Besides, a quasi-linear density stratification is presented in L_S, as shown in figure 5.4-(c)(d). We can thus estimate the Brunt-Vaisala frequency in this layer which corresponds to the frequency of the gravity wave. This frequency is defined as

$$N = \sqrt{-\frac{g}{\rho_0}\frac{d\rho_e}{dz}} \tag{5.1}$$

with ρ_0 the density reference, chosen as the density of fresh air. As shown in figure 5.4-(e)(f), buoyancy frequency reaches its maximum in the middle of this layer, at around $z = 9$cm for hydrogen case and $z = 10$cm for helium case. This maximum frequency is used to define the vertical extension of L_S and to determine the heights of two interfaces.

We take the 70% of the maximum buoyancy frequency as the criteria of the extension of stratified layer L_S. This choice will make the vertical component of environmental mean velocity achieves the same absolute value at two interfaces. In table 5.1, we present the method and results to determinate two interfaces z_{AS} between L_A and L_S and z_{SH} between L_S and L_H. Hydrogen case possesses larger stratified layer and a little larger homogeneous layer as well. The change of environmental density is sharper in helium stratified layer. This characteristic frequency can be captured in the spectrum analysis for vertical velocity at local monitoring point situated at the far field of the jet (figure 5.5). In the middle of the stratified layer, the peak of PSD corresponds to a frequency around 8Hz, close to the maximum Brunt-Vaisala frequency.

This three-layer quasi-steady flow structure is summarised in figure 5.6 on the right-hand side, and compared with original Linden's bi-layer structure on the left. Generally, the time-averaged flow structure obtained by DNS simulation is very close to that analysed in Linden's model. The main difference is the existence of a stratified layer between top homogeneous layer and lower quasi-fresh air. All vertical flow passing through this stratified layer is located in the jet region. In Linden's bi-layer model, this stratified layer is simplified into one interface. Besides, no-symmetrical flow structure in y-direction is observed for our case, due to the same-side openings configuration, which are not as assumed as in the original Linden's analysis (horizontal openings).

5.1.3 Jet evolution

In this section, we consider the part of the jet flow and its vertical evolution. The jet flow is characterised by a series of jet quantities defined in the jet theories as presented in section 2.2. The procedure to calculate these 1D quantities from the fully 3D DNS results is presented in section 4.5. The analysis will be useful for the chapter 6 where we evaluate the reliability of the jet theories in our configuration regarding the DNS results. In figure 5.7, we present the vertical evolution of 5 jet quantities and 3 jet parameters, obtained separately by 1D post-processing procedures both for helium and hydrogen cases.

In figures (a) and (b), we present respectively the variations of jet volume flux $\mathcal{Q}^{DNS}(z)$ and mass flux $\mathcal{Q}_m^{DNS}(z)$. We note firstly at injection $z = 0$, same volume flux is imposed for two

	DNS Hydrogen	DNS Helium
Altitude of max. $N(z)$	8.75 cm	9.90 cm
Corresponding max. N	6.74 Hz	7.72 Hz
70% max. N	4.72 Hz	5.40 Hz
Interface z_{AS}	**5.9 cm**	**7.9 cm**
Mean env. vertical velocity at interface z_{AS}	0.116 cm/s	0.615 cm/s
Interface z_{SH}	**11.3 cm**	**11.9 cm**
Mean env. vertical velocity at interface z_{SH}	-0.116 cm/s	-0.615 cm/s

Table 5.1: Determination of three-layer interfaces: z_{AS} between L_A and L_S and z_{SH} between L_S and L_H.

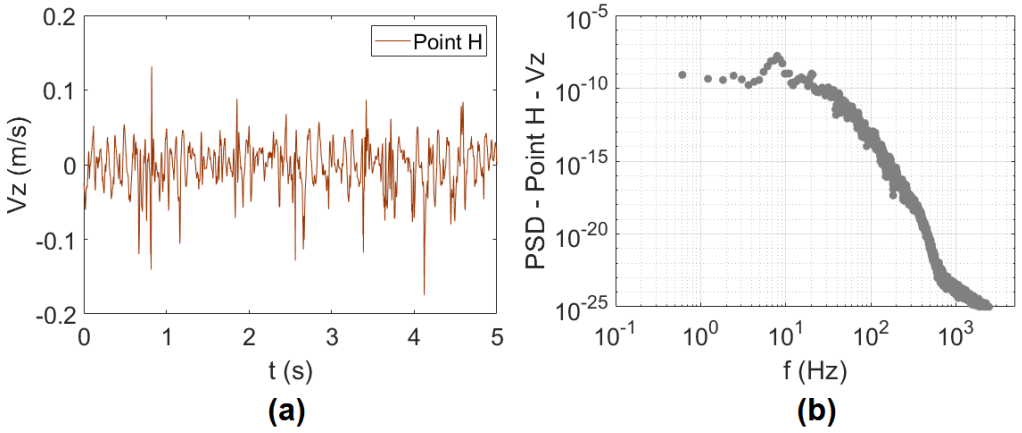

Figure 5.5: Time variation and the corresponding power spectral density (PSD) of the vertical velocity fluctuations at monitoring point H, (3cm, 0cm, 10cm) at far field of the jet in the middle of stratified layer. Helium case.

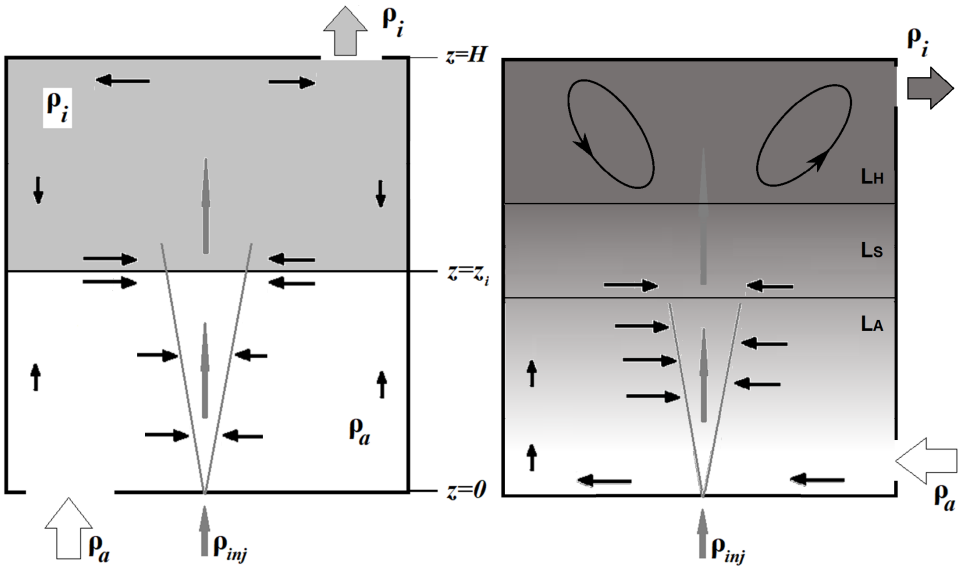

Figure 5.6: Bi-layer flow structure in quasi-steady regime. Left: original Linden's structure, right: flow structure in this study

cases. Generally both of these profiles increase with the development of the jet. The maximum flux is achieved at around $z = 17$cm, in the top homogeneous layer. Both the maximal volume flux and mass flux of helium jet is slightly larger than hydrogen jet. The jet development generates a 5 times increase of volume flux and a 20-50 times increase of mass flux in the jet, illustrating the obvious entrainment effect.

Near the injection where typically $z < 2$cm, the jet flow is still laminar thus we observe just a little rise of fluxes and entrainment effect is weak. This entrainment effect is remarkable for the region of laminar-turbulent jet development, typically for z =2-4cm, both of volume and mass fluxes rise sharply. This particularly relevant for the mass flux profiles as the entrainment gas is the ambient air which is much denser than the jet gas. The profiles reach local maxima at $z = 5 - 6$cm where the turbulent jet is well established. The volume flux keeps nearly constant in the stratified layer until $z = 11 - 12$cm where its buoyancy force decreases sharply with its development. At z =15-16cm, turbulent plume is established both for helium jet and hydrogen jet. Near the top opening ($z > 17$cm), the jet arrives at the ceiling and changes its direction. The vertical velocity is no longer dominant while both volume and mass fluxes sharply decrease.

In figures (c) and (d), we present respectively the vertical evolutions of jet momentum flux $\mathcal{M}^{DNS}(z)$ and mass momentum flux $\mathcal{M}_m^{DNS}(z)$. The mass momentum flux, indicating the jet vertical kinetic energy, increases with the jet development, as the upward buoyancy force does work. In the turbulent jet region where z =3-10cm, the two profiles of mass momentum fluxes are nearly coincided because the density difference in the jet is compensated by the velocity difference. Helium jet possesses higher vertical velocity and lower buoyancy force (as it is denser) in this region. The mass momentum flux differs between the two cases in the homogeneous layer. Generally for a Boussinesq jet, the jet momentum flux and the mass momentum flux possess the same monotonicity, clearly here it is not the case. The momentum flux decreases. The influence of the density difference changes completely its variation trend.

In figure (e), we present the variation of buoyancy flux $\mathcal{B}^{DNS}(z)$, decreasing along the jet in the two cases. Buoyancy flux is directly linked to the evolution of environmental density. The buoyancy flux is nearly the same for the two gases in the bottom layer L_A and the top homogeneous layer L_H, but differs in the intermediate stratified layer L_S. Helium jet possess higher buoyancy flux in this region due to a large thickness of L_S for the helium case. The two profiles are coincided at level zero in the top homogeneous layer as there is no longer density difference inside and outside the jet.

In figure (f), we present the variation of characteristic jet radius $b_G^{DNS}(z)$, defined in equation (4.43). It keeps constant in the laminar jet region $z < 4 - 6$cm and increases with the development of the jet when entrainment is present. Profiles for hydrogen jet and helium jet possess almost the same slope in the turbulent jet region as well as in the turbulent plume region, but horizontal extension for hydrogen jet is larger.

In figure (g), we present the shape change factor which is defined by $K^{DNS}(z) = L_{1\sigma}^{DNS}/2\pi b_G^{DNS}$ with $L_{1\sigma}^{DNS}$ is the perimeter of region Ω_b defined in equation (4.42). This factor is equal to 1 if the jet cross-section is a regular circle. The factor goes higher than 1 in laminar jet and beginning of turbulent jet region mainly due to the cross-flow. The cross-section becomes nearly a circle at $z > 6$cm for hydrogen case and $z > 8$cm for helium jet.

In figure (h), we present the convection-diffusion ratio $\lambda^{DNS}(z)$ calculated by equation (4.45). For air-hydrogen mixture, $\mathrm{Sc}_{H_2} = 1.42$ and for air-helium mixture, $\mathrm{Sc}_{He} = 1.73$. These values can be found at injection level. In the laminar jet region, λ increases and attains a peak around 2.2 at $z \approx 3.5$cm for hydrogen case and around 1.8 at $z \approx 4$cm for helium. This means that in laminar jet region, at radial direction, mass diffusion is more significant than momentum diffusion as the entrainment effect is not obvious in this region. The ratio continues to

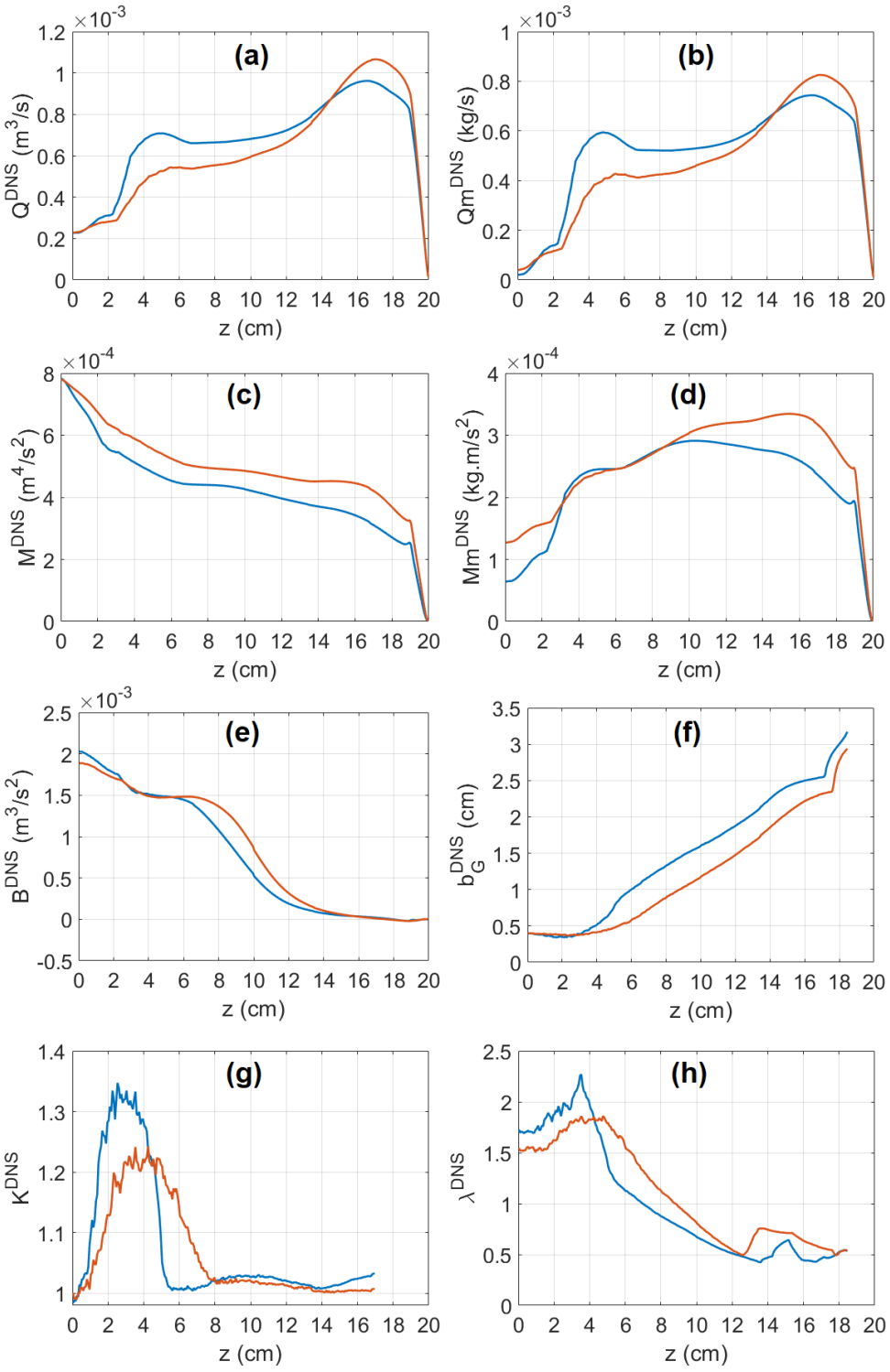

Figure 5.7: Comparison of profiles of characteristic jet quantities and parameters between DNS He and DNS H2. (a) profiles of jet volume flux $\mathcal{Q}^{DNS}(z)$; (b) profiles of jet mass flux $\mathcal{Q}_m^{DNS}(z)$; (c) profiles of jet momentum flux $\mathcal{M}^{DNS}(z)$; (d) profiles of jet mass momentum flux $\mathcal{M}_m^{DNS}(z)$; (e) profiles of buoyancy flux $\mathcal{B}^{DNS}(z)$; (f) profiles of characteristic jet radius under Gaussian assumption $b_G^{DNS}(z)$; (g) profiles of jet shape change factor $K^{DNS}(z)$; (h) profiles of convection-diffusion ratio $\lambda^{DNS}(z)$. Orange solid lines indicate DNS He results and blue solid lines correspond to DNS H2 results.

decrease in the turbulent jet and turbulent plume region. In the homogeneous layer, where a complete mixing occurs, the local diffusion-convection ratio converges to a constant value, identical for helium or hydrogen cases. This value corresponds to turbulent Schmidt number estimated around 0.6 in this case, in good agreement with the theory Craske et al. (2017).

We summary in the table 5.2 the variation of jet flow pattern, characteristic jet quantities and parameters with their corresponding altitudes in the cavity. Profiles of jet mass and volume fluxes depend on jet flow structure while its buoyancy flux depends on environmental density variation. In general, we observe similar profiles for helium and hydrogen cases.

z(cm) **Case H2**	z(cm) **Case He**	**Jet flow pattern**	**Three-layer structure**	$\mathcal{Q}$ or $\mathcal{Q}_m$	$\mathcal{M}$	$\mathcal{M}_m$	$\mathcal{B}$	b_G	K
0-2cm	0-3cm	Laminar jet	L_A	$\rightarrow$	$\searrow$	$\nearrow$	$\searrow$	$\rightarrow$	>1
2-4cm	3-6cm	Laminar-turbulent transition	L_A	$\nearrow$	$\searrow$	$\nearrow$	$\searrow$	$\rightarrow$	>1
4-6cm	6-8cm	Turbulent jet	L_A	$\rightarrow$	$\rightarrow$	$\nearrow$	$\rightarrow$	$\nearrow$	>1
6-10cm	8-11cm	Turbulent jet	L_S	$\rightarrow$	$\rightarrow$	$\nearrow$	$\searrow$	$\nearrow$	=1
10-11cm	11-12cm	Jet-plume transition	L_S	$\nearrow$	$\searrow$	$\nearrow$	$\searrow$	$\nearrow$	=1
11-15cm	12-16cm	Jet-plume transition	L_H	$\nearrow$	$\searrow$	$\nearrow$	$\rightarrow$	$\nearrow$	=1
15-20cm	16-20cm	Turbulent plume	L_H	$\nearrow\searrow$	$\searrow$	$\nearrow\searrow$	$\rightarrow$	$\nearrow$	=1

Table 5.2: Variation of jet flow pattern, characteristic jet quantities and parameters in the cavity and their corresponding heights

5.1.4 Inlet/outlet profiles and global balance

In this section, we focus on the inlet and outlet flows through the two vertical openings. In figure 5.8, we present firstly the time-averaged velocities. The inlet flow is laminar and its normal velocity u is nearly uniform through the bottom opening. Its y component is also uniform except for the area close to the horizontal ends due to the aspiration cone.

Conversely, the outlet velocity through the top opening is not uniform. The distribution of the velocity results from the toric flow occurring in the top part of the cavity. Meanwhile, in figure 5.9, spectrum analysis of y-direction velocity temporal variation at top opening centre shows a characteristic frequency around 2Hz corresponding to the clapping oscillation of outlet velocity.

In the second step, we seek to check the global balance of fluxes for the helium and hydrogen cases (table 5.3).

We set the same injection volume flux. As helium gas is twice heavier than hydrogen, the mass flux of helium injection is almost the double of hydrogen jet. Helium case possesses smaller inlet flux (around 10% compared with H2), which indicates its entrainment effect is little weaker than hydrogen case. The outlet volume flux is in the same order between helium and hydrogen cases. The mean outlet mixture density is quite close between two cases.

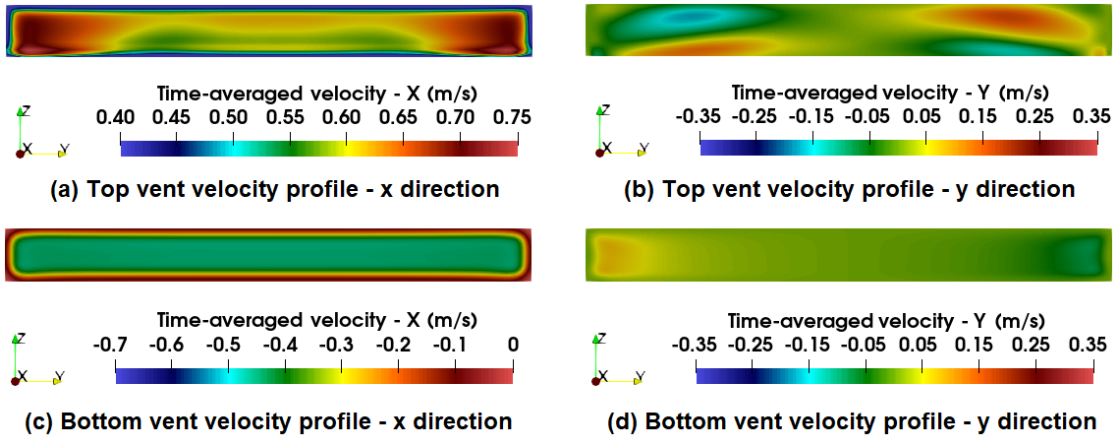

Figure 5.8: Time-averaged inlet-outlet velocity profiles. Helium case. (a,b) Top vent, (c,d) Bottom vent; (a,c) Normal velocity u, (b,d) Horizontal tangential velocity v.

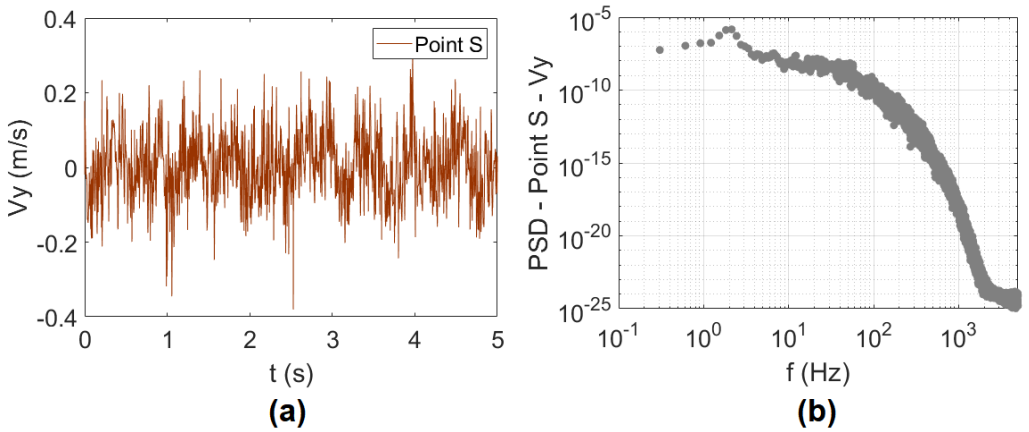

Figure 5.9: Temporal variation and corresponding power spectral density (PSD) for variation of y direction velocity at monitoring point S, (5cm, 0cm, 19.5cm) centre of top opening. Helium case.

	DNS helium	**DNS hydrogen**	**Difference (He-H2)/H2**
Injection volume flux Q_{inj} (m^3/s)	2.18×10^{-4}	2.18×10^{-4}	0%
Injection mass flux $\rho_{inj}Q_{inj}$ (kg/s)	0.35×10^{-4}	0.18×10^{-4}	+98%
Inlet volume flux $Q_{in}(m^3/s)$	3.56×10^{-4}	3.93×10^{-4}	-9.6%
Inlet mass flux $\rho_{air}Q_{in}(kg/s)$	4.16×10^{-4}	4.59×10^{-4}	-9.6%
Outlet volume flux $Q_{out}(m^3/s)$	5.80×10^{-4}	6.17×10^{-4}	-6.0%
Outlet mass flux $\rho_{out}Q_{out}(kg/s)$	4.51×10^{-4}	4.78×10^{-4}	-5.6%
Outlet mixture density $\rho_{out}(kg/m^3)$	0.778	0.774	+0.5%
Balance – volume flux $(Q_{out}-Q_{in}-Q_{inj})/Q_{out}$	1.0%	0.9%	
Balance – mass flux $(\rho_{out}Q_{out}-\rho_{air}Q_{in}-\rho_{inj}Q_{inj})/\rho_{out}Q_{out}$	0.1%	0.1%	
Ratio Q_{in}/Q_{inj}	1.64	1.80	
Ratio $\rho_{air}Q_{in}/\rho_{inj}Q_{inj}$	11.9	25.5	

Table 5.3: Comparison inlet-outlet fluxes of DNS helium with DNS hydrogen, global balance of volume flux and mass flux

The global balance of the time-averaged volume flux over the cavity, or called dilatation percentage, is around 1% for all two cases. Note that this error is related to the numerical post-processing output. The velocity field is stocked at vertex of cell in the CFD code while the post-processing integration is calculated on cell face.

The global balance of the time-averaged mass flux through the bottom and the top openings as well as the injection are calculated by integration operation of time-averaged field ($\overline{\rho \vec{u}}$), stocked on the cell face, the mass balance error is less than 0.1% for all two cases. The global conservation of mass flux is valid.

The helium inlet volume flux is 1.64 times of injection flux, while for hydrogen it is 1.80. This means that the injection volume flux cannot be correctly considered negligible in this case. However, for mass flux, the inlet mass flux is 11.9 times larger than injection mass flux for helium case and 25.5 times for hydrogen case. The injection mass flux may be considered negligible which will introduce only 8% error for helium and 4% error for hydrogen case.

Conclusion 5.1

In conclusion, the flow is mainly turbulent in the cavity thus its structure is characterised by the time-averaged velocity field. The flow pattern is in agreement with bi-layer structure assumed in the model of Linden et al. (1990). Quasi-fresh air is presented in the lower cavity and a homogeneous density layer is formed in the top part. The impenetrable interface defined in Linden's model corresponds to a stratified layer in which the vertical flow in the far-field of the jet is nearly zero and environmental density changes quasi-linearly. The jet flow provides the only connection between the top homogeneous layer and the bottom cavity.

The jet flow can be characterised by vertical variations of the jet quantities. The flow is laminar at injection. With the development of the jet, the flow transforms into turbulent and a pure turbulent jet is established in the middle height of the cavity. Due to entrainment effect, the jet flow varies into a jet-plume then a pure plume in the top layer.

Globally, the conservations of volume flux and mass flux in the cavity are valid whereas the injection volume flux cannot be considered negligible.

5.2 DNS-PIV flow comparison

In this section, we seek to compare DNS velocity fields with PIV experimental measurements on the mid-plane $y = 0$, perpendicular to two openings. As the flow is highly turbulent in both cases (DNS and PIV), we seek to compare the distribution of statistical quantities, typically the time-averaged velocity and its RMS on the observation plane.

5.2.1 Time-averaged velocity

We firstly compare the time-averaged velocity fields. As only one camera was operated in PIV measurement (type 2D2C), we only have two velocity components parallel to the measure plane $y = 0$.

Time-averaged vertical velocity field

The vertical velocity is the key parameter in the jet theories and is representative to assess the jet modelling. In figure 5.10, we present the distribution of vertical velocity on this observation plane $y = 0$, for PIV and DNS helium case.

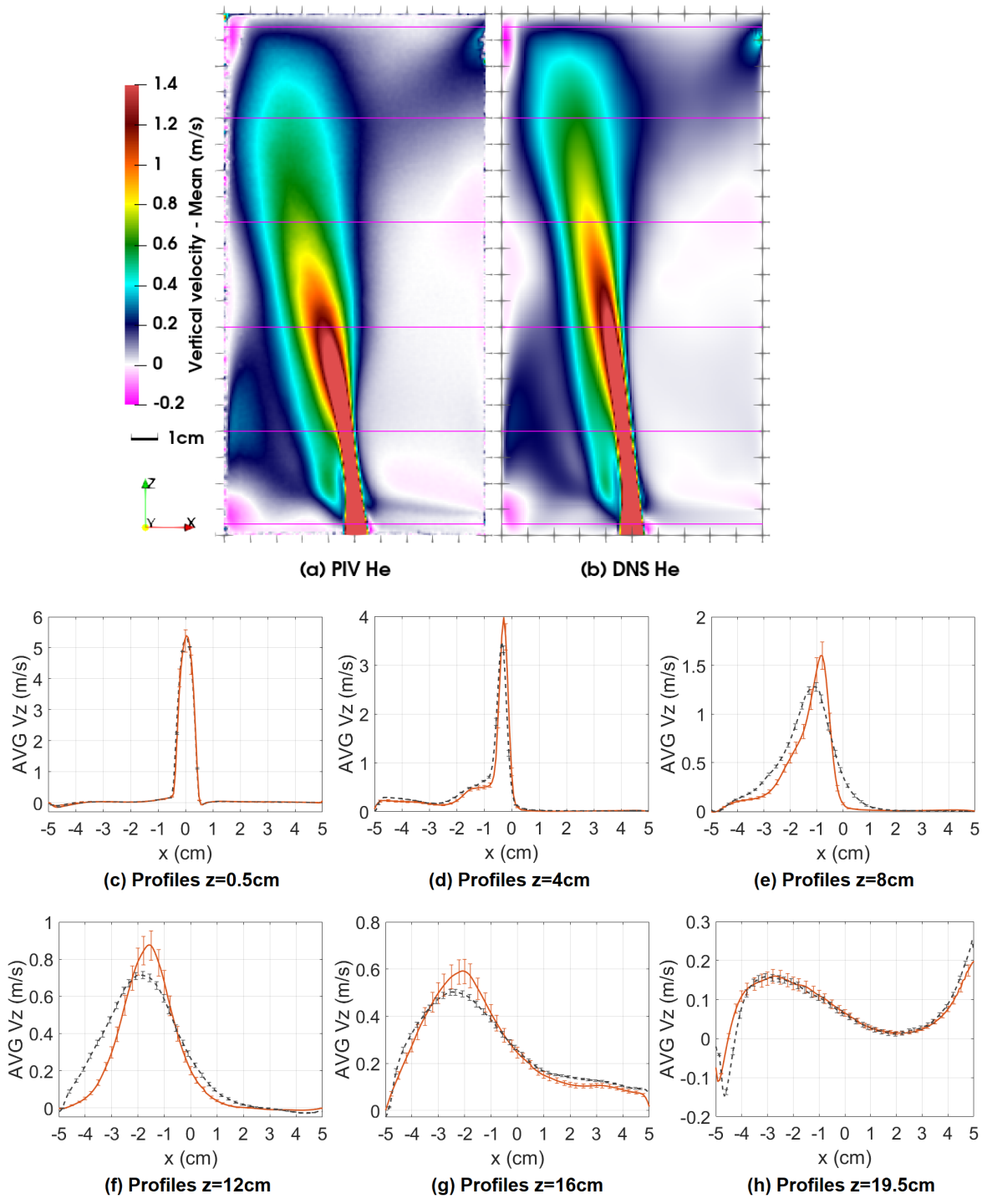

Figure 5.10: Comparison of time-averaged vertical velocity, on the mid-plane $y = 0$: (a) PIV He (b) DNS He, (c)-(h) horizontal profiles on z =0.5cm, 4cm, 8cm, 12cm, 16cm and 19.5cm. Profiles $z = 0.5$cm and $z = 19.5$cm represent the mid-level of two openings while other 4 profiles represent respectively: $z = 4$cm, laminar-turbulent transition area of the jet; $z = 8$cm, turbulent jet area; $z = 12$cm, turbulent plume area; $z = 16$cm, in the centre of the top homogeneous layer. Orange solid lines indicate DNS profiles while black dashed lines are PIV results, error bars correspond to total measurement accuracy with 95% confidence interval.

In figure 5.10-(a)(b), the jet region can be easily identified. The jet centre velocity decreases along the jet due to the buoyancy force. The radius of the jet becomes larger with its development, as the consequence of jet entrainment effect. The vertical velocity is nearly zero on the left-hand side of the jet in the stratified layer and on right-hand side all along the cavity.

The contour of the vertical velocity are almost identical for small vertical velocity (around 0.2-0.4m/s) in PIV and DNS cases. The drop of jet inertia seems more pronounced in PIV case. In order to compare more precisely the distribution, we presented in figure 5.10-(c)(h) a series of horizontal profiles taken from the above results.

- At z = 0.5cm and 4cm, the profiles DNS and PIV are almost superposed except for the jet centre. The maximum velocity in the jet centre at injection is around 5.5m/s, in agreement with a Poiseuille injection axis-symmetrical profile. The radius of the jet shrinks a little at z = 4cm compared with injection area. The jet centre is lightly inclined towards left-hand side at this altitude.

- At z = 8cm and 12cm, the profiles DNS and PIV have similar shape. The expansion of the jet is much larger than below area as the result of entrainment effect. PIV profiles present Gaussian form with larger horizontal expansion compared with DNS profiles. PIV jet centre is inclined a little more than DNS (-0.8cm vs -1.1cm at z = 8cm), with a lower jet centre velocity (around 20%) compared with DNS case as well.

- At z = 16cm, where the jet transforms into a pure plume, the profiles DNS and PIV are almost superposed except for the jet centre region. PIV jet centre is situated just a little on the left of DNS centre, with a smaller centre velocity.

- At z = 19.5cm, we have a very good agreement of profiles DNS and PIV. The jet flow blends in with outflux through the top opening, generating S profiles at this level. The outlet velocity presents an obvious component in vertical direction.

Time-averaged x-direction velocity field

The horizontal velocity is representative for entrainment effect, and it is used to assess the inlet and outlet fluxes modelling through two openings. In figure 5.11, we present the distribution of time-averaged horizontal x-direction velocity on the observation plane $y = 0$, for PIV and DNS helium as well as six horizontal profiles.

In figure 5.11-(a)(b), we note that the area near two openings presents the maximum of the x-direction velocity. The jet inclination is clearly identified. We seek more detailed analysis from its variation along six horizontal lines:

- At z = 0.5cm, profiles DNS and PIV are superposed. The horizontal velocity is nearly invariable along the inlet flow through the bottom opening until the border of the jet ($x = 2 - 5$cm). On the left of the jet (x-negative region), local horizontal velocity is towards the jet centre.

- At z = 4cm, profiles DNS and PIV are almost similar. In the jet centre, PIV result represents a higher x-component than DNS.

- At z = 8cm and 12cm, shapes of DNS and PIV profiles are similar, but we can identify the PIV results present higher x-direction velocities and its jet centre is lightly more inclined. The difference between PIV and DNS is much remarkable on the left-hand side of the jet where the DNS jet seems more concentrated in the centre. At z = 12cm, PIV

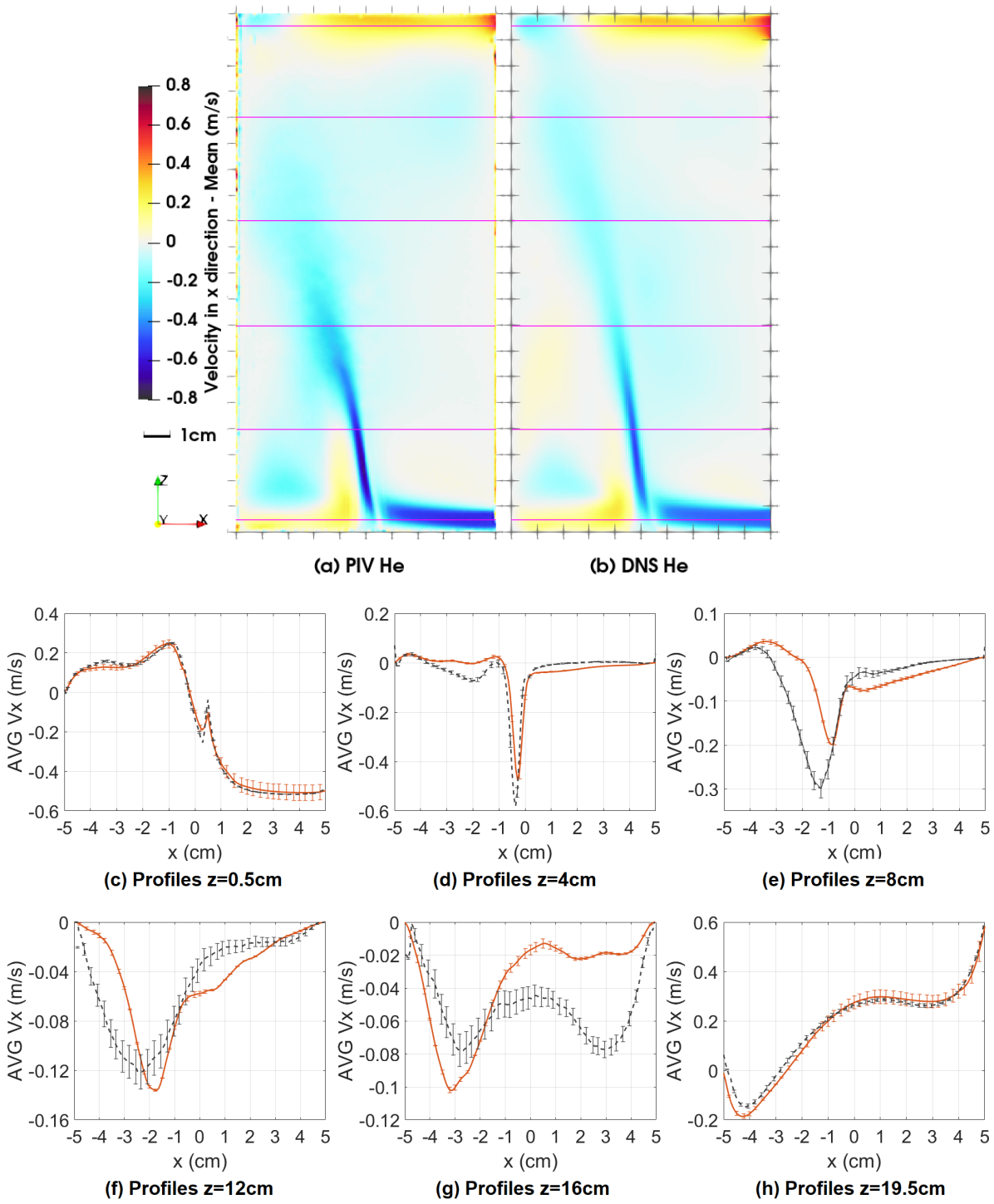

Figure 5.11: Comparison of time-averaged x-direction horizontal velocity, on the mid-plane $y = 0$: (a) PIV He (b) DNS He, (c)-(h) horizontal profiles on z =0.5cm, 4cm, 8cm, 12cm, 16cm and 19.5cm, orange solid lines indicate DNS profiles while black dashed lines are PIV results, error bars correspond to total measurement accuracy with 95% confidence interval.

measurement becomes more inaccurate in the jet centre as local RMS becomes much higher than DNS. PIV horizontal velocity is larger on the left-hand side of the jet but smaller than DNS on the other side.

- At z = 16cm, jet centre could be identified as the only peak in DNS profile. There is another peak in PIV profile at x = 3cm where local horizontal velocity is much larger than DNS.

- At z = 19.5cm, two profiles are almost identical. A very good agreement on the outlet flux could be identified.

General remark

Generally, a good agreement is found for time-averaged velocity field between PIV and DNS. There are larger differences for x-direction velocity component, especially for the turbulent jet region around z = 8cm where large scale horizontal movement of the jet centre is identified in PIV but not in DNS. Compared to z-direction velocity which is dominated by injection inertia, x-direction velocity is more self-motion, directly linked to global turbulent flow and jet entrainment effect.

5.2.2 Velocity RMS

The flow in the cavity is highly turbulent. In order to evaluate the turbulent flow, we consider comparing the velocity RMS measured in PIV and DNS cases.

RMS of vertical velocity field

In figure 5.12, we present the distribution of vertical velocity RMS on the observation plane $y = 0$, for PIV and DNS helium and 6 horizontal profiles for detailed comparison.

In figure 5.12-(a)(b), we can identify the turbulent jet zones in the cavity both for PIV and DNS cases. PIV result displays a larger extension of turbulent region.

The development of turbulent flow begins on the jet border, presented as two peaks. PIV flow seems much more turbulent than DNS in this region. Then turbulence progressively invades the jet centre.

When a turbulent jet is established, the RMS profiles present only one peak, corresponding to the jet centre. A good agreement between PIV and DNS profiles is found for z = 8cm where the jet is completely turbulent. The extension of PIV jet is little larger than that of DNS, which is also shown in time-averaged profiles before.

In the top homogeneous layer, the jet flow is completely transformed into a plume where a plateau could be observed in the profiles at z = 16cm and z =19.5cm, representing a large turbulent flow region at these altitudes. The vertical velocity RMS is in the same error interval for PIV and DNS results.

RMS of x-direction velocity field

The RMS of x-direction velocity is used to analyse the horizontal oscillation of the jet. In figure 5.13, we present its distribution on the measurement plane $y = 0$ as well as a series of horizontal profiles.

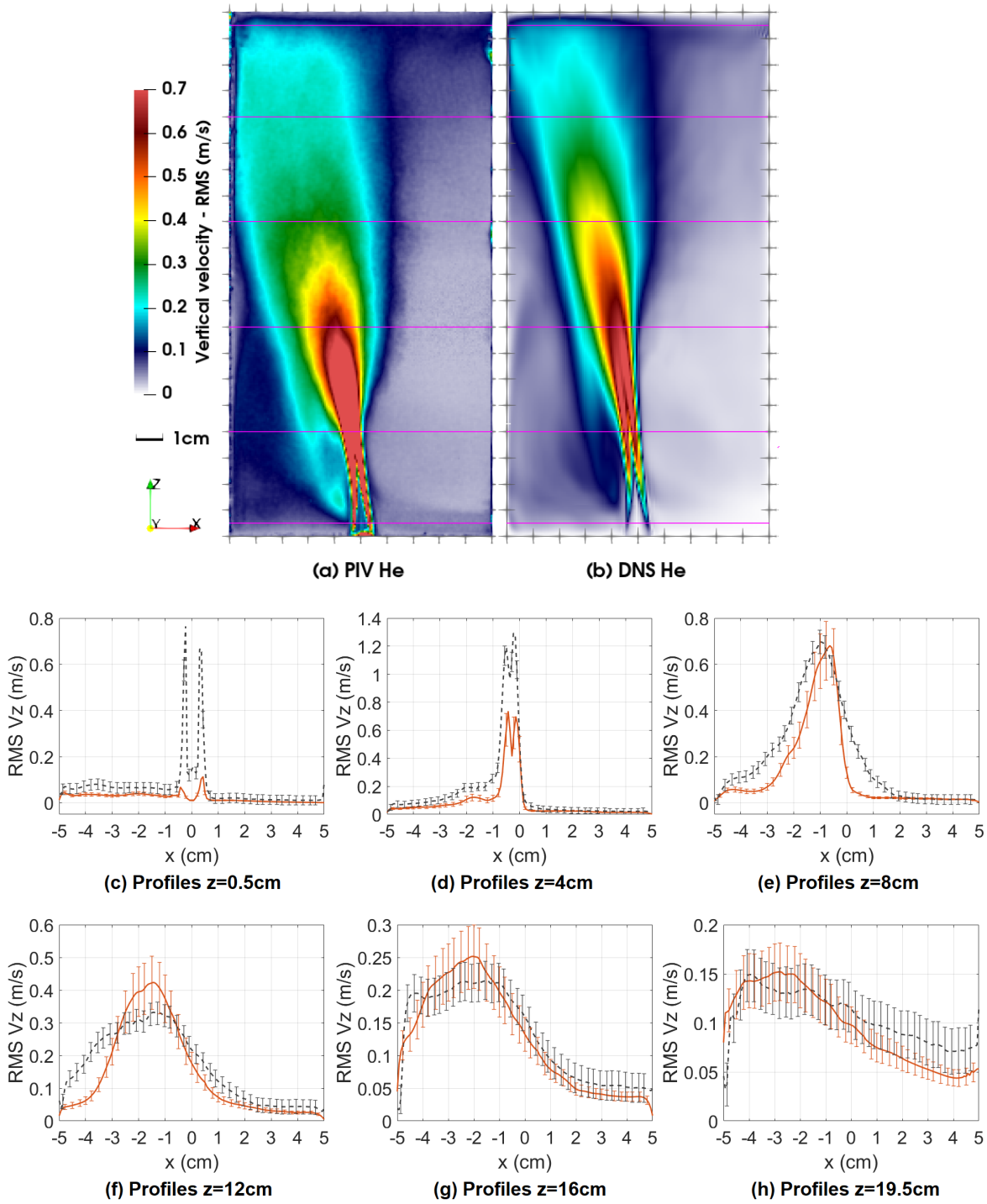

Figure 5.12: Comparison of RMS of vertical velocity, on the mid-plane $y = 0$: (a) PIV He (b) DNS He, (c)-(h) horizontal profiles on z =0.5cm, 4cm, 8cm, 12cm, 16cm and 19.5cm, orange solid lines indicate DNS profiles while black dashed lines are PIV results, error bars correspond to total measurement accuracy with 95% confidence interval.

The difference between PIV and DNS are located for $z < 12$cm. Profiles of DNS and PIV are quite similar in turbulent jet-plume region ($z > 12$cm).

For $z = 0.5$cm where the jet is still laminar, a good agreement is found for inlet flow region. In the recirculation zone in x-negative side of the jet, PIV case presents larger RMS in x-direction (0.15m/s vs 0.08m/s). At $z = 4$cm, where the turbulent jet is just established, even if the jet centre is located at same position at this altitude for PIV and DNS, a large difference at the jet centre is still observed in these profiles. RMS at jet centre for PIV is twice larger than DNS. Between $z = 4$cm and $z = 8$cm, large differences between two figures are observed. The jet extension as well as the local x-direction velocity RMS becomes much larger for PIV case at $z = 8$cm. This means the horizontal oscillations in turbulent jet region, observed in PIV measurement, is not correctly captured by DNS.

General remark

Generally, the DNS simulation generates enough fluctuations in the turbulent plume region ($z > 12$cm), where local RMS, both in x and z directions, are comparable with PIV measurement. However, DNS flow in jet region ($z = 4 - 12$cm) is not as turbulent as observed by PIV measurement, especially in x-direction.

5.2.3 Jet inclination and jet centre evolution

We consider evaluating the jet development and compare its evolution at jet centre in the DNS He, DNS H2 and PIV He cases. The results are presented in figure 5.14. The jet centre at given altitude is defined as the point where situated the maximum time-averaged vertical velocity at this altitude.

In figure (a), we present the position of jet centre in the plane $y = 0$. For DNS simulation, hydrogen jet is more inclined compared with helium jet. PIV helium jet centre is generally situated between DNS helium jet centre and DNS hydrogen one. But at the laminar and turbulent jet region, typically for $z < 6$cm, PIV jet centre is almost identical with that of DNS helium jet.

Figure (b) shows the time-averaged vertical velocity variation at jet centre, which is identical in laminar jet region where $z < 2$cm, then differs in the turbulent jet region. From $z = 2$cm to $z = 12$cm, DNS helium jet possesses the largest vertical velocity while PIV profile is situated between DNS helium and DNS hydrogen. Three profiles are quite identical in turbulent plume region for $z > 12$cm.

For vertical velocity RMS, presented in figure (c), surprisingly a good agreement between DNS hydrogen with PIV helium is found for $z < 4$cm. DNS helium RMS is smaller than the other two. From $z = 4$cm to $z = 8$cm, both DNS profiles are below the PIV profile. The profile peak, indicating the establishment of a turbulent jet, is situated at around z =4cm for DNS H2, z =5cm for PIV He and z =6cm for DNS He. Hydrogen injection possesses only half of density and momentum of helium as well as a little larger upward buoyancy force. Its turbulent jet flow is thus established earlier in the same environmental variation.

We present in figure (d) the ratio of vertical velocity RMS on its time-average, quantifying their turbulence level. The turbulent jet development is quite similar between DNS hydrogen and PIV helium where a constant ratio is established at $z = 6$cm. DNS helium establishes lately at $z = 8$cm. In the well-established turbulent region, all of them possess same level of turbulent flow ratio around 50%.

Figure (e) presents the centre density variation along the jet. We can identify the density difference between helium and hydrogen at injection level. The development of the turbulent

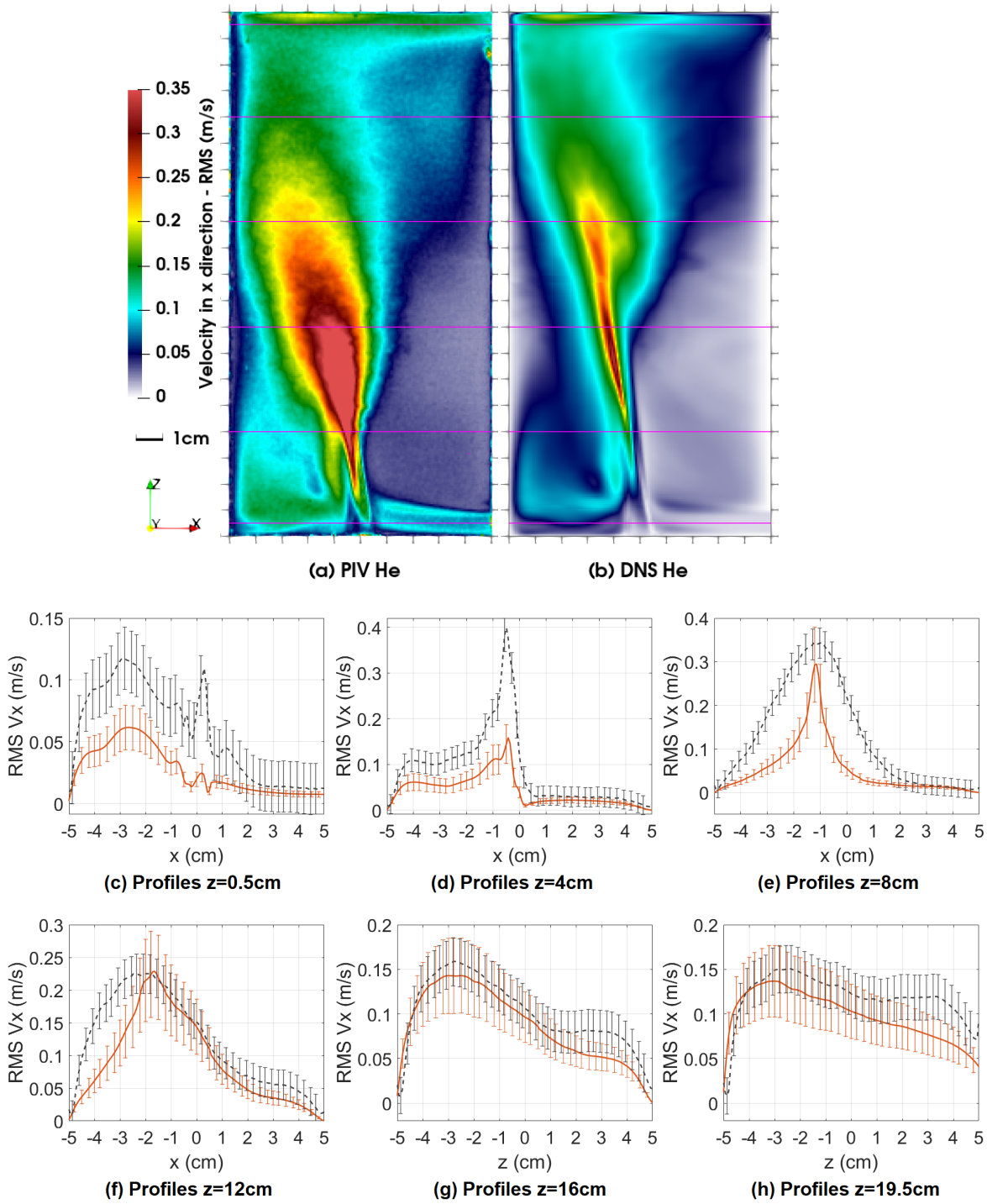

Figure 5.13: Comparison of RMS of x-direction horizontal velocity, on the mid-plane $y = 0$: (a) PIV He (b) DNS He, (c)-(h) horizontal profiles on z =0.5cm, 4cm, 8cm, 12cm, 16cm and 19.5cm, orange solid lines indicate DNS profiles while black dashed lines are PIV results, error bars correspond to total measurement accuracy with 95% confidence interval.

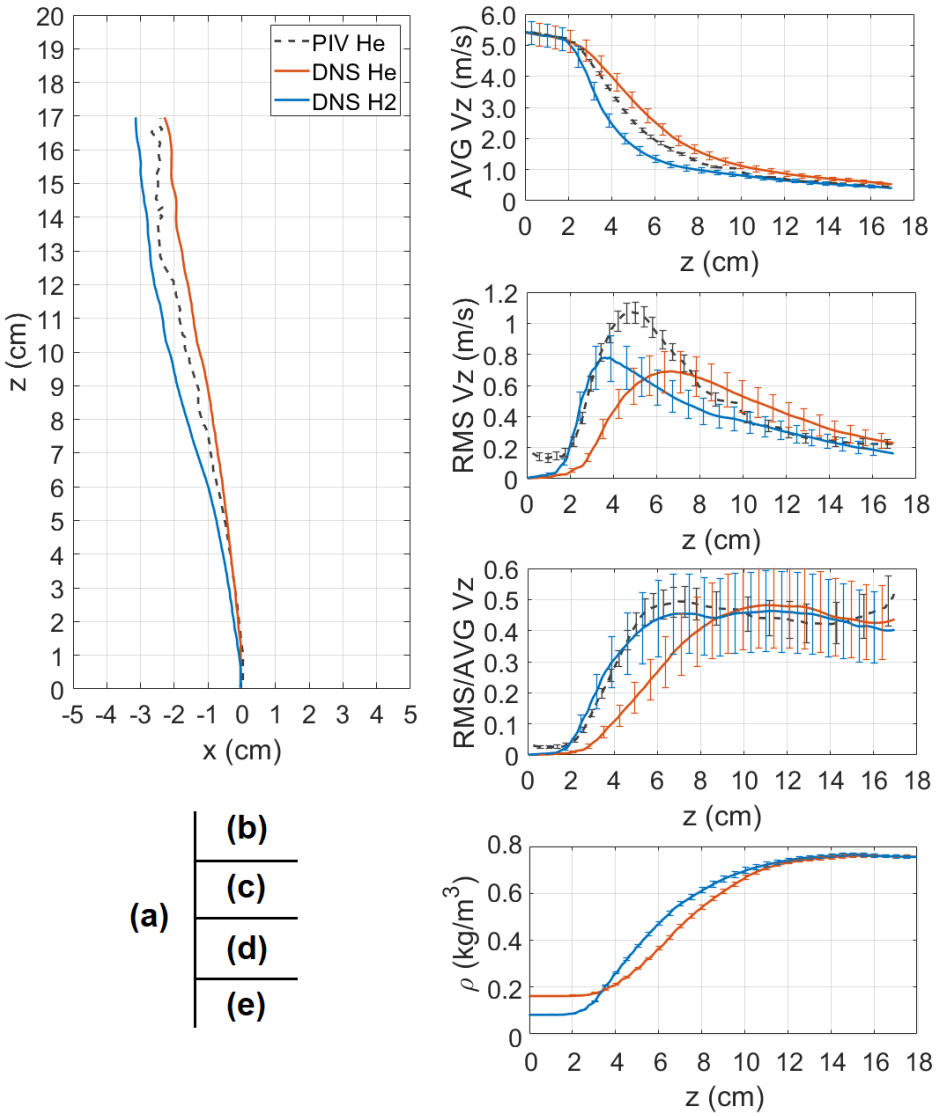

Figure 5.14: Comparison of jet centre variation between DNS He, DNS H2 and PIV He. (a) evolution of jet centre position with the development of the jet; (b) variation of time-averaged (AVG) vertical velocity at jet centre; (c) variation of vertical velocity RMS at jet centre; (d) variation of ratio RMS/AVG of vertical velocity with development of the jet; (e) variation of local mixture density at jet centre. Orange solid lines indicate DNS He results, blue solid lines correspond to DNS H2 results while black dashed lines are PIV He results. Error bars correspond to total measurement accuracy with 95% confidence interval.

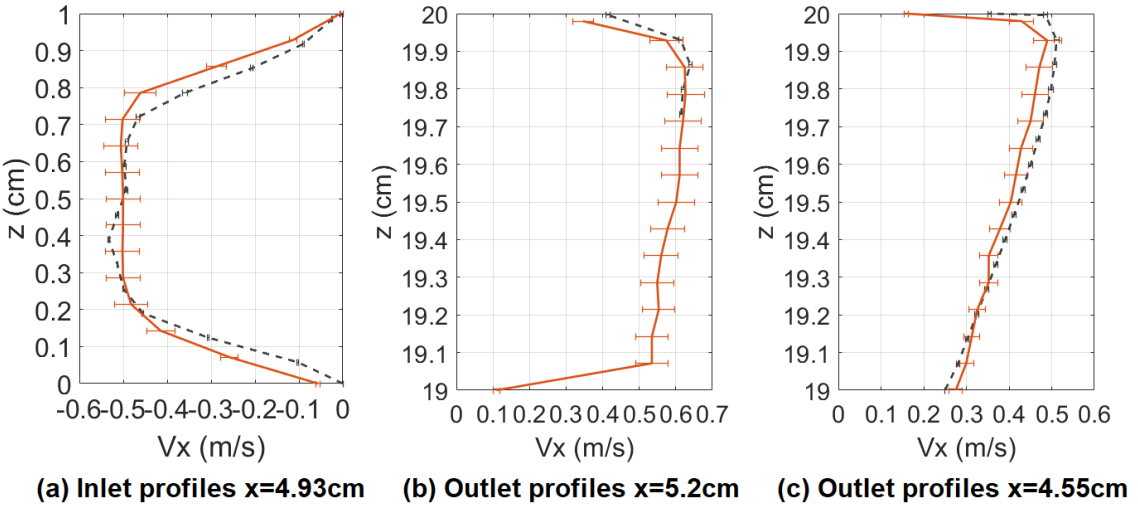

Figure 5.15: Comparison of inlet/outlet vertical profiles through two openings between DNS and PIV time-averaged results, orange solid lines indicate DNS profiles while black dashed lines are PIV results, error bars correspond to total measurement accuracy with 95% confidence interval.

flow and jet entrainment facilitate the mixing in the horizontal direction thus the jet centre density decreases all along the jet. It becomes stable and identical for both of them in the top homogeneous layer.

5.2.4 Inlet-outlet profiles

Another key indicator is the velocity profiles through the two openings, illustrating the aspiration and entrainment effects of the jet flow in the cavity. In figure 5.15, three vertical profiles of the normal velocity are presented at different x locations along the inlet and outlet vents. Indeed, integrated outlet profiles for PIV case is not easy to be captured. In figure 5.15-(b), we present the profiles at $x = 5.2$cm located within the wall thickness. Only the top 0.3cm region possesses measurements for PIV due to the parallax effect of the cavity wall when the camera takes photos. In figure 5.15-(c), we present the profiles at $x = 4.55$cm inside the cavity.

Both inlet and outlet profiles present a good agreement for PIV and DNS. In figure 5.15-(b), the outlet velocity at $z = 19.8$cm is nearly identical for DNS and PIV. If we take the integration of these profiles to estimate the plane inlet/outlet fluxes, we have: for inlet flux from figure (a), PIV 0.367m^2/s, DNS 0.360m^2/s (+2%); and for outlet flux from figure (c), PIV 0.304m^2/s, DNS 0.295m^2/s (-3%). Relative errors are both largely smaller than the measurement accuracies which validates the comparison. Note that no information is given about the uniformity of these profiles along the y-axis.

Conclusion 5.2

Considering the PIV-DNS comparison for time-averaged fields, jet evolution and inlet-outlet profiles, we confirm that **DNS simulation is valid and most of the phenomena observed in the main cavity are correctly modelled**, such as turbulent flow, jet flow, far field flow, aspiration effect, entrainment effect etc. Consequently, DNS simulation results can be treated as reference.

However, DNS flow in jet region ($z = 4 - 12$cm) is not as turbulent as observed by PIV measurement, especially in x-direction.

5.3 Light gas concentration distribution

In hydrogen safety experimental research, helium is often considered as a good substitutive gas because its density is much lower than air while possessing low operational safety risk. Helium concentration results are thus used to predict the hydrogen risk (Fuster et al. (2017)). We have seen in section 5.1 that in the present case, DNS helium and DNS hydrogen possess similar flow structure. In this section, we will compare their concentration distributions to verify this statement.

Besides, hydrogen risk is in fact related to its instantaneous concentration distribution but not systematically to its time-averaged field. In the second step, we are interested in the comparison between instantaneous and time-averaged concentrations to see if time-averaged results could be considered indicative or conclusive in risk analysis.

5.3.1 Helium-hydrogen comparison

We first focus on the distribution of time-averaged light gas concentration, illustrated in figure 5.16. The vertical variations of light gas concentration at far-field are similar (three-layer structure) between hydrogen and helium cases. Their concentrations in the homogeneous layer are almost identical. Helium interface altitude is little higher than hydrogen.

The major difference between these two cases is the inclination of the jet. The hydrogen jet is more inclined towards x-negative direction compared with helium jet. From horizontal profiles figures 5.16-(d)(e), we observe a peak translation with comparable concentration at jet centre between two cases. Besides, the horizontal extension of hydrogen jet seems larger than helium one.

The temporal variation of light gas concentration in the cavity is mainly located in the jet region, as shown in figure 5.18. Maximum local concentration RMS may reach 20% at the turbulent jet border. In the far field of the jet as well as in the top homogeneous layer, concentration varies very little in the quasi-steady state. Integration in the whole cavity gives their global mean of the RMS fluctuations: 2.55% for hydrogen case and 2.66% for helium case. Therefore, the concentration temporal variation is globally comparable between two cases.

5.3.2 Temporal variation of concentration

The time dynamics of instantaneous concentration differs in the jet region and outside. In figure 5.17, based on 100k samples in quasi-steady state, local Probability Density Function (PDF) of concentration temporal variation can be approximated from its temporal histogram. Two monitoring points are considered: point J at jet border and point H at far field of the jet.

The concentration PDF is not symmetrical at jet border. Local time-averaged concentration (15.0%) does not correspond to the concentration the most probably observed in this location, represented by the peak in its histogram (7.8%). Concentration temporal variation at this point is very large, with its RMS equal to 7.4%, almost a half of its average. Its 1-σ interval (average±RMS) contains 82% of samples, largely superior to that in standard Gaussian distribution (68%).

Reversely, in the far field of the jet (point H), concentration PDF is nearly Gaussian. Its time-averaged value (23.4%) corresponds to the most frequently presented concentration. Its 1-σ interval (average±RMS) contains 67.4% of samples, very close to its theoretical value 68%. Besides, local concentration RMS (2.9%) is much smaller compared with point J. Note that this

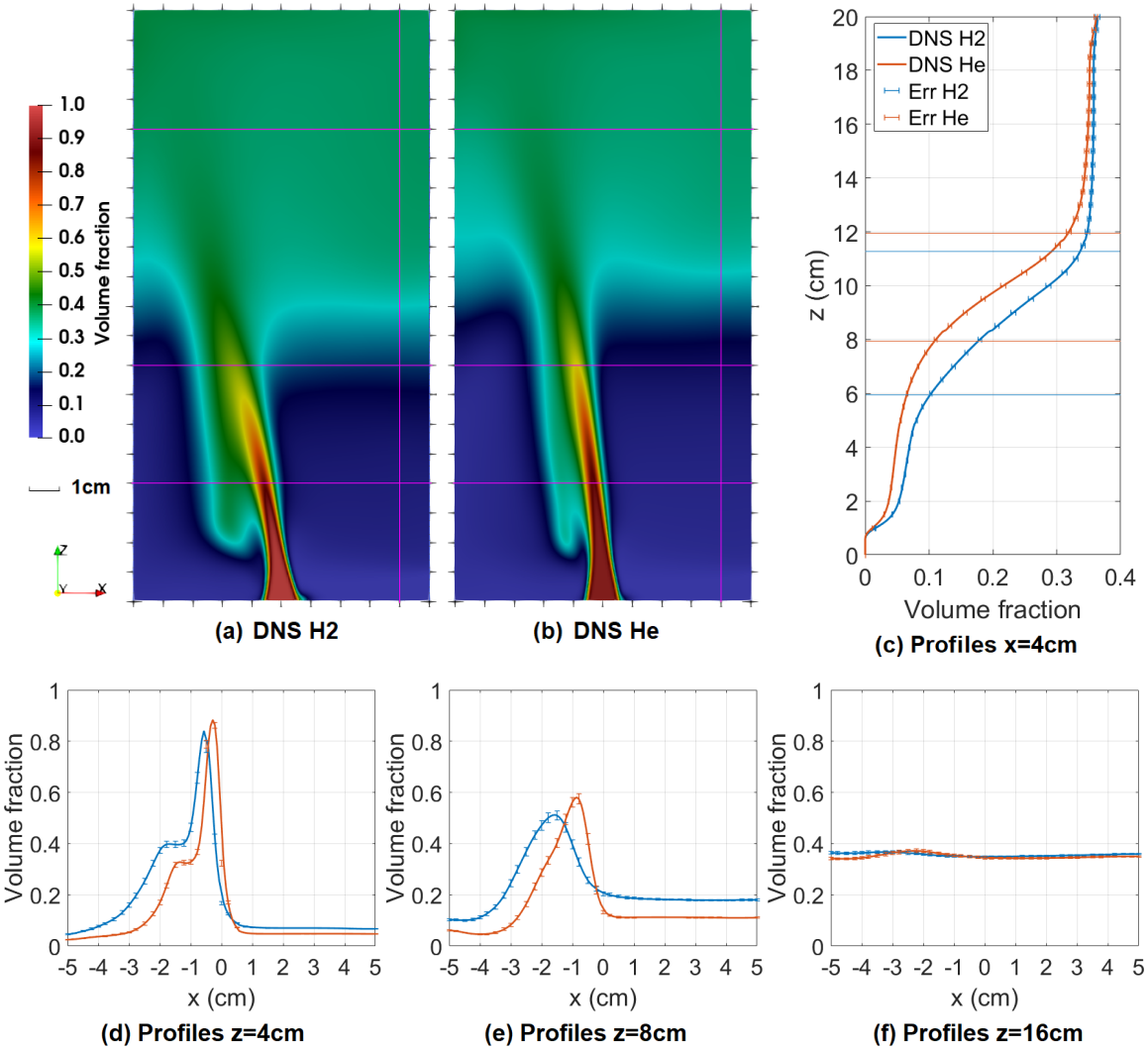

Figure 5.16: Comparison He/H2 concentration on the cavity mid-plane $y = 0$ (a) He case (b) H2 case, with three horizontal profiles (d)(e)(f) at different levels and one vertical profile (c) for $x = 4$cm. Orange solid lines indicate DNS He profiles while blue solid lines are DNS H2 profiles. Error bars correspond to total measurement accuracy with 95% confidence interval.

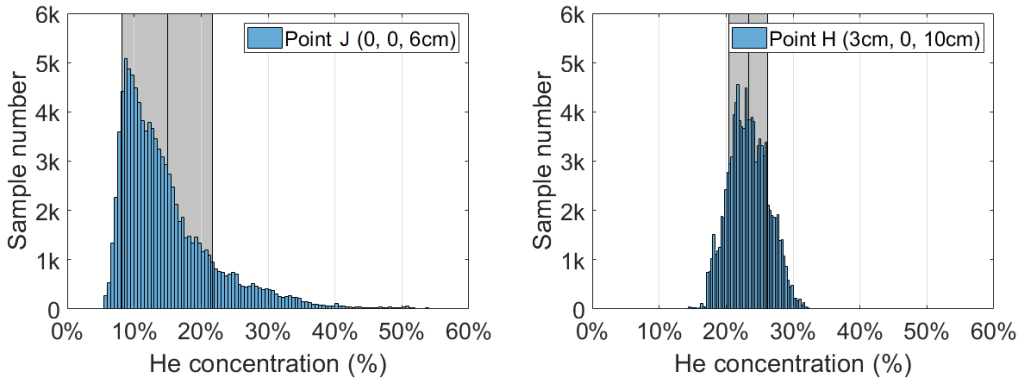

Figure 5.17: Histogram of instantaneous concentration variation at two monitoring points, helium case. Left: Point J (0,0,6cm) at jet border, right: Point H (3cm,0,10cm) in the centre of stratified layer at far field of the jet. 1-σ intervals are coloured in grey.

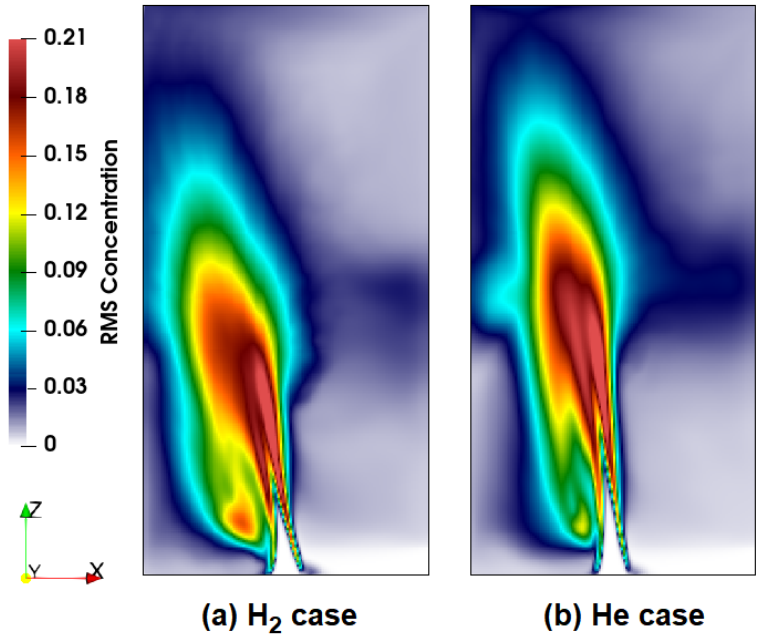

Figure 5.18: Distribution of light gas concentration RMS fluctuations at mid-plane y =0, left: hydrogen case, right: helium case.

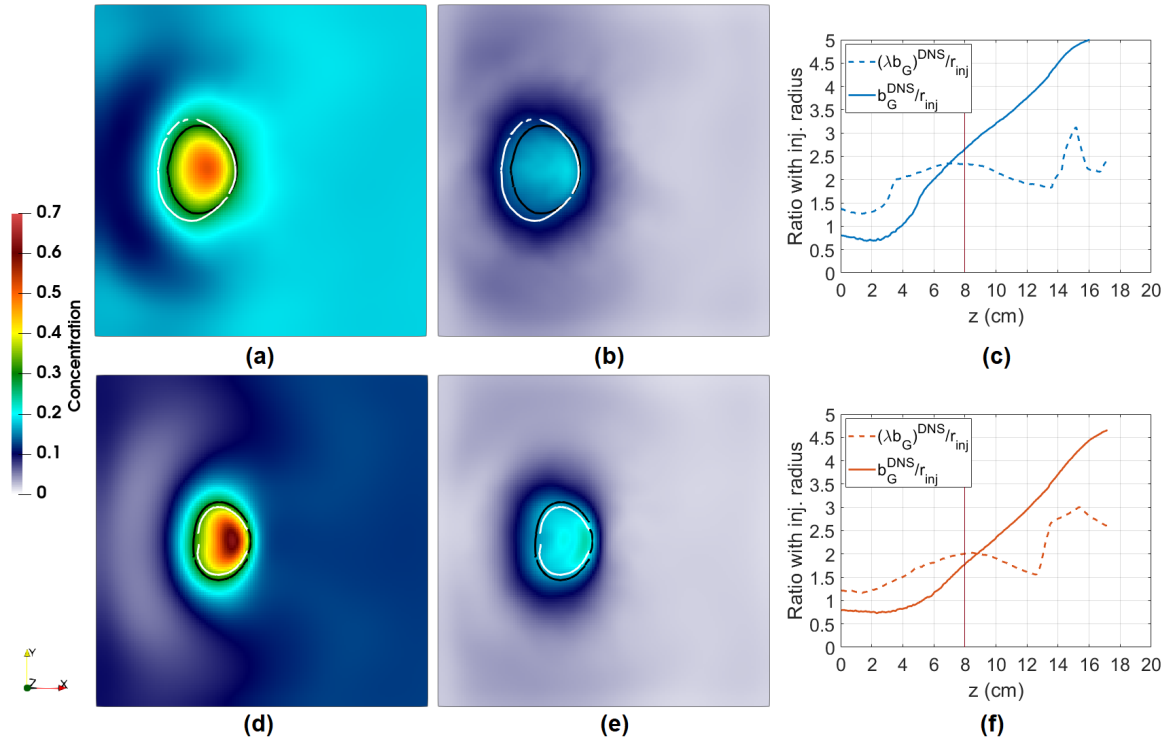

Figure 5.19: Comparison of characteristic jet radius $b_G^{DNS}(z)$ defined by Gaussian vertical velocity distribution on x-y plane and related characteristic concentration radius $(\lambda b_G)^{DNS}(z)$. (a)-(c) hydrogen case, (d)-(f) helium case. (a)(d) time-averaged light gas concentration at z =8cm; (b)(e) concentration RMS fluctuations at z =8cm, in the same colour scale. In these 4 figures, white contours indicate regions 1-σ of time-averaged vertical velocity, defined in eq. (4.42), black contours are regions 1-σ of time-averaged concentration, defined in eq. (4.44). (c)(f) variation of $b_G^{DNS}(z)$ and $(\lambda b_G)^{DNS}(z)$ along the jet.

point H is selected in the mi-height of stratified layer L_S where local concentration RMS fluctuations are maximal in the far field region. In contrast, as seen in figure 5.18, concentration RMS fluctuations are less than 1% in L_A and L_H.

We now discuss the reliability of time-averaged concentration field in risk analysis context.

Jet region

For the jet region, two sorts of information are needed in risk analysis: the risk region, in which concentration time fluctuations may present risk, as well as the associated concentration in this region for consequence evaluation.

If we admit that time-averaged concentration field could be **directly** used to determine the risk region, we shall note that this region, defined from average concentration field, does not accord with the "jet region" defined in jet theories because the latter one is associated with vertical velocity cross-section. In fact, the concentration cross-section (or density) is characterised by $(\lambda b_G)(z)$, defined in equation (4.44). DNS results (figure 5.19(c)(f)) show that this parameter is almost constant (about twice of injection radius) below the homogeneous layer whereas the characteristic jet radius $b_G(z)$ increases along the jet axis.

Nonetheless, we still cannot consider this parameter (λb_G) as the indicator of the risk region due to instability of jet flow. For illustration, we present in figure 5.19, cross-section distributions of average concentration (a)(d) as well as the corresponding RMS fluctuation (b)(e) in the same colour scale, at an altitude where $\lambda \approx 1$. The density characteristic region defined from $(\lambda b_G)(z = 8(cm))$ is shown in black contours in these figures. This region clearly does not cover all the area which potentially presents a risk. On one hand, the concentration at border of this region (30%) is much larger than the environmental concentration at this altitude (around 20% for H2, 15% for He). On the other hand, in the area where the average concentration is larger than 20%, local RMS fluctuations can also reach to 20%, which means that the average concentration does not make sense to calculate the lower bound of local concentration variation. Consequently, average concentration field cannot provide indications of jet risk region. This region must be estimated under the conservative safety strategy.

However, average concentration, associated with its RMS fluctuations, is clearly indicative in terms of order of magnitude of concentrations in risk analysis.

Far-field region

For the far-field region, as local concentration RMS is generally less than 1%, time-averaged concentration field is indicative (even conclusive) in determination of risk region and relevant consequence evaluation.

We have seen in the section 5.1.2 that the steady-state far-field concentration distribution can be characterised by a three-layer structure. We discuss in this part if this structure can be correctly represented by a few instantaneous concentration fields only.

We present in figure 5.20, the spatio-histogram of concentration distribution in the cavity (where jet region presents only a very little part). The concentration distribution is divided into 1000 intervals (0.1% for each) and the histogram is based on the numbers of points counted in each interval. There are 150x150x300 thus 6.75 million of monitoring points, uniformly distributed in the whole cavity. The histogram is coloured differently in three layers L_A, L_S and L_H.

For illustration, we present results of one instantaneous concentration field in figures (a)(b). The concentration distribution is clearly related to three-layer structure. Bottom layer L_A

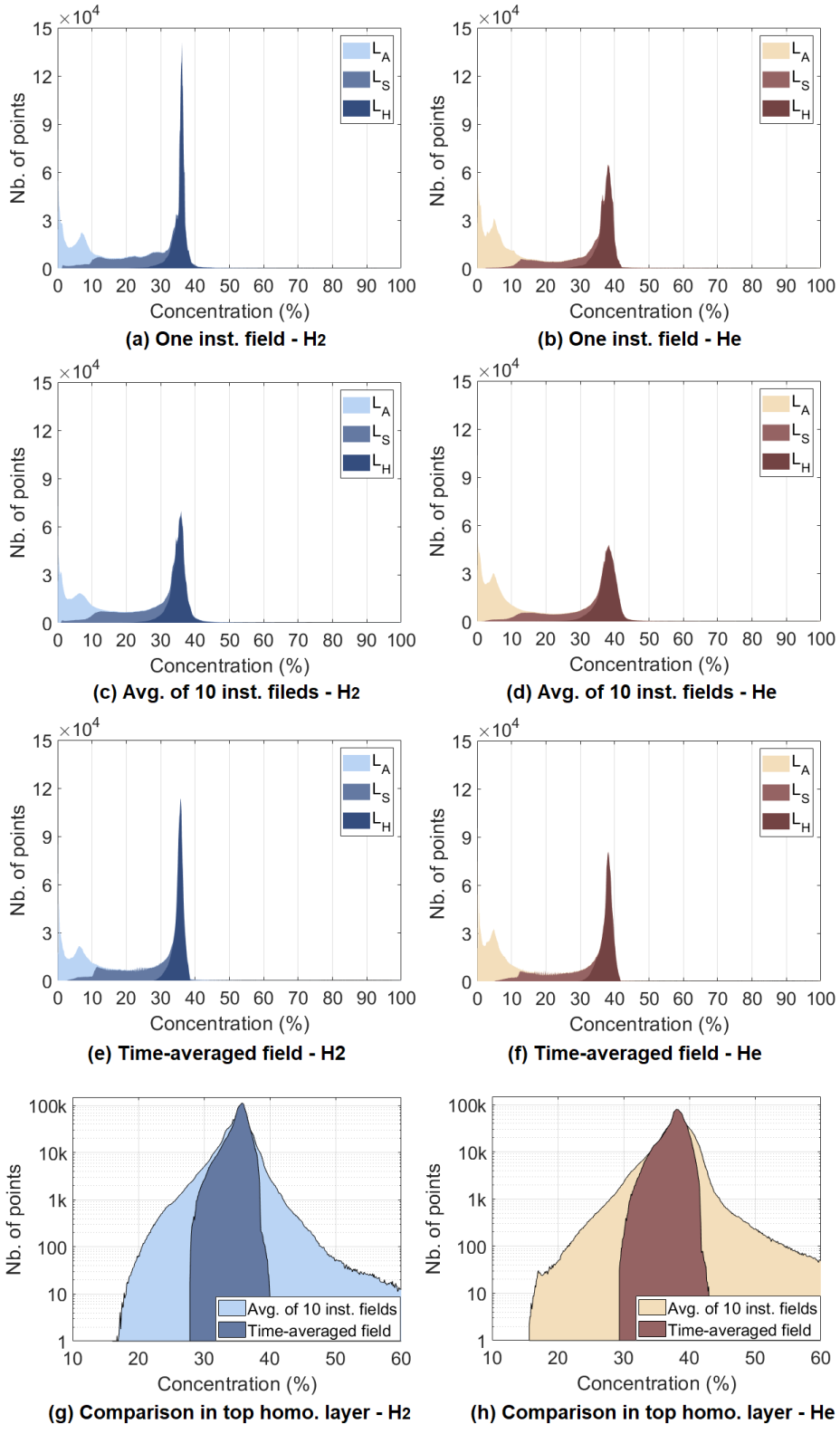

Figure 5.20: Histogram of concentration distribution in the main cavity . (a)(b) present one instantaneous concentration field; (c)(d) are the average histograms of 10 instantaneous concentration fields; (e)(f) are the histograms based on the time-averaged concentration fields. Results are presented with three-layer structure. L_A bottom quasi-fresh air layer, L_S intermediate stratified layer and L_H top homogeneous layer. (g)(h) illustrate the difference of histogram in the top homogeneous layer L_H between instantaneous fields and time-averaged field in log scale.

covers mainly all points of concentration lower than 10%. In stratified layer L_S, local concentration is almost uniformly distributed from 10% to 30%. A clear peak is observed in the top layer L_A, corresponding to the homogeneous concentration. Jet region is negligible in this figure as there are very few samples where local concentration is larger than 50%.

We consider comparing time-averaged concentration field with instantaneous fields. In figures (c)(d), the spatio-temporal histograms are presented, based on 10 independent instantaneous fields (with samples separating time 1s). The histogram is counted first separately for each instant, then averaged in each concentration interval. For comparison, another two histograms, based on time-averaged concentration fields, are presented in figures (e)(f). Their distributions in the layers L_A and L_S are almost the same. We thus focus on the top homogeneous layer L_H.

In figures (g)(h), we compare specifically histograms in L_H for the average of 10 instantaneous fields and time-averaged field in logarithm scale. We note that their peaks are in the same position with its horizontal extension much larger for instantaneous fields. We note that this additional horizontal extension for instantaneous fields contains samples in higher concentration intervals (40%-60%). This may present potential risk which cannot be estimated from the time-averaged field.

In general, the three-layer structure, obtained from average concentration field, can be simply calculated from 10 instantaneous concentration fields.

Conclusion 5.3

Firstly, by comparing DNS helium and hydrogen results, we confirm that, in this case, helium can be used as a substitutive gas for hydrogen risk analysis. These two cases present similar bi-layer distribution, same homogeneous concentration and comparable concentration RMS fluctuations. The main difference between two cases is the jet inclination, where hydrogen jet inclines a little more.

Secondly, time-averaged concentration field can be considered indicative (even conclusive) in risk analysis except in the jet area. In the jet region, average field cannot provide indications of jet risk region. This region must be estimated under the conservative safety strategy. In the far field region, steady-state concentration peak can be characterised by several instantaneous fields only.

5.4 Summary and discussion

In this chapter, we have presented the simulation results and its comparison with experimental measurements. We mainly focus on:

- Time-averaged flow pattern and its comparison with the bi-layer structure assumed in model of Linden et al. (1990)
- Jet evolution in the cavity
- Global conservation of volume flux and mass flux
- Comparison DNS-PIV for time-averaged velocity and RMS
- Comparison helium-hydrogen on concentration distribution
- Comparison instantaneous concentration fields with the time-averaged field

The flow is mainly turbulent in the cavity, thus its structure is characterised by the time-averaged fields. The principle of Linden's bi-layer flow structure is valid in the present case, but its interface is extended into a stratified layer in which mixture density varies quasi-linearly. The jet flow changes its form with its development: laminar jet, turbulent jet, turbulent jet plume, pure plume. Concentration distribution is similar between hydrogen and helium cases and time-averaged concentration is generally indicative in risk analysis.

Comparison DNS-PIV presents generally encouraging results. Most physical phenomena observed in the cavity are correctly modelled by DNS. Their differences are mainly shown on the x-direction velocity RMS in turbulent jet region.

In fact, the numerical modelling of a turbulent jet is technically much more difficult than that of a pure plume, as reported in Bernard-Michel et al. (2019). The turbulent jet flow is more sensitive to environmental perturbations while in PIV measurement, small perturbations at injection jet border, or other wispy environmental movements, even not obvious, may change completely the jet form and its axis in its development. As this kind of perturbation is usually aleatory, its influence appears more clearly in RMS fields rather than time-averaged fields.

Despite these differences, the numerical results is considered valid and will be treated as "ground truth" in the following study of the models. In the next chapter, DNS-deduced profiles of 1D jet quantities, will be compared with theoretical results based on different turbulent jet models.

Part IV

1D modelling

Chapter 6

Turbulent jet models applied in stratified environment

In this chapter, we compare DNS estimated 1D profiles of the jet with theoretical models, to evaluate the performance of these models applied in stratified environment. Two profiles are specifically analysed: jet volume flux, which is directly used in global conservation equation in ventilation model (see chapter 3), as well as Top-hat jet concentration, which is indicative in safety analysis. Recall that the jet extension defined in jet theories by its velocity field does not make sense in safety analysis thus will not be detailed analysed. There are two aspects particularly considered in the modelling, the Boussinesq approximation, under which the density difference is neglected, as well as the entrainment modelling, with a constant or variable entrainment coefficient. Three approaches presented in chapter 2, Boussinesq models of Morton et al. (1956) and Kaminski et al. (2005), and non-Boussinesq model of Rooney and Linden (1996) will be analysed.

Model of Morton et al. (1956) is based on the Boussinesq approximation and constant entrainment coefficient, commonly used in hydrogen safety assessment (Fuster et al. (2017)). However, as the key parameter entrainment coefficient is very sensible to the estimated concentration, its partial use is generally based on a highly conservative method. The choice of this coefficient is not related to its physical value, but a universal one, in order to guarantee the safety margin in risk analysis. As a result, additional cost is required for compensate the wrong estimation of concentration. We study in the first section, the influence of each assumption applied in this model and seek to reduce the sensitivity of entrainment coefficient.

Besides, model of Rooney and Linden (1996) is also proposed to be used. In the second section, we will present the performance of this non-Boussinesq model and to compare it with the Boussinesq approach. In the models of Morton et al. (1956) and Rooney and Linden (1996), entrainment is modelled by a constant coefficient α. We will compare in the third section of this chapter, the variation of this entrainment coefficient, estimated by DNS results, with its choice in α–constant models.

In the last part, we analyse the performance of typical α–variable turbulent jet model, that of Kaminski et al. (2005). In this model, Richardson number is used as an indicator of jet flow based on which the entrainment coefficient is predicted. We compare the predicted α profile with DNS deduced α profile. Then a quasi-analytical approach is presented to see if this α–variable model could be directly used in hydrogen injection problem.

Most of the modelling results presented in this chapter is based on hydrogen case while helium case presents similar profiles and same remarks (He results presented in appendix F).

6.1 Boussinesq approaches with constant entrainment coefficient

Morton et al. (1956) proposed a turbulent jet model under Boussinesq approximation. Explicit analytical solutions are provided for pure plume (with small momentum injection) as presented in equations (2.41)-(2.45) for homogeneous environment. Hunt and Kaye (2001) proposed a three-step correction for a general injection condition by introducing a virtual origin displacement. In this approach, the entrainment coefficient α_T, under Top-hat assumption and assumed constant along the jet, shall be provided beforehand.

6.1.1 Conservative safety approach

We present firstly the conservative safety approach, where entrainment coefficient is chosen equal to 0.05 in a conservative way (for any injection flux), as this choice provides always overestimated concentration for a general jet or plume. Analytical solutions (2.41)-(2.45) are directly applied with point source and small injection assumption (virtual origin displacement neglected).

$$\mathcal{Q}(z) = \frac{6}{5}\left(\frac{9}{10}\right)^{1/3} \pi^{2/3} {\alpha_T}^{4/3} \mathcal{B}_0^{1/3} z^{5/3} \tag{6.1}$$

with $\alpha_T = 0.05$. Then the Top-hat reduced gravity is deduced by

$$G'_T(z) = \frac{\mathcal{B}_0}{\mathcal{Q}(z)} \tag{6.2}$$

with $\mathcal{B}_0$ is calculated by injection condition. Light gas concentration is then deduced by $G'_T(z)$

$$X_{1,T}(z) = \frac{\rho_a}{\rho_a - \rho_{inj}} \frac{G'_T(z)}{g} \tag{6.3}$$

For illustration, we present in figure 6.1 the profiles $\mathcal{Q}(z)$ and $X_{1,T}(z)$ for hydrogen case obtained from this method, compared with DNS deduced profiles considered as reference. The volume flux is largely underestimated and the estimated hydrogen concentration is always larger than the DNS reference value. The above formula is not applicable until z =14cm and jet concentration decreases in the rest of the cavity. In this case, the conservative strategy provides a very large safety margin while the homogeneous layer could not be correctly modelled. This margin will generate large additional cost just due to the bad estimation of the model.

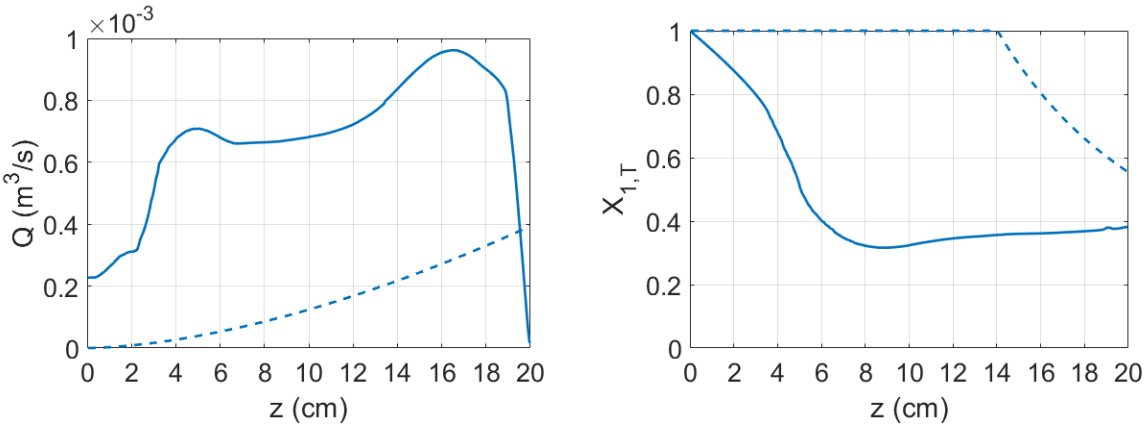

Figure 6.1: Profiles conservative approach with α_T =0.05. Left: variation of jet volume flux $\mathcal{Q}(z)$, right: variation of Top-hat concentration $X_{1,T}(z)$. Hydrogen case, DNS deduced profiles in solid lines, 1D modelling in dashed lines.

6.1.2 Injection volume flux correction

We apply the first correction of the model on the injection volume flux by introducing the notion of virtual origin. We consider the injection flux is as in the middle range of a pure buoyancy plume whose source is situated at $z_t < 0$ below the injection level, and whose buoyancy flux is conserved along the plume and equal to $\mathcal{B}_0$. This virtual plume is developed to possess the same cross-section volume flux as injection flux at injection level $z = 0$. Consequently,

$$Q_{inj} = \mathcal{Q}(0) = \frac{6}{5}\left(\frac{9}{10}\right)^{1/3} \pi^{2/3} {\alpha_T}^{4/3} \mathcal{B}_0^{1/3} (-z_t)^{5/3} \tag{6.4}$$

We have thus a relation between α_T and z_t. We change the value of α_T to minimise discrepancy of concentration profile between DNS estimated profiles and analytical solutions in the lower mixing layer L_A where the unstratified environment assumption could be considered valid. We obtain

$$\alpha_T = 0.065 \text{ for hydrogen case, } \alpha_T = 0.058 \text{ for helium case} \tag{6.5}$$

which correspond to the value of pure turbulent jet.

We present in figure 6.2 the profiles of jet volume flux $\mathcal{Q}(z)$ and Top-hat concentration $X_{1,T}(z)$ obtained by 1D modelling and DNS. The estimation of jet volume flux is valid for area $z < 2$cm then for z =11-16cm where presented respectively the laminar jet flow and turbulent plume flow. 1D model underestimates the volume flux at turbulent jet region. For hydrogen concentration, the 1D estimation is good below the stratified layer around z <10cm and underestimates in the top homogeneous layer. This is mainly because the Morton's analytical solution is based on unstratified environment assumption where the far-field environmental density is considered as fresh air all along the jet. This hypothesis is valid only in the lower part of the cavity.

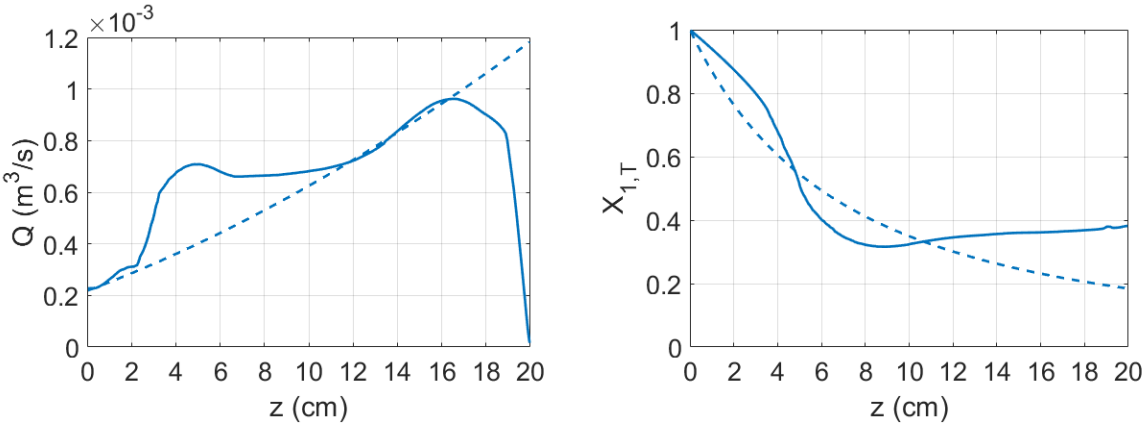

Figure 6.2: Injection volume flux correction approach with α_T =0.065. Left: variation of jet volume flux $\mathcal{Q}(z)$, right: variation of Top-hat concentration $X_{1,T}(z)$. Hydrogen case, DNS deduced profiles in solid lines, 1D modelling in dashed lines.

6.1.3 Quasi-analytical approach considering environmental variation

The third approach is to solve conservation equations numerically by 4^{th} order Runge-Kutta method (RK4) with "accurate" initial conditions and variation of environmental density along the jet, called here quasi-analytical solutions.

Classic Boussinesq model is provided by Morton et al. (1956) based on three characteristic jet quantities: volume flux $\mathcal{Q}$, momentum flux $\mathcal{M}$ and buoyancy flux $\mathcal{B}$. Conservation equations of the jet are called Morton's equation (see section 2.3.2)

$$\begin{cases} \dfrac{d\mathcal{Q}}{dz} = 2\alpha_T \sqrt{\pi \mathcal{M}} \\ \dfrac{d\mathcal{M}}{dz} = \dfrac{\mathcal{B}\mathcal{Q}}{\mathcal{M}} \\ \dfrac{d\mathcal{B}}{dz} = -N^2 \mathcal{Q} \end{cases} \tag{6.6}$$

with $N^2 = -\dfrac{g}{\rho_0}\dfrac{d\rho_e}{dz}$ the square of the Brunt-Vaisala buoyancy frequency.

The initial conditions $\mathcal{Q}(0), \mathcal{M}(0), \mathcal{B}(0)$ are provided by DNS measurement at $z = 0$. $N^2(z)$ profile is calculated by $\rho_e^{DNS}(z)$ in 4^{th} order. These differential equations are solved numerically by 4^{th} order Runge-Kutta method with altitude discretisation $dz = \delta x$ the mesh cell size.

As here the environmental density $\rho_e(z)$ is provided by DNS results, thus we are no longer in a homogeneous environment assumption. We need to determine the entrainment coefficient α_T in this case. As the buoyancy flux $\mathcal{B}$ is the only characteristic jet quantity influenced directly by the variation of $\rho_e(z)$, the entrainment coefficient α_T is chosen to minimise the discrepancy between $\mathcal{B}^{DNS}(z)$ and that calculated by theoretical models in the top homogeneous layer. The value of α_T is selected as

$$\alpha_T = 0.052 \text{ for hydrogen case, } \alpha_T = 0.038 \text{ for helium case} \tag{6.7}$$

which correspond physically to a pure turbulent jet.

In figure 6.3, we present the variation of three characteristic jet quantities in Morton's model as well as the variation of Top-hat concentration evolution $X_{1,T}(z)$, both for DNS estimated profiles and quasi-analytical solutions. The modelling results are much more precise compared with previous approaches.

- The estimation of $\mathcal{Q}(z)$ is not bad at the beginning of the jet ($z < 2.5$cm) where the jet flow is laminar. It is followed by a sudden increase until $z \approx 5$cm due to specific geometrical configuration in the present case (same-side vertical openings). Detailed analysis has presented in chapter 5.
- Profiles of momentum flux $\mathcal{M}(z)$ are very dissimilar. Momentum flux decreases in DNS due to large density difference of air and hydrogen. Boussinesq models cannot therefore provide good estimation of this quantity.
- Two profiles of $\mathcal{B}(z)$ nearly superpose in the homogeneous layer typically for $z > 12$cm. Profiles reach to zero in the upper part of the cavity. A difference around 20% could be found at the altitude 3-7cm.
- The estimation of hydrogen concentration $X_{1,T}(z)$ is good all along the jet, especially in the homogeneous layer where two profiles converge to the same level. The estimation of light gas concentration is much better if we take into account the variation of environmental density.

6.1.4 Sensitivity of entrainment coefficient

We discuss in this section the sensitivity of entrainment coefficient α_T. As in Morton's model, this coefficient is chosen constant along the jet, its value is reported highly sensitive to the modelling results, especially for the concentration modelling. (Bernard-Michel (2014))

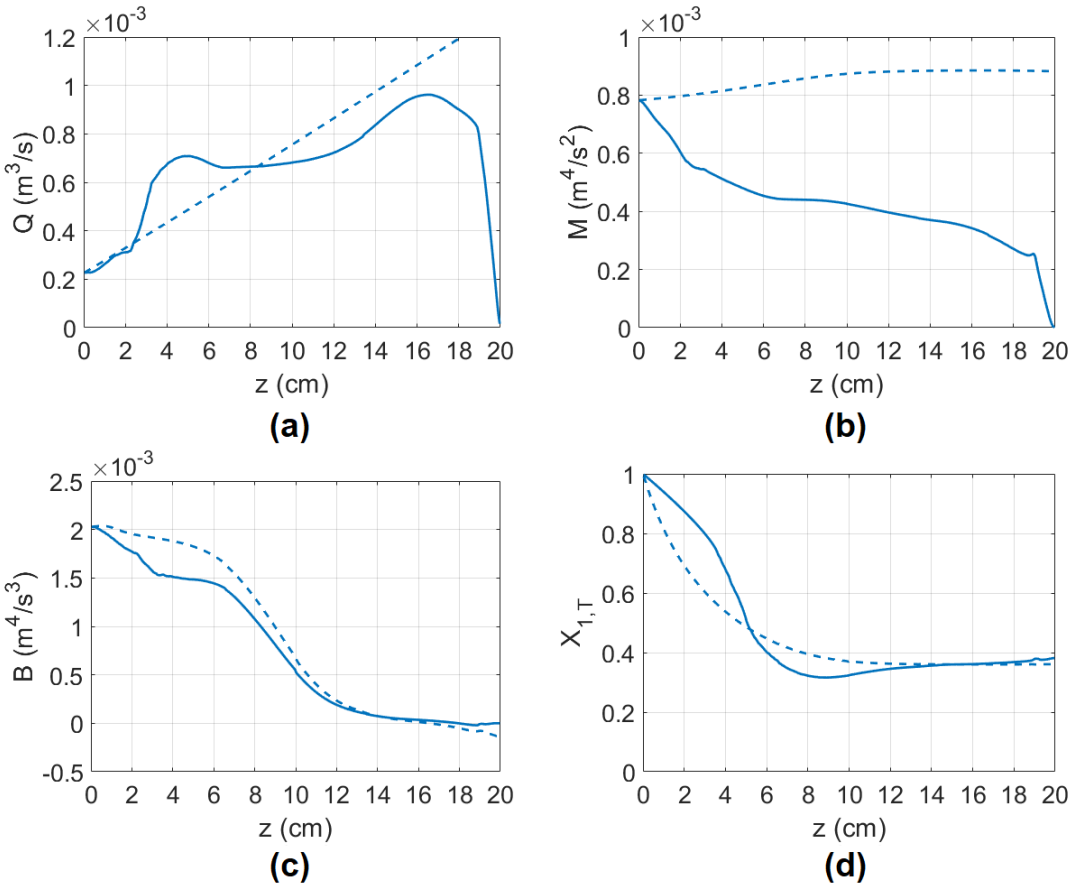

Figure 6.3: Quasi-analytical Boussinesq approach with α_T =0.052, considering the variation of far-field environmental density. (a) variation of jet volume flux $\mathcal{Q}(z)$, (b) variation of jet momentum flux $\mathcal{M}(z)$, (c) variation of jet buoyancy flux $\mathcal{B}(z)$, (d) Top-hat concentration $X_{1,T}(z)$. Hydrogen case, DNS deduced profiles in solid lines, 1D modelling in dashed lines.

We begin with the original conservative approach. In figure 6.4-(a)(b), we present the comparison of profiles $\mathcal{Q}(z)$ and $X_{1,T}(z)$ obtained with α_T =0.05 and 0.10, compared with reference DNS profiles. We remark an obvious sensitivity of the value of α_T. Passage from α_T =0.05 to 0.10 will result in an increase 2.52 times of jet volume flux and a decrease 33.5% (in absolute value) of concentration at z = 20cm. A wrong estimation of this value will generate large errors in modelling. If α_T is applied as 0.10, the modelled concentration is underestimated for region z >15cm thus the conservative safety strategy is not always guaranteed. That is why in the practical use, a highly conservative value α_T =0.05 is preferred to be always applied.

If we take the correction of injection volume flux, but still apply Morton's analytical solutions in unstratified environment, we have results as presented in 6.4-(c)(d). If we pass α_T from 0.05 to 0.10, the modelled jet volume flux will still increase 1.83 times, but its concentration decreases only 10.4% in absolute value. Compared with the above results, the sensitivity of entrainment coefficient is largely reduced for concentration estimation.

Lastly, we take the quasi-analytical approach considering environment variation. Results are presented in 6.4-(e)(f). If we change α_T from 0.05 to 0.10, the jet volume flux will still increase 1.79 times but for hydrogen concentration, it will only decrease 4.6% in absolute value. Height of homogeneous layer keeps the same. Consequently, we could consider this approach provides an error-controllable concentration modelling in the jet.

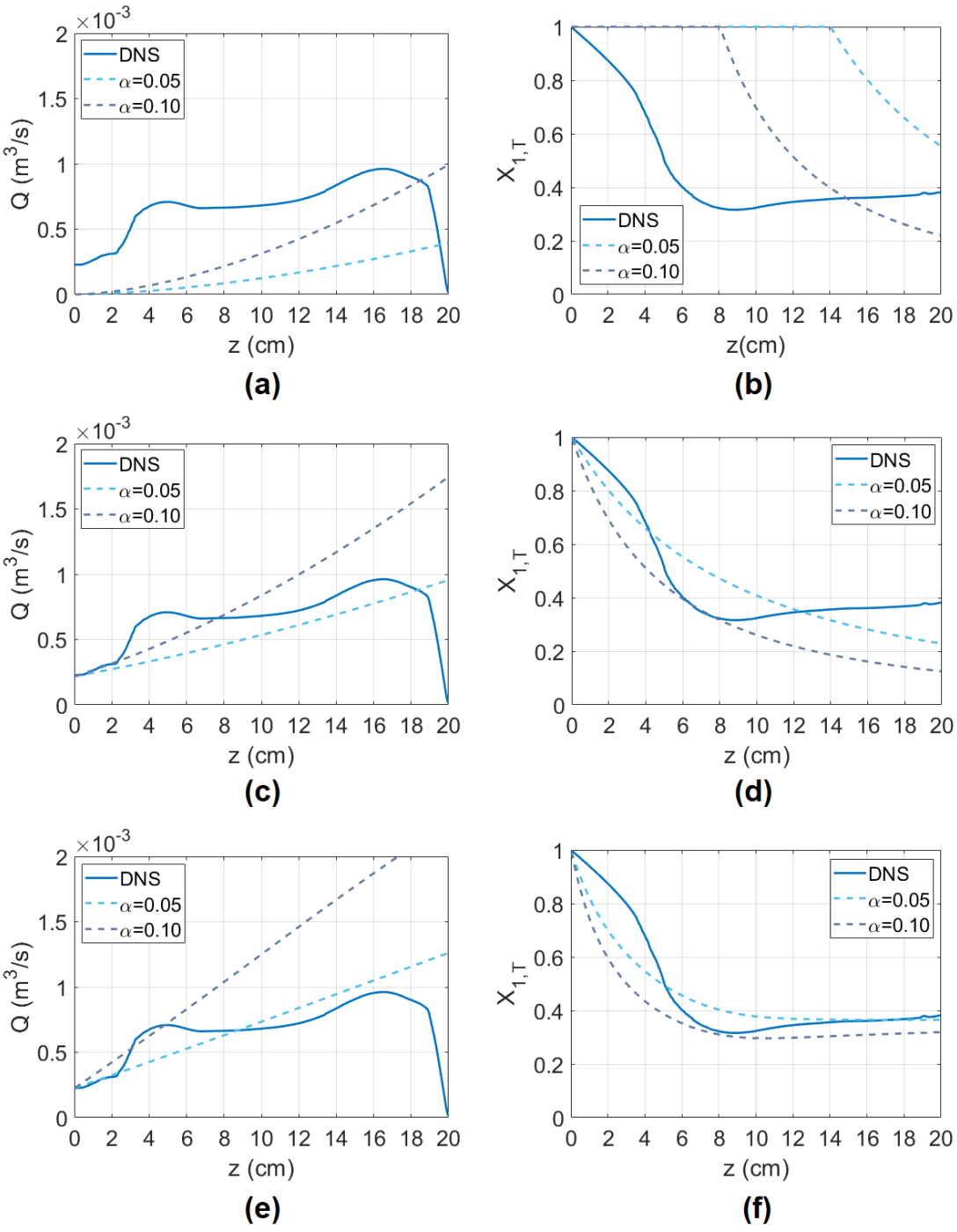

Figure 6.4: Evaluation of sensitivity of entrainment coefficient, comparison profiles DNS and 1D Boussinesq modelling with α_T =0.05 and 0.10. Hydrogen case. (a)(b) Profiles $\mathcal{Q}(z)$ and $X_{1,T}(z)$ obtained by conservative approach; (c)(d) Profiles $\mathcal{Q}(z)$ and $X_{1,T}(z)$ obtained after correction of injection volume flux; (e)(f) Profiles $\mathcal{Q}(z)$ and $X_{1,T}(z)$ obtained by quasi-analytical approach considering environmental variation.

Conclusion 6.1

In conclusion, direct use of analytical solutions of Morton et al. (1956) presents two aspects of limits. Firstly is the unknown variation of environmental density, which is commonly observed in a confined environment where injected hydrogen gas accumulates in the cavity. Secondly is the entrainment coefficient is not easy to determine and very sensible to final results. That is why in practical use, a very conservative approach is always required, generating huge safety margin and large additional cost. A good estimation is obtained if we provide reasonable corrections of injection flux and environmental variation. However, Morton's Boussinesq model cannot correctly evaluate the influence of density difference in the mixing, which provides wrong estimation of jet momentum flux profile.

The high sensitivity of entrainment coefficient is due to wrong assumptions applied in the resolution. Physical corrections, as for injection flux or environmental variation will improve the sensitivity of entrainment coefficient in hydrogen concentration modelling. Among these corrections, injection flux correction can be directly used in natural ventilation model (will be detailed analysed in chapter 7) but environment change cannot be directly integrated in ventilation model. Generally, the more physical conditions are applied in the model, the more precise the prediction will be and the less sensitivity of entrainment coefficient will present to concentration modelling result.

6.2 Non Boussinesq approaches with constant entrainment coefficient

In non-Boussinesq model of Rooney and Linden (1996), the conservation of volume flux is no longer assumed. The flow is considered compressible. Three characteristic jet quantities are used: the volume flux $\mathcal{Q}$, the mass flux $\mathcal{Q}_m$ and the momentum mass flux $\mathcal{M}_m$. Under Top-hat assumption, the conservation equations could be rewritten as an ODE system (2.62)-(2.64) where only characteristic jet quantities appear.

$$\begin{cases} \dfrac{d\mathcal{Q}_m}{dz} = 2\alpha_T \rho_e \sqrt{\dfrac{\pi \mathcal{M}_m}{\rho_0}} \\ \dfrac{d\mathcal{M}_m}{dz} = g\left(\rho_e - \dfrac{\mathcal{Q}_m}{\mathcal{Q}}\right)\dfrac{\mathcal{Q}\mathcal{Q}_m}{\mathcal{M}_m} \\ \dfrac{d\mathcal{Q}}{dz} = 2\alpha_T \sqrt{\dfrac{\pi \mathcal{M}_m}{\rho_0}} \end{cases} \tag{6.8}$$

6.2.1 Quasi-analytical approach and evaluation of Boussinesq effect

Similar as that done in Boussinesq case, the above ODE system can be solved numerically by 4^{th} order Runge-Kutta method with initial conditions $\mathcal{Q}(0), \mathcal{Q}_m(0), \mathcal{M}_m(0)$ provided by injection conditions. The environmental density profile is provided by DNS $\rho_e^{DNS}(z)$ as well. The reference density ρ_0 is selected as that of the fresh air $\rho_0 = \rho_a$.

The method to determine α_T is the same as before. We select α_T to minimise the discrepancy of buoyancy flux $\mathcal{B}(z)$ between DNS estimated profile and that from Rooney's model, as this parameter characterises the variation of buoyancy force and density difference between inside and outside the jet. A simple relation is used to deduce $\mathcal{B}$:

$$\mathcal{B} = \frac{g}{\rho_a}(\rho_e \mathcal{Q} - \mathcal{Q}_m) \tag{6.9}$$

Note that in non Boussinesq model, the definition of entrainment coefficient is different with that in Boussinesq case. An additional term $\sqrt{\frac{\rho_T(z)}{\rho_0}}$ is added in its definition. See equation (2.57). Here we have from DNS results,

$$\alpha_T = 0.124 \text{ for hydrogen case, } \alpha_T = 0.082 \text{ for helium case} \tag{6.10}$$

This does not represent any jet form as in non Boussinesq model, entrainment coefficient is no longer an indicator of jet flow pattern (it depends on mixture density as well).

In figure 6.5, we present profiles of characteristic jet quantities: volume flux $\mathcal{Q}(z)$, mass flux $\mathcal{Q}_m(z)$, mass momentum flux $\mathcal{M}_m(z)$, buoyancy flux $\mathcal{B}(z)$ as well as the Top-hat jet hydrogen concentration $X_{1,T}(z)$, for DNS hydrogen case and 1D non Boussinesq quasi-analytical modelling.

- The model provides nearly linear profiles for $\mathcal{Q}$ and $\mathcal{Q}_m$, which are accurate around the injection laminar jet region $z < 3$cm. The model provides a relative error around 20-25% in the homogeneous layer for $\mathcal{Q}$ and $\mathcal{Q}_m$.
- The estimation of buoyancy flux (d) is accurate especially for homogeneous layer where $z > 10$cm. The model overestimates the buoyancy flux $\mathcal{B}$ around 20-25% for 3cm $< z <$ 8cm.
- The profile of jet concentration (e) is well modelled in the cavity. The top homogeneous layer clearly appears and its height is well estimated.
- The estimation of mass momentum represents the most important difference between Boussinesq model and non-Boussinesq model. Not as in Boussinesq case, non Boussinesq model provides good estimation of mass momentum flux for region $z < 8$cm.

Furthermore, if we compare the estimation of volume flux $\mathcal{Q}(z)$ and hydrogen concentration $X_{1,T}(z)$ between Boussinesq model and non-Boussinesq model, as presented in figure 6.6, we will find that two profiles are quite similar. In the stratified layer below the interface, the estimated jet volume fluxes are almost identical for two cases. The non-Boussinesq estimated concentration is lightly larger than that of Boussinesq. In the top homogeneous layer, non-Boussinesq model provides a larger $\mathcal{Q}$ and the same concentration as in Boussinesq case.

In summary, compared with Boussinesq approach, non Boussinesq model provides a good estimation of mass momentum profile, but their performance is quite identical for other characteristic jet quantities and parameters.

The treatment of momentum term, which represents the jet kinetic energy, is quite different whether we study in Boussinesq case or not (see detailed demonstration in appendix A). In Boussinesq model, the density difference is totally ignored that the revolution of momentum flux in the jet is entirely based on the reference density whereas in non-Boussinesq model, the density difference is well considered in conservation equations.

6.2.2 Sensitivity of entrainment coefficient

Rooney and Linden (1996) provided a non-Boussinesq approach and associated analytical solutions, see equations (2.68)-(2.73). The same as in Morton's Boussinesq model, these analytical solutions are for a pure plume with no momentum at injection. An additional virtual origin correction is usually needed, see Carlotti and Hunt (2005). Besides, analytical solutions are valid only for homogeneous environment where both environmental density ρ_e and buoyancy flux $\mathcal{B}$ are assumed constant along the jet.

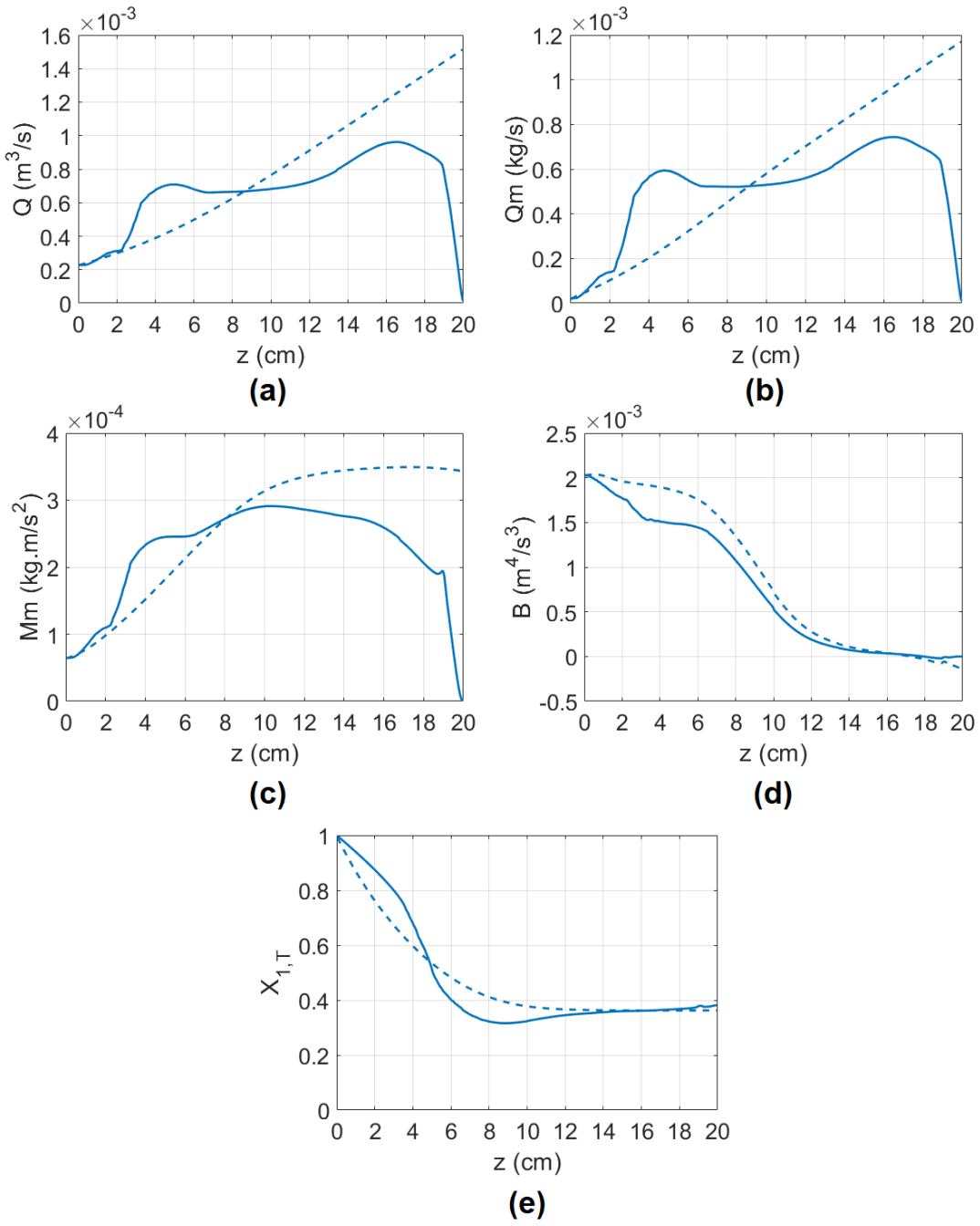

Figure 6.5: Quasi-analytical non Boussinesq approach with α_T =0.124, considering the variation of far-field environmental density. (a) variation of jet volume flux $\mathcal{Q}(z)$, (b) variation of jet mass flux $\mathcal{Q}_m(z)$, (c) variation of jet mass momentum flux $\mathcal{M}_m(z)$, (d) variation of jet buoyancy flux $\mathcal{B}(z)$, (e)Top-hat concentration $X_{1,T}(z)$. Hydrogen case, DNS deduced profiles in solid lines, 1D modelling in dashed lines.

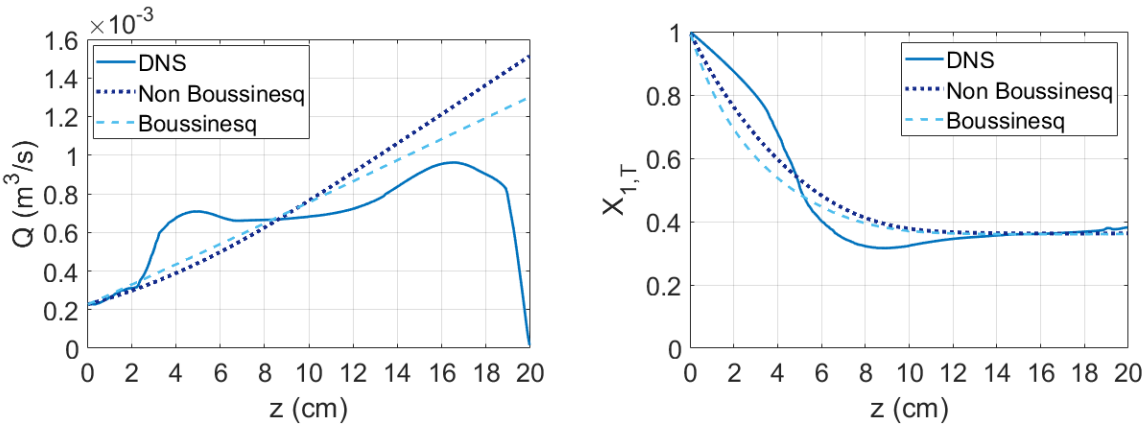

Figure 6.6: Comparison of quasi-analytical resolution in Boussinesq approach and non Boussinesq approach. Left: variation of jet volume flux $Q(z)$, right: variation of Top-hat concentration $X_{1,T}(z)$. Hydrogen case, DNS deduced profiles in solid lines, 1D modelling in dashed lines.

Same as presented in the section 6.1.4, we examine the sensitivity of entrainment coefficient with different approaches of non-Boussinesq model. In figure 6.7, we present modelling results of volume flux and hydrogen concentration profiles with two values of entrainment coefficient, 0.05 and 0.10. And for three approaches: (a)(b) correspond to direct application of Rooney's analytical solutions eq. (2.68)-(2.73) without any correction, like the conservative safety method applied in Boussinesq model. (c)(d) present the results of analytical solutions but with injection correction (by introducing virtual origin displacement). Lastly, (e)(f) represent the quasi-analytical approach proposed in the above section 6.2.1.

Use of analytical solutions results in high sensitivity of α_T to modelling results. Change of entrainment coefficient from 0.05 to 0.10 will make the jet volume flux doubles (2.00 times for its direct use and 1.92 times after injection correction). Hydrogen concentration decreases 18.3% in absolute value for direct application and 15.1% after injection correction. However, compared with Boussinesq results (figure 6.4), the sensitivity of α_T as well as the overestimated hydrogen concentration (safety margin) for non Boussinesq solutions is smaller. Non Boussinesq model provides relatively a better estimation.

If we consider the environmental variation and apply quasi-analytical approach, this change for α_T from 0.05 to 0.10 will keep 1.81 times increase for volume flux but largely reduced to 6.3% decrease in absolute value for hydrogen concentration in the jet.

Conclusion 6.2

In conclusion, compared with Boussinesq models, use of non Boussinesq approaches presents following aspects of interests. The variation of density difference is considered in the demonstration and the modelling of momentum term is much better than in Boussinesq case. If environmental variation is correctly provided, the jet evolution (volume flux and concentration) will be almost identical to that in Boussinesq case, very well matching with DNS reference profiles. Besides, direct use of non Boussinesq analytical solutions generates a safety margin smaller than Boussinesq solutions.

Besides, the entrainment coefficient in non Boussinesq model is larger than that in Boussinesq model due to additional term in its definition.

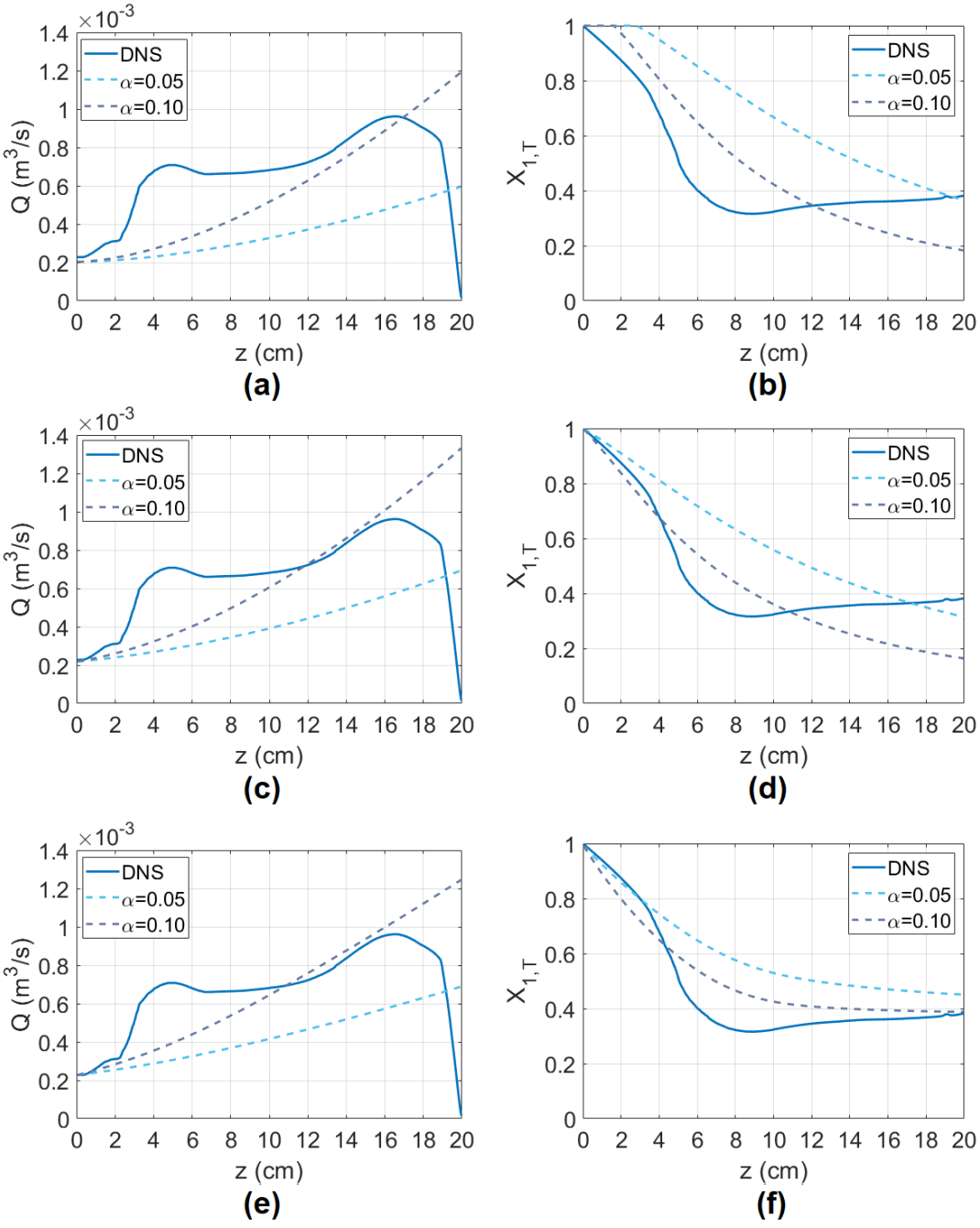

Figure 6.7: Evaluation of sensitivity of entrainment coefficient, comparison profiles DNS and 1D non Boussinesq modelling with α_T =0.05 and 0.10. Hydrogen case. (a)(b) Profiles $\mathcal{Q}(z)$ and $X_{1,T}(z)$ obtained by direct application of Rooney's analytical approach; (c)(d) Profiles $\mathcal{Q}(z)$ and $X_{1,T}(z)$ obtained after correction of injection volume flux; (e)(f) Profiles $\mathcal{Q}(z)$ and $X_{1,T}(z)$ obtained by quasi-analytical approach considering environmental variation.

6.3 Turbulent jet modelling with variable entrainment coefficient

Experimental studies show that the entrainment coefficient is variable with jet development (e.g. Cariteau (2010b)). In this section, we study the variation $\alpha(z)$ along the jet. On the one hand, we test the reliability of several models in the literature to provide the variation of $\alpha(z)$. On the other hand, we test the performance of α-variable turbulent jet models, such as that of Kaminski et al. (2005).

6.3.1 Variation of entrainment coefficient along the jet

The entrainment coefficient possesses different definitions under Boussinesq or non-Boussinesq assumptions (see equation (4.72)). It depends also on the profile assumption of jet parameter (Top-hat or Gaussian). The relation between Top-hat entrainment coefficient α_T and Gaussian α_G is simple: $\alpha_T = \sqrt{2}\alpha_G$. In this section, only Top-hat entrainment coefficients are presented and analysed.

The variation of α_T can be estimated indirectly from entrainment velocity, which can be measured from DNS time-averaged results. We analyse separately the DNS deduced profiles $\alpha_T^{DNS}(z)$ in Boussinesq and non-Boussinesq cases.

Boussinesq case

Under the Boussinesq approximation and Top-hat assumption, the entrainment coefficient is linked to the entrainment velocity and vertical velocity: $\alpha_T(z) = u_e(z)/w_T(z)$.

We present in the figure 6.8-(a)(b) the variation of DNS estimated Boussinesq entrainment coefficient along the jet $\alpha_T^{DNS-B}(z)$, for hydrogen and helium cases, as well as the best-estimated constant α_T determined by quasi-analytical resolution in section 6.1.3 (0.052 for H2 and 0.038 for He). The variation of $\alpha_T^{DNS-B}(z)$ presents generally a continuous increase along the jet. Comparing with jet evolution (table 5.2), we divide the profile into 5 regions.

- **Laminar region** where z <2-3cm, entrainment coefficient is very little and nearly zero. The jet flow is completely laminar, and the entrainment effect is not obviously presented.

- **Turbulent flow developing region** where 2cm< z < 4cm for H2 and 3cm< z < 6cm for He, entrainment coefficient continues increasing along the jet. The jet flow is more and more turbulent, the entrainment effect is more and more important.

- **Pure turbulent jet region** where 4cm< z < 11cm for H2 and 6cm< z < 12cm for He, the jet flow is completely turbulent and keeps in the jet form. The entrainment coefficient is stable with α_T=0.04-0.05, corresponding to a pure turbulent jet.

- **Jet-plume region** where 11cm< z < 15cm for H2 and 12cm< z < 15cm for He, the entrainment effect is more and more significant with decreasing buoyancy and momentum force. The jet is becoming progressively a turbulent plume. At z = 15cm, the entrainment coefficient corresponds to a quasi-pure turbulent plume with α_T=0.12-0.15.

- **Outflow region** where z > 15cm, the pressure difference across top opening begins to influence the flow direction as the opening is situated vertically in the lateral wall. The momentum force in vertical direction decreases sharply and the entrainment coefficient as well. The turbulent jet theory is no longer applicable.

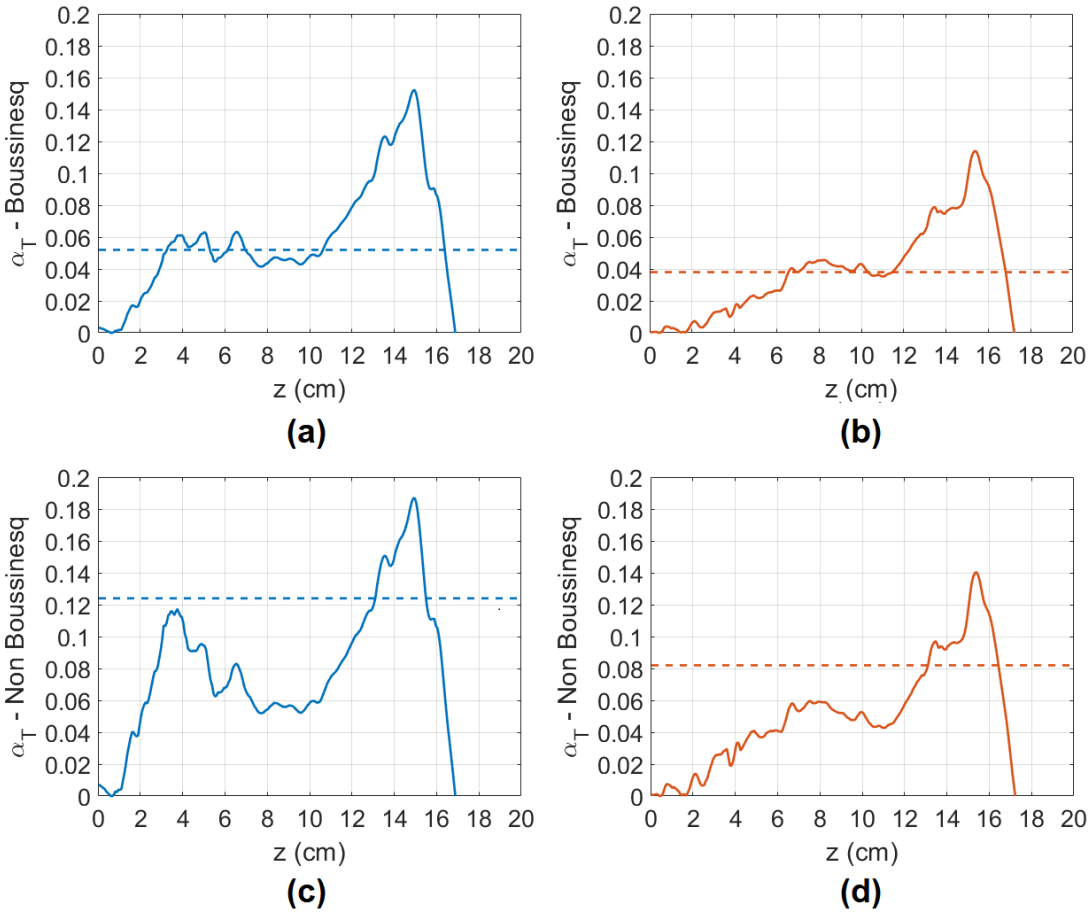

Figure 6.8: Variation of entrainment coefficient along the jet, DNS profiles and best-estimated values in α−constant models. (a) hydrogen jet under Boussinesq approximation, (b) helium jet under Boussinesq approximation, (c) hydrogen jet for non Boussinesq case, (d) helium jet for non Boussinesq case. DNS results are in solid lines while best-estimated values are in dashed lines.

We compare the profile of $\alpha_T^{DNS-B}(z)$ with best-estimated α_T obtained from quasi-analytical α-constant approach (in section 6.1.3). The best-estimated value corresponds to the pure turbulent jet region where local variation of α_T^{DNS-B} is in a plateau. This value is representative to the flow regime mostly presented in the jet development. Roughly speaking, we may also consider it corresponds to the value of the entrainment coefficient averaged along the jet.

The variation of $\mathcal{B}(z)$, which, according to Morton's theory, is directly linked to the Brunt-Vaisala buoyancy frequency and associated with the slope change of environmental density variation $\rho_e(z)$.

$$\frac{d\mathcal{B}}{dz} = -N^2\mathcal{Q}, \text{ with } N = \sqrt{-\frac{g}{\rho_0}\frac{d\rho_e}{dz}} \tag{6.11}$$

As presented in figure 5.4(e)(f), this buoyancy frequency presents a clear peak in the jet development, around $z = 9$cm for hydrogen case and $z = 10$cm for helium case, corresponding to the levels where environmental stratification is the most obviously presented. In quasi-analytical resolution, $\mathcal{B}(z)$ is selected as the key quantity to determine the value of α_T. Therefore, the best-estimated α_T must be chosen to provide good modelling results in the stratified region where environmental density changes sharply with increasing altitude, especially for the level

where N reaches to its maximum. In the present case, this stratified region is nearly coincided with the pure turbulent jet plateau where $\alpha_T^{DNS-B}(z)$ changes little.

Non-Boussinesq case

In non-Boussinesq model, the entrainment coefficient is defined not only related to entrainment velocity and vertical velocity, but also with the mixture density:

$$\alpha_T(z) = \frac{u_e(z)}{w_T(z)\sqrt{\frac{\rho_T(z)}{\rho_0}}} \tag{6.12}$$

with $\rho_0 = \rho_a$ density of fresh air chosen as reference in this study, very dense comparing to pure helium (density ratio 7:1) and pure hydrogen (density ratio 14:1).

We present in the figure 6.8-(c)(d) the variation of DNS estimated non Boussinesq entrainment coefficient along the jet, defined in equation (4.86). As the density variation is considered in non-Boussinesq model, the difference α_T between hydrogen case and helium case is significant at z =4-8cm where a turbulent jet is developing.

If we consider the choice of best-estimated α_T applied in non Boussinesq quasi-analytical approach, as presented in section 6.2.1 (0.124 for hydrogen case and 0.082 for helium case), these best-estimated values are equal to the DNS measured α_T^{DNS} at jet-plume transition area at around $z = 13$cm. Their values are quite different with injection gas.

All above observations illustrate the limit of non Boussinesq model. Non Boussinesq entrainment coefficient is not directly related to jet flow pattern. Thus, its value is generally much more difficult to determine. For example, in this case, a turbulent jet of helium and hydrogen does not possess the same non-Boussinesq α_T, even if their flow patterns are very similar. The α_T calculated in this section cannot be directly used for other configurations.

6.3.2 Modelling of entrainment coefficient by jet Richardson number

In the literature, jet Richardson number is considered as an indicator of jet-plume transition and associated entrainment coefficient variation. The jet Richardson number is defined as the ratio of buoyancy effect and the flow shear effect.

$$\mathrm{Ri}(z) = \frac{b_T}{{w_T}^2}\frac{\rho_e - \rho_T}{\rho_0}g \tag{6.13}$$

with $\rho_0 = \rho_a$ the density reference equal to that of fresh air.

In figure 6.9 on the left, we present the variation of Richardson number along the jet, estimated from DNS results. The jet Richardson number increases along the jet, in agreement with the transition of jet flow: laminar jet - turbulent jet - turbulent jet-plume - turbulent plume. It is less than 0.1 for a pure jet and around 1 for jet-plume transition.

Model of Papanicolaou et al. (2008)

Papanicolaou et al. (2008) summarised from experimental study a formula for entrainment coefficient as function of jet Richardson number

$$\alpha = \alpha_j - (\alpha_j - \alpha_p)\frac{\mathrm{Ri(z)}}{\mathrm{Ri}_p} \tag{6.14}$$

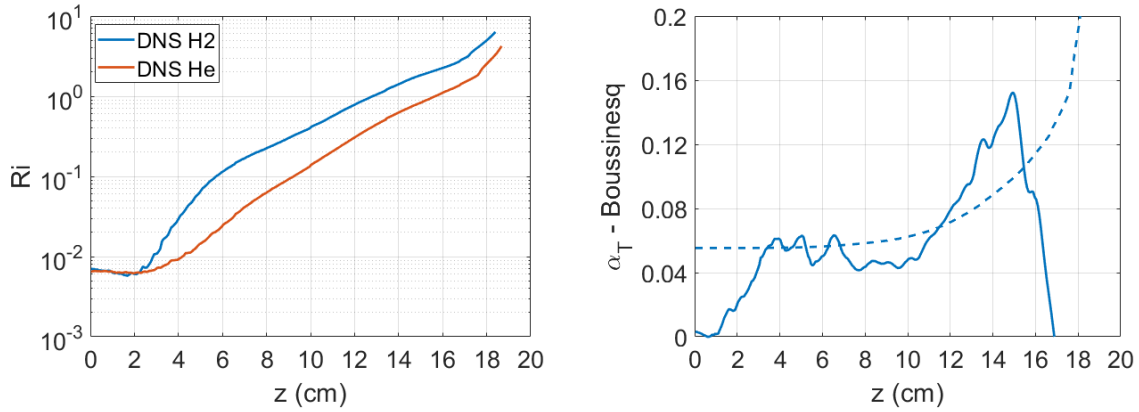

Figure 6.9: DNS evaluation of jet Richardson number variation and associated simple modelled entrainment coefficient variation. Left: DNS deduced variation of jet Richardson number, hydrogen jet in blue line, helium jet in orange line. Right: variation of entrainment coefficient deduced by model of Papanicolaou et al. (2008) in dashed lines, compared with DNS profile in solid lines, hydrogen case.

with parameters $\alpha_j, \alpha_p, \mathrm{Ri}_p$ determined by experiments.

We present in the figure 6.9 on the right the variation of entrainment coefficient, obtained by formula of Papanicolaou et al. (2008), for hydrogen case as an example. The parameters are chosen $\alpha_j = 0.055$,$\alpha_p = 0.083$, $\mathrm{Ri}_p = 0.522$ as recommended by Jirka (2004). This modelling seems not too bad, except for laminar injection flow region ($z < 3$cm). However, the relation α with Richardson number seems not as simple as linear, as presented in this model, the Richardson number increases three decades along the jet but entrainment coefficient clearly does not.

Model of Kaminski et al. (2005)

Modelling of entrainment coefficient variation can also be found in α−variable turbulent jet models such as that of Kaminski et al. (2005). This model is proposed for a turbulent jet under Boussinesq approximation and in a homogeneous environment ($\rho_e(z)$ =constant). The entrainment coefficient is a function with jet altitude $\alpha(z)$, depending on jet radius $b_T(z)$, jet Richardson number $\mathrm{Ri}(z)$ and a parameter $A(z)$ called buoyancy parameter variable along the jet.

$$\alpha(z) = \frac{0.135}{2} + \left(1 - \frac{1}{A(z)}\right)\mathrm{Ri}(z) + \frac{b_T(z)}{2}\frac{d\ln A(z)}{dz} \tag{6.15}$$

Carazzo et al. (2006) proposed an empiric formula for this buoyancy parameter. $A(z)$ depends on whether the flow is a pure jet, in jet-plume transition or a pure plume, see equation (2.52). The jet-plume part begins at altitude L_{mix} and ends at $5L_{mix}$, with the characteristic length L_{mix}, named Fischer's mixing length (Fischer et al. (1979)), calculated by

$$L_{mix} = \pi^{1/4}\mathrm{Ri}_{\mathrm{inj}}^{-1/2}\frac{d}{2} \tag{6.16}$$

where $\mathrm{Ri}_{\mathrm{inj}}$ is injection Richardson number, could be evaluated by the injection conditions, here around 0.006 for both cases. Numerical application gives L_{mix} =8.7cm for hydrogen case and 9cm for helium case, theoretically corresponding to the beginning height of the pure jet region as if the jet were immersed in a homogeneous environment.

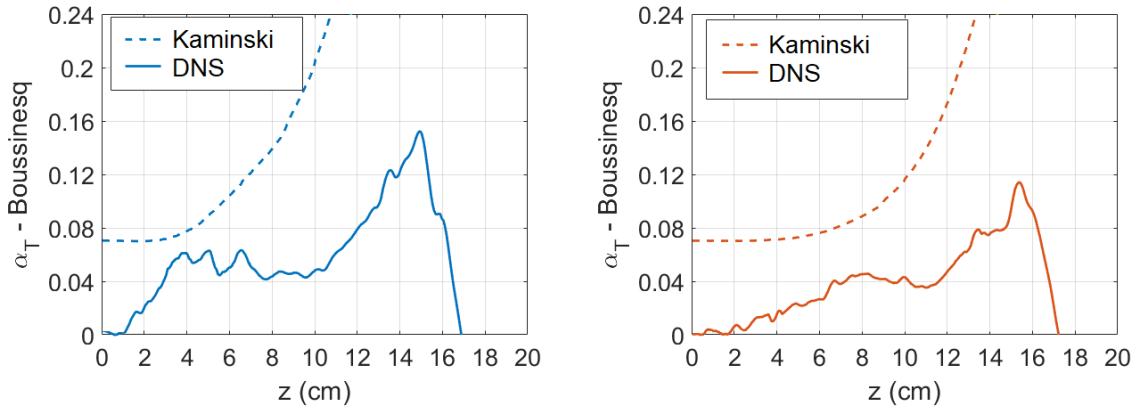

Figure 6.10: Kaminski's α–variation profiles, deduced by DNS jet Richardson number variation, compared with DNS estimated variation of $\alpha_T(z)$ as reference. Left: hydrogen jet, right: helium jet.

By applying these empiric formulas, using DNS estimated Top-hat jet radius $b_T^{DNS}(z)$ and Richardson number $\mathrm{Ri}^{DNS}(z)$, we obtained the profile of $\alpha(z)$ calculatewd from equation (6.15), presented in figure 6.10 in dashed lines. Kaminski's model overestimates entirely the entrainment coefficient. One main reason is its wrong modelling at injection point $z = 0$. DNS results shows that the flow is very regular and laminar at injection level where local entrainment coefficient is nearly zero. However, Kaminski's modelling provides a pure turbulent jet just after injection with $\alpha_0 \approx 0.07$.

We shall particularly note that the Kaminski's formulation eq. (6.15) is valid rigorously only if the jet is in a homogeneous environment, see demonstration in appendix A.2 for more details. That is why this formula is not applicable for z =8-10cm typically the jet is immersed in a highly stratified environment.

6.3.3 Application of Kaminski's α–variable turbulent jet model

Model of Kaminski et al. (2005) is a Boussinesq approach with variable entrainment coefficient, applied in homogeneous environment. Like classic Boussinesq model of Morton et al. (1956), the conservation equations of Kaminski et al. (2005) are based on three characteristic jet quantities, the volume flux $\mathcal{Q}$, the momentum flux $\mathcal{M}$ and the buoyancy flux $\mathcal{B}$. The buoyancy flux is considered as a constant $\mathcal{B}_0$ as this model is valid only for homogeneous environment. The conservation equations are like that of classic Boussinesq model of Morton et al. (1956) but with variable entrainment coefficient $\alpha(z)$.

$$\begin{cases} \dfrac{d\mathcal{Q}}{dz} = 2\alpha(z)\sqrt{\pi\mathcal{M}} \\ \dfrac{d\mathcal{M}}{dz} = \dfrac{\mathcal{B}_0\mathcal{Q}}{\mathcal{M}} \\ \dfrac{d\mathcal{B}}{dz} = 0 \end{cases} \tag{6.17}$$

with $\alpha(z)$ calculated from expression (6.15).

We aim at solving this system numerically, by using 4^{th} order Runge-Kutta method. The initial conditions $\mathcal{Q}(0), \mathcal{M}(0), \mathcal{B}_0$ are provided by DNS measurements. The entrainment coefficient $\alpha(z)$ is calculated by characteristic jet quantities. In formula of $\alpha(z)$ (6.15), the jet radius can be calculated by $b_T(z) = \mathcal{Q}(z)/\sqrt{\pi\mathcal{M}(z)}$, and the Richardson number can be written with jet quantities:

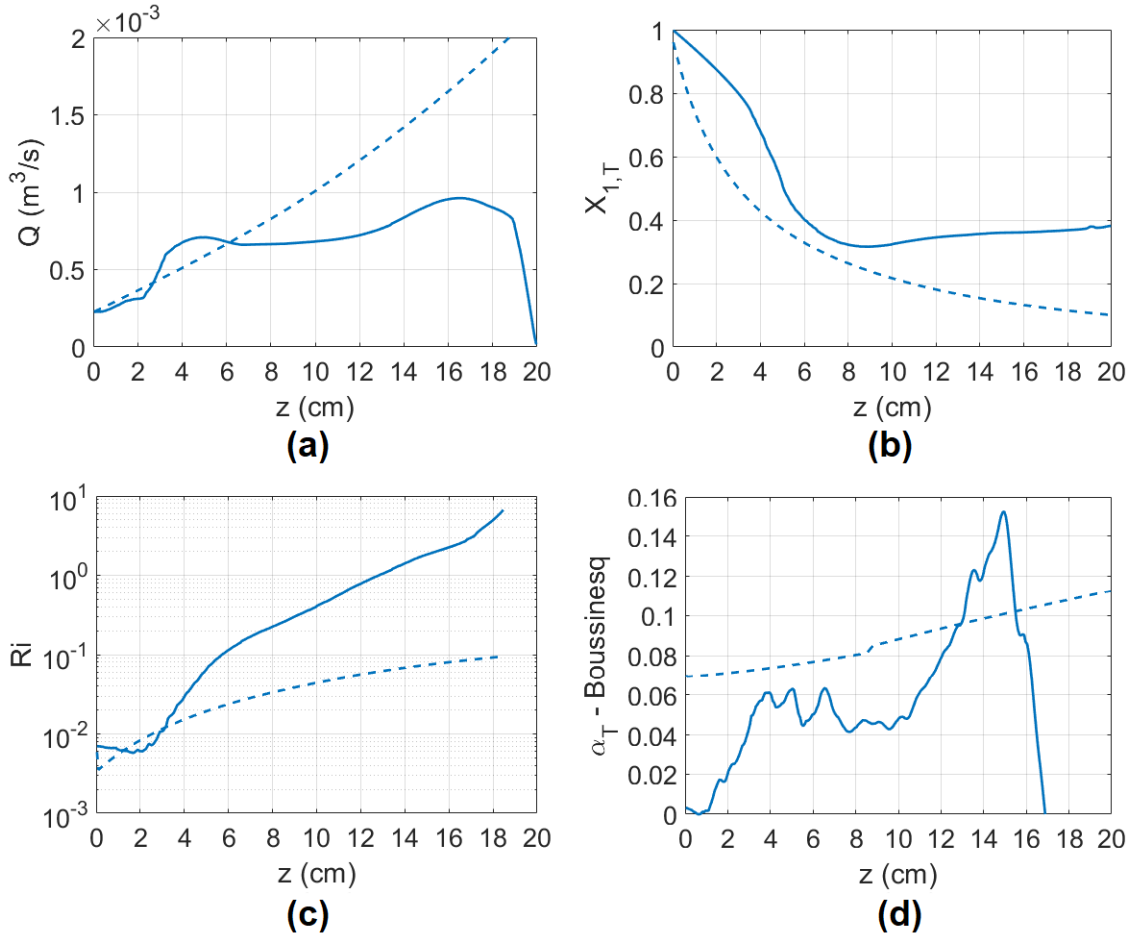

Figure 6.11: Evaluation of Kaminski's α–variable Boussinesq turbulent jet models. (a) variation of jet volume flux $\mathcal{Q}(z)$, (b) variation of jet Top-hat concentration $X_{1,T}(z)$, (c) variation of jet Richardson number, (d) variation of entrainment coefficient $\alpha_T(z)$. Hydrogen case, DNS reference results in solid lines and results from 1D models in dashed lines.

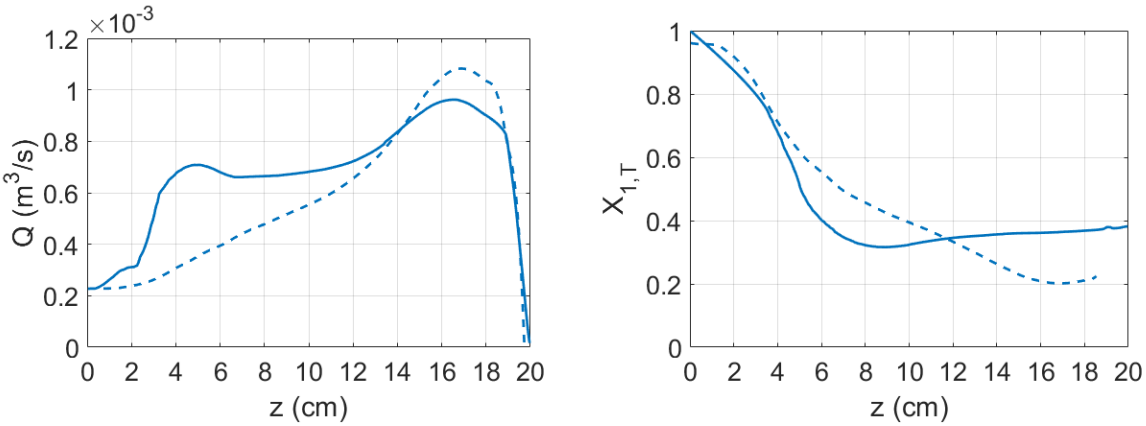

Figure 6.12: Resolution of Kaminski's jet conservation equations (6.17) by DNS estimated α profile. Left: jet volume flux $\mathcal{Q}(z)$, right jet Top-hat concentration $X_{1,T}(z)$. Hydrogen case, DNS reference results in solid lines and results from 1D models in dashed lines.

$$\mathrm{Ri}(z) = \frac{1}{\sqrt{\pi}} \frac{\mathcal{B}_0 \mathcal{Q}^2(z)}{\mathcal{M}^{5/2}(z)} \tag{6.18}$$

The variation $\alpha(z)$ shall be provided beforehand for system resolution. It is considered as a constant equal to α_0 in the first iteration. Then the ODE (6.17) will be solved numerically to obtain profiles of $\mathcal{Q}(z)$ and $\mathcal{M}(z)$. The profile of $\alpha(z)$ is deduced and used in the next iteration.

In figure 6.11, we present the variation of volume flux $\mathcal{Q}(z)$, hydrogen concentration $X_{1,T}(z)$, Richardson number $Ri(z)$ and entrainment coefficient $\alpha_T(z)$ obtained by Kaminski's α-variable model, compared with DNS. The model provides good estimation for the region $z < 7$cm, in the lower mixing layer where far-field environmental density varies little. However, beyond this limit, Kaminski's model overestimates the jet volume flux and underestimates the jet concentration. This is because the unstratified environment assumption is no longer valid. In addition, the Richardson number is largely underestimated (up to 1/10) all along the jet. The estimation of entrainment coefficient is not accurate as well.

In order to examine if the error is due to the bad estimation of entrainment coefficient along the jet, we take the DNS estimated $\alpha_T^{DNS-B}(z)$ into quasi-analytical resolution of system 6.17. The results comparisons are presented in figure 6.12. Evidently, the modelling results match better with DNS profiles. However, this approach does not provide a good estimation for concentration variation in the top homogeneous layer. This is due to the variation of environmental density is not considered in the model.

Conclusion 6.3

In conclusion, the entrainment coefficient varies with the development of the jet. In Boussinesq case, its variation is associated with jet flow pattern. The best-estimated value in α-constant model corresponds to its physical value measured from DNS at the level where the local buoyancy frequency reaches its maximum. This remark is not valid for non Boussinesq case where entrainment coefficient depends also on the density variation.

α-variable models like Kaminski et al. (2005) could not provide accurate estimated profiles as this model is supposed to be applied in unstratified environment only. The far-field environmental density variation will largely influence the development of the jet and variation of entrainment coefficient along the jet.

6.4 Summary and discussion

In this chapter, we focus on turbulent jet models applied in stratified bi-layer type environment. We have presented:

- Applications of Boussinesq and non Boussinesq α-constant jet models
- Variation of entrainment coefficient along the jet developed in stratified environment
- Applications of Boussinesq α-variable jet model

We focus on the model performance and the choice of entrainment coefficient α_T. The analysis consists of two aspects of modelling, (i) if the Boussinesq approximation is applied, and (ii) if the entrainment coefficient is chosen constant or variable along the jet.

The analysis is divided into three parts. Firstly we focus on constant entrainment coefficient models, classic Boussinesq model of Morton et al. (1956) and non-Boussinesq model of Rooney and Linden (1996).

Both Boussinesq and non Boussinesq models possess analytical solutions. These analytical solutions cannot provide accurate variations of jet quantities as both of them are valid in homogeneous environment only. If the environmental variation is provided, both Boussinesq and non-Boussinesq models can provide a good estimation of jet concentration variation $X_{1,T}(z)$. The sensitivity of entrainment coefficient is also well improved.

Secondly, we discuss the variation of entrainment coefficient $\alpha(z)$ along the jet and its best-estimated choice in α-constant models.

The entrainment coefficient varies with the jet development. It depends on the jet model selected and the profile assumption (Gaussian or Top-hat) adopted in the modelling. No general conclusion is found for non Boussinesq case as α^{NB} depends on jet density evolution. In Boussinesq case, the entrainment coefficient depends generally only on the flow pattern. Jet Richardson number can be considered as an indicator of variation $\alpha(z)$. The best-estimated α_T in α-constant models corresponds to the jet regime mostly presented in the cavity, and matches its physical value measured from DNS at the level where the local buoyancy frequency reaches its maximum.

Thirdly, we test the reliability of several α-variable models applied in bi-layer environment. The validity of these models is limited in the lower part of the cavity where environmental density changes little. Application of these models in stratified environment should be coupled with ventilation model providing environmental change.

From results obtained in this chapter, a summary of pros and cons of different turbulent jet models is presented in table 6.1, for its practical use for air-hydrogen mixing problem in bi-layer-like stratified environment.

In condition of large injection flow rate, the hydrogen risk may be not only presented in the jet region, but also in the whole top part of the cavity. We will present the global concentration modelling in the next chapter.

Model	Pros	Cons
Morton's model *Boussinesq* *α-constant* Eq. (6.6)	- Classical model commonly used - Existence of analytical solution for homogeneous environment - Entrainment coefficient depends only on flow pattern and can be measured from velocity field - Good estimation if environmental variation is provided and entrainment coefficient is well selected - Sensitivity of entrainment coefficient to modelling results will largely improved if environmental variation is provided	- Boussinesq approximation not valid with air-hydrogen mixture - Analytical solution cannot well model jet quantities in homogeneous layer - Entrainment coefficient sensible to modelling performance - No clear method to determine entrainment coefficient - Modelling of momentum term totally wrong
Rooney's model *Non-Boussinesq* *α-constant* Eq. (6.8)	- Conservation equations valid physically - Existence of analytical solution for homogeneous environment - Good modelling of momentum term - Good estimation if environmental variation is provided and entrainment coefficient is well selected - Sensitivity of entrainment coefficient to modelling results will largely improved if environmental variation is provided	- Analytical solution cannot well model jet quantities in homogeneous layer - Entrainment coefficient sensible to modelling performance - Entrainment coefficient depends on jet gas and reference density, no general correspondence with flow pattern - No clear method to determine the value of entrainment coefficient
Kaminski's model *Boussinesq* *α-variable* Eq. (6.17)	- Explicit formula of entrainment coefficient as function of Richardson number - Entrainment coefficient variable to adapt its real variation - Good modelling of volume flux if environmental variation is well provided	- Laminar jet region not well modelled - Unstratified modelling cannot well estimate quantities variation in homogeneous layer - Modelling of momentum term totally wrong - Buoyancy flux and hydrogen volume fraction not well modelled

Table 6.1: Pros and cons of use of turbulent jet models in industrial context for air-hydrogen mixing in bi-layer environment

Chapter 7

Solving bi-layer parameters

In 1D modelling, the light gas distribution can be characterised by the profile of light gas concentration (volume fraction) at far field of the jet, or called environmental concentration as a function of altitude. Linden et al. (1990) have proposed a classical natural ventilation model with two-vented cavity. In this model, the distribution of light gas concentration in the far field of the jet is considered as in bi-layer structure, with a homogeneous layer situated in the top cavity. Global conservation equations are established by flow pattern analysis. Analytical solutions are then deduced with turbulent jet models.

In this chapter, we will firstly evaluate, from DNS reference results, best-estimated bi-layer parameters (interface height z_i and homogeneous concentration $X_{1,i}$) and verify the validity of a series of global conservation equations assumed in the ventilation model. Then we propose to improve the formulation of ventilation solutions by applying different physical assumptions.

7.1 Bi-layer modelling and its best-estimated solutions

In this section, we seek to determine the best-estimated (BE) bi-layer parameters from DNS results. The best-estimated parameters are the solutions of Linden's bi-layer model, based on which all conservation equations established in the model are valid. These parameters will be determined from hydrostatic pressure variation and global balance. From DNS, the best-estimated results are summarised in table 7.2 in the end of this section.

7.1.1 Hydrostatic pressure, neutral level and discharge parameter

We select the hydrostatic pressure at $z = 0$ outside the studied cavity as the hydrostatic reference. Ambient air, with uniform density ρ_a, presents in the exterior of the cavity. Thus, the exterior hydrostatic pressure varies linearly with altitude z.

$$P_e(z) = -\rho_a g z, \text{ with } P_e(0) = 0 \tag{7.1}$$

The interior hydrostatic pressure profile depends on variation of environmental density $\rho_e(z)$ inside the cavity where the interior hydrostatic pressure at $z = 0$ is linked to inlet kinetic energy, deduced from Bernoulli's theorem:

$$P_i(z) = P_i(0) - \int_0^z \rho_e(s) g ds, \text{ with } P_i(0) = P_e(0) - \frac{c_b}{2}\rho_a u_b^2 \tag{7.2}$$

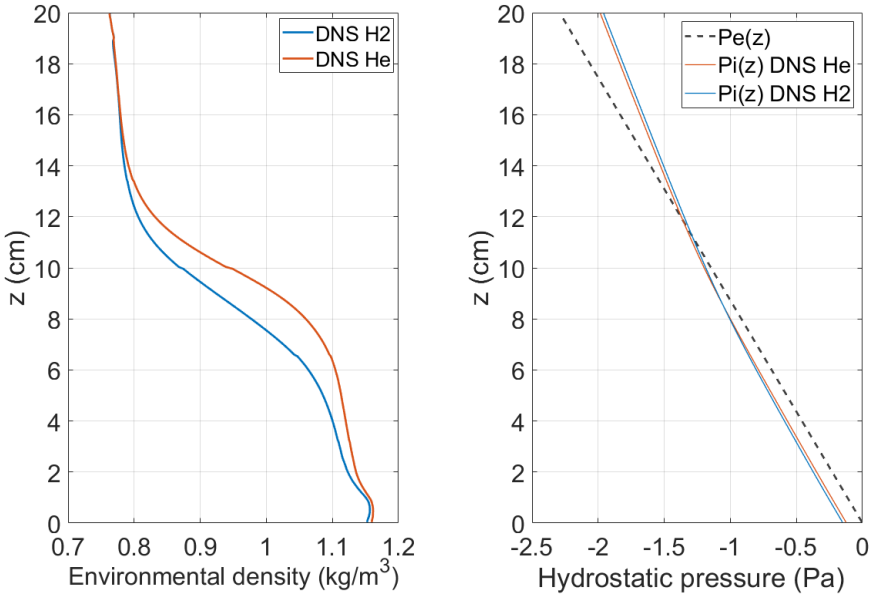

Figure 7.1: Variation of environmental density (left) and hydrostatic pressure (right) inside and outside the cavity. DNS Hydrogen case in blue lines and DNS helium case in orange lines.

where $c_b = 0.61$ a typical choice of inlet discharge parameter by Vauquelin et al. (2017a). We retain this value for the following study.

At ceiling of the cavity, where is situated top opening, the difference between interior and exterior pressure will be linked to outlet flux kinetic energy

$$P_e(H) - P_i(H) = -\frac{c_t}{2}\rho_{out}u_t^2 \tag{7.3}$$

As the vertical extension of two opening is relatively small comparing with cavity height, the inlet/outlet flux through two openings can be characterised by its mean values. We note u_t, u_b mean velocity respectively for top and bottom opening. Its DNS estimated values can be calculated simply by

$$u_b^{DNS} = \frac{Q_b^{DNS}}{S_b}, \quad u_t^{DNS} = \frac{Q_t^{DNS}}{S_t} \tag{7.4}$$

with $S_b = S_t = WH_v = 10cm^2 = 0.001m^2$ surface of the two openings. From the linear relation of P_e (7.1), using DNS deduced profile $\rho_e^{DNS}(z)$ in relation (7.2), we obtain $P_e(H) - P_i(H)$. Then regrouping it with equation (7.3), we obtain $c_t = 0.446$ for hydrogen case, $c_t = 0.428$ for helium case. Both of them are smaller than c_b chosen equal to 0.61, in agreement with conclusion of Vauquelin et al. (2017a).

In figure 7.1, we present the DNS estimated variation of environmental density as well as hydrostatic pressure profiles inside and outside the cavity obtained from above equations. Hydrostatic pressure profile is quite identical for helium and hydrogen cases. Besides, inside and outside pressure profiles cross at neutral level z_n where $P_e(z_n) = P_i(z_n)$. Its value will be calculated from DNS interior pressure profile, summarised in table 7.2 at the end of this section.

7.1.2 Determination of best-estimated bi-layer parameters

Model of Linden et al. (1990) is based on the bi-layer distribution of light gas concentration thus also for mixture density. The modelled density distribution divides the cavity into two

parts. The mixture density is considered equal to fresh air in the bottom layer and homogeneous in the top layer. By identification of global conservation equations of mass and volume, we let the best-estimated value of ρ_i equal to DNS estimated mean outlet density deduced from outlet mass flux $Q_{m,t}^{DNS}$ and volume flux Q_t^{DNS}:

$$\rho_i^{BE} = \frac{Q_{m,t}^{DNS}}{Q_t^{DNS}} \tag{7.5}$$

The best-estimated mixture density as well as corresponding volume fraction $X_{1,i}^{BE}$ for hydrogen and helium cases are presented in table 7.2 at the end of this section.

In hydrogen risk analysis context, the best-estimated interface altitude shall be set to make the total amount of light gas accumulated in the cavity, calculated from bilayer modelling, equal to DNS, in order to have the same system enthalpy. Therefore, the best-estimated bi-layer interface altitude z_i^{BE} results from the identification of the following integral estimated from DNS and from bi-layer model.

$$I^{DNS} = \int_0^H X_{1,e}^{DNS}(z)dz, \quad I^{BE} = X_{1,e}^{BE}(H - z_i^{BE}) \tag{7.6}$$

The best-estimated interface height z_i^{BE} is thus defined as

$$z_i^{BE} = H - \frac{I^{DNS}}{X_{1,i}^{BE}} \tag{7.7}$$

with $X_{1,i}^{BE}$ the best-estimated homogeneous concentration, corresponding to the mean concentration of outlet gas. The obtained results z_i^{BE} are summarised in table 7.2 at the end of this section.

In figure 7.2, we present the best-estimated bi-layer profiles compared with DNS. Profiles of hydrostatic pressure are calibrated by identification of neutral plan z_n.

7.1.3 Estimation of inlet/outlet fluxes

In the model of Linden et al. (1990), inlet and outlet volume fluxes Q_t, Q_b are calculated from bi-layer parameters z_i, ρ_i. The demonstration are presented in section 3.1.5 by applying Bernoulli's theorem and hydrostatic pressure variation. Recall the expressions of volume flux through bottom opening Q_b and outlet volume flux through top opening Q_t: equations (3.18) and (3.19).

$$Q_t = S_t \sqrt{2c_t \frac{\rho_a - \rho_i}{\rho_i} g(H - z_n)} \tag{7.8}$$

$$Q_b = S_b \sqrt{2c_b \frac{\rho_a - \rho_i}{\rho_a} g(z_n - z_i)} \tag{7.9}$$

Then, the inlet and outlet mass fluxes will be then deduced simply by

$$Q_{m,b} = \rho_a Q_b, \quad Q_{m,t} = \rho_i Q_t \tag{7.10}$$

We present in the table 7.1 estimation results from above equations by using best-estimated bi-layer parameters (columns Linden BE) in table 7.2. Generally the above equations provide very good estimation of these fluxes. The inlet volume and mass fluxes are correctly calculated while the outlet fluxes are estimated with an error around 1%.

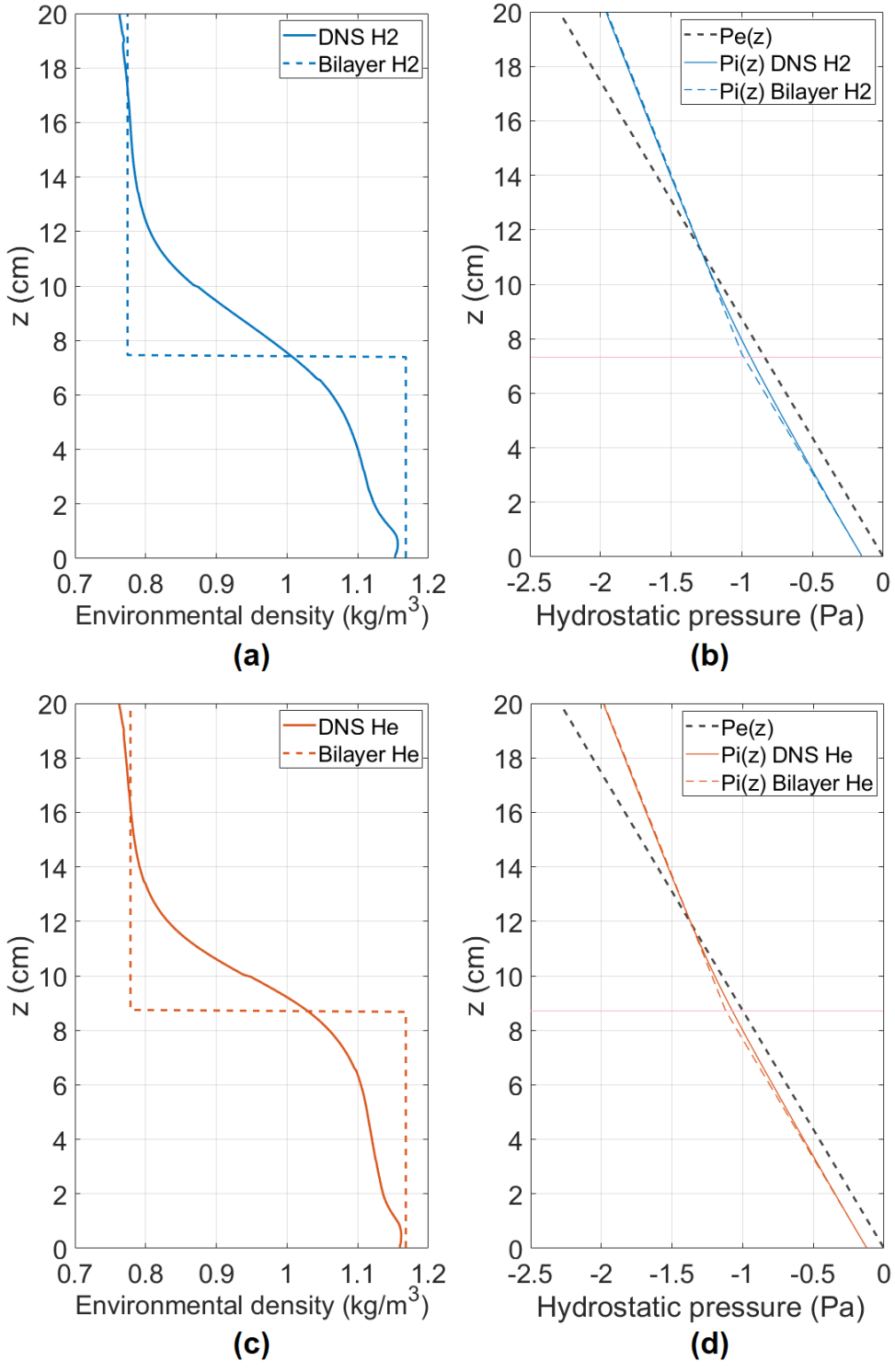

Figure 7.2: Comparison best-estimated bi-layer distribution with DNS. (a) variation of mixture density for hydrogen case, (b) variation of hydrostatic pressure for hydrogen case, (c) variation of mixture density for helium case, (d) variation of hydrostatic pressure for helium case. DNS estimated profiles in solid lines, bi-layer modelling results in dashed lines.

	H2 DNS	**H2 Linden BE**	**H2 Error**(*)	**He DNS**	**He Linden BE**	**He Error**(*)
$Q_{inj}(\times 10^{-4} m^3/s)$	2.183	2.183		2.183	2.183	
$Q_b(\times 10^{-4} m^3/s)$	3.934	3.934	**0.00%**	3.558	3.558	**0.00%**
$Q_t(\times 10^{-4} m^3/s)$	6.171	6.243	**1.16%**	5.779	5.842	**0.74%**
$Q_{m,inj}(\times 10^{-4} kg/s)$	0.1775	0.1775		0.3515	0.3515	
$Q_{m,b}(\times 10^{-4} kg/s)$	4.597	4.597	**0.00%**	4.158	4.158	**0.00%**
$Q_{m,t}(\times 10^{-4} kg/s)$	4.779	4.835	**1.16%**	4.514	4.547	**0.74%**
Global balance Volume flux(**)	0.88%	**2.02%**		1.00%	**1.72%**	
Global balance Mass flux(***)	0.09%	**1.24%**		0.11%	**0.84%**	
Ratio Q_{inj}/Q_t	35%	35%		38%	37%	
Ratio $Q_{m,inj}/Q_{m,t}$	3.7%	3.7%		7.8%	7.7%	

(*): (Linden BE-DNS)/DNS; (**): $(Q_t - Q_b - Q_{inj})/Q_t$; (***): $(Q_{m,t} - Q_{m,b} - Q_{m,inj})/Q_{m,t}$

Table 7.1: Inlet/outlet volume flux and mass flux: comparison between results measured from DNS and estimation from Linden best-estimated bi-layer parameters. Analyse of global balance.

Conclusion 7.1

We have the best-estimated Linden's bi-layer solutions presented in the following table, which ensure good estimations of inlet/out mass and volume fluxes through the two openings.

	Hydrogen	**Helium**
c_b	0.61	0.61
c_t	0.446	0.428
z_n^{BE}(cm)	11.25	11.90
z_i^{BE}(cm)	7.41	8.72
ρ_i^{BE}(kg/m^3)	0.7744	0.7784
$X_{1,i}^{BE}$(%)	36.22%	38.69%

Table 7.2: Summary of choice of discharge parameters and best-estimated solutions of the Linden's bi-layer model

7.2 Validity of conservation assumptions

In this section, we seek to verify the validity of conservation assumptions required in Linden's model by applying the above best-estimated bi-layer parameters.

Firstly we shall note that the global conservations of volume flux (equation (3.20)) and mass flux (3.24) have already been validated for DNS results in section 5.1.4. Consequently, these conservations are also valid for Linden's best-estimated results as a good agreement is presented for the estimation of inlet-outlet fluxes in table 7.1. The global conservation equa-

tions are valid with 2% error of volume flux ($Q_t = Q_b + Q_{inj}$) and 1% error of mass flux ($Q_{m,t} = Q_{m,b} + Q_{m,inj}$).

In original Linden's model, the injection volume flux Q_{inj} is neglected in global conservation of volume flux ($Q_t = Q_b$). This assumption is clearly not valid in the present case. The injection volume flux presents around 35-37% of volume in the outlet flux. Nonetheless, we may consider the injection mass flux is negligible as this presents only 4% for hydrogen case and 8% for helium case in the total outlet mass flux through the top opening.

We focus now on another two conservation equations assumed in Linden's model.

7.2.1 Conservation of specific buoyancy flux below bi-layer interface

In turbulent jet modelling, the variation of far-field environmental density is characterised by jet buoyancy flux. Linden's model proposes to treat this quantity as a constant below the interface level $z < z_i$ (see equation (3.23)) as this area is assumed homogeneous with density ρ_a. In order to differentiate it with the ordinary definition of jet buoyancy flux (equation (2.22)), we define here a specific jet buoyancy flux $\mathcal{B}^*(z)$ **as if the jet were placed in the fresh air environment.**

$$\mathcal{B}^*(z) = \int_{P\in\Omega(z)} \frac{\rho_a - \rho(P)}{\rho_0} g \cdot w(P) dS(P) = \frac{g}{\rho_0}\left(\rho_a \mathcal{Q}(z) - \mathcal{Q}_m(z)\right) \tag{7.11}$$

with P a point in the jet at altitude z and $\Omega(z)$ jet region at this altitude. $\rho_0 = \rho_a$ the reference density. Note that $\mathcal{B}^*(0) = \mathcal{B}(0)$ but generally $\mathcal{B}^*(z) \neq \mathcal{B}(z)$ where the latter one is its ordinary definition calculated with variable far field density $\rho_e(z)$.

In figure 7.3, we present the DNS estimated profiles of this specific buoyancy flux, $\mathcal{B}^{*DNS}(z)$, comparing with injection buoyancy flux $\mathcal{B}_0$. We note clearly this specific buoyancy flux $\mathcal{B}^{*DNS}(z)$ is nearly constant around $\mathcal{B}_0$ below the bi-layer interface z_i^{BE}. The maximum difference is achieved at z =3cm for H2 case and at z = 4cm for He case, both of them possess relatively 8% error. At best-estimated bi-layer interface $z = z_i^{BE}$, the relative difference between $\mathcal{B}^{*DNS}(z_i^{BE})$ and $\mathcal{B}_0$ is 6.2% for hydrogen case and 2.9% for helium case. Consequently, the conservation of specific buoyancy flux below the interface is valid with a relative error within 8%.

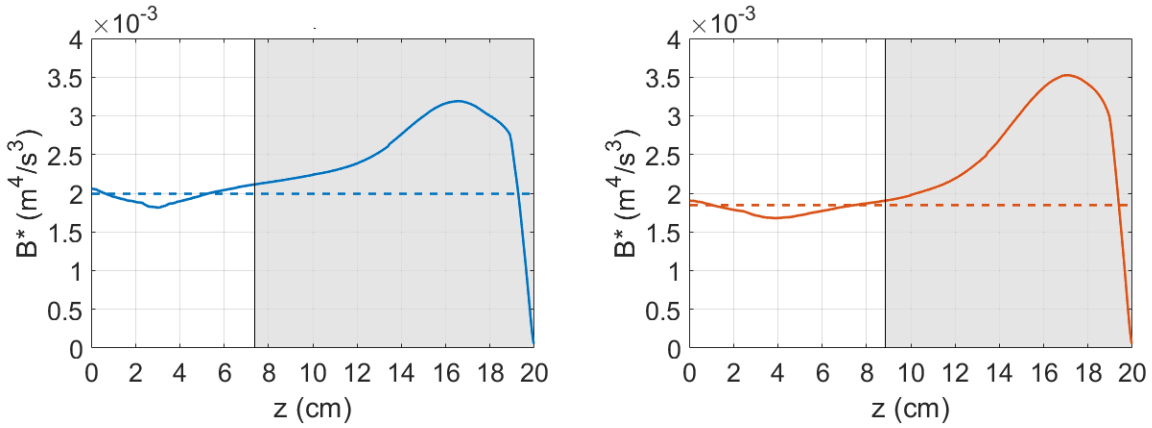

Figure 7.3: Variation of $\mathcal{B}^{*DNS}(z)$ along the jet (solid lines), calculated from DNS 1D profiles, and comparison with injection buoyancy flux $\mathcal{B}_0$ (dashed lines). Left: hydrogen case, right: helium case. Zone $z > z_i$ is coloured in grey. $\mathcal{B}^{*DNS}(z)$ are nearly constant below the interface.

7.2.2 Conservation of volume flux and reduced gravity in the top homogeneous layer

In model of Linden et al. (1990), two additional conservation equations connecting the jet flow at interface with the homogeneous layer are also assumed. These two equations are conservation of volume flux and conservation of reduced gravity within the bi-layer homogeneous layer.

- First one, the volume flux going through the top opening Q_t shall be equal to the vertical volume flux in the jet at interface level, direct consequence of conservation of volume flux within the bi-layer homogeneous layer, see equation (3.21)

$$Q_t = \mathcal{Q}(z_i) \tag{7.12}$$

- Second one, the environmental reduced gravity in the top homogeneous layer is assumed equal to that in the jet at interface level **as if the jet were placed in the fresh air environment**, see equation (3.27)

$$g' = \frac{\rho_a - \rho_T(z_i)}{\rho_a} g \tag{7.13}$$

  This equation is clearly equivalent to

$$\rho_i = \rho_T(z_i) \tag{7.14}$$

We seek to validate these two equations (7.12) and (7.14). In table 7.3, DNS and Linden best-estimated solutions for Q_t and ρ_i are compared respectively with DNS estimated $\mathcal{Q}(z_i^{BE})$ and $\rho_T(z_i^{BE})$. The relative error for equation (7.12) is around 6% for hydrogen and 3% for helium. Equation (7.14) seems more accurate as its relative error between both sides of the equation is less than 2% for all cases.

Remark: Regrouping equations (7.12) and (7.14), we deduce the equation conservation of mass flux in the top homogeneous layer:

$$Q_{m,t} = \mathcal{Q}_m(z_i) \tag{7.15}$$

	H2 DNS	**H2 Linden BE**	**He DNS**	**He Linden BE**
$\mathcal{Q}(z_i^{BE})(\times 10^{-4} m^3/s)$	6.63		5.63	
$Q_t(\times 10^{-4} m^3/s)$	6.17	6.24	5.80	5.84
Error Q_t(*)	**7.4%**	**6.2%**	**-3.0%**	**-3.7%**
$\rho_T(z_i^{BE})(kg/m^3)$	0.788		0.766	
ρ_i (kg/m^3)	0.774	0.774	0.778	0.778
Error ρ_i(**)	**1.7%**	**1.7%**	**-1.6%**	**-1.6%**

(*): ([DNS $\mathcal{Q}(z_i^{BE})$]-[DNS Q_t or Linden BE Q_t])/[DNS Q_t or Linden BE Q_t]
(**): ([DNS $\rho_T(z_i^{BE})$]-[DNS ρ_i or Linden BE ρ_i])/[DNS ρ_i or Linden BE ρ_i]

Table 7.3: Validation of conservation of volume flux and reduced gravity in the top homogeneous layer. Comparison DNS and Linden best-estimated solutions for Q_t and ρ_i with DNS-estimated $\mathcal{Q}(z_i^{BE})$ and $\rho_T(z_i^{BE})$.

Conclusion 7.2

The best-estimated solutions of bi-layer parameters as well as its associated quantities calculated from Linden's model satisfy following conservation assumptions:

- Global conservation of mass flux: $Q_{m,t} = Q_{m,b} + Q_{m,inj}$
- Global conservation of volume flux: $Q_t = Q_b + Q_{inj}$
- Conservation of specific jet buoyancy flux below bi-layer interface: $\mathcal{B}^*(z) = \mathcal{B}_0$, for $z < z_i$
- Conservation of volume flux in the top homogeneous layer: $Q_t = \mathcal{Q}(z_i)$
- Conservation of reduced gravity in the top homogeneous layer: $g' = G'_T(z_i)$
- Conservation of mass flux in the top homogeneous layer: $Q_{m,t} = \mathcal{Q}_m(z_i)$

7.3 Improvements of Linden's model

In this section, we will present 4 aspects of improvements of Linden's model. The objective of this model is to solve bi-layer parameters (z_i the altitude of interface and $X_{1,i}$ homogeneous concentration) by using following conditions as input. Recall that $X_{1,i}$ is directly associated with ρ_i and g'.

- Geometrical configurations, i.e. height of the cavity H, surface of two openings S_b, S_t
- Injection conditions, including injected gas density ρ_{inj}, volume flux Q_{inj}, buoyancy flux $\mathcal{B}_0 = \frac{\rho_a - \rho_{inj}}{\rho_a} g Q_{inj}$.
- Discharge coefficients through two openings c_b, c_t.
- Additional jet parameters: Top-hat jet entrainment coefficient α_T and jet virtual origin displacement z_t if this notion is applied in the resolution.

We will see that the conservation equations in ventilation model can be transformed into the following form:

$$\frac{\xi^5}{1-\xi} = \frac{\mathcal{A}^2}{\mathcal{C}^3 \mathcal{H}^4} \tag{7.16}$$

and

$$g' = \frac{1}{\mathcal{C}^\#} {\mathcal{B}_0}^{2/3} (\xi \mathcal{H})^{-5/3} \tag{7.17}$$

with $\xi, \mathcal{A}, \mathcal{C}, \mathcal{C}^\#, \mathcal{H}$ defined differently according to assumptions applied in the resolution. We have seen in chapter 3 that these formulations are available for Linden-Morton solutions and Linden-Rooney solutions (see section 3.2.1 and 3.2.2).

7.3.1 Overview of different physical assumptions

The improvements will be focused on fours additional physical assumptions in the system resolution (as presented in section 3.2.1 - Assumptions 7-10). Here are noted "DIBO".

- **Assumption D (Small/Large density range):** Under small density assumption, the ratio $\rho_a/\rho_i \approx 1$. This ratio is neglected in equation (7.8) and this equation will be written as

$$Q_t = \sqrt{2c_t g'(H - z_n)} \tag{7.18}$$

  Under large density assumption, this equation is written as

$$Q_t = \sqrt{2c_t g' \frac{\rho_a}{\rho_i}(H - z_n)} \tag{7.19}$$

- **Assumption I (Small injection volume/mass flux and choice of conservation principle):** The injection flux is considered relatively small compared with inlet flux. The small injection assumption can be applied in sense of volume flux or mass flux. Under small injection volume flux assumption, the Q_{inj} will be neglected in global conservation of volume flux $Q_t = Q_b + Q_{inj}$. This conservation will be rewritten as

$$Q_t = Q_b \tag{7.20}$$

  Under small injection mass flux assumption, the $Q_{m,inj}$ will be neglected in global conservation of mass flux $Q_{m,t} = Q_{m,b} + Q_{m,inj}$. This equation will be rewritten as

$$Q_{m,t} = Q_{m,b} \tag{7.21}$$

- **Assumption B (Jet modelling - Boussinesq/non Boussinesq):** The jet evolution is solved differently in different turbulent jet models. The jet evolution will be calculated at interface ($z = z_i$) then coupled with global conservation equations.

  Under Boussinesq approximation, where the mixture density is considered close to that of fresh air, Morton's analytical solutions (equations (2.41) and (2.43)) will be used.

  Under non-Boussinesq approach, Rooney's analytical solutions (equations (2.69) and (2.72)) will be used.

- **Assumption O (Virtual origin correction):** In original Linden's model, point source assumption is applied. The injection radius and flux is considered small enough to neglect the virtual origin displacement.

  This virtual origin correction could be used in the ventilation model. As presented in figure 7.4, we consider the point source of the jet is situated at $z = z_t < 0$ below the real injection altitude. The virtual jet source is purely buoyancy. The jet is assumed to be developed from $z = -z_t$ to $z = 0$ to achieve the correct injection flux at $z = 0$. Meanwhile, in ventilation modelling, we imagine a virtual cavity from $z = -z_t$ to $z = H$, presented in dashed lines in this figure. The virtual inlet flux is equal to the sum of $Q_b + Q_{inj}$ and. The classical ventilation model will then be applied in this virtual cavity with height $H - z_t$.

In the following sections, we will present how the formulations change if we apply different physical assumptions. We first study assumptions D and I for global conservation equations. These two assumptions will determine the formulation of $\mathcal{A}$ in equation (7.16). In the second phase, we study the influence of assumption B in turbulent jet modelling. This assumption will determine the formulation of $\mathcal{C}$ and $\mathcal{C}^{\#}$ in equations (7.16) and (7.17). And finally we will see how assumption O will influence the formulation of ξ and $\mathcal{H}$ in these equations.

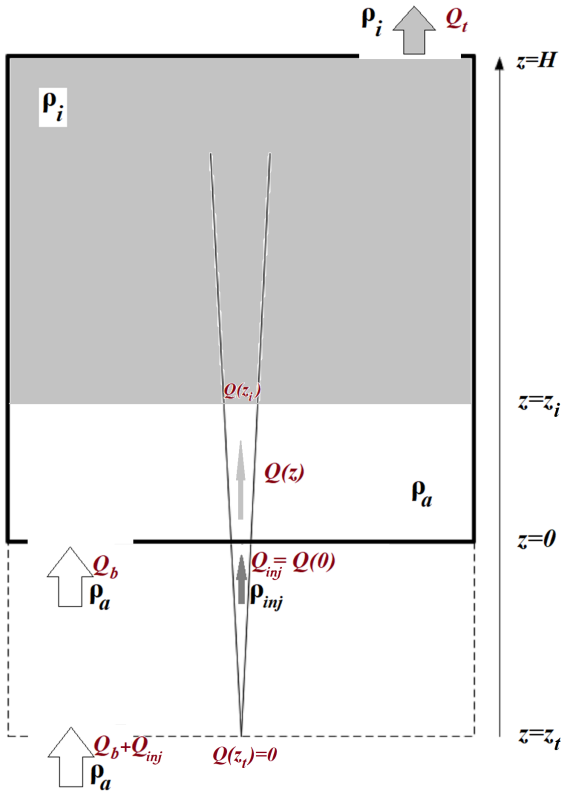

Figure 7.4: Sketch of the notion of jet virtual origin displacement in ventilation model

7.3.2 Small/Large density range and choice of conservation principle

Case 1: Small density range with conservation of volume flux

As presented in section 3.2.1, the Linden-Morton solutions are based on small density range assumption where the term ρ_a/ρ_i is eliminated in equation Q_t (7.8). Besides, principle of conservation of volume flux is used with small injection assumption applied on volume flux. The term Q_{inj} is neglected in global conservation of volume flux $Q_t = Q_b + Q_{inj}$. Consequently, the conservation of volume flux is rewritten as:

$$Q_t = S_t \sqrt{2c_t g'(H - z_n)} = S_b \sqrt{2c_b g'(z_n - z_i)} = Q_b \tag{7.22}$$

Using this equation to eliminate the term z_n, the outlet volume flux Q_t will be re written as

$$Q_t = A \sqrt{g'(H - z_i)} \tag{7.23}$$

where A is called effective surface of the two openings, defined as

$$A = \frac{\sqrt{c_t} S_b S_t}{\sqrt{\frac{1}{2}\left(\frac{c_t}{c_b} S_t^2 + S_b^2\right)}} \tag{7.24}$$

Further demonstration in section 3.2.1 shows this term A appears in final equation (7.16) to replace the term $\mathcal{A}$.

Case 2: Large density range with conservation of volume flux

As presented in section 3.2.2, the Linden-Rooney solutions are based on large density range assumption thus the term ρ_a/ρ_i kept in place in equation Q_t (7.8). With principle of conserva-

tion of volume flux is used with small injection assumption applied on volume flux, we have this conservation written as

$$Q_t = S_t \sqrt{2c_t \frac{\rho_a}{\rho_i} g'(H - z_n)} = S_b \sqrt{2c_b g'(z_n - z_i)} = Q_b \tag{7.25}$$

We regroup the term ρ_a/ρ_i with c_t to define a new c_t^*

$$c_t^* = c_t \frac{\rho_a}{\rho_i} \tag{7.26}$$

The equation comes to the same form of equation (7.22). Thus we have the following A^* replacing the term $\mathcal{A}$ in final equation (7.16).

$$A^* = \frac{\sqrt{c_t^*}\, S_b S_t}{\sqrt{\frac{1}{2}\left(\frac{c_t^*}{c_b} S_t^2 + S_b^2\right)}} \tag{7.27}$$

Case 3: Large density range with conservation of mass flux

We have seen in section 5.1.4 that neglecting injection volume flux in global balance will introduce 35% error while this error decreases to 4% if we neglect injection mass flux instead of volume flux. Therefore, we consider to apply conservation of mass flux with small injection assumption applied on $Q_{m,inj}$. Thus we have the global conservation of mass flux by applying equations (7.8) and (7.9).

$$Q_{m,t} = \rho_i Q_t = \rho_i S_t \sqrt{2c_t \frac{\rho_a - \rho_i}{\rho_i} g(H - z_n)} = \rho_a S_b \sqrt{2c_b \frac{\rho_a - \rho_i}{\rho_a} g(z_n - z_i)} = \rho_a Q_b = Q_{m,b} \tag{7.28}$$

This equation can be simplified to

$$S_t \sqrt{2c_t \frac{\rho_i}{\rho_a} g'(H - z_n)} = S_b \sqrt{2c_b g'(z_n - z_i)} \tag{7.29}$$

Same as done in case 2, we regroup term ρ_i/ρ_a with c_t to define a new c_t^{**}:

$$c_t^{**} = c_t \frac{\rho_i}{\rho_a} \tag{7.30}$$

and we have

$$A^{**} = \frac{\sqrt{c_t^{**}}\, S_b S_t}{\sqrt{\frac{1}{2}\left(\frac{c_t^{**}}{c_b} S_t^2 + S_b^2\right)}} \tag{7.31}$$

will replace the term $\mathcal{A}$ in final equation (7.16). In this case, the outlet volume flux can be written as

$$Q_{m,t} = \rho_i Q_t = \rho_a A^{**} \sqrt{g'(H - z_i)} \tag{7.32}$$

Numerical application

The numerical values of these parameters are presented in table 7.4, calculated from DNS best-estimated solutions. As $\rho_i < \rho_a$, we have $c_t^{**} < c_t < c_t^*$. The value of c_t^*, applied in case 2 with conservation of volume flux, is in the same order as c_b. The value c_t^{**} applied in case 3 with conservation of mass flux, is only a half of c_b. The assumption applied in the resolution

will influence largely the value of discharge parameter as well as the effective surface up to 50% in the present case.

Discharge parameter	H2	He
c_b	0.61	0.61
c_t	0.446	0.428
c_t^*	0.673	0.642
c_t^{**}	0.296	0.285

Effective opening surface	H2	He
S_b, $S_t(cm^2)$	10	10
$A(cm^2)$	7.18	7.09
$A^*(cm^2)$	8.00	7.91
$A^{**}(cm^2)$	6.31	6.23

Table 7.4: Numerical application of discharge parameters and effective opening surface under different assumptions, results calculated from DNS best-estimated results

7.3.3 Turbulent jet modelling

The jet is assumed to be immersed in a homogeneous environment with density ρ_a below the bi-layer interface. Therefore, analytical jet solutions can be applied in the ventilation model. Its formulation depends on the jet model chosen, Morton's solutions for Boussinesq model, as well as Rooney's solutions for non Boussinesq model.

Morton's Boussinesq model

As presented in section 3.2.1, Morton's Boussinesq solutions equations (2.41) and (2.43) are used in Linden-Morton solutions, these equations are written as

$$\mathcal{Q}(z) = C(\mathcal{B}_0(z-z_t)^5)^{1/3} \tag{7.33}$$

$$G'_T(z) = \frac{1}{C}\left({\mathcal{B}_0}^2(z-z_t)^{-5}\right)^{1/3} \tag{7.34}$$

with C a universal constant depending only on the entrainment constant α_T.

$$C = 2.4852{\alpha_T}^{4/3} \tag{7.35}$$

and z_t the virtual origin displacement defined in the jet theory. This term is neglected in Linden-Morton solutions by applying point source assumption.

Demonstration in section 3.2.1 shows the constant C will be replaced to the term $\mathcal{C}$ and $\mathcal{C}^{\#}$ in final equations of the model (7.16) and (7.17).

Rooney's non Boussinesq model

As presented in section 3.2.2, Rooney's non Boussinesq solutions equations (2.68), (2.69) and (2.71) are used in Linden-Rooney solutions, these equations are written as

$$\mathcal{Q}_m(z) = C\rho_a(\mathcal{B}_0(z-z_t)^5)^{1/3} \tag{7.36}$$

$$\mathcal{Q}(z) = C^*(z)(\mathcal{B}_0(z-z_t)^5)^{1/3} \tag{7.37}$$

$$G'_T(z) = \frac{1}{C^*(z)}\left({\mathcal{B}_0}^2(z-z_t)^{-5}\right)^{1/3} \tag{7.38}$$

with $C^*(z)$ a function of z

$$C^*(z) = C\left(1 + \left(\frac{z_B}{(z - z_t)}\right)^{5/3}\right) = 2.4852{\alpha_T}^{4/3}\left(1 + \left(\frac{z_B}{(z - z_t)}\right)^{5/3}\right) \tag{7.39}$$

z_t is the virtual origin displacement defined in the jet theory. This term is neglected in Linden-Rooney solutions by applying point source assumption. And z_B is the characteristic length of Boussinesq effect defined in equation (2.74). Note that z_B depends on the value of α_T and $\mathcal{B}_0$.

If we apply the conservation principle for volume flux, as presented in section 3.2.2, $C^*(z_i)$ will replace the term $\mathcal{C}$ and $\mathcal{C}^\#$ in final equation of the model (7.16) and (7.17), see equations (3.47) and (3.49).

The formulation will be a little complicated if we apply the conservation equation for mass flux. In this case, it is the term $C\rho_a$ thus a constant appears in formulation of $\mathcal{Q}_m$ but the term $C^*(z)$ appears in formulation of G'_T. Therefore, we cannot apply directly the demonstration in section 3.2.1.

We neglect here the term z_t to simply the formulation. Regrouping (7.29) and (7.36) with equation (7.15) connecting jet mass flux at interface with outlet mass flux, we have

$$Q_{m,t} = \rho_a A^{**}\sqrt{g'(H - z_i)} = \mathcal{Q}_m(z_i) = C\rho_a(\mathcal{B}_0 z_i^5)^{1/3} \tag{7.40}$$

Replacing g' by $G'_T(z_i)$ and applying equation (7.38), the above equation can be rewritten as

$$\frac{z_i^5}{H - z_i} = \frac{A^{**2}}{C^*(z_i)C^2} \tag{7.41}$$

Compared with formulation equation (7.16), we have

$$\mathcal{C} = {C^*}^{1/3}(z_i)C^{2/3} \tag{7.42}$$

However, for equation (7.17), we have $\mathcal{C}^\# = C^*(z_i)$ by direct application of equation (7.38).

7.3.4 Virtual origin correction

We have seen in section 3.2, when virtual origin displacement is neglected, we have $\xi = z_i/H$ and $\mathcal{H} = H$ terms appear in the final equations of the model (7.16) and (7.17).

If we consider virtual origin correction in ventilation model, the system will be solved in a virtual cavity from $z_t < 0$ to H with z_t virtual origin displacement defined in the jet models. Thus, in this case, the total height of the virtual cavity is $H - z_t$ and the height of interface above the virtual origin is $z_i - z_t$. Consequently, we have

$$\xi = \frac{z_i - z_t}{H - z_t}, \quad \mathcal{H} = H - z_t \tag{7.43}$$

in equations (7.16) and (7.17).

The length of virtual origin displacement z_t depends on applied turbulent jet model and the value of α_T, which may be different in Boussinesq and non Boussinesq cases. In a general case, the literature reported α_T will be used. Then z_t will be calculated from injection condition. In order to well fix the influence of virtual origin correction in system resolution, here we apply double conditions both at injection level $z = 0$ and at best-estimated interface level z_i^{BE} to determine the values of α_T and z_t.

Boussinesq case

We apply conditions on jet volume flux.

$$\begin{cases} Q_{inj} = \mathcal{Q}(0) = 2.4852{\alpha_T}^{4/3}\mathcal{B}_0^{1/3}(-z_t)^{5/3} \\ Q_t = \mathcal{Q}(z_i^{BE}) = 2.4852{\alpha_T}^{4/3}\mathcal{B}_0^{1/3}(z_i^{BE} - z_t)^{5/3} \end{cases} \tag{7.44}$$

We obtain the best-estimated solutions

$$\alpha_T = 0.093,\ z_t = -8.54\text{cm for hydrogen case}, \quad \alpha_T = 0.070,\ z_t = -10.9\text{cm for helium case} \tag{7.45}$$

We note here the additional virtual origin displacement is equal to almost the half of cavity height thus may not be neglected.

Non Boussinesq case

As injection flux is pure light gas (with known density), the injection condition identification will be equivalent for volume flux (7.37) and for mass flux (7.36). Therefore,

$$\begin{cases} Q_{m,inj} = \mathcal{Q}_m(0) = 2.4852\rho_a\mathcal{B}_0^{1/3}{\alpha_T}^{4/3}(-z_t)^{5/3} \\ Q_t = \mathcal{Q}_m(z_i^{BE}) = 2.4852\rho_a\mathcal{B}_0^{1/3}{\alpha_T}^{4/3}(z_i^{BE} - z_t)^{5/3} \end{cases} \tag{7.46}$$

We obtain the best-estimated solutions

$$\alpha_T = 0.148,\ z_t = -1.19\text{cm for hydrogen case}, \quad \alpha_T = 0.105,\ z_t = -2.40\text{cm for helium case} \tag{7.47}$$

The value α_T for non Boussinesq model is larger than that in Boussinesq case. The virtual original displacement z_t is largely smaller than that obtained in Boussinesq case.

And by applying injection conditions, we have

$$z_B = 5.64\text{cm for hydrogen case}, \quad z_B = 7.20\text{cm for helium case} \tag{7.48}$$

which is in the same order of the cavity height. The non Boussinesq effect is thus obviously presented in the jet flow within the whole cavity.

Important remark: We note that the α_T obtained in this section are different with that presented in the chapter 6. This is because we suppose the jet is immersed in a homogeneous environment with density ρ_a below the interface. Therefore, the α_T applied in Linden's bi-layer model shall be equivalent to the physical value of α_T **as if the jet were placed in an unstratified environment**. Practically, Boussinesq α_T will be chosen from literature depending on jet form. However, it is difficult to determine the non Boussinesq α_T as this value depends also on the jet mixture density.

Conclusion 7.3

We summarise the following procedure for solving bi-layer parameters. z_i can be solved from ξ and $X_{1,i}$ is directly linked to ρ_i and g'. As these two equations are coupled, it can be solved numerically by iteration (Newton's method). We may use $\mathcal{A} = A$ and $\mathcal{C} = C$ for the first iteration. The obtained z_i and ρ_i will be used to calculate $\mathcal{A}$ and $\mathcal{C}$ for the next iteration.

Solving bi-layer parameters

$$\begin{cases} \dfrac{\xi^5}{1-\xi} = \dfrac{\mathcal{A}^2}{\mathcal{C}^3\mathcal{H}^4} \\ g' = \dfrac{1}{\mathcal{C}^{\#}}{\mathcal{B}_0}^{2/3}(\xi\mathcal{H})^{-5/3} \end{cases}$$

Parameter	Formulation	Condition
$\mathcal{A}$	$A = \dfrac{\sqrt{c_t}S_bS_t}{\sqrt{\frac{1}{2}\left(\frac{c_t}{c_b}S_t^2+S_b^2\right)}}$	Small density range assumption, small injection volume flux
	$A^* = \dfrac{\sqrt{c_t^*}S_bS_t}{\sqrt{\frac{1}{2}\left(\frac{c_t^*}{c_b}S_t^2+S_b^2\right)}}$	Large density range, small injection volume flux
	$A^{**} = \dfrac{\sqrt{c_t^{**}}S_bS_t}{\sqrt{\frac{1}{2}\left(\frac{c_t^{**}}{c_b}S_t^2+S_b^2\right)}}$	Large density range, small injection mass flux
$\mathcal{C}$ and $\mathcal{C}^{\#}$	$\mathcal{C} = \mathcal{C}^{\#} = 2.5{\alpha_T}^{4/3}$	Morton's Boussinesq model
	$\mathcal{C} = \mathcal{C}^{\#} = 2.5{\alpha_T}^{4/3}\left(1+\left(\frac{z_B}{(z_i-z_t)}\right)^{5/3}\right)$	Rooney's non Boussinesq model with conservation of volume flux
	$\mathcal{C} = 2.5{\alpha_T}^{4/3}\left(1+\left(\frac{z_B}{(z_i-z_t)}\right)^{5/3}\right)^{1/3}$	Rooney's non Boussinesq model with conservation of mass flux ($z_t = 0$ if virtual origin correction is not applied)
	$\mathcal{C}^{\#} = 2.5{\alpha_T}^{4/3}\left(1+\left(\frac{z_B}{(z_i-z_t)}\right)^{5/3}\right)$	
ξ and $\mathcal{H}$	$\xi = \dfrac{z_i}{H},\ \mathcal{H} = H$	Virtual origin correction not applied
	$\xi = \dfrac{z_i - z_t}{H - z_t},\ \mathcal{H} = H - z_t$	Virtual origin correction z_t applied in the ventilation model

with $c_t^* = \dfrac{\rho_a}{\rho_i}c_t, \quad c_t^{**} = \dfrac{\rho_i}{\rho_a}c_t, \quad z_B = 0.58 \cdot {\alpha_T}^{-4/5} \cdot \dfrac{{\mathcal{B}_0}^{2/5}}{g^{3/5}}$

7.4 Impact of different assumptions on bi-layer parameters resolution

In this section, we will evaluate the impact of different assumptions (noted D, B, I, O in section 7.3.1) on bi-layer parameters resolution. We realise 8 calculations, by using 8 different methods (noted (i)-(viii)) with different assumptions summarised in table 7.5. We focus on two parameters in this calculation. The height of top homogeneous layer $H - z_i$ indicating the inflammable region of risk and its concentration (volume fraction) $X_{1,i}$ to evaluate the consequence (deflagration or detonation). The obtained results, as well as their absolute errors compared with that deduced in section 7.1 from DNS best-estimated parameters, are presented respectively in figure 7.5 for inflammable height and figure 7.6 the concentration error.

The absolute results as well as the estimation of outlet fluxes under each method are presented in appendix G.

Method	**Assp. D** (#1)	**Assp. B** (#2)	**Assp. I** (#3)	**Assp. O** (#4)	ξ	$\mathcal{H}$	$\mathcal{A}$	$\mathcal{C}$	$g' = \frac{\rho_a - \rho_i}{\rho_a} g$
(i)	Small	B	Volume	N	$\frac{z_i}{H}$	H	A	C	$\frac{\mathcal{B}_0^{2/3}}{C z_i^{5/3}}$
(ii)	Small	B	Volume	Y	$\frac{z_i - z_t}{H - z_t}$	$H - z_t$	A	C	$\frac{\mathcal{B}_0^{2/3}}{C(z_i - z_t)^{5/3}}$
(iii)	Large	B	Volume	N	$\frac{z_i}{H}$	H	A^*	C	$\frac{\mathcal{B}_0^{2/3}}{C z_i^{5/3}}$
(iv)	Large	B	Volume	Y	$\frac{z_i - z_t}{H - z_t}$	$H - z_t$	A^*	C	$\frac{\mathcal{B}_0^{2/3}}{C(z_i - z_t)^{5/3}}$
(v)	Large	NB	Volume	N	$\frac{z_i}{H}$	H	A^*	$C\left(1 + \left(\frac{z_B}{z_i}\right)^{5/3}\right)$	$\frac{\mathcal{B}_0^{2/3}}{C\left(1+\left(\frac{z_B}{z_i}\right)^{5/3}\right) z_i^{5/3}}$
(vi)	Large	NB	Volume	Y	$\frac{z_i - z_t}{H - z_t}$	$H - z_t$	A^*	$C\left(1 + \left(\frac{z_B}{z_i - z_t}\right)^{5/3}\right)$	$\frac{\mathcal{B}_0^{2/3}}{C\left(1+\left(\frac{z_B}{z_i - z_t}\right)^{5/3}\right) z_i^{5/3}}$
(vii)	Large	NB	Mass	N	$\frac{z_i}{H}$	H	A^{**}	$C\left(1 + \left(\frac{z_B}{z_i}\right)^{5/3}\right)^{1/3}$	$\frac{\mathcal{B}_0^{2/3}}{C\left(1+\left(\frac{z_B}{z_i}\right)^{5/3}\right) z_i^{5/3}}$
(viii)	Large	NB	Mass	Y	$\frac{z_i - z_t}{H - z_t}$	$H - z_t$	A^{**}	$C\left(1 + \left(\frac{z_B}{z_i - z_t}\right)^{5/3}\right)^{1/3}$	$\frac{\mathcal{B}_0^{2/3}}{C\left(1+\left(\frac{z_B}{z_i - z_t}\right)^{5/3}\right) z_i^{5/3}}$

(#1): Small/Large density range assumption
(#2): Jet resolution model (B: Boussinesq; NB: Non Boussinesq)
(#3): Choice of conservation and small injection flux in global balance (Mass: Mass flux; Volume: Volume flux)
(#4): Virtual origin displacement (N if not considered, Y if considered)

Iteration step 1: Solving z_i by $\frac{\xi^5}{1-\xi} = \frac{\mathcal{A}^2}{\mathcal{C}^3 \mathcal{H}^4}$, **Iteration step 2:** Solving ρ_i then $X_{1,i}$ by applying formula in the last column

$$A = \frac{\sqrt{c_t}\ S_b S_t}{\sqrt{\frac{1}{2}\left(\frac{c_t}{c_b} S_t^2 + S_b^2\right)}}, \quad A^* = \frac{\sqrt{\frac{\rho_a}{\rho_i} c_t}\ S_b S_t}{\sqrt{\frac{1}{2}\left(\frac{\rho_a}{\rho_i}\frac{c_t}{c_b} S_t^2 + S_b^2\right)}}, \quad A^{**} = \frac{\sqrt{\frac{\rho_i}{\rho_a} c_t}\ S_b S_t}{\sqrt{\frac{1}{2}\left(\frac{\rho_i}{\rho_a}\frac{c_t}{c_b} S_t^2 + S_b^2\right)}}, \quad C = 2.4852 \alpha_T^{4/3}, \quad z_B = 0.5791 \cdot {\alpha_T}^{-4/5} \cdot \frac{{\mathcal{B}_0}^{2/5}}{g^{3/5}}$$

Table 7.5: Determination of bi-layer parameters: 8 methods with different applied assumptions (Boussinesq approximation, virtual origin displacement, small jet simplification, etc.) Methods (i)-(iv) for Morton's Boussinesq jet solutions, (v)-(viii) for Rooney's non-Boussinesq jet solutions.

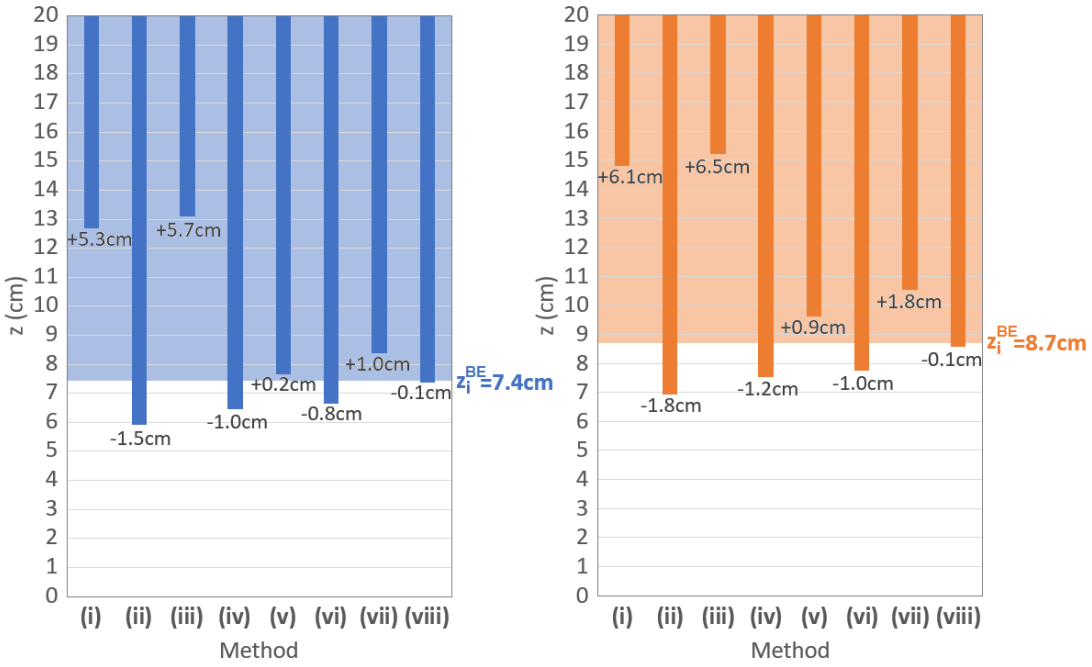

Figure 7.5: Estimation of height of inflammable region ($H - z_i$), results comparison with different methodologies (table 7.5). Left: hydrogen case, right: helium case. Vertical axis indicates the absolute vertical position in the cavity $0 < z <$20cm. The length of bar indicates the height of estimated height of inflammable region with their extremities z_i calculated from each method. Reference result is selected from its DNS best-estimated bi-layer parameters, coloured in blue (hydrogen) or orange (helium) in figure background. Data labels indicate the absolute error of estimation.

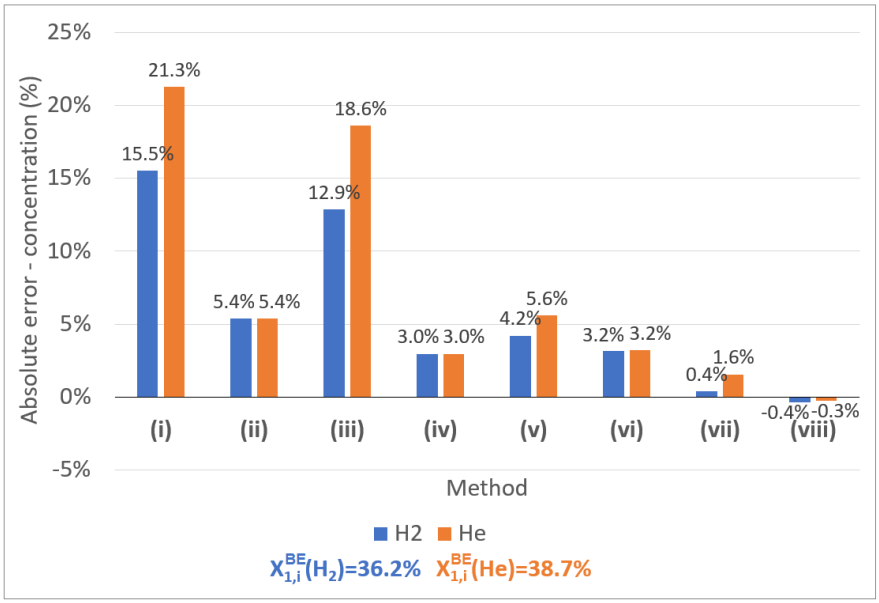

Figure 7.6: Estimation of volume fraction absolute difference $X_{1,i} - X_{1,i}^{BE}$ in top homogeneous layer, results comparison. Based on DNS deduced best-estimated result, the absolute error from each method (i)-(viii) are presented in bars with hydrogen case coloured in blue and helium case in orange. Positive bars indicate overestimated values and negative bars are underestimated values. The precise absolute error are indicated in data labels.

Method (i) is the original ventilation model presented in Linden et al. (1990), initially proposed to solve thermal air-conditioning problem. Here for its use in air-hydrogen mixing problem, the method provides a very inaccurate estimation of bi-layer parameters. The height of top homogeneous layer is largely underestimated (> 5cm, 1/4 height of cavity), which does not accord with conservative safety strategy. While the mixture concentration is largely overestimated (+20%), which is pertinent in conservative safety principle but generates large additional cost (L'Hostis et al. (2012)). Consequently, the direct use of original Linden's model presents important limits in air-hydrogen mixing problem. In order to improve the performance of Linden's model, four approaches can be considered.

Firstly, small density range assumption is clearly not valid, as for methods (i) and (ii), both of them estimate very badly the bi-layer parameters.

Secondly, virtual origin displacement shall be considered in the resolution. Methods (ii) (iv) (vi) (viii) are 4 methods that virtual origin displacement is considered in the calculation. Their relative errors are obviously smaller than that of the other 4 methods (i), (iii), (v), (vii) where the virtual origin correction is not applied. The introduction of this parameter will improve the concentration estimation and reduce its safety margin. Besides, this correction makes the inflammable region from an underestimated height into overestimated, therefore providing a conservative safety estimation (more serious consequence).

The influence of virtual origin displacement is obvious in Boussinesq case (ii) (iv) compared with (i) (iii). The introduction of this parameter will largely reduce its safety margin (around 10% concentration in absolute value) and generates 7cm (1/3 cavity height) difference of flammable region. For non Boussinesq cases (vi) (viii) compared with (v) (vi), the introduction of virtual origin displacement will not generate remarkable difference for concentration estimation. This is mainly because the virtual origin displacement is much longer for Boussinesq cases (larger than 10cm, 1/2 cavity height) than non-Boussinesq cases (around 1-2cm, 1/10 cavity height). Therefore, in the case when this virtual origin displacement cannot be correctly estimated, we prefer to use non Boussinesq jet model to reduce its influence.

Thirdly, for non-Boussinesq methods applying in jet resolution, small injection simplification is better to be applied for mass flux rather than for volume flux in global balance. In this case, conservation of mass flux should be applied in the resolution. Methods (v) and (vi) are calculated from conservation of volume flux and methods (vii) and (viii) are for mass flux. Comparing (vi) and (viii), where virtual origin correction is correctly applied for both methods, we note that the method (viii) provides the most accurate bi-layer parameters among these methods. The method (vi) provides a flammable region 1cm higher (1/20 cavity height) and 3% larger in absolute value for homogeneous concentration estimation.

However, if we turn to figure 0.4 in thesis introduction, we will find our case is such particular that the homogeneous layer concentration $X_{1,i}$ just happens into the interval 30%-40% where hydrogen-air mixture may probable generates the most serious consequence (detonation). In this interval, even if the concentration estimation possesses only 3% difference, the evaluation of detonation consequence will be totally different.

Lastly, Morton's Boussinesq turbulent jet solutions seems as applicable as Rooney's non Boussinesq solutions in the resolution in condition that other physical assumptions are reasonably applied. We compare method (iv) using Morton's solutions and method (vi) using Rooney's solutions. These two methods provide nearly same bi-layer parameters, flammable region and concentration. All these two solutions are competent to provide good bi-layer estimation if the virtual origin displacement is correctly calculated.

Generally, the large density assumption is the most important factor to improve the model reliability. Virtual origin correction is the second aspect which is absolutely necessary for large release rate. Both Boussinesq and non Boussinesq model can provide good estimation if

entrainment parameter α_T is well selected. For non Boussinesq approach, it is better to apply conservation of mass flux rather than volume flux. We shall particularly note that the above conclusions and remarks are valid only for this reference case. In order to generalise it into industrial practical use, some more tests shall be done with different release flow regimes.

Conclusion 7.4

In conclusion, original Linden's model presents some limits in its practical use. Firstly, small density range assumption must absolutely not be applied as this will generate large safety margin of concentration and wrongly estimate the flammable volume. Secondly, virtual origin displacement shall be considered in the turbulent jet solutions, especially for Morton's Boussinesq solutions. Besides, in this case, mass flux conservation principle is preferred to be used rather than volume flux. The later one generates around 3% in absolute error in concentration estimation.

However, both Boussinesq and non Boussinesq turbulent jet solutions can be applied in the resolution. Non Boussinesq method is preferred only if the virtual origin displacement could not be correctly estimated.

7.5 Summary and discussion

In this chapter, we have presented

- Best-estimated bi-layer solutions for ventilation model, based on DNS time-averaged concentration distribution
- Validity of a series of conservation assumptions applied in Linden's model
- Four additional physical assumptions and corresponding modified formulations of the ventilation model
- Results comparisons that justify the adaptation of physical assumptions applied for the hydrogen injection and hydrogen-air mixing problem

Linden's natural ventilation model is proposed to be used to calculate hydrogen distribution in two-vented cavity. However, the direct application of this model presents several limits. It usually provides bad estimation of interface level thus wrong flammable risk volume. Besides, this model provides large safety margin in concentration estimation which generates additional cost. The improvements of Linden's model are based on several additional physical assumptions applied in the model resolution.

Our study is divided into two steps. Firstly, we calculate, from DNS results, the best-estimated bi-layer solutions which meet all conservation assumptions in the model. These best-estimated solutions will be used as reference in the following step.

In the second phase, we propose four aspects to improve the performance of Linden's model. By comparing with DNS deduced best-estimated solutions, we have found that:

- Small density range assumption is not valid.
- Boussinesq or non Boussinesq jet solutions provide same accuracy level if other assumptions and parameters are correctly imposed.

- Virtual origin displacement should be considered, especially when Boussinesq model is applied for the jet modelling.
- Small injection assumption in global balance is preferred to be applied on mass flux rather than volume flux.

We shall particularly note that non-Boussinesq jet model presents an important constraint for its practical use. The non-Boussinesq entrainment coefficient, which depends not only on the flow pattern but also on mixture density in the jet and the selected reference density, does not possess a universal value for all cases. In this chapter, we have used its "measured" value from DNS results. But practically, its experimental measured values from helium cannot be used directly in hydrogen problem. The estimation of entrainment coefficient in non Boussinesq case is very difficult if we do not have full information of the jet evolution (velocity and density).

On the contrary, in Boussinesq jet models, entrainment coefficient is related only to flow pattern and depends only on injection volume flux and buoyancy flux. Various empirical formulas can be found in the literature. However, in Linden's model, the resolution is realised as if the jet were immersed in an unstratified environment. The environmental variation will reduce the buoyancy flux and thus will facilitate the entrainment effect. Consequently, the entrainment coefficient applied in the ventilation model is larger than its physical value calculated in chapter 6.

Conclusions and perspectives

Hydrogen presents high risk of deflagration and detonation. Therefore, its indoor use requires specific security measures. The air-hydrogen mixture risk is characterised by its concentration distribution in the confined environment. In accidental situations, hydrogen escapes and rises in form of a plume-jet that entrains ambient air, facilitating the natural ventilation and the mixing. Depending on the release flow rate, the risk region may be located only in the jet region. Or, for large release, a dangerous flammable mixture could be formed occupying the whole top part of the confined environment. In this study, we focus on a specific configuration: a cavity with two passive vents at different levels. This configuration facilitates natural ventilation effects and thus is recommended according to related security guidelines.

Predictive models have been developed to estimate hydrogen concentration distribution in the cavity, as that proposed by Linden et al. (1990). This model is commonly used in industrial context. However, it is found that this model often provides inaccurate estimation in large release flow rate conditions. Therefore, prejudicial conservative safety strategy has to be applied. This approach results in large safety margin in the related hydrogen concentration estimation, generating large additional cost. The objective of this thesis is to identify the reasons why predictive model is not applicable for certain situations and try to improve the applicability and the performance of the model.

In order to examine different approaches of modelling, we shall provide a reference test case in which mixing flows and hydrogen concentration field are well solved. We carried out fine DNS simulations based on a well-defined geometrical configuration.

The gas flow in the cavity is highly turbulent. Time-averaged velocity fields are thus used to characterise the quasi-steady flow. The flow pattern is in agreement with bi-layer structure assumed in the model of Linden et al. (1990). The impenetrable interface defined in Linden's model corresponds to a stratified layer in which environmental density changes quasi-linearly. A three-layer structure is thus introduced. Meanwhile, the jet changes its flow regime with its development: laminar jet - turbulent jet - turbulent jet-plume - pure plume. A comparison PIV-DNS validates the numerical simulation. Then 3D DNS fields are integrated to calculate the characteristic quantities of the jet and of the hydrogen distribution. DNS-deduced 1D profiles are then considered as the ground truth for comparison with different theoretical models. The 1D modelling is divided into two parts.

In the first phase, we study the reliability of several turbulent jet models applied in the stratified three-layer type environment. These models can be classified by two main assumptions: Boussinesq approximation and entrainment modelling. We first apply two α-constant models, Boussinesq model of Morton et al. (1956) and non Boussinesq approach of Rooney and Linden (1996). The analytical solutions of these models cannot be applied directly in the stratified environment. A quasi-analytical approach is thus proposed, taking into account the variation of environmental density. The choice of entrainment coefficient is particularly discussed compared with its physical value measured from DNS. In Boussinesq case, the best-estimated α in the model corresponds to its physical value in the jet regime mostly presented

in the cavity and matches the DNS measured value at the level where the local buoyancy frequency reaches its maximum. However, no general conclusion can be drawn for non Boussinesq model, as in this case, the entrainment coefficient depends also on the mixture density.

In fact, the entrainment coefficient varies with jet development. Richardson number is considered as an indicator to its variation. The reliability of several α-variable models like Kaminski et al. (2005) is also tested. The validity of these models is found limited in the lower part of the cavity where environmental density changes little. Application of these models in stratified environment should be coupled with other models providing environmental change.

In the second phase, we consider improving the applicability of the ventilation model. Linden's nature ventilation model is based on the bi-layer distribution assumption. The environmental density is assumed equal to that of fresh air below the interface and homogeneous above the interface. The direct use of this model provides, in the present case, a wrong estimation of flammable risk volume and a large safety margin in the concentration estimation. Improvements of this model are based on a series of additional assumptions applied in the model resolution. Four aspects are considered. Firstly small density range assumption is not valid thus cannot be used to linearise the conservation equations. Secondly, virtual origin displacement of the jet should be considered in the ventilation model, especially when Boussinesq model is applied for the jet. Thirdly, small injection assumption in global balance is preferred to be applied on mass flux rather than volume flux. Lastly, non Boussinesq jet model provides better solutions and is preferred to be used if virtual origin displacement cannot be correctly estimated. Finally, we shall particularly note that the jet resolution is realised as if the jet were immersed in a homogeneous environment. Consequently, the entrainment coefficient applied in the ventilation model should be chosen larger than its physical value defined in jet theories.

This work presents several perspectives.

First is about the jet modelling. In the resolution with α-constant models, the entrainment coefficient α should be provided beforehand. This coefficient is in fact not easy to determine in industrial context. Therefore, we consider using α-variable models. For example, in Kaminski's model, Richardson number is used as an indicator of α variation whereas its formula seems not directly applicable for this reference case. Other approaches such as that with source parameter Γ could be considered in the future work. If the variation of α could be correctly estimated, prejudicial conservative safety strategy applied for $\alpha = 0.05$ may be no longer necessary. This will save large additional cost related to the large safety margin generated from wrong estimation of this parameter.

The second point is about the bi-layer assumption. In Linden's ventilation model, the concentration distribution is treated as homogeneous above the interface. However, from DNS results, this "interface" is in fact a stratified layer in which environmental density varies with altitude. Compared with the height of the cavity, the vertical extension of this stratified layer may be not just simply ignored. We may integrate this three-layer structure into the ventilation model by assuming linear variation of environmental density in the intermediate stratified layer. We have developed one possibility presented in appendix H. In this three-layer model, the conservation equations are non-linear thus the system can only be solved numerically. This model needs to be validated by numerical simulations or experimental studies.

Last but not least, from a numerical point of view, in this study, DNS simulation provides excellent estimation of gas flow and concentration distribution. However, it is difficult to apply DNS method in large scale environment due to its high computation requirements. On one hand, DNS simulations solve directly Navier-Stokes equations. Its resolution of Poisson equation usually needs to inverse a large matrix at every time step. On the other hand, the mesh cell size depends on Kolmogorov micro-scale. For example, in this study, the full simulation

on a 2L cavity needs 6 million hours computation resources with 2k processors in parallel. For a larger geometry, DNS simulation often requires enormous computation resources and storage space. Industry thus prefers to use turbulent models likes RANS or URANS in practical research, but it is reported that these Reynolds-averaged methods may not capable of providing accurate estimation of hydrogen concentration in the turbulent jet. Therefore, we may consider to use other numerical approaches like LES, to evaluate their differences with DNS results in order to save computational costs, and at the same time, to guarantee the simulation quality.

Appendix

Appendix A

Detailed demonstration of three turbulent jet models

A.1 Boussinesq model Morton et al. (1956)

In this section, we present the detailed demonstration of conservation equations of Boussinesq model Morton et al. (1956). We re-write firstly the differential steady-state conservation equations in cylindric-polar system, taking into account the axisymmetric assumption then we do integration by applying model assumptions. The cylinder-polar coordinates system is used as (r,θ,z) with r the radial position from the jet axis, z vertical position (height/altitude). The origin is placed at injection point. We have in this coordinates system differential of position $d\overrightarrow{x} = dr\,\overrightarrow{e_r} + rd\theta\,\overrightarrow{e_\theta} + dz\,\overrightarrow{e_z}$ and the velocity vector $\overrightarrow{u} = u\,\overrightarrow{e_r} + v_\theta\,\overrightarrow{e_\theta} + w\,\overrightarrow{e_z}$.

Step 1: Differential conservation equations in cylinder-polar system

Conservation of volume flux

The conservation of volume flux is valid only under incompressible assumption.

$$\mathbf{div}\left(\overrightarrow{u}\right) = \frac{1}{r}\frac{\partial(ru)}{\partial r} + \frac{\partial w}{\partial z} = 0 \tag{A.1}$$

This equation can be rewritten as

$$\frac{\partial}{\partial r}(ru) + \frac{\partial}{\partial z}(rw) = 0 \tag{A.2}$$

Conservation of mass flux

We associate equations of conservation of mass and volume flux, we obtain:

$$0 = \mathbf{div}\left(\rho\overrightarrow{u}\right) = \rho\ \mathbf{div}\left(\overrightarrow{u}\right) + \overrightarrow{u}\cdot\overrightarrow{\mathbf{grad}}\ \rho = 0 + \left(\overrightarrow{u}\cdot\overrightarrow{\mathbf{grad}}\right)\rho \tag{A.3}$$

Thus,

$$u\frac{\partial\rho}{\partial r} + w\frac{\partial\rho}{\partial z} = 0 \tag{A.4}$$

Conservation of momentum in radial direction

We have the conservation of momentum in steady state:

$$\left(\rho\overrightarrow{u}\cdot\overrightarrow{\mathbf{grad}}\right)\overrightarrow{u} = -\overrightarrow{\mathbf{grad}}\ P + \mathbf{div}\,\overline{\overline{\tau}} + \rho g\,\overrightarrow{e_z} \tag{A.5}$$

with P time-averaged pressure field, $\overline{\overline{\tau}} = \left[\tau_{ij}\right]$ is the viscous stress tensor, $g = 9.81 m/s^2$ gravitational acceleration and $\overrightarrow{e_z} = (0,\ 0,\ -1)$ the downward unity vector. Under incompressible assumption, we have the term $\left(\mathbf{div}\ \overline{\overline{\tau}}\right)\Big|_r = \mu\left(\frac{1}{r}\frac{\partial}{\partial r}\left(r\frac{\partial u}{\partial r}\right) + \frac{\partial^2 u}{\partial z^2}\right)$ is in second order derivation thus will be neglected.

The radial projection of momentum equation is

$$\left(\rho\overrightarrow{u}\cdot\overrightarrow{\mathbf{grad}}\right)u = -\frac{\partial P}{\partial r} \tag{A.6}$$

which can be written as

$$u\frac{\partial u}{\partial r} + w\frac{\partial u}{\partial z} = -\frac{1}{\rho}\frac{\partial P}{\partial r} \tag{A.7}$$

We define a coefficient γ_ρ:

$$\gamma_\rho = \frac{\rho}{\rho_0} \tag{A.8}$$

In Boussinesq approximation, γ_ρ will be treated as a constant 1 (see eq. (2.4)), the projection in radial direction can be written as

$$u\frac{\partial u}{\partial r} + w\frac{\partial u}{\partial z} = -\frac{1}{\gamma_\rho}\frac{1}{\rho_0}\frac{\partial P}{\partial r} \approx -\frac{1}{\rho_0}\frac{\partial P}{\partial r} \tag{A.9}$$

Conservation of momentum in vertical direction

The vertical projection of momentum equation can be written as:

$$\rho\left(\overrightarrow{u}\cdot\overrightarrow{\mathbf{grad}}\right)w - \rho_e g + \left(\mathbf{div}\ \overline{\overline{\tau}}\right)\Big|_z + \rho g = 0 \tag{A.10}$$

The far field environment is considered stable thus with zero radial velocity, thus we have $\frac{\partial P}{\partial z} = -\rho_e g$ the vertical gradient of pressure.

Also, note that $\left(\mathbf{div}\ \overline{\overline{\tau}}\right)\Big|_z = \mu\left(\frac{1}{r}\frac{\partial}{\partial r}\left(r\frac{\partial w}{\partial r}\right) + \frac{\partial^2 w}{\partial z^2}\right)$ under incompressible assumption. We neglect this term because it is a second-order derivation concerning w.

Then we have

$$\left(\overrightarrow{u}\cdot\overrightarrow{\mathbf{grad}}\right)w = \frac{\rho_e - \rho}{\rho}g \tag{A.11}$$

The conservation of momentum in vertical direction could be written to

$$u\frac{\partial w}{\partial r} + w\frac{\partial w}{\partial z} = \frac{\rho_e - \rho}{\rho}g = \frac{1}{\gamma_\rho}G' \approx G' \tag{A.12}$$

As under Boussinesq approximation, γ_ρ can be treated as a constant 1.

Step 2: Integral conservation equations

We integrate the differential conservation equations in the jet horizontal cross-section, applying assumptions of the model.

Conservation of volume flux by using entrainment assumption

By integrating equation (A.2) across the plume, we obtain:

$$\frac{d}{dz}\int_0^\infty rw\,dr = -[ru]_0^\infty = -(ru)|_\infty \tag{A.13}$$

The inflow from jet border (at radius b_T) is driven by the entrainment into the turbulent jet. Increase of volume flux in the jet is due to entrainment effect which pushes the environment fluid in the far field of the jet entering into the jet. Thus, we consider

$$-(ru)|_\infty = -(ru)|_{b_T} = b_T u_e \tag{A.14}$$

Thus, by using entrainment assumption

$$\frac{d\mathcal{Q}}{dz} = 2\pi(-(ru)|_\infty) = 2\pi b_T u_e = 2\pi\alpha_T b_T w_T \tag{A.15}$$

Besides, under Top-hat assumption, by identification of $\mathcal{Q}$ and $\mathcal{M}$ we have

$$w_T = \frac{\mathcal{M}}{\mathcal{Q}}, \quad b_T = \frac{\mathcal{Q}}{\sqrt{\pi\mathcal{M}}} \tag{A.16}$$

Using this relation, we have

$$\frac{d\mathcal{Q}}{dz} = 2\alpha_T\sqrt{\pi\mathcal{M}} \tag{A.17}$$

Conservation of buoyancy flux

Recall that the buoyancy flux $\mathcal{B}$ is defined as

$$\mathcal{B} = \int_0^\infty G' w \cdot 2\pi r dr = \int_0^\infty \left(\frac{\rho_e - \rho}{\rho_0}\right) g w \cdot 2\pi r dr \tag{A.18}$$

Consider

$$\frac{d}{dz}\int_0^\infty rw(\rho_e - \rho)\,dr = \int_0^\infty (\rho_e - \rho) r\frac{\partial w}{\partial z}dr + \int_0^\infty rw\frac{\partial(\rho_e - \rho)}{\partial z}dr \tag{A.19}$$

By using equations (A.1) and (A.4), this equation can be written as

$$\frac{d}{dz}\int_0^\infty rw(\rho_e - \rho)\,dr = -\int_0^\infty (\rho_e - \rho)\frac{\partial ru}{\partial r}dr - \int_0^\infty ru\frac{\partial(\rho_e - \rho)}{\partial r}dr + \int_0^\infty rw\frac{d\rho_e}{dz}dr \tag{A.20}$$

Applying relation (2.12), the first two terms integrate to 0, by adding constant 2π on both side of the equation, we obtain

$$\frac{d\mathcal{B}}{dz} = -N^2\mathcal{Q} \tag{A.21}$$

with

$$N^2 = -\frac{g}{\rho_0}\frac{d\rho_e}{dz} \tag{A.22}$$

is the square of the ambient Brunt-Vaisala buoyancy frequency.

Conservation of momentum

Integrating the equation of conservation of momentum in vertical direction (A.12), we have

$$\int_0^\infty \left(u\frac{\partial w}{\partial r} + w\frac{\partial w}{\partial z}\right) r dr = \int_0^\infty \frac{1}{\gamma_\rho} G' r dr \tag{A.23}$$

Beside, we have

$$\int_0^\infty u\frac{\partial w}{\partial r} r dr = [ruw]_0^\infty - \int_0^\infty w\frac{\partial ru}{\partial r}dr \tag{A.24}$$

The first term on the right-hand side is zero, by using equation (A.2), noting that $w\frac{\partial w}{\partial z} = \frac{1}{2}\frac{\partial w^2}{\partial z}$, we have

$$\int_0^\infty \left(u\frac{\partial w}{\partial r} + w\frac{\partial w}{\partial z}\right) r dr = \frac{1}{2}\int_0^\infty \frac{\partial w^2}{\partial z} r dr + \frac{1}{2}\int_0^\infty \frac{\partial w^2}{\partial z} r dr = \frac{d}{dz}\int_0^\infty w^2 r dr \tag{A.25}$$

Consequently by using equations (A.23), (A.25) and (2.26) and under Boussinesq approximation, we have

$$\frac{d\mathcal{M}}{dz} = \int_0^\infty \frac{1}{\gamma_\rho} G' \cdot 2\pi r dr \approx \int_0^\infty G' \cdot 2\pi r dr \tag{A.26}$$

Besides, by using Top-hat assumption (A.26), (2.24), (2.26) and (2.28), we have

$$\frac{d\mathcal{M}}{dz} = \int_0^{b_T} G'_T 2\pi r dr = \frac{\int_0^{b_T} G'_T w_T 2\pi r dr \int_0^{b_T} w_T 2\pi r dr}{\int_0^{b_T} w_T^2 2\pi r dr} = \frac{\mathcal{BQ}}{\mathcal{M}} \tag{A.27}$$

A.2 Boussinesq model Kaminski et al. (2005)

In this section, we present the detailed demonstration of conservation equations of Boussinesq model Kaminski et al. (2005). Note that this demonstration is based on Boussinesq approximation and valid only for homogeneous environment where far field density ρ_e does nor change along the jet.

Step 1: Additional conservation equation

Like classic Boussinesq model Morton et al. (1956), the conservation equations consist of that of volume flux, momentum flux and buoyancy flux. Conservation equations of momentum flux $\mathcal{M}$ and of buoyancy flux $\mathcal{B}$ are under the same demonstration as presented in equations (A.21) and (A.26). By applying under the homogeneous environment assumption, we have

$$\frac{d\mathcal{M}}{dz} = \int_0^\infty G' \, 2\pi r dr, \text{ with } G'(r,z) = \frac{\rho_e - \rho(r,z)}{\rho_0} g \tag{A.28}$$

$$\frac{d\mathcal{B}}{dz} = 0 \tag{A.29}$$

An additional conservation equation is based on the conservation of mass flux and volume flux (A.3) by changing ρ to G' as G' is a linear function of ρ under unstratified assumption.

$$\left(\overrightarrow{u} \cdot \overrightarrow{\mathbf{grad}}\right) G' = 0 \tag{A.30}$$

Regrouping with (A.2)

$$\frac{\partial}{\partial r}(ruG') + \frac{\partial}{\partial z}(rwG') = 0 \tag{A.31}$$

By using the conservation of momentum in vertical direction (A.12), we have

$$\frac{\partial}{\partial r}(ruw) + \frac{\partial}{\partial z}\left(rw^2\right) = rG' \tag{A.32}$$

Then from equations of conservation of volume flux (A.2) and of momentum (A.32), we deduce the following balance equation.

$$\frac{\partial}{\partial r}\left(\frac{1}{2}ruw^2\right) + \frac{\partial}{\partial z}\left(\frac{1}{2}rw^3\right) = rwG' \tag{A.33}$$

By integrating it on horizontal plane, we have the third conservation equation:

$$\frac{d}{dz}\int_{r=0}^{\infty}\frac{1}{2}w^3 2\pi r dr = \mathcal{B} \tag{A.34}$$

Step 2: Associating general profiles with Top-hat profiles

For a general case, where the distribution of $w(r,z)$ and $G'(r,z)$ are arbitrary, 2 shape functions may be introduced as follows. Shape functions $f(r,z)$ and $h(r,z)$ are null when r towards infinity (far-field) for any z.

$$w(r,z) = w_m(z)\, f(r,z) \tag{A.35}$$

$$G'(r,z) = G'_m(z)\, h(r,z) \tag{A.36}$$

with $w_m(z)$ the maximum vertical velocity in the centre of the jet ($r = 0$), $G'_m(z)$ the maximum reduced gravity in the centre of the jet.

In order to provide the relation between w_m and w_T, G'_m and G'_T, We define following dimensionless integral variables where $r^* = r/e_r$ dimensionless parameter with e_r length unit.

$$I_0(z) = \int_{r^*=0}^{\infty} f(r^*,z)\cdot 2\pi r^* dr^* \tag{A.37}$$

$$I_1(z) = \int_{r^*=0}^{\infty} f(r^*,z)\, h(r^*,z)\cdot 2\pi r^* dr^* \tag{A.38}$$

$$I_2(z) = \int_{r^*=0}^{\infty} h(r^*,z)\cdot 2\pi r^* dr^* \tag{A.39}$$

$$I_3(z) = \int_{r^*=0}^{\infty} f^2(r^*,z)\cdot 2\pi r^* dr^* \tag{A.40}$$

$$I_4(z) = \int_{r^*=0}^{\infty} f^3(r^*,z)\cdot 2\pi r^* dr^* \tag{A.41}$$

Besides, under Top-hat assumption, we have

$$\int_0^{\infty} G' 2\pi r dr = \pi b_T^2 G'_T \tag{A.42}$$

By identification of $\mathcal{B}, \mathcal{M}$ and (A.42), we have

$$b_T = \frac{\sqrt{I_3}I_2}{\sqrt{\pi}I_1}e_r,\quad w_T = \frac{I_1}{I_2}w_m,\quad G'_T = \frac{I_1^2}{I_2 I_3}G'_m \tag{A.43}$$

Step 3: Solving conservation equation

The idea is to solve conservation equations (A.28), (A.29) and (A.34) by applying additional Top-hat assumption then to generalise it by using the above relations (A.43).

Under Top-hat profiles assumption, we have firstly the conservation of buoyancy (A.29), the same as in original model of Morton et al. (1956).

$$\frac{d}{dz}\left(b_T^2 w_T G'_T\right) = 0 \tag{A.44}$$

Also, we have the conservation of momentum (A.28), also same as in Morton et al. (1956).

$$\frac{d}{dz} b_T^2 w_T^2 = b_T^2 G_T' \tag{A.45}$$

The third conservation equation is about volume flux. By using the integral profiles (A.43), we rewrite the new conservation equation (A.34) as

$$\frac{d}{dz} b_T^2 w_T^3 = \frac{2}{A} b_T^2 w_T G_T' - b_T^2 w_T^3 \frac{d\ln A}{dz} - C b_T w_T^3 \tag{A.46}$$

with coefficient

$$A(z) = \frac{I_2 I_4}{I_1 I_3}, \quad C(z) = \frac{\sqrt{I_3} I_2}{\sqrt{\pi} I_1 I_4} \tag{A.47}$$

Besides, note that

$$\frac{d b_T^2 w_T^3}{dz} = \frac{d(b_T^2 w_T^2 \cdot w_T)}{dz} = w_T \frac{d b_T^2 w_T^2}{dz} + b_T^2 w_T^2 \frac{d w_T}{dz} \tag{A.48}$$

$$\frac{d b_T^2 w_T^2}{dz} = \frac{d(b_T^2 w_T \cdot w_T)}{dz} = w_T \frac{d b_T^2 w_T}{dz} + b_T^2 w_T \frac{d w_T}{dz} \tag{A.49}$$

Eliminating $\frac{dw_T}{dz}$, we have

$$\frac{d b_T^2 w_T}{dz} = -\frac{1}{w_T^2} \frac{d b_T^2 w_T^3}{dz} + \frac{2}{w_T} \frac{d b_T^2 w_T^2}{dz} \tag{A.50}$$

We identify on the left-hand side in equation (A.50) the derivative of volume flux, grouping it with (A.44) and (A.45) by its expressions as a function of A and C (A.47), finally we obtain following conservation equation of volume flux.

$$\frac{d}{dz} \pi b_T^2 w_T = 2\pi \alpha b_T w_T \tag{A.51}$$

where α entrainment coefficient no longer constant but variable along the jet, is defined by

$$\alpha(z) = \frac{C(z)}{2} + \left(1 - \frac{1}{A(z)}\right) \mathrm{Ri}(z) + \frac{b_T(z)}{2} \frac{d\ln A(z)}{dz} \tag{A.52}$$

with $A(z)$ and $C(z)$ two parameters and Ri(z) local Richardson number defined by

$$\mathrm{Ri} = \frac{I_2^2}{I_1 \sqrt{I_3}} \frac{G_m' e_r}{w_m^2} = \frac{b_T G_T'}{w_T^2} \tag{A.53}$$

Note that $\mathcal{Q} = \pi b_T^2 w_T$, this equation can be rewritten in the form of conservation equation of volume flux of Morton (2.3.2) but with entrainment coefficient $\alpha(z)$ variable along the jet.

$$\frac{d\mathcal{Q}}{dz} = 2\alpha(z) \sqrt{\pi \mathcal{M}} \tag{A.54}$$

A.3 Non-Boussinesq model Rooney et Linden (1996)

In this section, we present the detailed demonstration of non-Boussinesq model Rooney and Linden (1996). Note that in this model, no more incompressible condition is assumed. The conservation equations consist of conservation of mass and momentum. We need a third conservation equation that related to the fluid state and enthalpy to enclose the system as 3 characteristic quantities are defined.

First equation: Conservation of mass

We rewrite the differential steady-state conservation of mass

$$\mathbf{div}\left(\rho\overrightarrow{u}\right) = \frac{1}{r}\frac{\partial(\rho r u)}{\partial r} + \frac{\partial \rho w}{\partial z} = 0 \tag{A.55}$$

This equation can be rewritten as

$$\frac{\partial}{\partial r}(ru\rho) + \frac{\partial}{\partial z}(rw\rho) = 0 \tag{A.56}$$

By integrating equation (A.56) from jet centre to infinity, we obtain:

$$\frac{d}{dz}\int_0^\infty \rho w r dr = -[ru\rho]_{r\to\infty} = -(ru)|_\infty \rho_e \tag{A.57}$$

where ρ_e is the environment density at far field of the jet.

The inflow from infinity is driven by the entrainment into the turbulent jet, thus $u < 0$. Under Top-hat assumption, we have

$$-(ru)|_\infty = -(ru)|_{r=b_T} = b_T u_e \tag{A.58}$$

Thus,

$$\frac{d\mathcal{Q}_m}{dz} = 2\pi b_T u_e \rho_e \tag{A.59}$$

Second equation: Conservation of momentum

Regrouping differential equation of momentum in vertical direction (A.12) with conservation of mass equation (A.56), we have

$$\frac{\partial}{\partial r}(r\rho u w) + \frac{\partial}{\partial z}\left(r\rho w^2\right) = (\rho_e - \rho) g r \tag{A.60}$$

By integrating equation (A.60) from the jet centre to infinity far field at rest, we obtain:

$$\frac{d}{dz}\int_0^\infty \rho w^2 r dr = g\int_0^\infty (\rho_e - \rho) r dr \tag{A.61}$$

Thus, we have conservation of momentum

$$\frac{d\mathcal{M}_m}{dz} = 2\pi g \int_0^\infty (\rho_e - \rho) r dr \tag{A.62}$$

Under Top-hat assumption, this equation can be rewritten as

$$\frac{d\mathcal{M}_m}{dz} = 2\pi g \int_0^{b_T} (\rho_e - \rho) r dr = \pi g (\rho_e - \rho_T) b_T^2 \tag{A.63}$$

Third equation: Equation enthalpy and conservation of volume flux

We begin with thermodynamic definition of enthalpy: $dH = dQ + VdP$ with dQ the heat change of the system, V the volume of the system considered constant and dP the thermodynamic pressure change. We have firstly the enthalpy time change rate for a general system

$$\dot{H} = \dot{Q} + V\dot{P} \tag{A.64}$$

with $\dot{Q}$ the total heat in power input to the system, dot superscripts denote time derivatives, which is zero as we study in a isotherm condition. In a steady state, the pressure has no time independence. Thus, we have

$$\dot{H} = 0 \tag{A.65}$$

Besides, the enthalpy flux $\dot{H}$ at altitude z in the jet can also be written as

$$\dot{H}(z) = \int_{S(z)} \rho h \overrightarrow{u} \cdot \overrightarrow{e_z} dS \tag{A.66}$$

with $S(z)$ jet section area at altitude z, ρ, h, $\overrightarrow{u}$ the local mass density, enthalpy and velocity in the jet, $\overrightarrow{e_z}$ is jet direction (assumed vertical). By definition, we have $h = c_v T + P/\rho$ with $c_v T$ the density of internal energy with T temperature in K and c_v the specific heat capacity. Thus, we have

$$0 = \int_{S(z)} (c_v T\rho + P)\overrightarrow{u} \cdot \overrightarrow{e_z} dS \tag{A.67}$$

We apply ideal gas state equation $P = \rho RT$, so that $c_v T\rho + P = \rho T(c_v + R) = \rho T c_p$ with c_p isobar heat capacity assumed constant. By using divergence theorem, we have

$$\frac{c_p}{R}\int_{\tau(z)} P\ \mathbf{div}\left(\overrightarrow{u}\right) d\tau = -\frac{c_p}{R}\int_{\tau(z)} \overrightarrow{u} \cdot \overrightarrow{\mathbf{grad}}\,(P)\, d\tau \tag{A.68}$$

where $\tau(z)$ the volume enclosed by surface $S(z)$. We approximate the pressure across the jet to be uniform and equal to the ambient pressure just outside the jet boundary. In cylinder-polar system, we have

$$P\int_0^\infty \left(\frac{\partial ru}{\partial r} + \frac{\partial rw}{\partial z}\right) dr = -\frac{dP}{dz}\int_0^\infty wr dr \tag{A.69}$$

Taking w negligible outside the jet boundary, using assumption $-(ru)|_\infty = -(ru)|_{r=b_T} = b_T u_e$, we obtain

$$\frac{dQ}{dz} = 2\pi b_T u_e - \frac{Q}{P}\frac{dP}{dz} \tag{A.70}$$

In hydrostatic ambient, we have $\frac{dP}{dz} = -\rho_e g$ with $P \approx 1$atm. Thus, the term $P/\frac{dP}{dz}$ is in order of magnitude 10^4m, largely superior to the height extension of the jet for majority cases (in this study 0.2m). Hence, the second term in (A.70) $\frac{Q}{P}\frac{dP}{dz}$ can be correctly neglected.

Consequently, the consideration of enthalpy leads to a conservation of volume flux.

$$\frac{dQ}{dz} = 2\pi b_T u_e \tag{A.71}$$

Appendix B

Virtual origin displacement in the non Boussinesq case

Carlotti and Hunt (2005) present a two-step correction method for non-Boussinesq jet to determine this virtual source displacement. The approach is very similar as in Boussinesq case presented in section 2.5.3. The total virtual origin displacement can be divided into three parts

$$z_t = z_v + z_{avs} + z_0 \tag{B.1}$$

with z_0 the injection geometry correction, z_v source correction and z_{avs} the jet-length-based correction, detailed as follows. After correction, a general jet is transferred into a pure point plume with its origin situated at $z = z_t$.

Step 1: Source correction

In the first step, we transfer the general point source $(\mathcal{Q}_m(0), \mathcal{M}_m(0), \mathcal{B}_0)$ to a forced plume $(0, \zeta\mathcal{M}_m(0), \mathcal{B}_0)$ with $\zeta^5 = 1 - \Gamma_0$ linked to source parameter. Here for non-Boussinesq case, this parameter is defined as

$$\Gamma_0 = \frac{5\sqrt{\rho_e}}{8\sqrt{\pi}\alpha_T}\frac{\mathcal{B}_0\mathcal{Q}_{m,0}^2}{\mathcal{M}_{m,0}^{5/2}} \tag{B.2}$$

This step introduces another source displacement z_v called source correction origin displacement. The source-related correction is exact.

Step 2: Jet-length-based correction

In the second step, we transfer the forced plume obtained by the second step $(0, \zeta\mathcal{M}_m(0), \mathcal{B}_0)$ to a pure plume $(0,\ 0,\ \mathcal{B}_0)$. This will introduce another source displacement z_{avs} called jet-length-based correction origin displacement. The jet-length-based correction is valid only for jet length far from the origin (z enough large).

Formulas for virtual origin displacement in non Boussinesq case

For calculation of z_v and z_{avs}, we shall firstly define a characteristic length of non-Boussinesq effect noted z_B. Below this level the non-Boussinesq effects is dominant.

$$z_B = \left(\frac{25}{36}\right)^{3/5}\left(\frac{25}{48}\right)^{-1/5}\pi^{-2/5}{\alpha_T}^{-4/5}\frac{{\mathcal{B}_0}^{2/5}}{g^{3/5}} \tag{B.3}$$

The two displacements z_v and z_{avs} are related to the source parameter Γ_0 and can be divided into 3 cases.

Case $\Gamma_0 = 1$

If $\Gamma_0 = 1$, only a single correction related to source is needed.

$$z_v = -\frac{\sqrt{10}}{3\pi^{1/4}\alpha_T^{1/2}} \frac{\mathcal{M}_{m,0}^{3/4}}{\rho_e^{3/4}\mathcal{B}_0^{1/2}} \tag{B.4}$$

and the correction displacement related to jet length is zero.

$$z_{avs} = 0 \tag{B.5}$$

Case $\Gamma_0 < 1$

In this case, we call it a forced plume (or forced jet). The source-related correction is

$$\frac{z_v}{z_B} = -\frac{3}{5}\mathfrak{M}^{3/4}\mathcal{F}_f\left(\frac{g}{\rho_e}\frac{\mathcal{Q}_{m,0}}{\mathcal{B}_0}\frac{1}{\mathfrak{M}^{5/4}}\right) \tag{B.6}$$

with z_B defined in equation (2.74), $\mathcal{F}_f$ a function defined by

$$\mathcal{F}_f(X) = \int_0^X \frac{1}{(u^2+1)^{1/5}}\,\mathrm{d}u \tag{B.7}$$

as well as a dimensionless parameter $\mathfrak{M}$ defined by

$$\mathfrak{M} = \left(\left(\frac{\mathcal{M}_{m,0}}{\rho_e}\frac{g^{4/5}}{\mathcal{B}_0^{6/5}}\left(\frac{36}{25}\left(\frac{25}{48}\right)^{1/3}\pi^{2/3}{\alpha_T}^{4/3}\right)^{3/10}\right)^{5/2} - \left(\frac{g}{\rho_e}\frac{\mathcal{Q}_{m,0}}{\mathcal{B}_0}\right)^2\right)^{2/5} \tag{B.8}$$

The jet-length-based correction is

$$\frac{z_{avs}}{z_B} = -0.5012\ \mathfrak{M}^{3/4} \tag{B.9}$$

Case $\Gamma_0 > 1$

In this case, we call it a lazy plume. The source-related correction is

$$\frac{z_v}{z_B} = -\frac{3}{5}\mathfrak{G}^{3/5}\mathcal{F}_l\left(\frac{g}{\rho_e}\frac{\mathcal{Q}_{m,0}}{\mathcal{B}_0}\frac{1}{\mathfrak{G}}\right) \tag{B.10}$$

with $\mathcal{F}_l$ a function defined by

$$\mathcal{F}_l(X) = \int_1^X \frac{1}{(u^2-1)^{1/5}}\,\mathrm{d}u \tag{B.11}$$

as well as a dimensionless parameter $\mathfrak{G}$ defined by

$$\mathfrak{G} = \sqrt{\left(\frac{g}{\rho_e}\frac{\mathcal{Q}_{m,0}}{\mathcal{B}_0}\right)^2 - \left(\frac{\mathcal{M}_{m,0}}{\rho_e}\frac{g^{4/5}}{\mathcal{B}_0^{6/5}}\left(\frac{36}{25}\left(\frac{25}{48}\right)^{1/3}\pi^{2/3}{\alpha_T}^{4/3}\right)^{3/10}\right)^{5/2}} \tag{B.12}$$

The jet-length-based correction is

$$\frac{z_{avs}}{z_B} = -0.8526\ \mathfrak{G}^{3/5} \tag{B.13}$$

Appendix C

Effect of vertical openings in ventilation model

In industrial context, the height of openings sometimes may not be neglected, such as the case of garage. Based on experimental studies in CEA (see Bernard-Michel et al. (2012), Cariteau (2012)), Bernard-Michel (2014) summarised the effect of vertical opening in model of Linden et al. (1990). In this section, we present in detail this correction for the calculation of inlet/outlet volume through the two openings. As the height of two vents (1cm) is relatively small in this problem, numerical application of following modification shows only 3% error of outlet flux compared with original Linden's model. Consequently, this correction will not be applied in resolution.

C.1 Geometrical assumption of two openings and related velocity profiles

In the correction of Bernard-Michel (2014), the height of openings is considered. We note T_t, T_b the height of top and bottom opening respectively and W_t, W_b its related width, as presented in figure C.1 on the left. We suppose the bottom edge of the bottom opening is coincided with the cavity floor where $z = 0$ and the top edge of the top opening is coincided with the ceiling of the cavity where $z = H$.

In this case, the inlet/outlet velocity is not a constant but as functions of altitude z. The neutral level $z = z_n$ and/or the interface level $z = z_i$ may be situated through the two openings.

We distinguish two cases, one for small top opening, where the whole top opening is situated above the neutral level $z_n < H - T_t$, as presented in the left-hand-side sketch in figure C.1. In this case, the flow through the top opening is totally outward. However, if the top opening is large enough so that the neutral level is situated through the top opening, as presented in the right-hand-side sketch in figure C.1, where $z_n > H - T_t$, the flow through the top opening can be divided by two parts, an outward flow, for the area $z_n < z < H$, and an inward flow, corresponding to the area $H - T_t < z < z_n$.

We note $u_t(z)$ the outlet velocity through the top opening, with $u_t(z) > 0$ indicating outlet flux (outward direction) and $u_t(z) < 0$ indicating inlet flux (inward direction). Similarly, we note $u_b(z)$ the inlet velocity through the bottom opening, with $u_b(z) > 0$ when flow enters into the cavity and $u_b(z) < 0$ when flow exits the cavity.

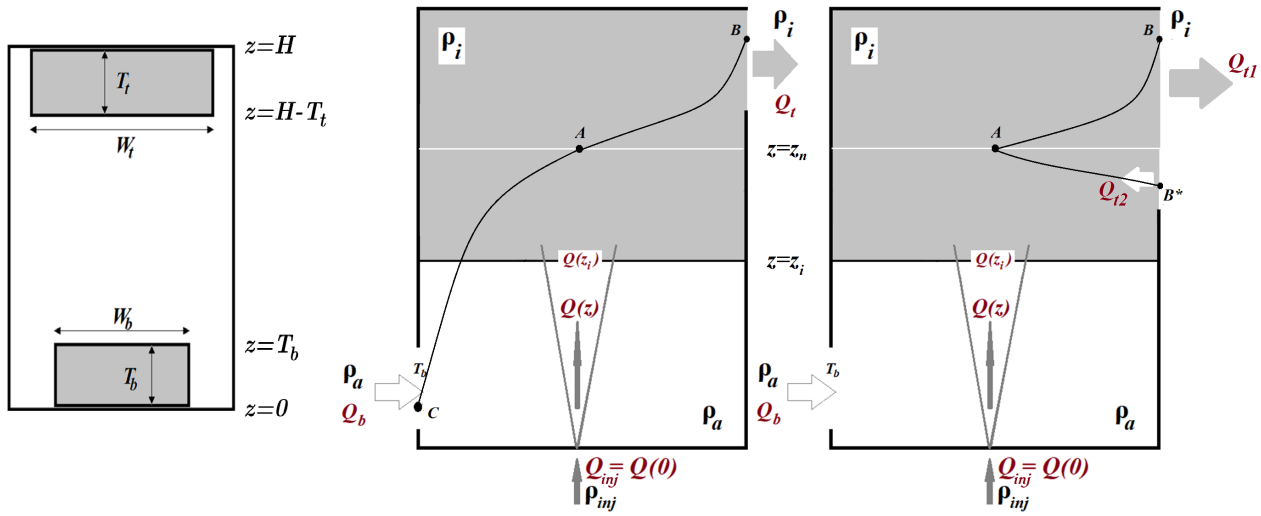

Figure C.1: Sketch for application of theorem of Bernoulli in a two-vented cavity. Left: definition of geometrical parameters of two openings. Middle: case where $z_n < H - T_t$. Right: case where $z_n > H - T_t$

Flow through top opening

Top opening and outward flux

We apply Bernoulli's equation between a point A, situated on the neutral plan $z_A = z_n$, and a point B, situated on the border of top vent with altitude $z > z_n$, as presented in figure C.1. As the cross-section surface is largely bigger than that of the top opening, by using the incompressible flow assumption, we assume that the fluid velocity $u_A \approx 0$ and we have $u_B = u_t(z)$ the velocity at point B. Thus, the Bernoulli's equation is written as

$$\rho_i \frac{u_t^2(z)}{2} = P_e(z_n) - P_e(z) - \rho_i g(z - z_n) = (\rho_a - \rho_i) g(z - z_n) \tag{C.1}$$

We shall take into account the pressure loss from openings, for this purpose we introduce a coefficient c_t depending on geometry form for top vent. By introducing $g' = \frac{\rho_a - \rho_i}{\rho_a} g$ the environmental reduced gravity in the homogeneous layer, we have finally

$$u_t^2(z) = 2c_t \frac{\rho_a}{\rho_i} g'(z - z_n) \tag{C.2}$$

Top opening and inward flux

For case $z_n > H - T_t$, the flow is inward for area $H - T_t < z < z_n$. We take another border point B^* in this area. As in this case the flow at B^* is inward so that if we apply the Bernoulli's theorem from B^* to A, we have a same equation except $\rho_{B^*} = \rho_a$, so that the term ρ_a/ρ_i will disappear in the final result. We have in this case

$$u_t^2(z) = 2c_t g'(z_n - z) \tag{C.3}$$

Note that here $u_t(z)$ is negative because of its inward direction.

Top opening general formula

Regrouping equations (C.2) and (C.3), we can write for a general format

$$u_t^2(z) = 2c_t g' \Gamma_{\rho_i} |z - z_n| \tag{C.4}$$

where coefficient Γ_{ρ_i} is equal to 1 for $z < z_n$ (inflow) and equals ρ_a/ρ_i for $z > z_n$ (outflow).

Flow through bottom opening

We suppose that there is always inflow for the bottom openings ($T_b < z_i$). In fact, if the top edge of the bottom opening is above the interface ($T_b > z_i$), then we could divide the bottom opening with two parts, one for $0 < z < z_i$ as the real bottom opening and the rest $z_i < z < T_b$ could be considered as a part of the top opening, so applying equation (C.4).

The analysis is similar by establishing Bernoulli's equation between point A situated on the neutral plane and the point C with an altitude z, situated on border of inlet opening, presented in the left-hand-side sketch in figure C.1. We shall note that the difference between the interior pressure and the exterior pressure at level z is due to density difference for mixed layer between level z_i and z_n, so that we have

$$P_i(z) - P_e(z) = g(\rho_a - \rho_i)(z_i - z_n) \tag{C.5}$$

Thus, by supposing small inlet opening compared with cross-section of the cavity, we have the Bernoulli's equation

$$u_b^2(z) = 2c_b g'(z_n - z_i) \tag{C.6}$$

with c_b geometrical pressure loss coefficient and $u_b(z)$ inlet velocity at level z. We note that in this case the inlet velocity u_b is a constant and independent on z. Consequently, the position of bottom opening is not important when its top edge is below the bi-layer interface, only the difference $z_n - z_i$ will be introduced in the velocity equation.

C.2 Inlet/outlet flux through the openings

By definition, for a general case, the volume flux through the two openings can be calculated by integrating the corresponding velocity profile

$$Q_b = \int_0^{T_b} u_b(z)\, W_b dz, \quad Q_t = \int_{H-T_t}^{H} u_t(z)\, W_t dz \tag{C.7}$$

Volume flux through the top opening

Depended on different position of neutral plan, we have seen the flow through the upper opening will be totally outward or inward/outward, as presented in figure C.1. We note Q_{t1} the volume flux corresponding to outward flow above the neutral plan and $Q_{t2} < 0$ that of inward flow below the neutral plan. The total outlet flux could be defined as

$$Q_t = Q_{t1} + Q_{t2} \tag{C.8}$$

Applying the equation (C.2), integrating outward velocity $u_t(z)$ for $H - T_t < z < H$ if $z_n < H - T_t$ or for $z_n < z < H$ if $z_n > H - T_t$, we have

$$Q_{t1} = \frac{2}{3}\sqrt{2c_t g' \frac{\rho_a}{\rho_i}}\, W_t \left((H - z_n)^{3/2} - (H - T_t - z_n)^{3/2} \xi_{z_n < H - T_t}\right) \tag{C.9}$$

with c_t the top-vent pressure loss coefficient and $\xi_{z_n < H-T_t} = 1$ if $z_n < H - T_t$ and 0 if not.

Similarly, by integrating $u_t(z)$ from equation (C.3), we have

$$Q_{t2} = -\frac{2}{3}\sqrt{2c_t g'} W_t (z_n - \max(z_i,\ H - T_t)\ )^{3/2} \xi_{z_n > H - T_t} \tag{C.10}$$

We have $Q_{t2} = 0$ if $z_n < H - T_t$ which corresponds with analysis in the above paragraph.

Volume flux through the bottom opening

Note that the above Q_{t2} corresponds only inflow between plane $z = z_i$ and plane $z = z_n$. This is correct if $z_i < H - T_t$. If $z_i > H - T_t$, there is an additional influx for pure air through the lower part of the top opening $H - T - t < z < z_i$, which will be considered as a part of influx through the "lower" opening. Thus, an additional term in effective inflow surface for lower opening is needed. We define the effective inflow surface

$$S_b^{\#} = W_b T_b + W_t \left(z_i - (H - T_t)\right) \xi_{z_i > H - T_t} \tag{C.11}$$

From Bernoulli's equation (C.6), the inlet velocity is uniformly distributed in the effective inlet opening, we can easily have

$$Q_b = S_b^{\#} \sqrt{2 c_b g' (z_n - z_i)} \tag{C.12}$$

with c_b effective bottom-vent pressure loss coefficient related to $S_b^{\#}$.

Numerical application for reference cases

We present here the numerical application for the above analysis to reference cases in this study. As we are in the case $z_i < H - T_t$, there will be no change for the flux through the bottom opening. For the top one, we present in the following table the difference estimation Q_t under horizontal opening assumption (presented in chapters 3 and 7) or vertical opening assumption equation (C.9). The difference is quite small (around 3%) which means in the reference cases, vertical openings will not introduce huge additional error in ventilation modelling. By the way, the consideration will reduce the estimation error of Q_t by comparing results measured from DNS time-averaged velocity field.

Case	Q_t ($\times 10^{-4}$ m^3/s) **H.O.**	Q_t ($\times 10^{-4}$ m^3/s) **V.O.**	**Relative difference** (%)
Hydrogen	6.24	6.06	2.9%
Helium	5.84	5.65	3.2%

Table C.1: Estimation of outlet volume flux Q_t under horizontal opening (H.O.) assumption and vertical opening assumption (V.O.), results comparison

Appendix D

Mesh construction

Equi-distant mesh (EDM)

We construct firstly an equi-distant mesh with cell length $\delta x \approx 0.7mm$ identical for three directions. The main cavity, the exterior domain and the connection areas could be constructed without problem as these are all cuboid geometry. 14 mesh steps (cells) divide 1cm length everywhere in every direction, corresponding to, in the main cavity, 140 cells for both direction x and y and 280 cells for direction z. There are 5.488M cells in the main cavity.

The injection pipe is a cylinder which cannot be meshed perfectly with the main cavity. In order to maintain the mesh regularity, we decide to mesh it with regular square meshes. In the first row of figure D.2, we present on the left-hand side, existed equi-distant meshing for the injection region on the underside surface of the main cavity, with injection circle coloured in grey. The objective is to choose cells on this surface representing injection pipe region to minimise the difference between the green area and the yellow area presented in the figure. Injection pipe cells are illustrated on the right-hand side coloured in purple with the rest surface, coloured in red, defined in the wall group. Then we stretch the blue zone in the z-negative direction to create the pipe cells.

The three-view diagram of this equi-distant mesh is presented in figure D.1 (left), in which wall boundary conditions are applied for area coloured in light red, injection boundary conditions in blue and free surface group in light green. The mesh contains 15.44M cells among which only 35.5% of them are located in the main cavity.

Local grid refinement mesh (LGRM)

In order to well simulate the turbulent structure and reach the Kolmogorov length scale, we shall consider a refinement of the grid. Due to computation resource consideration, the global refinement is not possible. We shall consider building a local grid refinement (LGR) mesh in which cell length can up to 0.2mm in the jet zone.

We present in the figure D.1 (right) the local grid refinement mesh. In the main cavity, the Local grid refinement is particularly applied in the jet zone in x-y directions. For both direction, 3 segments are defined. in the centre of the cavity where $x \in [-2cm, 2cm], y \in [-2cm, 2cm]$ the cell length is 0.2mm uniform and identical in both x and y direction. Then the cell length increases linearly in each direction and up to 0.45mm at each corner of the main cavity. In z direction, the cell length is equal to 0.25mm for $x \in [0cm, 2cm] \cup [18cm, 20cm]$ and linearly increases to the middle height of the cavity where cell length in z direction is around 0.5mm.

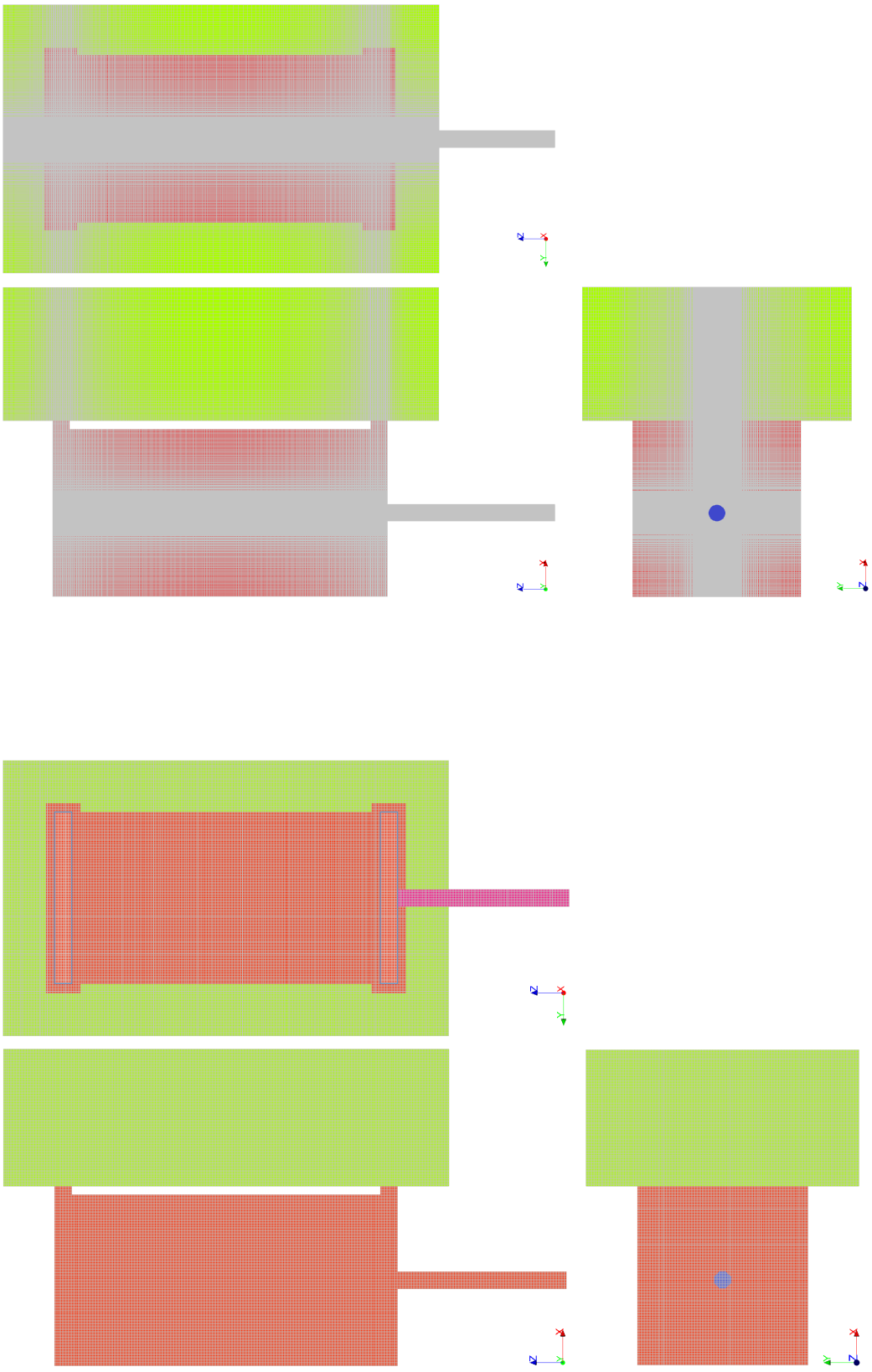

Figure D.1: Three-view diagram of equi-distant mesh (left) and local grid refinement mesh (right), wall boundary group in red, injection group in blue and free surface group in light green

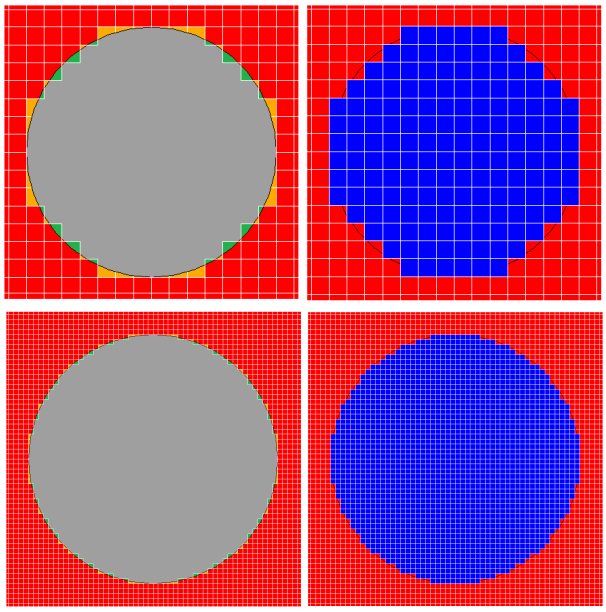

Figure D.2: Injection area meshing method. Left: equi-distant meshing for the injection region on the underside surface of the main cavity, with injection circle in grey. Right: The underside surface meshing, red zone corresponds to wall group, blue zone is defined as the injection area. First row: Global equi-distant mesh (cell size 0.7mm), second row: Refinement mesh (cell size 0.2mm)

In the injection pipe, the cell length is uniform 0.2mm identical in x-y direction and 0.25mm in z direction. We apply the same method to create the mesh injection pipe (see second row of figure D.2). Besides, the grid is uniformly distributed in middle connection zones, 0.45mm in x-y directions and 0.25mm in z direction.

In exterior domain, we shall firstly let the grid density in the connected area identical as in the main cavity to ensure the regularity of the mesh. In x direction, cell length is from 0.45mm on the left edge, exponentially increases to 2mm on the right extremity. In y direction, cell length is from 0.45mm at $y = \pm 5cm$, exponentially increases to 2mm on the extremities. In z direction, cell size is from 0.25mm at $z = 20cm$, exponentially increases to 1.0mm at $z = 23cm$, idem for $z = 0$ to $-3cm$. In the middle, cell size is from 0.25mm at $z = 1cm$, exponentially increases to 2.0mm at $z = 10cm$ and idem for $z = 19cm$ to $z = 10cm$. In addition, we shall keep in the same time the difference cell length between 2 adjacent cells less than 5% in each direction to ensure the mesh regularity.

Finally, a local grid refinement mesh is constructed. It contains totally 80.2M cells where around 70% of them are located in the main cavity. We optimise the computation resource concentrating the flow structure in the main cavity.

Three surface groups

Three surface groups are defined corresponding to three type of boundary conditions.

At the bottom boundary (underside) of the injection pipe where $z = -h$, we defined an injection surface group to provide injection boundary condition. Apart from this surface, all boundary surfaces will be classified as two groups, a wall group and a free surface group, where two different boundary conditions will be applied.

The main cavity possesses six surfaces among which 4 have no openings with other objects,

the front one, the back one, the top one and the left one. They are both defined in wall group. Bottom surface is also in wall group except for the area connecting injection tube where, in fact, is inside the calculation domain (so not a boundary). Idem for right surface, the boundary faces are classified in wall group except for the two rectangular areas of vents.

The two connection zones, connecting the main cavity and the exterior domain, possess each of them, 4 lateral boundary surfaces, all defined in wall group.

For exterior domain, five of its six surfaces (except for the left one) are not connecting to other objects. They are all defined in free surface group. Things will be little complicated on its left surface connecting to the middle connection zones. This surface is divided into 2 parts corresponding to wall group and free surface group. The projection of the right extremity surface of the main cavity on this surface is all defined in wall group, except for the connection area where is inside the calculation domain thus not a boundary. Apart from that, around each of the two vents areas, a extension of thickness W_v both in y direction and z direction will be also considered in the wall group. This represents thickness of plexiglass, used afterwards to manufacture the experimental facility. Other zone on this surface will be classified as free surface group.

Appendix E

Full results of DNS-PIV comparison

In this section, we present the original and full results of DNS-PIV comparison, which consist of two PIV results with different observation time lag (0.1ms and 0.5ms), DNS helium case and DNS hydrogen case for information. PIV 0.5ms case is more accurate in most part of the cavity but the time lag 0.5ms is too large to calibrate large velocity presented in the jet centre after injection. Therefore, results in this zone for PIV 0.5ms is not accurate and cannot be directly used in comparison. Two PIV results with different observation time lag shall be afterwards superposed to construct the final PIV statistical fields. See section 4.6.4 for more information. Observation plane is y =0. DNS helium is used to compare with PIV in order to validate DNS simulation.

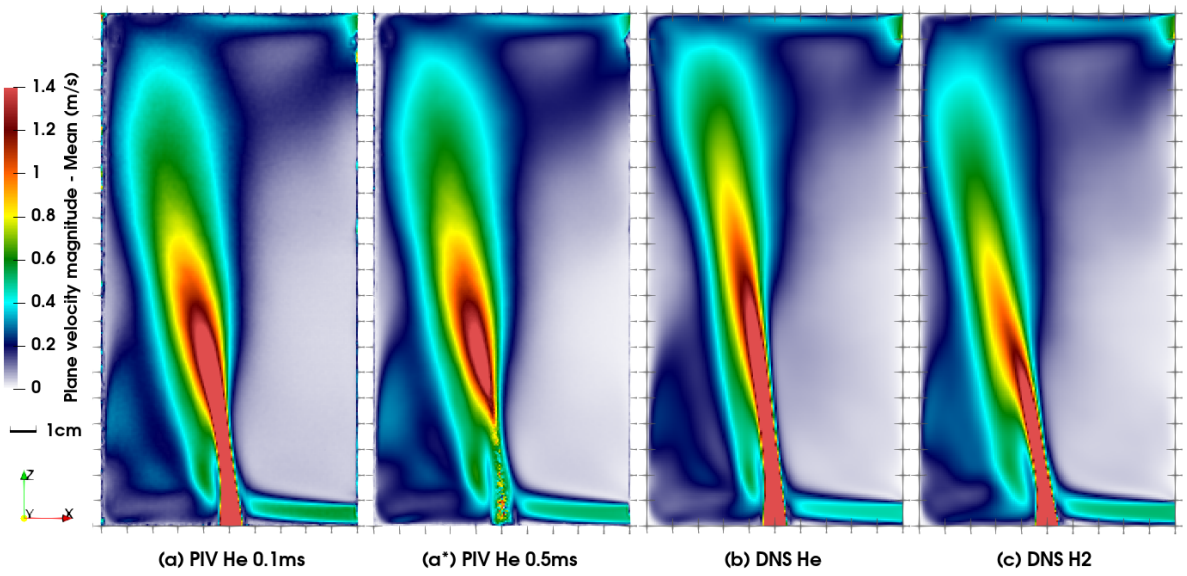

Figure E.1: Time-averaged plane velocity magnitude comparison: (a)&(a*) two PIV results with different measure time interval, (b) DNS He and (c) DNS H2. Observation plane : y =0.

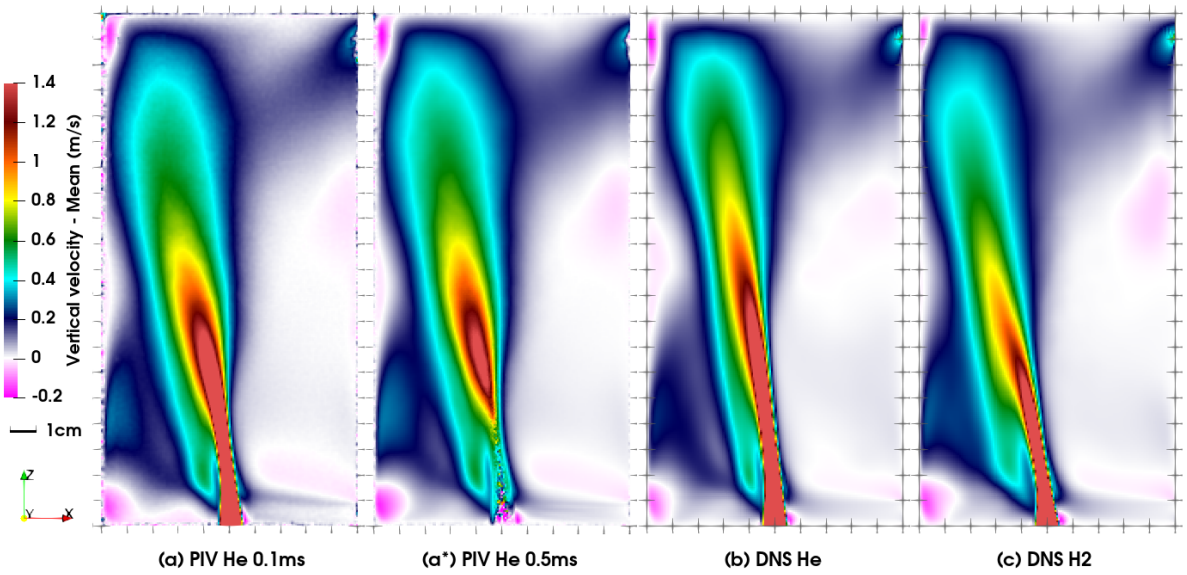

Figure E.2: Time-averaged vertical velocity comparison: (a)&(a*) two PIV results with different measure time interval, (b) DNS He and (c) DNS H2. Observation plane : y =0.

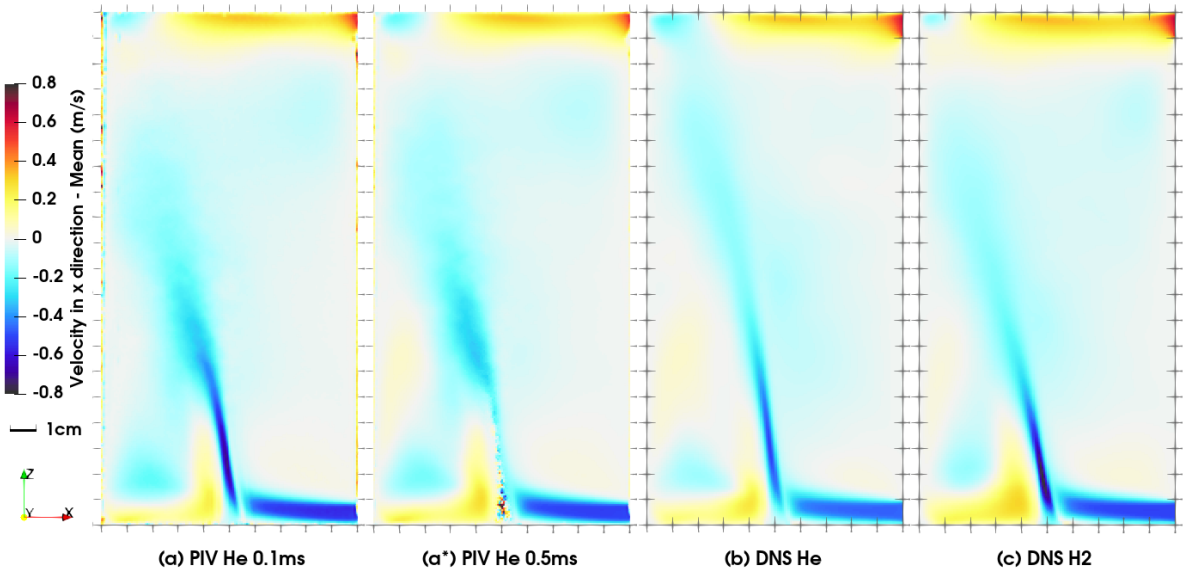

Figure E.3: Time-averaged x-direction velocity comparison: (a)&(a*) two PIV results with different measure time interval, (b) DNS He and (c) DNS H2. Observation plane : y =0.

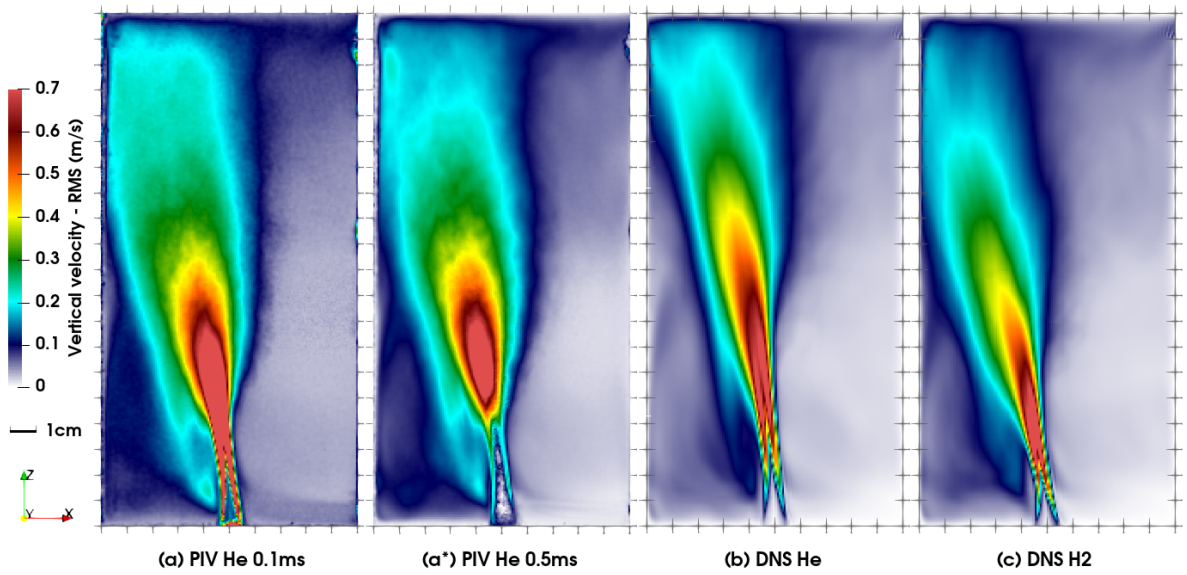

Figure E.4: RMS vertical velocity comparison: (a)&(a*) two PIV results with different measure time interval, (b) DNS He and (c) DNS H2. Observation plane : y =0.

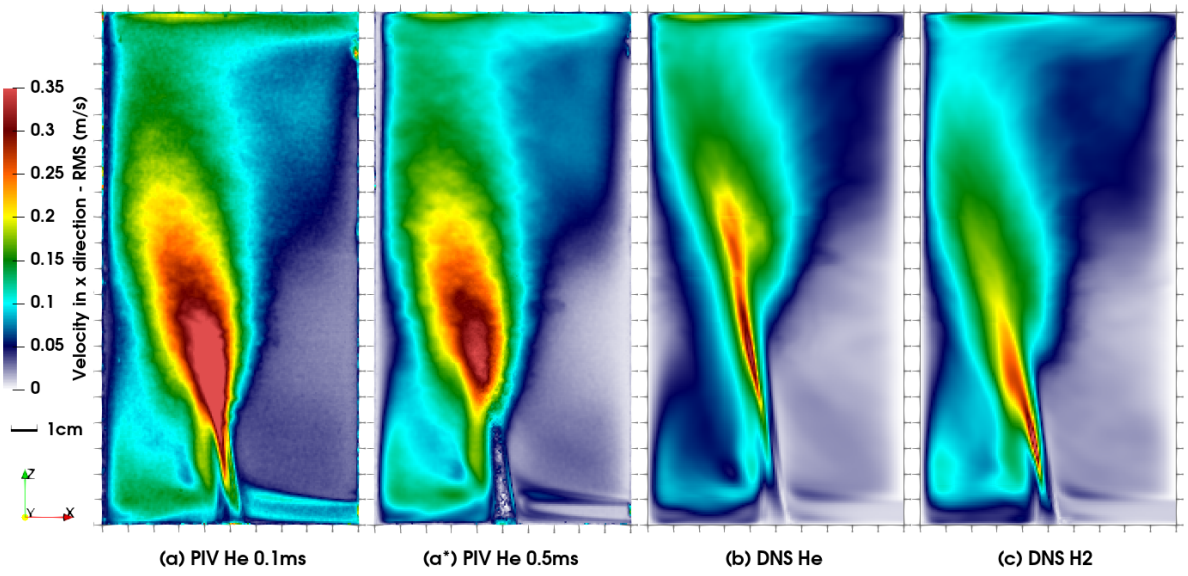

Figure E.5: RMS x-direction velocity comparison: (a)&(a*) two PIV results with different measure time interval, (b) DNS He and (c) DNS H2. Observation plane : y =0.

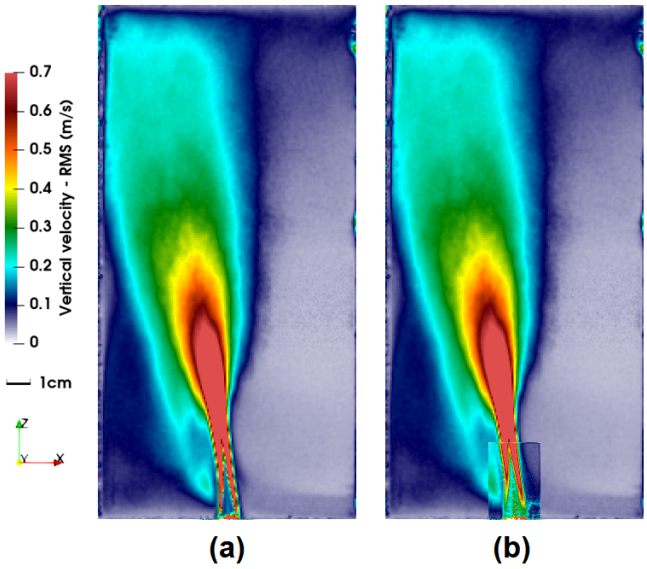

Figure E.6: Change of interrogation window in injection area for PIV RMS vertical velocity field. (a) non overlapped square window 32x32, (b) non overlapped square window 8x8, measure interval time lag 0.1ms.

We may observe that the gradient of vertical velocity RMS is very large in the jet border just after injection for PIV measurement results. This is due to the selection of interrogation window in first post-processing. The window is chosen as 32x32 pixels in this study and as presented in figure E.6(a). If we change this window into 8x8 pixels in figure E.6(b), the velocity RMS at jet border is well captured. However, as injection area is large velocity zone, 8x8 window is not enough to capture high velocity in the jet centre, thus its results could not be directly used in the result analysis.

Appendix F

Turbulent jet modelling results for helium case

In this part, we present turbulent jet modelling results for helium case, which are not presented in chapter 6. Generally, helium modelling results are similar to that of hydrogen.

Modelling results are presented in the same order as in chapter 6. We start with Boussinesq model with constant α. Three approaches are applied: conservative approach with $\alpha_T = 0.05$, injection flux correction and quasi-analytical approach considering environmental variation. We are also interested in the sensibility of entrainment coefficient in each approach. The same procedure is applied for α-constant non Boussinesq model as well. In the third part, we present profiles obtained from Kaminski's α-variable model, with profile $\alpha(z)$ applied from modelling and DNS respectively.

F.1 Boussinesq approaches with constant entrainment coefficient

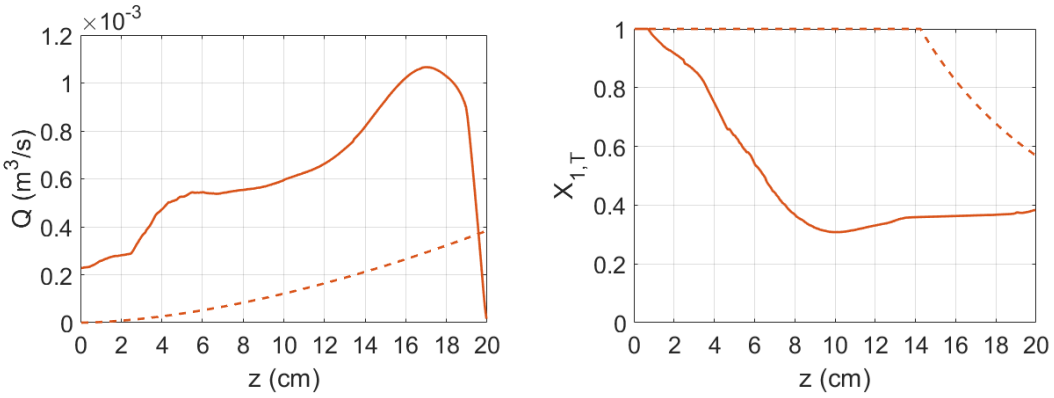

Figure F.1: Profiles conservative approach with α_T =0.05. Left: variation of jet volume flux $Q(z)$, right: variation of Top-hat concentration $X_{1,T}(z)$. Helium case, DNS deduced profiles in solid lines, 1D modelling in dashed lines.

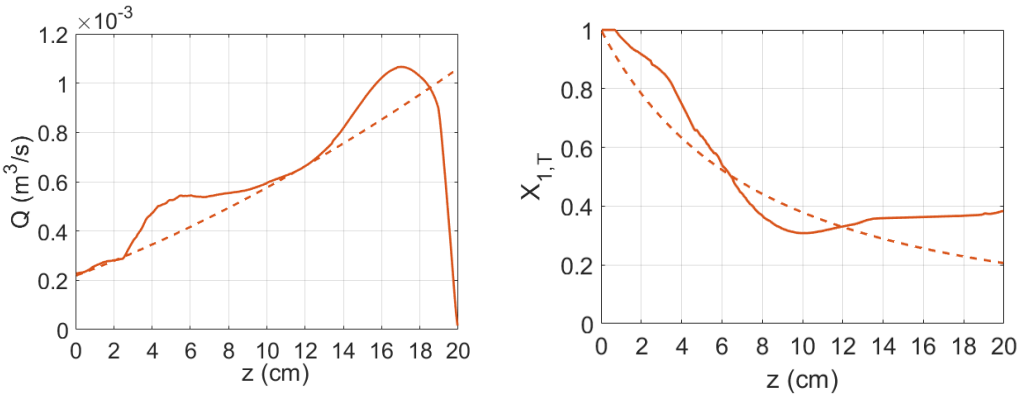

Figure F.2: Injection volume flux correction approach with α_T =0.058. Left: variation of jet volume flux $\mathcal{Q}(z)$, right: variation of Top-hat concentration $X_{1,T}(z)$. Helium case, DNS deduced profiles in solid lines, 1D modelling in dashed lines.

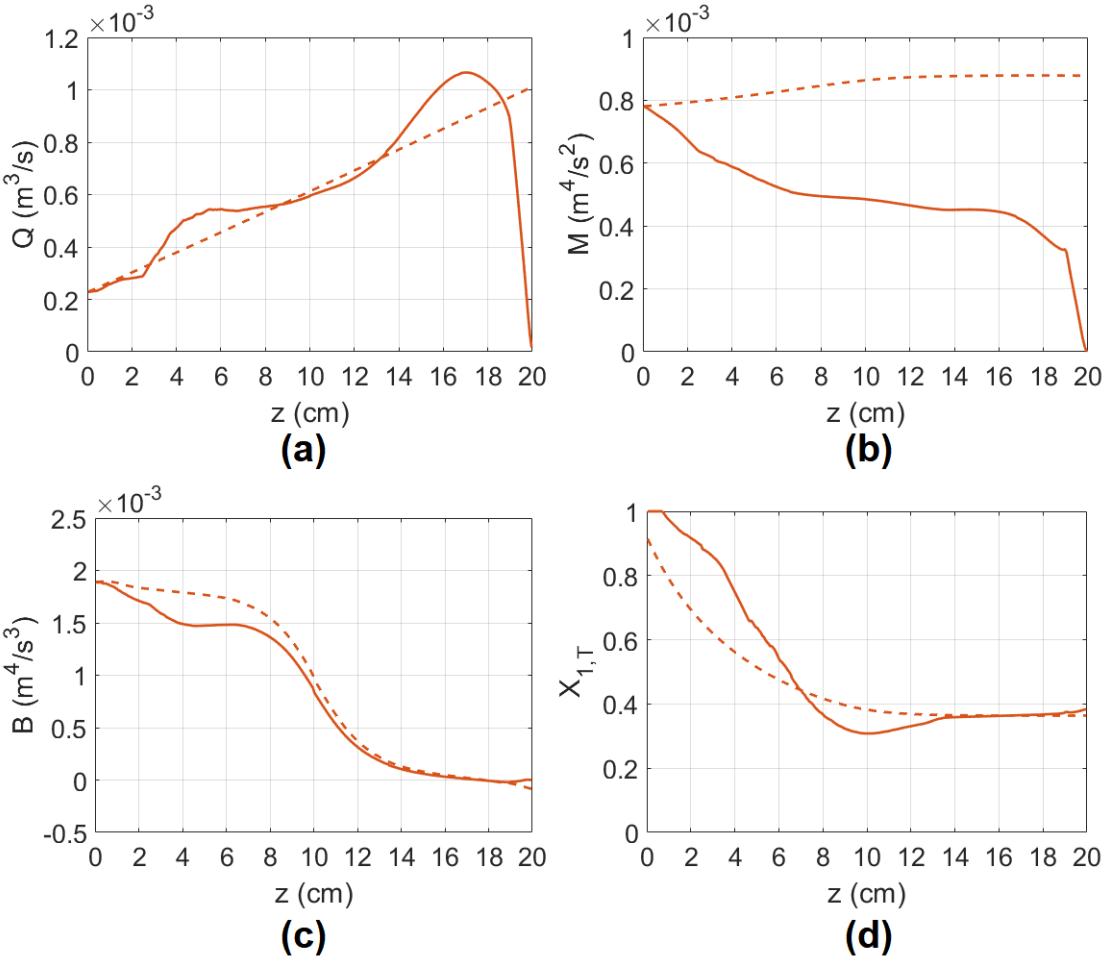

Figure F.3: Quasi-analytical Boussinesq approach with α_T =0.038, considering the variation of far-field environmental density. (a) variation of jet volume flux $\mathcal{Q}(z)$, (b) variation of jet momentum flux $\mathcal{M}(z)$, (c) variation of jet buoyancy flux $\mathcal{B}(z)$, (d) Top-hat concentration $X_{1,T}(z)$. Helium case, DNS deduced profiles in solid lines, 1D modelling in dashed lines.

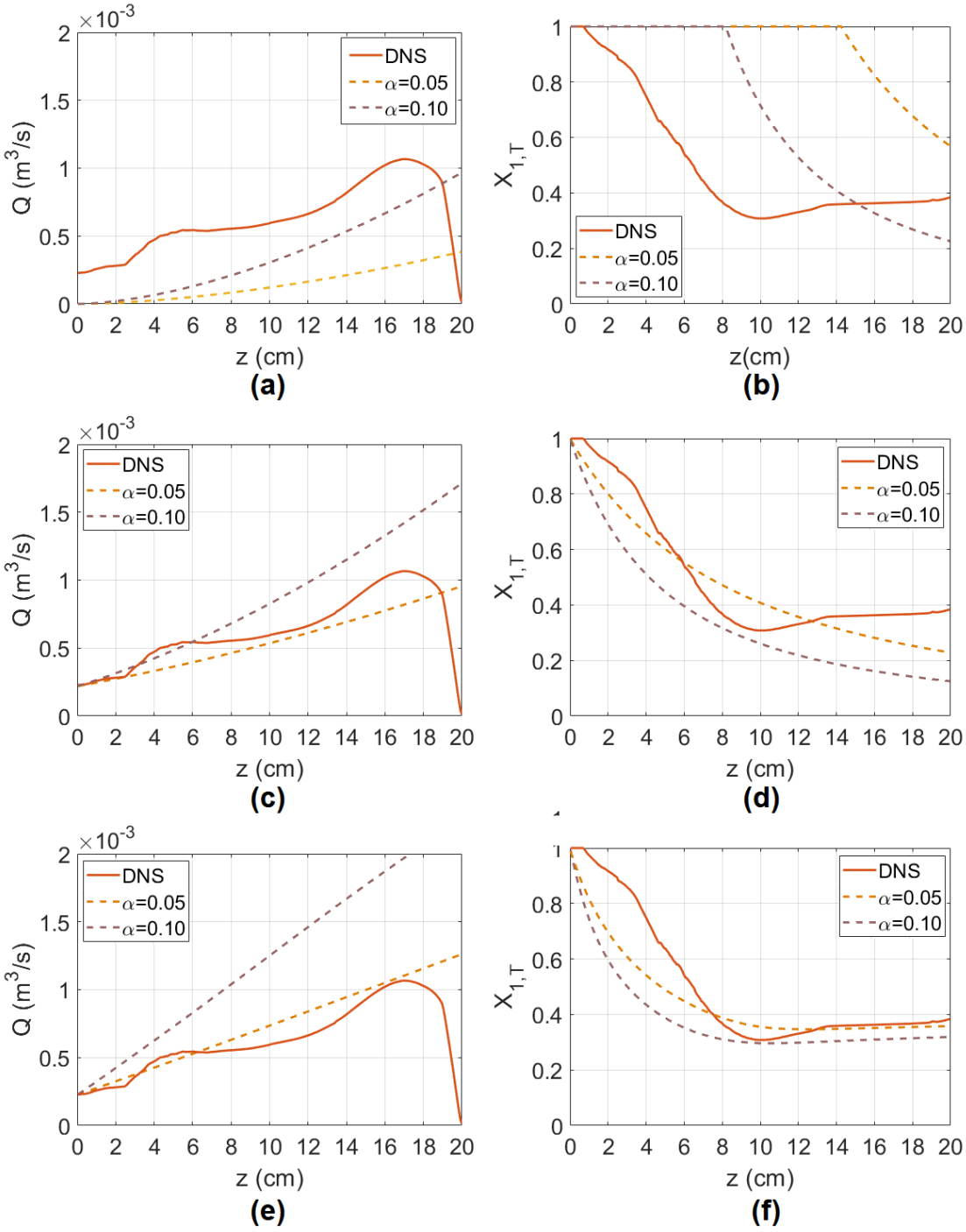

Figure F.4: Evaluation of sensitivity of entrainment coefficient, comparison profiles DNS and 1D Boussinesq modelling with α_T =0.05 and 0.10. Helium case. (a)(b) Profiles $\mathcal{Q}(z)$ and $X_{1,T}(z)$ obtained by conservative approach; (c)(d) Profiles $\mathcal{Q}(z)$ and $X_{1,T}(z)$ obtained after correction of injection volume flux; (e)(f) Profiles $\mathcal{Q}(z)$ and $X_{1,T}(z)$ obtained by quasi-analytical approach considering environmental variation.

F.2 Non Boussinesq approaches with constant entrainment coefficient

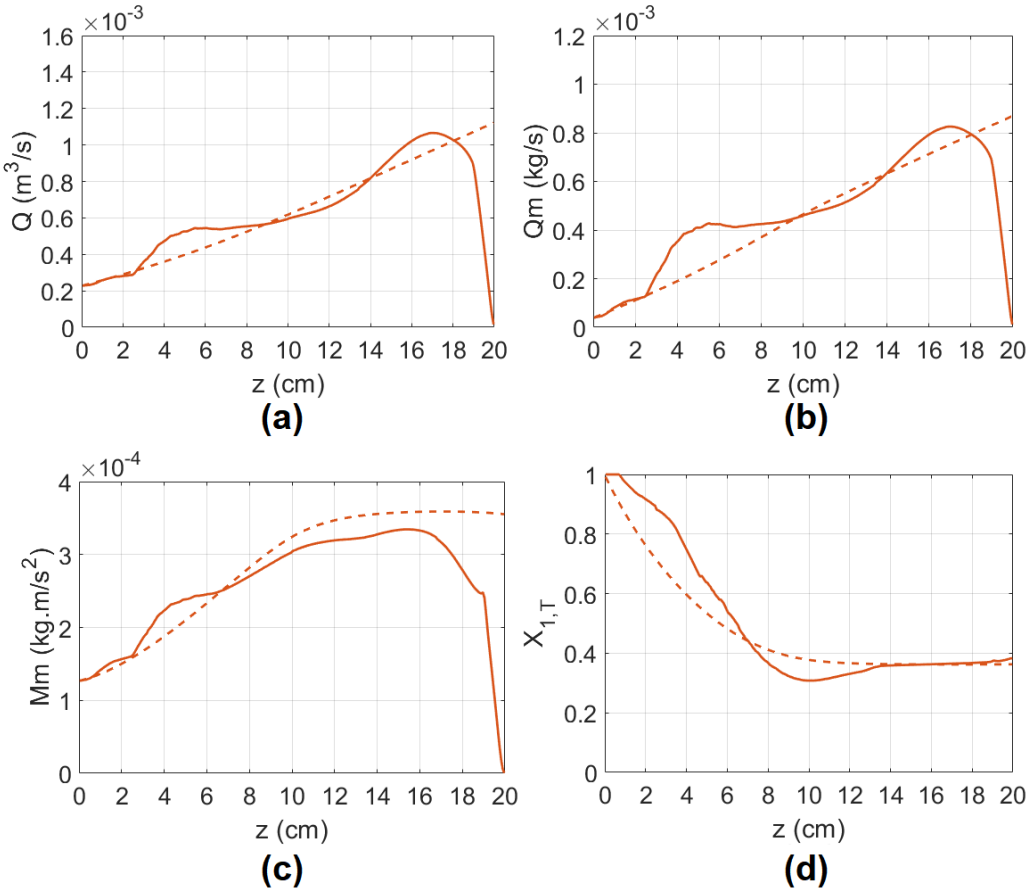

Figure F.5: Quasi-analytical non Boussinesq approach with α_T =0.082, considering the variation of far-field environmental density. (a) variation of jet volume flux $\mathcal{Q}(z)$, (b) variation of jet mass flux $\mathcal{Q}_m(z)$, (c) variation of jet mass momentum flux $\mathcal{M}_m(z)$, (d) Top-hat concentration $X_{1,T}(z)$. Helium case, DNS deduced profiles in solid lines, 1D modelling in dashed lines.

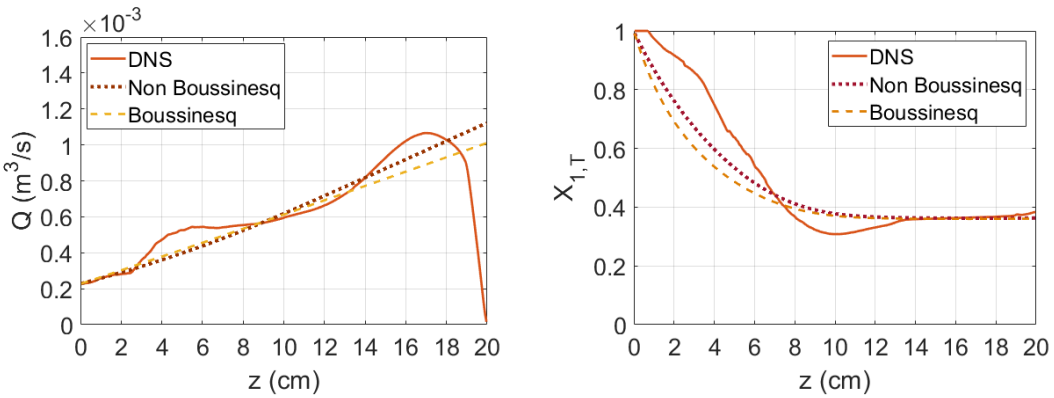

Figure F.6: Comparison of quasi-analytical resolution in Boussinesq approach and non Boussinesq approach. Left: variation of jet volume flux $\mathcal{Q}(z)$, right: variation of Top-hat concentration $X_{1,T}(z)$. Helium case, DNS deduced profiles in solid lines, 1D modelling in dashed lines.

F.3 Boussinesq approaches with variable entrainment coefficient

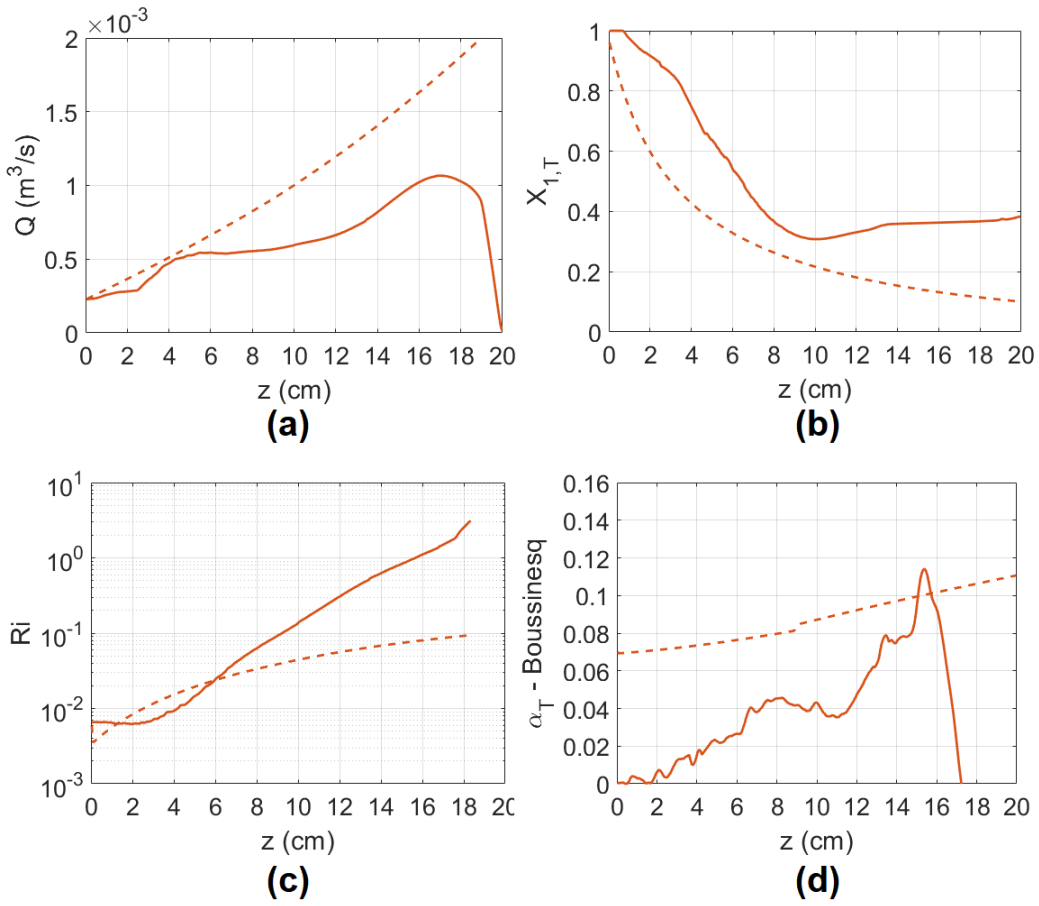

Figure F.8: Evaluation of Kaminski's α–variable Boussinesq turbulent jet models. (a) variation of jet volume flux $\mathcal{Q}(z)$, (b) variation of jet Top-hat concentration $X_{1,T}(z)$, (c) variation of jet Richardson number, (d) variation of entrainment coefficient $\alpha_T(z)$. Helium case, DNS reference results in solid lines and results from 1D models in dashed lines.

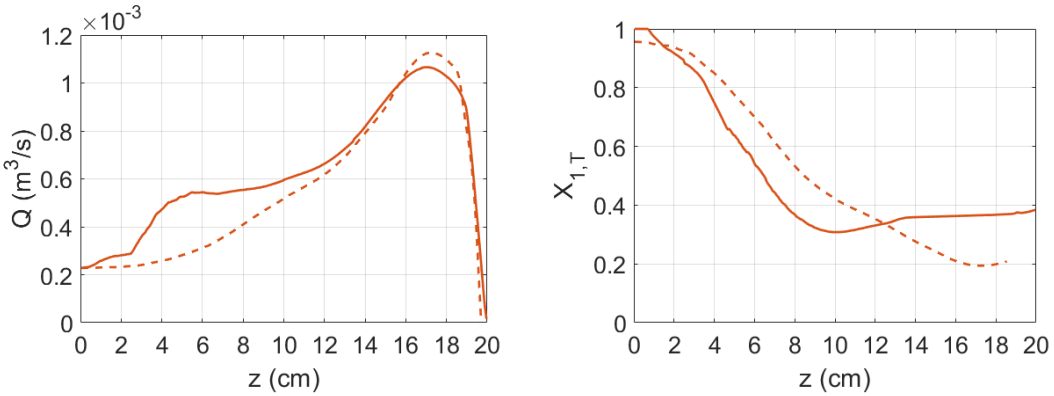

Figure F.9: Resolution of Kaminski's model by DNS estimated α profile. Left: jet volume flux $\mathcal{Q}(z)$, right jet Top-hat concentration $X_{1,T}(z)$. Helium case, DNS reference results in solid lines and results from 1D models in dashed lines.

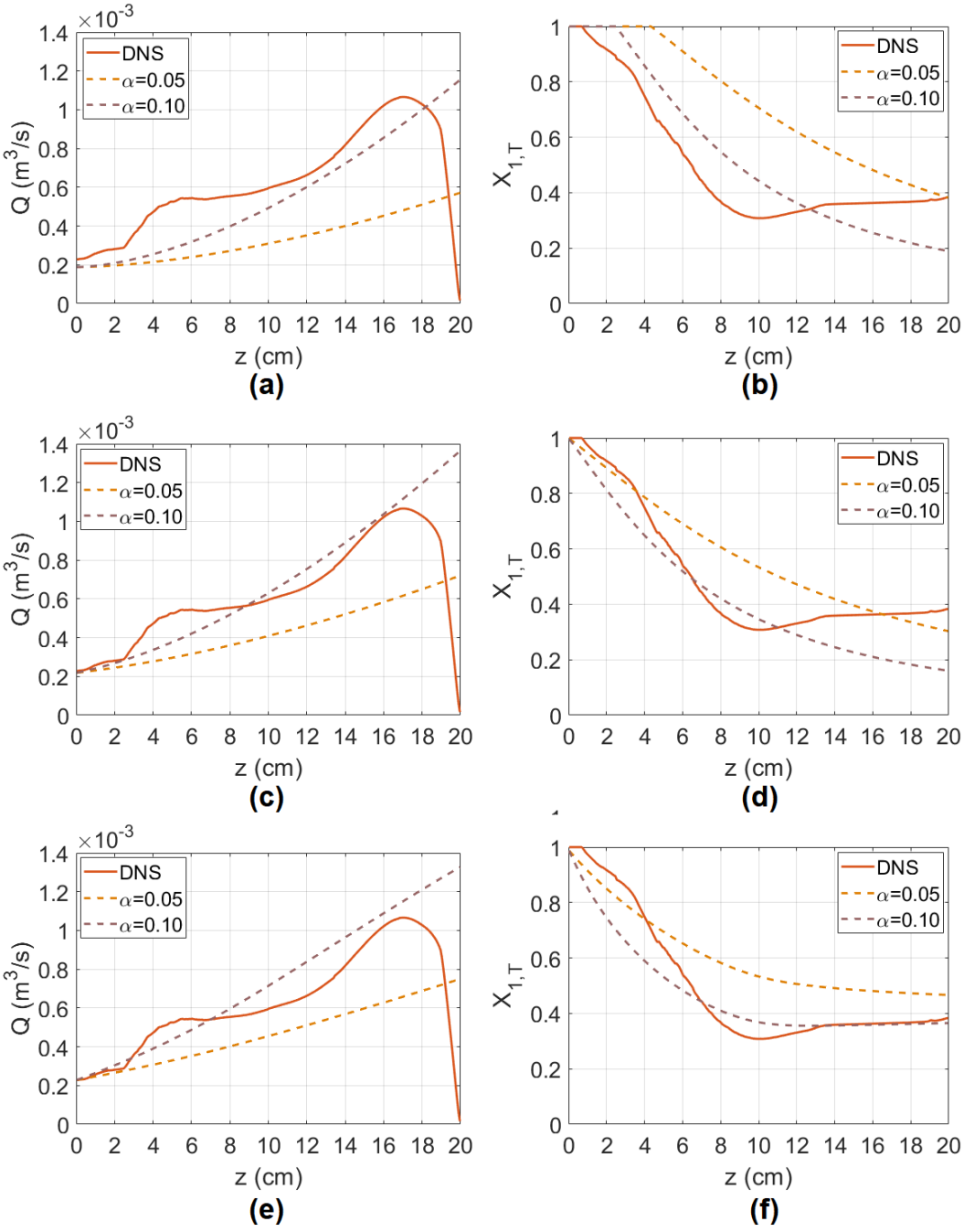

Figure F.7: Evaluation of sensitivity of entrainment coefficient, comparison profiles DNS and 1D non Boussinesq modelling with α_T =0.05 and 0.10. Helium case. (a)(b) Profiles $\mathcal{Q}(z)$ and $X_{1,T}(z)$ obtained by direct application of Rooney's analytical approach; (c)(d) Profiles $\mathcal{Q}(z)$ and $X_{1,T}(z)$ obtained after correction of injection volume flux; (e)(f) Profiles $\mathcal{Q}(z)$ and $X_{1,T}(z)$ obtained by quasi-analytical approach considering environmental variation.

Appendix G

Full bi-layer modelling results

In this part, we present the full estimation results for each bi-layer modelling methods (i)-(viii), presented in section 7.4 in table 7.5. We present in the first table the bilayer parameters (interface height z_i and homogeneous concentration $X_{1,i}$) obtained from each method. In the second and third tables, we present respectively the estimation of outlet volume flux and mass flux as well as its relative errors compared with DNS measured values. The outlet mass and volume flux are calculated simply by conservation of species: $Q_t = Q_{inj}/X_{1,i}$ and $Q_{m,t} = \rho_i Q_t$.

Method	**H2** z_i (cm)	**H2** $X_{1,i}$ (%)	**He** z_i (cm)	**He** $X_{1,i}$ (%)
(i)	12.7	51.7%	14.8	59.9%
(ii)	5.9	41.6%	6.9	44.1%
(iii)	13.1	49.1%	15.2	57.3%
(iv)	6.4	39.2%	7.5	41.6%
(v)	7.6	40.4%	9.6	44.3%
(vi)	6.6	39.4%	7.7	41.9%
(vii)	8.4	36.6%	10.5	40.3%
(viii)	7.4	35.8%	8.6	38.4%

Table G.1: Estimation of bi-layer parameters (interface height z_i and homogeneous concentration $X_{1,i}$) with different assumptions, methods (i)-(viii) presented in table 7.5

Method	**H2** Q_t ($\times 10^{-4}$ m^3/s)	**Error** (%)	**He** Q_t ($\times 10^{-4}$ m^3/s)	**Error** (%))
(i)	4.22	-31.6%	3.64	-37.2%
(ii)	5.25	-15.0%	4.95	-14.6%
(iii)	4.45	-27.9%	3.81	-34.3%
(iv)	5.57	-9.7%	5.24	-9.6%
(v)	5.40	-12.5%	4.93	-15.0%
(vi)	5.54	-10.2%	5.21	-10.1%
(vii)	5.96	-3.4%	5.42	-6.5%
(viii)	6.09	-1.3%	5.68	-2.0%

Table G.2: Estimation of outlet volume flux Q_t and relative error (compared with DNS measured value) with different assumptions, methods (i)-(viii) presented in table 7.5

Method	**H2** $Q_{m,t}$ ($\times 10^{-4}$ kg/s)	**Error** (%)	**He** $Q_{m,t}$ ($\times 10^{-4}$ kg/s)	**Error** (%))
(i)	2.56	-46.5%	2.06	-54.5%
(ii)	3.76	-21.4%	3.59	-20.5%
(iii)	2.82	-40.9%	2.25	-50.1%
(iv)	4.13	-13.5%	3.92	-13.1%
(v)	3.94	-17.6%	3.56	-21.1%
(vi)	4.10	-14.2%	3.89	-13.8%
(vii)	4.59	-3.9%	4.14	-8.4%
(viii)	4.74	-0.8%	4.44	-1.7%

Table G.3: Estimation of outlet mass flux $Q_{m,t}$ and relative error (compared with DNS measured value) with different assumptions, methods (i)-(viii) presented in table 7.5

Recall the reference values from DNS obtained from integration of time-averaged fields on the top opening:

- Hydrogen case:
  z_i = 7.41cm, $X_{1,i}$ =36.2%, Q_t=6.17×10^{-4} m^3/s, $Q_{m,t}$ =4.78×10^{-4} kg/s
- Helium case:
  z_i = 8.72cm, $X_{1,i}$ =38.7%, Q_t=5.80×10^{-4} m^3/s, $Q_{m,t}$ =4.51×10^{-4} kg/s

Appendix H

A three-layer natural ventilation model

In this section, we present an analytical approach of ventilation modelling based on the three-layer structure as observed in DNS results. In fact, we have seen that a stratified layer exists between top homogeneous layer and bottom mixing layer whose vertical extension is not negligible in our simulation cases. The vertical velocity in this stratified layer is practically zero except in jet region. Hence, we may consider the top and bottom layers form two mass diffusion sources with constant hydrogen concentrations. Hydrogen diffuses in vertical direction in the stratified layer. According to Fick's law, in steady state, the hydrogen concentration as well as the mixture density varies linearly in the stratified layer. Therefore, the basic assumptions are the same as that presented in section 3.1.2 in Linden's model, except for the fourth assumption which is replaced by:

Assumption 4 (Three-layer distribution): In steady state, the cavity could be divided into three layers according to environmental mixture density distribution. The bottom layer L_A, called mixing layer, filled with fresh air of density ρ_a. A homogeneous layer L_H is situated at top part of the cavity, with homogeneous density ρ_i. A stratified layer L_S is between L_A and L_H, in which mixture density varies linearly with altitude. We note z_{AS} interface altitude between L_A and L_S and z_{SH} interface altitude between L_S and L_H. Consequently, we have

$$\rho_e(z) = \begin{cases} \rho_a & z \leq z_{AS} \\ \rho_a - (\rho_a - \rho_i)\frac{z - z_{AS}}{z_{SH} - z_{AS}} & z_{AS} < z < z_{SH} \\ \rho_i & z \geq z_{SH} \end{cases} \tag{H.1}$$

The corresponding volume fraction variation is deduced

$$X_{1,e}(z) = \begin{cases} 0 & z \leq z_{AS} \\ X_{1,i}\ \frac{z - z_{AS}}{z_{SH} - z_{AS}} & z_{AS} < z < z_{SH}, \ \text{with}\ X_{1,i} = \dfrac{\rho_a - \rho_i}{\rho_a - \rho_{inj}} \\ X_{1,i} & z \geq z_{SH} \end{cases} \tag{H.2}$$

Remark: Under above assumption, light gas mass fraction $Y_{1,e}(z)$ does not vary linearly in L_S.

The stratified layer L_S can also be characterised by its mid-plane altitude (noted z_i) and its vertical extension (noted $2h_s$ with h_s its half extension). Here the notation z_i will match the "bi-layer interface" notion in Linden's model.

$$z_i = \frac{z_{AS} + z_{SH}}{2}, \quad h_s = \frac{z_{SH} - z_{AS}}{2} \tag{H.3}$$

and

$$z_{AS} = z_i - h_s, \quad z_{SH} = z_i + h_s \tag{H.4}$$

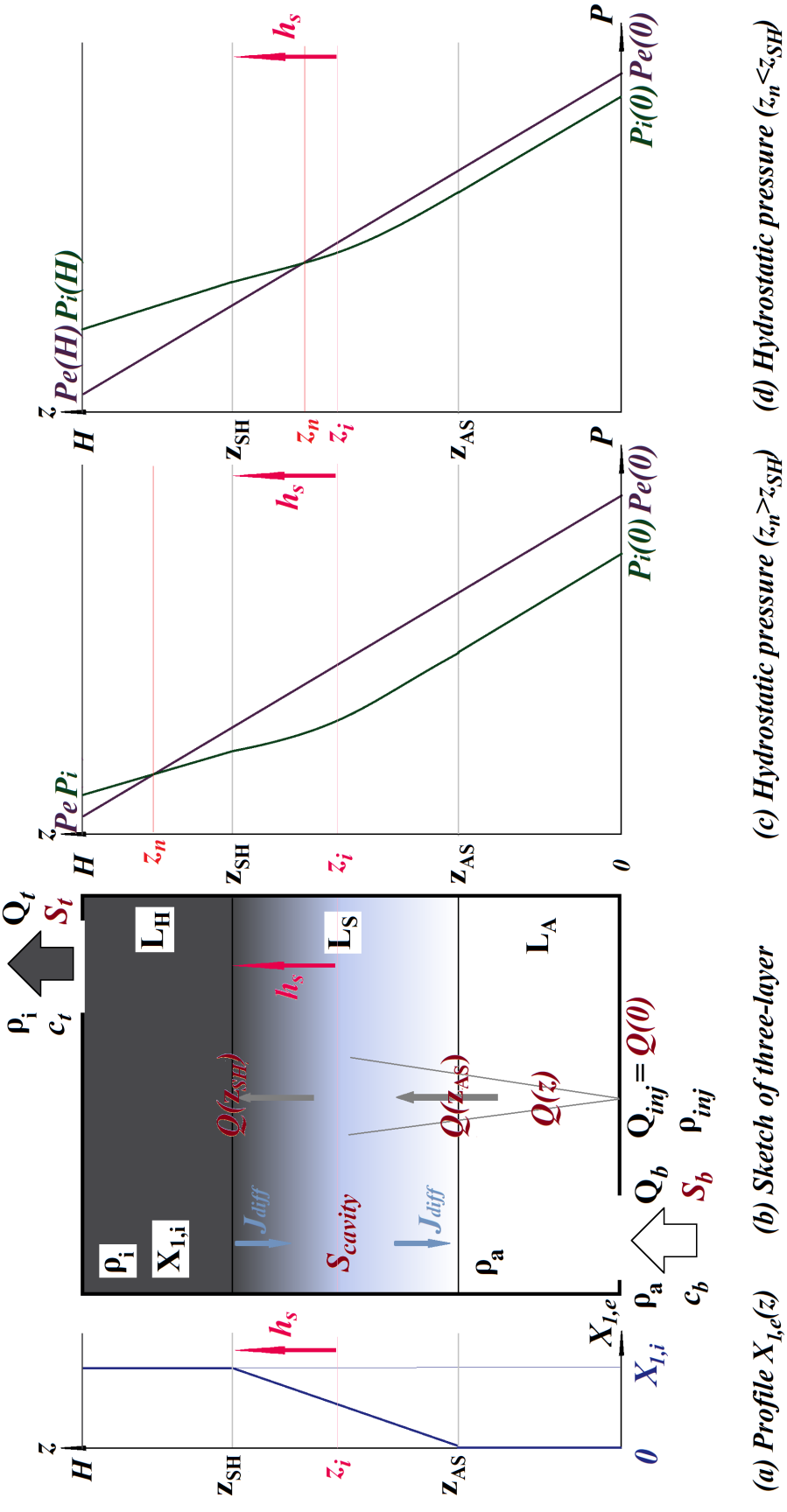

(a) Profile $X_{1,e}(z)$ (b) Sketch of three-layer (c) Hydrostatic pressure ($z_n > z_{SH}$) (d) Hydrostatic pressure ($z_n < z_{SH}$)

Figure H.1: Three-layer ventilation model. The cavity is divided into three layers: mixing layer L_A, stratified layer L_S and homogeneous layer L_H. Environmental density $\rho_e(z)$ is equal to that of air ρ_a in L_A, is homogeneous and equal to ρ_i in L_H, and linearly decreases in L_S. (a) Corresponding profile of environmental light gas volume fraction variation $X_{1,e}(z)$; (b) Sketch of three-layer structure; (c) Hydrostatic pressure variations in condition $z_n > z_{SH}$; (d) Hydrostatic pressure variations in condition $z_n < z_{SH}$ with z_n neutral level.

H.1 Hydrostatic pressure and neutral level

Exterior pressure

We set exterior pressure at $z = 0$ as the reference of hydrostatic pressure of the system ($P_e(0) = 0$), thus its variation along the cavity will be simply

$$P_e(z) = -\rho_a g z, \text{ for } 0 \le z \le H \tag{H.5}$$

We have at interface levels and at ceiling

$$P(z_{AS}) = -\rho_a g z_{AS}, \quad P(z_{SH}) = -\rho_a g z_{SH}, \quad P(H) = -\rho_a g H \tag{H.6}$$

Interior pressure

The interior pressure is calculated by its definition

$$P_i(z) = P_i(0) - g \int_0^z \rho_e(s) ds \tag{H.7}$$

By integrating equation (H.1), we have

$$P_i(z) = \begin{cases} P_i(0) & z = 0 \\ P_i(0) - \rho_a g z & 0 < z < z_{AS} \\ P_i(0) - \rho_a g z_{AS} & z = z_{AS} \\ P_i(0) - \rho_a g z_{AS} + \frac{1}{2}(\rho_a - \rho_i) g \frac{z^2 - z_{AS}^2}{z_{SH} - z_{AS}} - \left(\rho_a + \frac{(\rho_a - \rho_i) z_{AS}}{z_{SH} - z_{AS}}\right) g (z - z_{AS}) & z_{AS} < z < z_{SH} \\ P_i(0) - \rho_a g z_{AS} - \frac{\rho_a + \rho_i}{2} g (z_{SH} - z_{AS}) & z = z_{AH} \\ P_i(0) - \rho_a g z_{AS} - \frac{\rho_a + \rho_i}{2} g (z_{SH} - z_{AS}) - \rho_i g (z - z_{SH}) & z_{SH} < z < H \\ P_i(0) - \rho_i g H - (\rho_a - \rho_i) g \frac{z_{AS} + z_{SH}}{2} & z = H \end{cases} \tag{H.8}$$

We have for the top opening same equation as in bi-layer model

$$P_i(H) - P_e(H) = P_i(0) + (\rho_a - \rho_i) g (H - z_i) \tag{H.9}$$

If the flow through the bottom opening is outlet, we must have $P_i(0) > P_e(0) = 0$ thus $P_i(H) > 0$ the flow through the top opening must also be outlet. This is impossible as the jet entrainment generates aspiration effect on the openings. Hence $P_i(0) < P_e(0) = 0$, the flow through the bottom opening must be inlet. According to conservation principle, the flow through top opening must be outlet thus $P_i(H) - P_e(H) > 0$ and

$$|P_i(0)| < (\rho_a - \rho_i) g (H - z_i) \tag{H.10}$$

The variations of $P_e(z)$ and $P_i(z)$ are presented in the figure H.1 (c)(d).

Neutral plane

Same as in Linden's model, the neutral plane is defined as

$$P_i(z_n) = P_e(z_n) \tag{H.11}$$

The difference $P_e(z) - P_i(z)$ keeps constant in L_A, thus we must have $z_n > z_{AS}$. However, the neutral plane can be situated in L_S or L_H. If $P_e(z_{SH}) > P_i(z_{SH})$, as shown in figure H.1 (c), the neutral plane will be located in L_H. If not, it will be in L_S, as shown in figure H.1 (d). This condition is equivalent to the sign of quantity $P_e(z_{SH}) - P_i(z_{SH})$ which is equal to

$$P_e(z_{SH}) - P_i(z_{SH}) = -P_i(0) - (\rho_a - \rho_i) g \frac{z_{SH} - z_{AS}}{2} = -P_i(0) - (\rho_a - \rho_i) g h_s \tag{H.12}$$

- **Case 1:** $P_e(z_{SH}) - P_i(z_{SH}) > 0$

  z_n will be in L_H, consequently

$$P_i(z_n) = P_i(0) - \rho_a g z_{AS} - \frac{\rho_a + \rho_i}{2} g(z_{SH} - z_{AS}) - \rho_i g(z_n - z_{SH}) = -\rho_a g z_n = P_e(z_n) \tag{H.13}$$

  Regrouping it with relation (H.3), we have simply

$$-P_i(0) = (\rho_a - \rho_i) g(z_n - z_i) \tag{H.14}$$

  The conditions (H.10) and (H.12) positive are automatically valid.

- **Case 2:** $P_e(z_{SH}) - P_i(z_{SH}) < 0$

  z_n will be in L_S, consequently

$$P_i(z_n) = P_i(0) - \rho_a g z_{AS} + \frac{1}{2}(\rho_a - \rho_i) g \frac{z_n^2 - z_{AS}^2}{z_{SH} - z_{AS}} - \left(\rho_a + \frac{(\rho_a - \rho_i) z_{AS}}{z_{SH} - z_{AS}}\right) g(z_n - z_{AS}) = -\rho_a g z_n = P_e(z_n) \tag{H.15}$$

  Regrouping it with relation (H.3), we have simply

$$-P_i(0) = (\rho_a - \rho_i) g \frac{(z_n - z_{AS})^2}{4h_s} \tag{H.16}$$

  Thus the condition (H.12) negative is automatically valid and the condition (H.10) is equivalent to

$$\frac{(z_n - z_{AS})^2}{4h_s} < H - z_i \tag{H.17}$$

- **Case 3:** $P_e(z_{SH}) - P_i(z_{SH}) = 0$

  z_n will be equal to z_{SH}. In this case, both equations (H.14) and (H.16) will result in

$$-P_i(0) = (\rho_a - \rho_i) g h_s \tag{H.18}$$

H.2 Inlet/outlet velocity and flux

Bottom opening

The mean inlet velocity through the bottom opening is directly linked to the pressure loss $P_e(0) - P_i(0)$:

$$\rho_a \frac{u_b^2}{2c_b} = P_e(0) - P_i(0) = -P_i(0) \tag{H.19}$$

Applying above results (H.14) and (H.16), we have

$$u_b^2 = \begin{cases} 2c_b g'(z_n - z_i) & z_n \geq z_{SH} = z_i + h_s \\ 2c_b g' \frac{(z_n - z_{AS})^2}{4h_s} & z_n < z_{SH} = z_i + h_s \end{cases} \tag{H.20}$$

with g' environmental reduced gravity. Consequently,

$$Q_b = \begin{cases} S_b \sqrt{2c_b g'(z_n - z_i)} & z_n \geq z_i + h_s \\ S_b \sqrt{2c_b g' \frac{(z_n - z_i + h_s)^2}{4h_s}} & z_n < z_i + h_s \end{cases} \tag{H.21}$$

Top opening

Similarly, for top opening we have

$$\rho_i \frac{u_t^2}{2c_t} = P_i(H) - P_e(H) = P_i(0) - \rho_i g H - (\rho_a - \rho_i) g z_i + \rho_a g H = P_i(0) + (\rho_a - \rho_i) g (H - z_i) \quad \text{(H.22)}$$

Applying above results (H.14) and (H.16), we have

$$u_t^2 = \begin{cases} 2c_t g' \frac{\rho_a}{\rho_i} (H - z_n) & z_n \geq z_{SH} = z_i + h_s \\ 2c_t g' \frac{\rho_a}{\rho_i} \left((H - z_i) - \frac{(z_n - z_{AS})^2}{4h_s} \right) & z_n < z_{SH} = z_i + h_s \end{cases} \quad \text{(H.23)}$$

This quantity is always positive as condition (H.17) is valid in case $z_n < z_{SH}$. Consequently,

$$Q_t = \begin{cases} S_t \sqrt{2c_t g' \frac{\rho_a}{\rho_i} (H - z_n)} & z_n \geq z_i + h_s \\ S_t \sqrt{2c_t g' \frac{\rho_a}{\rho_i} \left((H - z_i) - \frac{(z_n - z_i + h_s)^2}{4h_s} \right)} & z_n < z_i + h_s \end{cases} \quad \text{(H.24)}$$

H.3 Conservation equations

The ventilation model is based on a series of conservation equations which are presented in this section. The conservation principle is first applied on the whole cavity: the volume flux, the mass flux and the species. Then particular conservation equations are established on the region $z > z_i$ or $z < z_i$ from steady flow pattern in the cavity.

Global conservation of volume flux and mass flux

Firstly, we have the conservation of volume flux in the whole cavity

$$Q_t = Q_b + Q_{inj} \quad \text{(H.25)}$$

and the global conservation of mass flux

$$\rho_i Q_t = \rho_a Q_b + \rho_{inj} Q_{inj} \quad \text{(H.26)}$$

Global conservation of species and buoyancy flux

Another equation is the conservation of species in the whole cavity, particularly that of injected light gas

$$Q_{inj} = Q_t X_{1,i} \quad \text{(H.27)}$$

Note that generally we have following relation

$$g' = \frac{\rho_a - \rho_i}{\rho_a} g = \frac{\rho_a - \rho_i}{\rho_a - \rho_{inj}} \frac{\rho_a - \rho_{inj}}{\rho_a} g = X_{1,i} G'(0) \quad \text{(H.28)}$$

The equation (H.29) is rewritten as

$$g' Q_t = G'(0) Q_{inj} = \mathcal{B}_0 \quad \text{(H.29)}$$

which is the global conservation of buoyancy flux in the cavity.

Conservation of volume flux for region $z > z_i$

Similar as in Linden's model, as the vertical velocity is assumed nearly zero except for jet region in stratified layer L_S, we have practically the conservation of volume flux in the region between any $z_{AS} < z < z_{SH}$ to H. Consequently

$$\text{For any } z \in [z_{AS}, z_{SH}],\ \ \mathcal{Q}(z) \approx Q_t \tag{H.30}$$

with $\mathcal{Q}(z)$ the jet volume flux, provided by jet models. Particularly this equation is valid for $z = z_i$ in which altitude environmental vertical velocity is considered strictly zero. Thus we have the conservation of volume flux for region $z > z_i$:

$$Q_t = \mathcal{Q}(z_i) \tag{H.31}$$

Conservation of species for region $z < z_i$

We consider the conservation of light gas for region $z < z_i$. In this region, the transportation of injected light gas with exterior is generated from convection and diffusion. For convection transportation:

- Inlet flow: fresh air thus no light gas
- Injection flow: pure light gas with volume flux Q_{inj}
- Jet flow at z_i: mixing gas with light gas volume flux $\mathcal{Q}(z_i)X_{1,T}(z_i)$.
- No convection flow outside jet region at $z = z_i$ as vertical velocity is zero at far-field.

For diffusion transportation, from Fick's law, diffusion flux goes from regions of high concentration (z_i^+) to regions of low concentration (z_i^-), with a magnitude that is proportional to the molar concentration (volume fraction) gradient.

- Diffusion flux is calculated from Fick's law:

$$J_{\text{diff}} = -D\frac{X_{1,i} - 0}{z_{SH} - z_{AS}} \tag{H.32}$$

  with D diffusion coefficient in m^2/s. The negative sign means the diffusion of light gas is towards z-negative direction.

Consequently, the conservation of light gas in region $z < z_i$ is written as follows, with $S_D = S_{cavity} - S_{jet}(z_i)$ the diffusion area (equal to total cross-section area minus jet cross-section area).

$$Q_{inj} + DS_D\frac{X_{1,i}}{2h_s} = \mathcal{Q}(z_i)X_{1,T}(z_i) \tag{H.33}$$

By multiplying the term $G'(0)$ on both sides and applying relation (H.28), we rewrite the above equation as

$$\mathcal{B}_0 + g'\frac{DS_D}{2h_s} = \mathcal{Q}(z_i)X_{1,T}(z_i)G'(0) = \mathcal{Q}(z_i)\frac{\rho_a - \rho_T(z_i)}{\rho_a}g = \mathcal{B}^*(z_i) \tag{H.34}$$

with $\mathcal{B}^*(z_i)$ the specific buoyancy flux at altitude $z = z_i$ in the jet. This specific buoyancy flux, which is defined in equation (7.11), is the jet buoyancy flux **as if the jet were immersed in an environment** ρ_a. Finally, this conservation equation is written as

$$g'\frac{DS_D}{2h_s} = \mathcal{B}^*(z_i) - \mathcal{B}_0 \tag{H.35}$$

Remark 1: Both sides of equation (H.35) shall be positive, thus $\mathcal{B}^*(z_i) > \mathcal{B}_0$. This may be a little strange. However, we shall note that $\mathcal{B}(0) = \mathcal{B}^*(0)$ but generally $\mathcal{B}(z) \neq \mathcal{B}^*(z)$ due to their different definitions. Here the increase of $\mathcal{B}^*$ is related to growth of jet volume flux (due to jet entrainment).

As $\rho_a > \rho_e(z)$ for any $z > 0$, we have in fact $\mathcal{B}^*(z_i) > \mathcal{B}_0 > \mathcal{B}(z_i)$. From figure 7.3, we can clearly find that the quantity $\mathcal{B}^*$ continuously increases in turbulent jet and plume regions.

Remark 2: Equation of diffusion (H.32) is established by Fick's law on light gas molar concentration (not mass). This is generally applied for gas diffusion. Therefore, we do have, through the diffusion area $S_D(z_i)$, the conservation of diffusion volume flux respectively for light-gas and air: $Q_{\text{diff},1} = Q_{\text{diff},2}$. However, this is not theoretically valid for diffusion mass flux $Q_{m,\text{diff},1} \neq Q_{m,\text{diff},2}$ due to density difference.

Consequently, the conservation of mass flux for region $z > z_i$ cannot be simply written as $\rho_i Q_t = \mathcal{Q}_m(z_i)$. And on the same time, the relation $g' = G'_T(z_i)$, which is assumed in original Linden's model, is not theoretically correct in this resolution.

DNS validation

Global conservation equations of volume flux, mass flux, species and buoyancy flux, as well as equation (H.31) have been already validated in chapter 7. We are interested in the estimation of h_s from equation (H.35) and comparison with its DNS estimated value calculated from table 5.1. Results are presented in following table. For helium case, this equation (H.35) is valid with only 1.5% error but it seems not for hydrogen case. This may be related to estimation accuracy difference of $B^{*DNS}(z_i^{BE})$ between two cases. Helium case is much more converged than hydrogen case. Its total simulation time is 3 times longer. As we have seen in figure 7.3, the quantity B^* is nearly constant equal to $\mathcal{B}_0$ below the interface so that a tiny error in its estimation at best-estimated interface height will generate large error in calculation of h_s.

	Hydrogen	**Helium**
$\mathcal{B}^{*DNS}(z_i^{BE}) - \mathcal{B}_0$ ($\times 10^{-4}$ m^3/s^2)	1.23	0.521
g'^{DNS} (m/s^2)	3.31	3.27
$S_D^{DNS}(z_i^{BE})$ (cm^2)	75.7	81.6
D ($\times 10^{-5}$m^2/s)	7.72	7.11
h_s from DNS - Table 5.1 (cm)	2.7	2
h_s from equation (H.35) (cm)	0.79	1.97
Relative error (%)	-70.7%	-1.5%

Table H.1: Calculation of demi-height of stratified layer h_s from three-layer ventilation model, comparison with DNS measured values.

H.4 System resolution

We have four parameters in this problem z_n, z_i, h_s, ρ_i (or g') and above four conservation equations. The resolution will be divided into three steps. Firstly, we apply global conservation equations (volume flux or mass flux) with expressions from section G.2 to eliminate z_n. Then we deduce the expression of Q_t with z_i. Secondly, we apply equation (H.31) to find z_i. The

variation $\mathcal{Q}(z)$ will be provided by jet models. We shall consider solving ODE of the jet evolution separately in unstratified and linear stratified environments. Finally, we apply equations (H.24), (H.29) and (H.35) to solve other parameters.

Solving global conservation equations

In order simplify mathematical formulations, we consider applying small injection assumption in the resolution. As presented in section 7.3, depended on the selected conservation principle (volume flux or mass flux), this small injection assumption may be applied on injection volume flux Q_{inj} or mass flux $Q_{m,inj}$.

Small volume injection flux

If injection volume flux is smaller enough (not valid for reference DNS cases), the term Q_{inj} may be neglected in global conservation of volume flux (H.25) and this equation will be rewritten simply as $Q_t = Q_b$. We regroup it with expressions of Q_b and Q_t obtained from section G.2, equations (H.21) and (H.24). We shall discuss two cases.

Case 1: $z_n > z_i + h_s$

The formulations of Q_b and Q_t are the same as presented in section 7.3.2 case 2.

Case 2: $z_n < z_i + h_s$

Note $z_n^* = z_i + \frac{(z_n - z_i + h_s)^2}{4h_s}$ and the formulations of Q_b and Q_t will be once again the same as presented in section 7.3.2 case 2 by changing z_n to z_n^*. The resolution will be the same as this term will be eliminated in the process.

Consequently, for both case, the outlet volume flux can be rewritten as

$$Q_t = A^* \sqrt{g'(H - z_i)} \tag{H.36}$$

with

$$A^* = \frac{\sqrt{c_t^*}\, S_b S_t}{\sqrt{\frac{1}{2}\left(\frac{c_t^*}{c_b} S_t^2 + S_b^2\right)}}, \quad c_t^* = c_t \frac{\rho_a}{\rho_i} \tag{H.37}$$

Small mass injection flux

In a general case, for light gas injection, the term $Q_{m,inj}$ may be neglected in global conservation of mass flux (H.26) and this equation will be rewritten simply as $\rho_i Q_t = \rho_a Q_b$. We regroup it with expressions of Q_b and Q_t obtained from section G.2, equations (H.21) and (H.24). The formulations of Q_b and Q_t are the same as presented in section 7.3.2 case 3 (by changing z_n to z_n^* in case $z_n < z_i + h_s$). However, an additional term will appear if we respect the similar definition of A.

$$Q_t = \frac{\rho_a}{\rho_i} A^{**} \sqrt{g'(H - z_i)} \tag{H.38}$$

with

$$A^{**} = \frac{\sqrt{c_t^{**}}\, S_b S_t}{\sqrt{\frac{1}{2}\left(\frac{c_t^{**}}{c_b} S_t^2 + S_b^2\right)}} \quad c_t^{**} = c_t \frac{\rho_i}{\rho_a} \tag{H.39}$$

General formula

We group above two cases into one formula for Q_t.

$$Q_t = \mathcal{A} \sqrt{g'(H - z_i)} \tag{H.40}$$

with $\mathcal{A}$ defined differently in two cases: it is equal to A^* in the first case and $A^{**}\rho_a/\rho_i$ in the second case.

Jet solutions

The second step is to provide jet solutions in order to regroup it with conservation equations. The resolution will be divided into two parts: in L_A (and L_H), the jet is immersed in an unstratified environment while in L_S, it is in linear stratified environment where $\rho_e(z)$ changes linearly with altitude. We have presented different unstratified solutions in section 7.3.3. However, for linear environment, this resolution is not evident as jet equations are generally non-linear. Specific analytical solutions are usually obtained from dimensional analysis, and we are even not sure if explicit analytical solutions exist.

For illustration, we reconsider Morton's equations for a general Boussinesq jet.

$$\frac{d\mathcal{Q}}{dz} = 2\alpha_T\sqrt{\pi\mathcal{M}}, \quad \frac{d\mathcal{M}}{dz} = \frac{\mathcal{B}\mathcal{Q}}{\mathcal{M}}, \quad \frac{d\mathcal{B}}{dz} = -N^2\mathcal{Q} \tag{H.41}$$

In linear stratified environment, the term $N^2 = -\frac{g}{\rho_a}\frac{d\rho_e}{dz} = \frac{g}{\rho_a}\frac{\rho_a-\rho_i}{2h_s} > 0$ is a positive constant. We consider power function form for three characteristic jet quantities:

$$\mathcal{Q}(z) = Q^{\#}(z-l_s)^q, \quad \mathcal{M}(z) = M^{\#}(z-l_s)^m, \quad \mathcal{B}(z) = B^{\#}(z-l_s)^b, \tag{H.42}$$

with l_s a constant length. By identification, we have $b = m = 4$ and $q = 3$. Thus, the third equation in (H.41) can be rewritten as $4B^{\#} = -N^2Q^{\#}$. As $N^2 > 0$, $Q^{\#}$ and $B^{\#}$ must be in different signs. This is not possible as both quantities must be positive.

The above analysis illustrates the difficulty to find explicit analytical jet solutions in linear stratified environment. By default, the numerical ODE resolution (e.g. RK4) shall be used.

Summary

We summarise here the resolution process. We have three unknown variables z_i, h_s, g', and three conservation equations (H.29), (H.31) and (H.35). Replacing Q_t by equation (H.40) and regrouping (H.29) and (H.31), these conservation equations can be rewritten as follows.

$$\begin{cases} z_i = H - \dfrac{\mathcal{B}_0^2}{g'^3\mathcal{A}^2} \\ \dfrac{\mathcal{B}_0}{g'} = \mathcal{Q}(z_i) \\ g'\dfrac{DS_D}{2h_s} + \mathcal{B}_0 = \mathcal{B}^*(z_i) \end{cases} \tag{H.43}$$

This system could be solved numerically by a double-iteration method. We first consider solving light gas injection problem by bi-layer methods as presented in chapter 7. The obtained z_i and g' will be used for first iteration in resolution of three-layer model. The initial h_s can be determined from the third equation in (H.43).

For iteration n, we have $z_i^{(n)}, g'^{(n)}, h_s^{(n)}$ as input. We solve firstly the evolution of jet volume flux $\mathcal{Q}(z)$ by using turbulent jet model dedicated to stratified environment $\rho_e(z)$ in equation (H.1), as presented in chapter 6. The resolution may be based on α-constant models as quasi-analytical approaches presented in section 6.1.3 and section 6.2.1. We may also consider using α-variable model as presented in section 6.3.3. Once we obtain the jet evolution, we consider solve the equation $\frac{\mathcal{B}_0}{g'} = \mathcal{Q}\left(H - \frac{\mathcal{B}_0^2}{g'^3\mathcal{A}^2}\right)$ for $g'^{(n+1)}$. Note that here g' is coupled in the term $\mathcal{A}$, this step may be done by a second iteration. Once $g'^{(n+1)}$ is determined, $z_i^{(n+1)}, h_s^{(n+1)}$ will be deduced respectively by the first and the third equations. Iteration will stop if the absolute differences between two consecutive solutions are within the defined threshold.

Bibliography

Abdalla, I. E., Cook, M. J., and Hunt, G. R. (2009). Numerical study of thermal plume characteristics and entrainment in an enclosure with a point heat source. *Engineering Applications of Computational Fluid Mechanics*, 3(4):608–630.

Angeli, P.-E., Bieder, U., and Fauchet, G. (2015). Overview of the TrioCFD code: main features, v&v procedures and typical applications to nuclear engineering. In *Proceedings of 16th International Topical Meeting on Nuclear Reactor Thermal Hydraulics (NURETH-16), Chicago, USA*.

Antonia, R., Browne, L., Rajagopalan, S., and Chambers, A. (1983). On the organized motion of a turbulent plane jet. *Journal of fluid mechanics*, 134:49–66.

Arcipreti, P. (2006). Air-steam condensation modelling in CFD codes - effect of light gas addiction. *Technical Report CEA/DEN*.

Baines, W. and Turner, J. (1969). Turbulent buoyant convection from a source in a confined region. *Journal of Fluid mechanics*, 37(01):51–80.

Bastiaans, R. J., Rindt, C., Nieuwstadt, F., and Van Steenhoven, A. (2000). Direct and large-eddy simulation of the transition of two-and three-dimensional plane plumes in a confined enclosure. *International journal of heat and mass transfer*, 43(13):2375–2393.

Bastiaans, R. J., Rindt, C., and Van Steenhoven, A. (1998). Experimental analysis of a confined transitional plume with respect to subgrid-scale modelling. *International journal of heat and mass transfer*, 41(23):3989–4007.

Batchelor, G. K. (1953). *The theory of homogeneous turbulence*. Cambridge university press.

Bauwens, C. and Dorofeev, S. (2014). CFD modeling and consequence analysis of an accidental hydrogen release in a large scale facility. *International journal of hydrogen energy*, 39(35):20447–20454.

Bernard-Michel, G. (2012). Rapport d'essais regroupant l'ensemble des résultats expérimentaux obtenus sur les sujets en milieu confiné. *CEA Technical Report*.

Bernard-Michel, G. (2014). Analyses des expériences Grand GAMELAN et modèles sur la distribution de concentration d'hélium : dispositif à deux évents. *CEA Technical Report*.

Bernard-Michel, G., Cariteau, B., Ni, J., Jallais, S., Vyazmina, E., Melideo, D., Baraldi, D., and Venetsanos, A. (2013). CFD benchmark based on experiments of helium dispersion in a 1 m3 enclosure–intercomparisons for plumes. *International Conference on Hydrogen Safety*.

Bernard-Michel, G. and Houssin-Agbomson, D. (2017). Comparison of helium and hydrogen releases in 1 m3 and 2 m3 two vents enclosures: Concentration measurements at different flow rates and for two diameters of injection nozzle. *International Journal of Hydrogen Energy*, 42(11):7542–7550.

Bernard-Michel, G., Saikali, E., and Houssin, D. (2017). Experimental measurements, CFD simulations and model for a helium release in a two vents enclosure. In *Proceeding of the International Conference on Hydrogen Safety, Hamburg, Germany*.

Bernard-Michel, G., Saikali, E., Sergent, A., and Tenaud, C. (2019). Comparisons of experimental measurements and large eddy simulations for a helium release in a two vents enclosure. *International Journal of Hydrogen Energy*, 44:8935 – 8953.

Bernard-Michel, G., Trochon, J., Vyazmina, E., and Gentilhomme, O. (2012). Résultat du benchmark ventilation sur 3 essais GAMELAN dans le cadre du projet ANR Dimitrhy. *CEA Technical Report*.

Bieder, U. (2007). Methodology for incompressible single phase flow in industrial applications. *CEA Technical Report*.

Bird, R. B., Stewart, W. E., and Lightfoot, E. N. (2007). *Transport Phenomena*. John Wiley & Sons.

Bloomfield, L. J. and Kerr, R. C. (2000). A theoretical model of a turbulent fountain. *Journal of Fluid Mechanics*, 424:197–216.

Boussinesq, J. (1897). *Théorie de l'écoulement tourbillonnant et tumultueux des liquides dans les lits rectilignes à grande section*, volume 1. Gauthier-Villars.

Brébec, J., Desmarais, T., Favier, A., Menetrier, M., Noel, B., Noel, R., Orsini, C., and Vanhaecke, J. (1998). *Mécanique des fluides : 2e année MP-MP*-PC-PC*, PSI-PSI*-PT-PT*. Hprépa, Hachette.

Brébec, J.-M., Desmarais, T., and Favier, A. (2004). *Thermodynamique : 2e année MP-MP*-PC-PC*, PSI-PSI*-PT-PT*. Hprépa, Hachette.

Candelier, F. and Vauquelin, O. (2012). Matched asymptotic solutions for turbulent plumes. *Journal of fluid mechanics*, 699:489–499.

Carasik, L., Sebilleau, F., Walker, S., and Hassan, Y. (2015). URANS simulations of thermal stratification in a large enclosure for severe accident scenarios. In *Proc. 16th International Topical Meeting on Nuclear Reactor Thermal Hydraulics (NURETH'16), Chicago, USA*, pages 1394–1407.

Carazzo, G., Kaminski, E., and Tait, S. (2006). The route to self-similarity in turbulent jets and plumes. *Journal of Fluid Mechanics*, 547:137–148.

Carazzo, G., Kaminski, E., and Tait, S. (2008). On the rise of turbulent plumes: Quantitative effects of variable entrainment for submarine hydrothermal vents, terrestrial and extra terrestrial explosive volcanism. *Journal of Geophysical Research: Solid Earth*, 113(B9).

Carazzo, G., Kaminski, E., and Tait, S. (2010). The rise and fall of turbulent fountains: a new model for improved quantitative predictions. *Journal of fluid mechanics*, 657:265–284.

Cariteau, B. (2010a). Dispersion de rejets d'hélium dans une enceinte : ventilation naturelle par un évent. *CEA Technical Report*.

Cariteau, B. (2010b). Résultats expérimentaux sur les régimes de dispersion d'un jet d'hélium dans une enceinte. *CEA Technical Report*.

Cariteau, B. (2012). Dispersion de rejets d'hélium dans une enceinte : ventilation naturelle par deux évents. *CEA Technical Report*.

Cariteau, B., Brinster, J., and Tkatschenko, I. (2011). Experiments on the distribution of concentration due to buoyant gas low flow rate release in an enclosure. *International Journal of Hydrogen Energy*, 36(3):2505–2512.

Cariteau, B. and Tkatschenko, I. (2012). Experimental study of the concentration build-up regimes in an enclosure without ventilation. *International Journal of Hydrogen Energy*, 37(22):17400–17408.

Cariteau, B. and Tkatschenko, I. (2013). Experimental study of the effects of vent geometry on the dispersion of a buoyant gas in a small enclosure. *International Journal of Hydrogen Energy*, 38(19):8030 – 8038.

Carlotti, P. and Hunt, G. (2017). An entrainment model for lazy turbulent plumes. *Journal of Fluid Mechanics*, 811:682–700.

Carlotti, P. and Hunt, G. R. (2005). Analytical solutions for turbulent non-boussinesq plumes. *Journal of Fluid Mechanics*, 538:343–359.

Caulfield, C.-C. P. and Woods, A. W. (1995). Plumes with non-monotonic mixing behaviour. *Geophysical & Astrophysical Fluid Dynamics*, 79(1-4):173–199.

Caulfield, C. P. (1991). *Stratification and buoyancy in geophysical flows*. PhD thesis, University of Cambridge.

Cetegen, B. M. and Kasper, K. D. (1996). Experiments on the oscillatory behavior of buoyant plumes of helium and helium-air mixtures. *Physics of fluids*, 8(11):2974–2984.

Chen, C. and Rodi, W. (1980a). *Vertical Turbulent Buoyant Jets: HMT, the Science and Applications of Heat and Mass Transfer Series*. Elsevier Science & Technology.

Chen, C. J. and Rodi, W. (1980b). Vertical turbulent buoyant jets: a review of experimental data. *NASA STI/Recon Technical Report A*, 80.

Chhabra, S., Huq, P., and Prasad, A. K. (2006). Characteristics of small vortices in a turbulent axisymmetric jet. *Journal of fluids engineering*, 128(3):439–445.

Cleaver, R., Marshall, M., and Lindenb, P. (1994). The build-up of concentration within a single enclosed volume following a release of natural gas. *Journal of Hazardous Materials*, 36:226–246.

Coffey, C. and Hunt, G. (2010). The unidirectional emptying box. *Journal of fluid mechanics*, 660:456–474.

Crapper, P. and Baines, W. (1977). Non Boussinesq forced plumes. *Atmospheric Environment (1967)*, 11(5):415–420.

Craske, J. and Hughes, G. O. (2019). On the robustness of emptying filling boxes to sudden changes in the wind. *Journal of Fluid Mechanics*, pages 868–884.

Craske, J., Salizzoni, P., and van Reeuwijk, M. (2017). The turbulent Prandtl number in a pure plume is 3/5. *Journal of Fluid Mechanics*, 822:774–790.

Craske, J. and van Reeuwijk, M. (2015a). Energy dispersion in turbulent jets. Part 1. Direct simulation of steady and unsteady jets. *Journal of Fluid Mechanics*, 763:500–537.

Craske, J. and van Reeuwijk, M. (2015b). Energy dispersion in turbulent jets. Part 2. A robust model for unsteady jets. *Journal of Fluid Mechanics*, 763:538–566.

Craske, J. and van Reeuwijk, M. (2016). Generalised unsteady plume theory. *Journal of Fluid Mechanics*, 792:1013–1052.

De Forme, E. (2010). *Principes des transferts convectifs*. Société Française de Thermique.

Devenish, B., Rooney, G., and Thomson, D. (2010). Large-eddy simulation of a buoyant plume in uniform and stably stratified environments. *Journal of Fluid Mechanics*, 652:75–103.

Edwards, P., Kuznetsov, V., David, W., and Brandon, N. (2008). Hydrogen and fuel cells: Towards a sustainable energy future. *Energy Policy*, 36:4356 – 4362.

El-Amin, M. (2009). Non-Boussinesq turbulent buoyant jet resulting from hydrogen leakage in air. *International Journal of Hydrogen Energy*, 34(18):7873–7882.

El-Amin, M. F., Sun, S., and Kanayama, H. (2010). Non-Boussinesq turbulent buoyant jet of a low-density gas leaks into high-density ambient. *Applied Mathematics and computation*, 217(8):3764–3778.

Elicer-Cortés, J., Fuentes, J., Valencia, A., and Baudet, C. (2000). Experimental study of transition to turbulence of a round thermal plume by ultrasound scattering. *Experimental thermal and fluid science*, 20(3-4):137–149.

Ezzamel, A., Salizzoni, P., and Hunt, G. R. (2015). Dynamical variability of axisymmetric buoyant plumes. *Journal of Fluid Mechanics*, 765:576–611.

Fischer, H. B., List, J. E., Koh, C. R., Imberger, J., and Brooks, N. H. (1979). *Mixing in inland and coastal waters*. Elsevier.

Fuster, B., Houssin-Agbomson, D., Jallais, S., Vyazmina, E., Dang-Nhu, G., Bernard-Michel, G., Kuznetsov, M., Molkov, V., Chernyavskiy, B., Shentsov, V., et al. (2015). Pre-normative research on the indoor use of fuel cells and hydrogen systems. *HyIndoor Project Deliverables*.

Fuster, B., Houssin-Agbomson, D., Jallais, S., Vyazmina, E., Dang-Nhu, G., Bernard-Michel, G., Kuznetsov, M., Molkov, V., Chernyavskiy, B., Shentsov, V., et al. (2017). Guidelines and recommendations for indoor use of fuel cells and hydrogen systems. *International Journal of Hydrogen Energy*, 42(11):7600–7607.

Gai, G. (2020). *Modeling of water sprays effects on premixed hydrogen-air explosion, turbulence and shock waves*. PhD thesis, Normandy University.

Giannissi, S., Shentsov, V., Melideo, D., Cariteau, B., Baraldi, D., Venetsanos, A., and Molkov, V. (2015). CFD benchmark on hydrogen release and dispersion in confined, naturally ventilated space with one vent. *International Journal of Hydrogen Energy*, 40(5):2415–2429.

Guermond, J.-L., Minev, P., and Shen, J. (2006). An overview of projection methods for incompressible flows. *Computer methods in applied mechanics and engineering*, 195(44):6011–6045.

Harlow, F. H., Welch, J. E., et al. (1965). Numerical calculation of time-dependent viscous incompressible flow of fluid with free surface. *Physics of fluids*, 8(12):2182.

Haynes, W. M. (2014). *CRC handbook of chemistry and physics*, volume 7. CRC press.

Hirsch, C. (2007). *Numerical Computation of Internal and External Flows: Fundamentals of Numerical Discretization*, volume 1. Butterworth-Heinemann.

Holford, J. M. and Hunt, G. R. (2001). The dependence of the discharge coefficient on density contrast–experimental measurements. In *Proceedings 14th Australasian Fluid Mechanics Conference (ed. BB Dally)*, pages 123–126.

Houssin, D. (2012). Ventilation naturelle par double évents. *Air Liquide Technical Report*.

Hunt, G. and Coffey, C. (2010). Emptying boxes–classifying transient natural ventilation flows. *Journal of Fluid Mechanics*, 646:137–168.

Hunt, G. and Kaye, N. (2001). Virtual origin correction for lazy turbulent plumes. *Journal of Fluid Mechanics*, 435:377–396.

Hunt, G. and Kaye, N. (2005). Lazy plumes. *Journal of Fluid Mechanics*, 533:329–338.

Hunt, G. and Linden, P. (1999). The fluid mechanics of natural ventilation-displacement ventilation by buoyancy-driven flows assisted by wind. *Building and Environment*, 34(6):707–720.

Hunt, G. and Linden, P. (2001). Steady-state flows in an enclosure ventilated by buoyancy forces assisted by wind. *Journal of Fluid Mechanics*, 426:355–386.

Hunt, G. and Linden, P. F. (2005). Displacement and mixing ventilation driven by opposing wind and buoyancy. *Journal of Fluid Mechanics*, 527:27–55.

Hunt, G. and Van den Bremer, T. (2011). Classical plume theory: 1937–2010 and beyond. *IMA journal of applied mathematics*, 76(3):424–448.

Hunt, G. R. and Holford, J. M. (2000). The discharge coefficient–experimental measurement of a dependence on density contrast. In *Proc. 21st AIVC Conference, The Hague, Netherlands*, pages 12–24.

IEA (2019). *The Future of Hydrogen*. World Energy Outlook 2019, IEA, Paris https://www.iea.org/reports/world-energy-outlook-2019 (18 Mar 2020).

Jallais, S. (2010). Assessment of engineering natural ventilation models. *Air Liquide Technical Report*.

Jallais, S., Vyazmina, E., Miller, D., and Thomas, J. K. (2018). Hydrogen jet vapor cloud explosion: a model for predicting blast size and application to risk assessment. *Process safety progress*, 37(3):397–410.

Jirka, G. H. (2004). Integral model for turbulent buoyant jets in unbounded stratified flows. Part 1: Single round jet. *Environmental Fluid Mechanics*, 4(1):1–56.

Kaminski, E., Tait, S., and Carazzo, G. (2005). Turbulent entrainment in jets with arbitrary buoyancy. *Journal of Fluid Mechanics*, 526:361–376.

Kaye, N. (2008). Turbulent plumes in stratified environments: a review of recent work. *Atmosphere-ocean*, 46(4):433–441.

Kaye, N. and Hunt, G. (2004). Time-dependent flows in an emptying filling box. *Journal of Fluid Mechanics*, 520:135–156.

Kleinstreuer, C. (1997). *Engineering fluid dynamics: an interdisciplinary systems approach*. Cambridge University Press.

Kotsovinos, N. E. (1975). A study of the entrainment and turbulence in a plane buoyant jet. *California Institute of Technology*.

Kotsovinos, N. E. (1976). A note on the spreading rate and virtual origin of a plane turbulent jet. *Journal of Fluid Mechanics*, 77(2):305–311.

Lee, J. and Chu, V. (2003). *Turbulent Jets and Plumes: A Lagrangian Approach*. Springer US.

Lee, S.-L. and Emmons, H. (1961). A study of natural convection above a line fire. *Journal of Fluid Mechanics*, 11(3):353–368.

Lemmon, E. W. and Jacobsen, R. (1999). A generalized model for the thermodynamic properties of mixtures. *International journal of thermophysics*, 20(3):825–835.

L'Hostis, B., Houssin-Agbomson, D., Jallais, S., Vyazmina, E., Dang-Nhu, G., Shentsov, D., Dey, R., Hooker, P., Baraldi, D., Weidner, E., et al. (2012). Indoor use of fuel cells and hydrogen systems. *HyIndoor Project Deliverable Report*.

Linden, P. (2000). *Perspectives in fluid dynamics: A collective introduction to current research – Convection in the environment*, pages 289–345. Cambridge University Press.

Linden, P., Lane-Serff, G., and Smeed, D. (1990). Emptying filling boxes: the fluid mechanics of natural ventilation. *Journal of Fluid Mechanics*, 212:309–335.

Linden, P. F. (1999). The fluid mechanics of natural ventilation. *Annual review of fluid mechanics*, 31(1):201–238.

List, E. (1982). Mechanics of turbulent buoyant jets and plumes. In *Turbulent buoyant jets and plumes*, pages 1–68. Elsevier.

Mahaffy, J., Chung, B., Song, C., Dubois, F., Graffard, E., Ducros, F., Heitsch, M., Scheuerer, M., Henriksson, M., Komen, E., et al. (2015). Best practice guidelines for the use of cfd in nuclear reactor safety applications-revision. Technical report, Organisation for Economic Co-Operation and Development.

Marrero, T. and Mason, E. (1973). Correlation and prediction of gaseous diffusion coefficients. *AIChE Journal*, 19(3):498–503.

Marrero, T. R. and Mason, E. A. (1972). Gaseous diffusion coefficients. *Journal of Physical and Chemical Reference Data*, 1(1):3–118.

McNaught, A., Wilkinson, A., of Pure, I. U., and Chemistry, A. (1997). *Compendium of Chemical Terminology: IUPAC Recommendations*. IUPAC Chemical Data Series. Blackwell Science.

Mehaddi, R., Vauquelin, O., and Candelier, F. (2012). Analytical solutions for turbulent Boussinesq fountains in a linearly stratified environment. *Journal of Fluid Mechanics*, 691:487–497.

Merilo, E., Groethe, M., Colton, J., and Chiba, S. (2011). Experimental study of hydrogen release accidents in a vehicle garage. *International Journal of Hydrogen Energy*, 36(3):2436–2444.

Michaux, G. and Vauquelin, O. (2010). Résolution analytique des équations du panache turbulent. In *SFT 2010*, pages Cd–Rom.

Ministère de l'Économie et des Finances, R. F. (2020). Stratégie nationale pour le développement de l'hydrogène décarboné en france. *Dossier de presse*.

Mohr, P., Taylor, B., and Newell, D. (1998). Codata recommanded values of the fundamental physical constants. *National Institute of Standards and Technology*, pages 8099–8104.

Molkov, V. and Shentsov, V. (2014). Numerical and physical requirements to simulation of gas release and dispersion in an enclosure with one vent. *International journal of hydrogen energy*, 39(25):13328–13345.

Morton, B. . (1959). Forced plumes. *Journal of Fluid mechanics*, 5(1):151–163.

Morton, B. (1967). Entrainment models for laminar jets, plumes, and wakes. *The Physics of Fluids*, 10(10):2120–2127.

Morton, B., Taylor, G. I., and Turner, J. S. (1956). Turbulent gravitational convection from maintained and instantaneous sources. *Proceedings of the Royal Society of London. Series A. Mathematical and Physical Sciences*, 234(1196):1–23.

Müller, B. (1998). Low-Mach-number asymptotics of the Navier-Stokes equations. In *Floating, Flowing, Flying*, pages 97–109. Springer.

Munson, B., Rothmayer, A., and Okiishi, T. (2012). *Fundamentals of Fluid Mechanics, 7th Edition*. John Wiley & Sons, Incorporated.

Neufeld, P. D., Janzen, A., and Aziz, R. (1972). Empirical equations to calculate 16 of the transport collision integrals ω (l, s)* for the lennard-jones (12–6) potential. *The Journal of Chemical Physics*, 57(3):1100–1102.

Ngondiep, A., Gonzalez, M., Patte-Rouland, B., and Paranthoën, P. (2012). Flows produced by a forced plume in a ventilated enclosure. In *Journal of Physics: Conference Series*, volume 395, page 012097. IOP Publishing.

Paillat, S. and Kaminski, E. (2014). Entrainment in plane turbulent pure plumes. *Journal of Fluid Mechanics*, 755-763.

Papanicolaou, P. N. and List, E. J. (1988). Investigations of round vertical turbulent buoyant jets. *Journal of Fluid Mechanics*, 195:341–391.

Papanicolaou, P. N., Papakonstantis, I. G., and Christodoulou, G. C. (2008). On the entrainment coefficient in negatively buoyant jets. *Journal of Fluid Mechanics*, 614:447–470.

Papanikolaou, E. and Venetsanos, A. (2005). CFD modelling for helium releases in a private garage without forced ventilation. *Proceedings of the Fist ICHS, Pisa, Italy*, pages 8–10.

Paranthoën, P. and Gonzalez, M. (2010). Mixed convection in a ventilated enclosure. *International Journal of Heat and Fluid Flow*, 31(2):172–178.

Parker, D., Burridge, H. C., Partridge, J., and Linden, P. (2020). A comparison of entrainment in turbulent line plumes adjacent to and distant from a vertical wall. *Journal of Fluid Mechanics*, 882-899.

Pham, M., Plourde, F., and Doan, K. (2007). Direct and large-eddy simulations of a pure thermal plume. *Physics of Fluids*, 19(12):125103.

Plourde, F., Pham, M. V., Kim, S. D., and Balachandar, S. (2008). Direct numerical simulations of a rapidly expanding thermal plume: structure and entrainment interaction. *Journal of Fluid Mechanics*, 604:99–123.

Prasad, K., Pitts, W., and Yang, J. (2010). Effect of wind and buoyancy on hydrogen release and dispersion in a compartment with vents at multiple levels. *International journal of hydrogen energy*, 35(17):9218–9231.

Prasad, K., Pitts, W. M., and Yang, J. C. (2011). A numerical study of the release and dispersion of a buoyant gas in partially confined spaces. *International Journal of Hydrogen Energy*, 36(8):5200–5210.

Prasad, K. and Yang, J. (2011). Vertical release of hydrogen in a partially enclosed compartment: Role of wind and buoyancy. *International Journal of Hydrogen Energy*, 36(1):1094–1106.

Press, W. H., Teukolsky, S. A., Vetterling, W. T., and Flannery, B. P. (2007). *Numerical recipes 3rd edition: The art of scientific computing*. Cambridge university press.

Priestley, C. and Ball, F. (1955). Continuous convection from an isolated source of heat. *Quarterly Journal of the Royal Meteorological Society*, 81(348):144–157.

Ramaprian, B. and Chandrasekhara, M. (1989). Measurements in vertical plane turbulent plumes. *J. Fluids Eng.*

Reid, R. C., Prausnitz, J. M., and Poling, B. E. (1987). *The properties of gases and liquids*. McGraw Hill Book Co., New York, USA.

Richardson, L. (1922). *Weather Prediction by Numerical Process*. Cambridge University Press.

Richardson, L. F. (1911). Ix. the approximate arithmetical solution by finite differences of physical problems involving differential equations, with an application to the stresses in a masonry dam. *Philosophical Transactions of the Royal Society of London. Series A, Containing Papers of a Mathematical or Physical Character*, 210(459-470):307–357.

Roache, P. J. (1998). *Verification and validation in computational science and engineering*, volume 895. Hermosa Albuquerque, NM, USA.

Rooney, G. and Linden, P. (1996). Similarity considerations for non-Boussinesq plumes in an unstratified environment. *Journal of Fluid Mechanics*, 318:237–250.

Rooney, G. and Linden, P. (1997). Strongly buoyant plume similarity and 'small-fire'ventilation. *Fire Safety Journal*, 29(4):235–258.

Rouse, H., Yih, C. S., and Humphreys, H. W. (1952). Gravitational convection from a boundary source. *Tellus*, 4(3):201–210.

Roux, M. (2017a). *TRUST/TrioCFD V1.7.6 Developer's training session*. CEA Technical Report.

Roux, M. (2017b). *TRUST/TrioCFD V1.7.6 User's training session*. CEA Technical Report.

Saad, Y. (2003). *Iterative methods for sparse linear systems*. SIAM.

Saikali, E. (2018). *Numerical modelling of an air-helium buoyant jet in a two vented enclosure*. PhD thesis, Sorbonne Université.

Saikali, E., Bernard-Michel, G., Sergent, A., Tenaud, C., and Salem, R. (2019). Highly resolved large eddy simulations of a binary mixture flow in a cavity with two vents: Influence of the computational domain. *International Journal of Hydrogen Energy*, 44(17):8856 – 8873.

Saikali, E., Sergent, A., Bernard-Michel, G., and Tenaud, C. (2017). Large eddy simulations of an air-helium buoyant jet in a two vented enclosure: influence of the outlet boundary condition. In *Proceeding of the 23ème Congrès Français de Mécanique, Lille, France*.

Saikali, E., Sergent, A., Wang, Y., Le Quéré, P., Bernard-Michel, G., and Tenaud, C. (2020). A well-resolved numerical study of a turbulent buoyant helium jet in a highly-confined two-vented enclosure. *International Journal of Heat and Mass Transfer*, 163:120470.

Salizzoni, P., Mathieu, C., Samuel, V., John D., C., and Reeuwijk, M. V. (2017). Etude du phénomène d'entrainement dans des jets turbulents dits Non-Boussinesq. In *Proceeding of the 23ème Congrès Français de Mécanique, Lille, France*.

Savitzky, A. and Golay, M. J. (1964). Smoothing and differentiation of data by simplified least squares procedures. *Analytical chemistry*, 36(8):1627–1639.

Scase, M. and Hewitt, R. (2012). Unsteady turbulent plume models. *Journal of fluid mechanics*, 697:455–480.

Shabbir, A. and George, W. K. (1994). Experiments on a round turbulent buoyant plume. *Journal of Fluid Mechanics*, 275:1–32.

Spicker, J. and Feitzinger, J. (1988). Improved methods for turbulence in astrophysics. *Astronomy and Astrophysics*, 191:186–192.

Thomas, L., Marino, B., Tovar, R., and Linden, P. (2008). Buoyancy-driven flow between two rooms coupled by two openings at different levels. *Journal of Fluid Mechanics*, 594:425–443.

Tran, H. L. (2013). *Numerical modelling of natural convection of binary mixtures: case of a helium buoyant jet in an air-filled enclosure*. Phd thesis, Université Pierre et Marie Curie - Paris VI.

Tritton, D. J. (2012). *Physical fluid dynamics*. Springer Science & Business Media.

Turrin, M. (2008). Review of chemical and physical properties of air, steam, helium and hydrogen mixtures. *Technical Report CEA/DEN*.

Van Den Bremer, T. and Hunt, G. (2010). Universal solutions for Boussinesq and non-Boussinesq plumes. *Journal of fluid mechanics*, 644:165–192.

Van Den Bremer, T. and Hunt, G. (2014). Two-dimensional planar plumes: non-Boussinesq effects. *Journal of fluid mechanics*, 750:245–258.

Van Reeuwijk, M. and Craske, J. (2015). Energy-consistent entrainment relations for jets and plumes. *Journal of Fluid Mechanics*, 782:333–355.

Van Reeuwijk, M., Salizzoni, P., Hunt, G. R., and Craske, J. (2016). Turbulent transport and entrainment in jets and plumes: A DNS study. *Physical Review Fluids*, 1(7):074301.

Vandroux, S. and Barthel, V. (2013). TrioU code validation data base: Best practice guidelines. *CEA Technical Report*.

Vauquelin, O. (2015). Oscillatory behaviour in an emptying–filling box. *Journal of Fluid Mechanics*, 781:712–726.

Vauquelin, O., Koutaiba, E., Blanchard, E., and Fromy, P. (2017a). The discharge plume parameter and its implications for an emptying–filling box. *Journal of Fluid Mechanics*, 817:171–182.

Vauquelin, O., Mehaddi, R., Casalé, E., and Valério, E. (2017b). Non-Boussinesq experiments on natural ventilation in a 2d semi-confined enclosure. *International Journal of Heat and Fluid Flow*, 65:323–327.

Vaux, S., Mehaddi, R., Vauquelin, O., and Candelier, F. (2019). Upward versus downward non-Boussinesq turbulent fountains. *Journal of Fluid Mechanics*, 867:374–391.

Versteeg, H. K. and Malalasekera, W. (2007). *An introduction to computational fluid dynamics: the finite volume method*. Pearson Education.

Veser, A., Kuznetsov, M., Fast, G., Friedrich, A., Kotchourko, N., Stern, G., Schwall, M., and Breitung, W. (2011). The structure and flame propagation regimes in turbulent hydrogen jets. *international journal of hydrogen energy*, 36(3):2351–2359.

Wang, H. and Law, A. W.-k. (2002). Second-order integral model for a round turbulent buoyant jet. *Journal of Fluid Mechanics*, 459:397–428.

Wang, Y., Sergent, A., Bernard-Michel, G., Le Quéré, P., and Saikali, E. (2019). Numerical assessment of confinement effect and flow structure in case of hydrogen release in a two-vented cavity. In Meyer, P., editor, *International Conference on Heat Transfer, Fluid Mechanics and Thermodynamics*, Wicklow, Ireland. P. Meyer.

Wesseling, P. (1995). Introduction to multigrid methods. *NASA technical report,*.

Wilke, C. (1950). A viscosity equation for gas mixtures. *The journal of chemical physics*, 18(4):517–519.

Williams, F. (1965). *Combustion Theory*. Addison-Wesley series in engineering sciences. Addison-Wesley Publishing Company.

Woodhouse, M. J., Phillips, J. C., and Hogg, A. J. (2016). Unsteady turbulent buoyant plumes. *Journal of Fluid Mechanics*, 794:595–638.

Woods, A. W. (1997). A note on non-Boussinesq plumes in an incompressible stratified environment. *Journal of Fluid Mechanics*, 345:347–356.

Woods, A. W., Caulfield, C., and Phillips, J. C. (2003). Blocked natural ventilation: the effect of a source mass flux. *Journal of Fluid Mechanics*, 495:119–133.

Wykes, M. S. D., Hogg, C., Partridge, J., and Hughes, G. O. (2019). Energetics of mixing for the filling box and the emptying-filling box. *Environmental Fluid Mechanics*, 19(4):819–831.

Xiao, J., Travis, J., and Breitung, W. (2009). Non-Boussinesq integral model for horizontal turbulent buoyant round jets. *Science and Technology of Nuclear Installations*, 2009.

Yuana, L.-M. and Cox, G. (1996). An experimental study of some line fires. *Fire Safety Journal*, 27(2):123–139.